Developments in composition and processing for MnAl - system alloys for permanent magnetic material applications

Elizabeth Veronica Davis-Fowell

Department of Materials Science and Engineering
University of Sheffield

This thesis is submitted for the degree of
Doctor of Philosophy

November 2024

I would like to dedicate this thesis to my loving mother, without whom none of this would have ever been possible, my ever-suffering colleagues in the FMM group and my supervisor, Professor Russell Goodall for his unending support on both this project and surviving a pandemic, endless health issues and the general ennui of being someone in their late 20s trying to find their way in another global economic crisis. Oh, and to myself, seeing as I wrote this and did all of the experimental work to fill it. Go me!

Declaration

I hereby declare that except where specific reference is made to the work of others, the contents of this dissertation are original and have not been submitted in whole or in part for consideration for any other degree or qualification in this, or any other university. This dissertation is my own work and contains nothing which is the outcome of work done in collaboration with others, except as specified in the text and Acknowledgements. This dissertation contains fewer than 80,000 words including appendices, bibliography, footnotes, tables and equations and has fewer than 150 figures.

Elizabeth Veronica Davis-Fowell
November 2024

Acknowledgements

And I would like to acknowledge Professors Russell Goodall, Daniel Allwood and Nicola Morely for their guidance and supervision during this project, Mr. Neil Hinds and Dr. Lisa Holland for their assistance in heat treatments and fabrication, Dr. Yunus Azakli for support during casting and Dr. Robert Moorehead for assistance in developing the Texture XRD measurement protocols and analysis.

Abstract

At present there is a growing demand for high performance permanent magnetic materials for electricity generation and electric propulsion. The scale of demand is such that some of the highest performing current materials, which depend on rare earth elements, cannot be produced in sufficient quantity. Not all combinations of required properties can be met with currently available systems but one candidate to occupy part of the materials capability gap is $\tau - MnAl$, though barriers remain to industrial application. Current issues with the commercialisation of this material are the low thermal stability and low BH_{Max} of the compositions and conditions explored thus far. This thesis explores a number of approaches to improve the performance in these aspects, involving compositional adjustment and thermomechanical processing.

The findings of this thesis can be expressed as: the alloying addition of Bi does not form a stable single $\tau - MnAl$ phase with the Bi dissolved in but instead a ternary system of $\tau - MnAl$, unreacted Bi and a MnBi intermetallic, increasing H_C at the expense of intrinsic magnetic properties; Ga as an alloying agent can be used in lower concentrations than previously investigated to improve the thermal stability of the $\tau - MnAl$ with improved intrinsic magnetic properties, which can be varied as a result of heat treatments to meet engineering specifications and that it is possible to plastically deform the precursor ϵ-phase such that, following heat treatments to precipitate transformation to the desired $\tau - MnAl$ phase, directional dependency can be observed in extrinsic magnetic properties, meaning that it is possible to indirectly influence the microstructure of the precursor state such that it affects the desired ferromagnetic state to improve material properties for generator and motor applications. Overall the findings of this thesis result in a targeted alloy composition with a proof of concept processing pathway that shows potential for optimisation as a low cost per kilo permanent magnet with thermal stability suitable for modern low requirement electric motor and generator applications

Table of contents

List of figures

List of tables

Chapter 1

Introduction

1.1 Motivation and Aims

The key motivation behind the work expressed in this thesis is to develop the metastable τ-MnAl system towards potential applications in electric motors and generators as a permanent magnetic material. The reasoning is discussed in this section but is broadly one of economics and a lack of suitable alternative to current magnetic materials for low-requirement applications at present within industrially viable materials. The overall aim of this research project was to investigate potential methods to improve the thermal stability of the target τ-phase, reduce material costs by way of reducing usage of expensive alloying agents and investigate potential techniques for improving extrinsic magnetic properties to improve the usability of any potential τ-MnAl derivative product in a permanent magnetic material application.

The thesis structure can be broken down to the following:

1. Introduction: A detailed discussion of the issues surrounding current permanent magnetic material production and usage, discussion of potential candidate materials for development to Gap Magnet specifications and explanation of candidate choice

2. Theory: A brief discussion of key magnetic theories touched upon in this thesis specific to the measurement of bulk, polycrystalline magnetic alloys

3. Literature Review: An in-depth discussion of the current state of research into developing τ-MnAl into an industrially viable permanent magnetic material and research gap analysis for work moving forward

4. Methodology: A discussion and description of experimental and analytical techniques used within the research presented within this thesis

5. MnAl Ternary Systems: A presentation of findings of initial casting and heat treatment trials for MnAlC, a reproduction study and comparison of MnAlGa and initial alloying experimentation in the MnAlBi ternary system

6. Composition and Processing Optimisation: An investigation into low Ga-concentration MnAlGa ternary alloys in order to determine optimum compositions, metastable stability and heat treatment optimisation as well as develop more understanding around the behaviour of the optimum material condition

7. Mechanical Processing Investigations for Extrinsic Magnetic Property Improvement: Thermo-mechanical compression testing of a target composition (designated MAG-E) to discover suitable plastic deformation temperature and strain ranges. Plane Strain Deformation processing to determine resulting texture and extrinsic magnetic property variation

8. Conclusions: Overall conclusions from experimental results chapters and potential future work to advance findings.

Contained within the thesis is also Appendix A, containing additional data and mathematical derivations to support conclusions within experimental chapters.

1.2 The Current Usage of NdFeB and Surrounding Issues of Application

Due to rising global CO_2 levels, urban smog and legislation present to limit the production of new petrol/diesel vehicles, there is now incentive towards developing an electrically propelled consumer vehicle [1] [2]. At present, the propulsion system for an electric car is achieved through the use of NdFeB magnets doped with Dy [3]. NdFeB is chosen as the base permanent magnetic material as it exhibits a Maximum Energy Product (BH_{Max}) of up to $358kJm^{-3}$, the comparison of which against other materials can be seen in Figure 1.1 but it is doped with Dy to raise the Coercivitiy (H_C) and thermal coefficient of H_C of the magnet to above the operating temperature of the propulsion system [4].

In 1983, Sumitomo Special Metals patented a sintered, hard magnetic material comprised of NdFeB, causing a significant increase in electric motor performance [6]. This

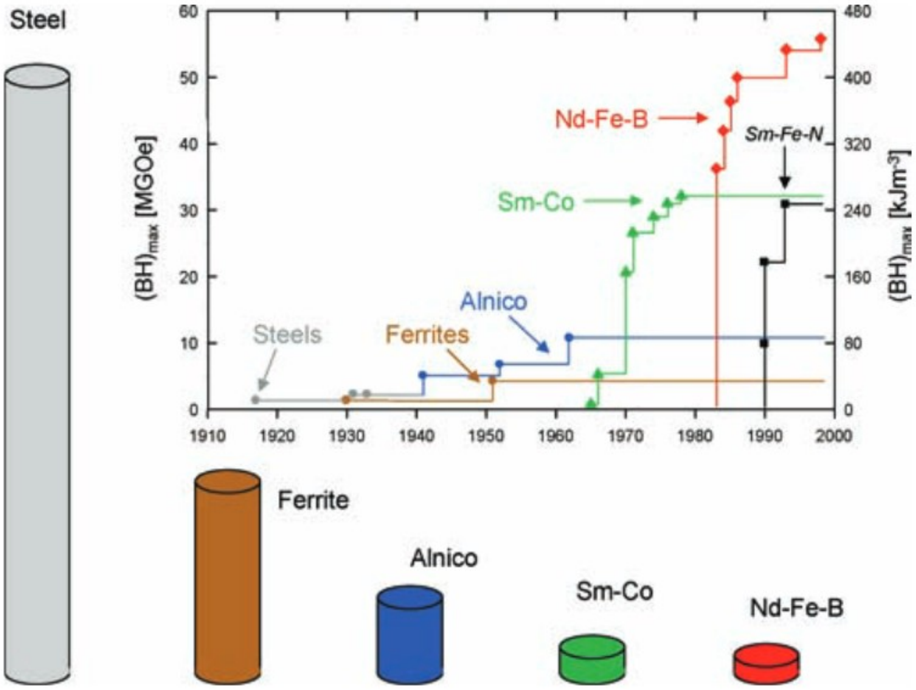

Fig. 1.1 The historic development in the energy density (BH_{max}) of hard magnetic materials in the 20th century. For each of the illustrated magnets, the scale has designed so that at a reference point 5 mm from the surface of the circular faces, a local field of $100mT$ is produced. Reproduced from Gutfleisch *et. al.* [5].

performance increase is due to the material's BH_{Max}, the ability of a material to store magnetic flux density and the maximum energy density able to be stored within a magnetic material by an applied field, H, antiparallel to the direction of magnetic flux, $B = \mu_0(H+M)$ where M is the magnetisation of a material, induced by the magnetic material i.e. where the product $-B \cdot H$ tends to its maxima within the second quadrant of a $B-H$ magnetic hysteresis loop [7]. For the context of electric motors, this is proportional to the mass of magnet required to achieve operation within specifications. The high BH_{Max} of NdFeB when compared to other materials has led to its current application in the automotive sector. In materials, the BH_{Max} can be determined as a fraction of $\mu_0 M_R H_C$ where M_R is the residual magnetisation, i.e. the magnetisation a ferromagnetic material posesses in the absense of an applied field after having been brought to saturation magnetisation, M_S.

Given that M_R and H_C are temperature dependent, the BH_{max} of a material is also temperature dependent. For NdFeB, M_R and H_C decrease as temperature increases and the material approaches its T_C [8]. To overcome this, doping the material with Dy was found to be effective in raising the magnetic anisotropy and thus the H_C of the material and the temperature coefficient of H_C, improving the high temperature performance of the alloy [9]. Dy is able to achieve this within the material by replacing the Nd within the lattice structure when included at $1at.\%$ [10].

Dy, however, is not easily sourced as a Heavy Rare Earth (HRE) element. Predominantly, it is sourced in southern China as part of a HRE oxide extraction operation, implying Dy is vulnerable to price fluctuations and availability issues due to geopolitical factors and a mono-dominant supply chain [11]. Between 2011 and 2012, there was speculation that China would limit supply of Dy, leading to a price increase of an order of magnitude [12]. There are also concerns over environmental pollution from Dy production [13]. Therefore, it suggests that there are incentives to develop a magnetic material that could fulfill applications of Dy-doped NdFeB without relying on HRE's, especially in applications where the specification on BH_{Max} are less demanding.

1.3 Gap Magnets and Economics

At present within common magnetic materials, there exists several gaps in capabilities with materials with $(1000 < H_C < 2000)kAm^{-1}$ and $(800 < \mu_0 M_R < 1200)mT$ currently not in wide-scale use, due to a lack of available bulk material comparable to metallic NdFeB, but there is significant focus within the industry on trying to create magnetic materials that fulfils capabilities in the range of $H_C > 500kAm^{-1}$ and $(800 < \mu_0 M_R < 1200)mT$ [14]. These magnetic materials are the subject of various review papers by J.M.D Coey [15], whereby they are referred to as Gap Magnets of three types as defined in Table 1.1 and graphically represented in Figure 1.2. These are primarily scaled by cost and M_S rather than BH_{Max}, as this variable can be improved with microstructural processing.

When considering candidate alloys to fulfil these gap requirements, many elements can be eliminated. Referencing Figure 1.3, one can see that most elements from Period 5 onward become prohibitive due to cost, with the exception of Pb, I and Sr. Therefore, RE's cannot form a primary alloying component of a Gap Magnet at current costs.

One potential candidate identified by Coey is metastable $\tau - MnAl$ [15]. With low component costs and properties within acceptable ranges for application as a Gap Magnet ($M_S = 600kAm^{-1}$, $K = 1700kJm^{-3}$, $T_C = 377°C$), this system has attracted significant interest over previous years. Issues that have been inherent with progressing the material to further application, however, are that of the state transforming to paramagnetic equilibrium states during processing and complex production routes leading to a degradation of the magnetic properties of the material, both inherently linked to the metastable nature of the material.

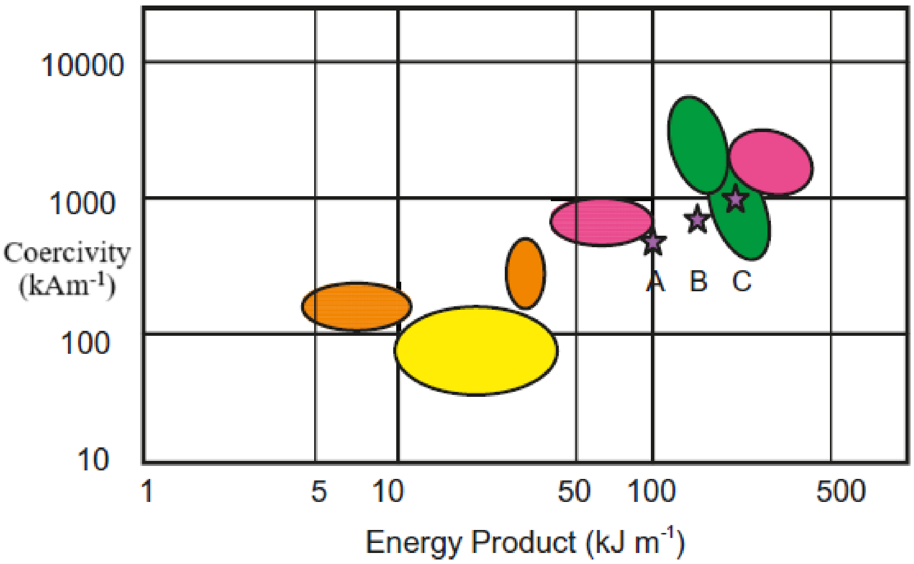

Fig. 1.2 This graphic was reproduced from *'Permanent Magnets: Plugging the Gap'* [15] and defines the position of his three required gap magnets that currently must be fulfilled by NdFeB or SmCo. The colour-coding indicates that ranges achievable with the four main magnetic alloy groups in circulation for bulk permanent magnet application with Pink indicating NdFeB, Green indicating SmCo, Yellow indicating Alnico and Orange indicating Ferrite alloys. By developing $\tau - MnAl$ into a Type A Gap Magnet, this may help mitigate the environmental and political concerns around the use of cobalt.

1.3.1 Candidate Materials and Target System for Thesis

When deciding which system to take forward from literature and develop closer to an industrially viable permanent magnetic material, it was key to understand and down-select from existing potential materials as speculative development of completely new magnetic materials is unlikely to be successful, and there are already several candidates competing for Gap Magnet status. These alternatives are already well discussed in existing review literature and the key findings and the reasons for down-selection in this work are discussed here for the primary candidate materials, though recognising that this list is not exhaustive [16][15][17]. Further, a brief summary can be found in Table 1.2

MnBi could be considered as a candidate material, with Cui *et. al.* achieving synthesis of a bulk MnBi magnet in 2014 with a $BH_{max} \approx 62kJm^{-3}$, within 50% of the requirements for a Type A Gap Magnet and below the theoretical limit for the system of $BH_{max} \approx 140kJm^{-3}$ [18]. Work by Yang *et. al.* also shows that H_C increases as a function of temperature due to c-axis elongation [19]. This material would be a prime candidate for a Gap Magnet, but Bi production is a byproduct of lead production and, as the 65th

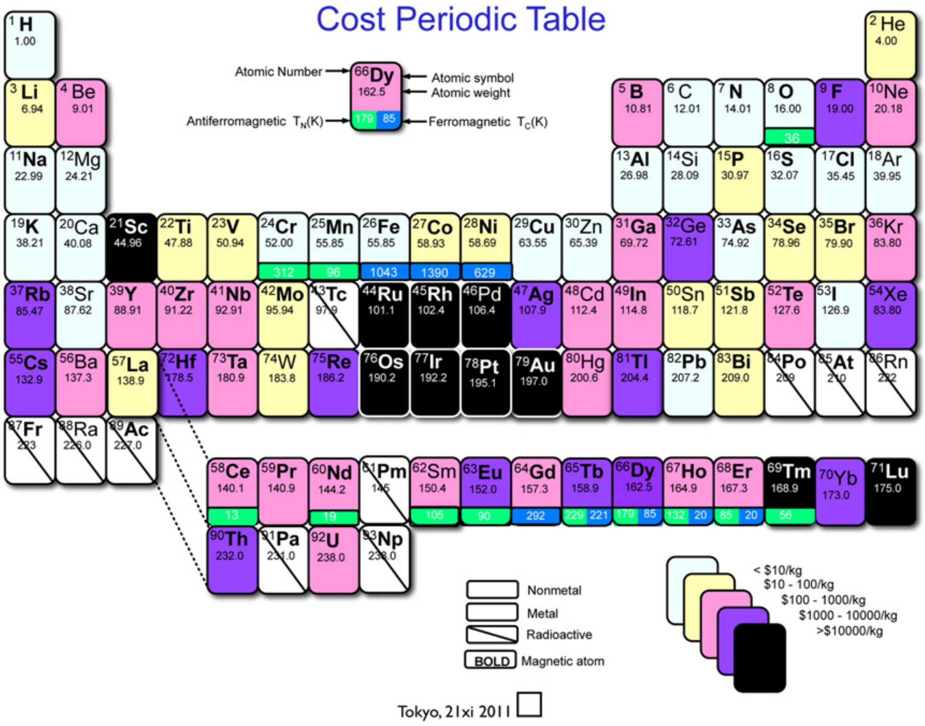

Fig. 1.3 When considering the economic impact of selecting elements, it is key to see that most elements heavier than period 4 immediately increase the price by significant orders of magnitude, due to their relative abundance on Earth or competition with other industries. When designing a Type A Gap Magnet, ensuring a low cost per kilogram is a key factor to replacing current materials, ensuring that the material must be based on the first row of transition metals with minimal Rare Earth content [15].

most abundant element within the Earth's crust, the lower cost of the material shown in Figure 1.3 is a consequence of a lack of applications [15] [20], which could change if it was adopted in a high value application.

Iron nitride is also a potential candidate. $\alpha'' - Fe_{16}N_2$ has a predicted maximum energy product over twice that of NdFeB and lower raw material cost given the lack of RE elements required as discussed by Wang (2020)[21]. With $(1300 < H_C < 1900)kAm^{-1}$ and $M_S \approx 2300kAm^{-1}$, the material would meet requirements. Bulk manufacture has yet to be demonstrated, implying the material needs development in larger-scale manufacturing before it could be considered for an application as the magnetic alloy in an electric motor. Further, this phase is known to thermally decompose to equilibrium states in the range of $(210 - 250)^{\circ}C$, meaning that if the operating temperature of an $\alpha'' - Fe_{16}N_2$ electric motor was similar to that of an NdFeB system at $180^{\circ}C$, there is little tolerance in an overheat fault before potentially seeing irreversible phase loss in magnetic material, thus suggesting

Type	$BH_{Max}[kJm^{-3}]$	$T_C[°C]$	$M_S[kAm^{-1}]$	$K[kJm^{-3}]$	Raw Material Costs [$\$kg^{-1}$]
A	100	> 275	570	500	10
B	150	> 275	690	750	20
C	200	> 275	800	1000	30

Table 1.1 Definitions of the requirements for Gap Magnetic materials as defined by J. M. D. Coey in *'Permanent Magnets: Plugging the Gap* [15]. Note that these material requirements set T_C, cost and M_S rather than H_C or M_R as it is considered in the text a considerable amount of work to improve Coercivity and Remanence, taking the course of decades, but that Curie Temperature and Saturation Magnetisation are characteristic of the phases present in the alloy itself.

that $\alpha'' - Fe_{16}N_2$ is not a suitable material for electric motors under existing designs [22] [23].

With a reported BH_{Max} of $135kJm^{-3}$ [24], $SmCo$ is an existing system that could be developed to fit Gap Magnet criteria defined in Table 1.1. Samarium is a RE with a similar extraction route as dysprosium, but as a light rare earth it is more abundant on Earth [11] and with a lower cost per unit mass, as defined by Figure 1.3. Whilst $SmCo_5$ is too expensive to qualify for Type C Gap Magnet, an alloyed system with α-Fe has been investigated to reduce system cost and improve M_S and BH_{max} [25]. For $SmCo_5$, $(678 < T_C < 686)°C$ [25] which is greater than that of Dy-doped NdFeB at $\approx 325°C$ [26], implying that it could see higher temperature applications without doping.

Despite advances on SmCo alloys, this material group is unsuitable due to price and controversy surrounding cobalt. Cobalt is primarily produced in areas currently subject to political instability, having impacts on the acceptability of the practices used to extract the minerals, the production rate and the cost [27]. Over half the primary global cobalt production was sourced from the province of Katanga in 2010 [28] and the mining has, in recent years, led to concerns over the local environment and impact on population from cobalt exposure [29][30][31]. Given supply and ethical concerns, cobalt is seen as undesirable for industrial application where alternatives exist.

Mn_2Ga is another potential candidate for a gap magnetic material. With a $T_C \approx 420°C$, $K_1 \approx 2000kJm^{-3}$ and $M_S \approx 305kAm^{-1}$, two of the Gap Magnet Criteria are fulfilled though significant development would be required to increase the M_S value to Type A specification by investigating additional alloying elements [32] [33]. However, consulting both Figure 1.3 and Table 1.1, it can be seen that an alloy comprised of a 2:1 ratio of Mn to Ga would imply a significantly higher cost per kg than other alloy systems discussed. This effectively prices out this system from further investigation as a Gap Magnet material under economic grounds.

Material	Pros	Cons
$MnBi$	High developed BH_{Max} near specification. Positive temperature coefficient of H_C Low Cost per kg	Bi is byproduct of Pb mining Cost low due to lack of bulk applications for Bi
$\alpha'' - Fe_{16}N_2$	Theoretical $BH_{Max} > 1MJm^{-3}$ $(1 < K_1 < 2)MJm^{-3}$ Alloy element costs exceedingly cheap	Thermal decay at $(210-250)^\circ C$ Magnetically soft
$SmCo$	$T_C > 650^\circ C$ $BH_{Max} > 100kJm^{-3}$	Co source is politically controversial and unstable High cost per kilo
Mn_2Ga	High K_1/Low M_S implies magnetic hardness High T_C	Low M_S Cost per kg > Type C criteria
$\tau - MnAl$	Fulfils all intrinsic Gap Magnet Criteria	Metastable and decays $> 450^\circ C$ Challenging fabrication route

Table 1.2 A Table of the potential Gap Magnet Candidate materials considered when scoping the research contained within this thesis, with the pros and cons clearly listed. Following this exercise, $\tau - MnAl$ was downselected as the most viable candidate to be brought forward for industrial use as a permanent magnetic material.

The final candidate often discussed in review papers around emerging permanent magnetic materials is that of $\tau - MnAl$. Fulfilling all intrinsic Gap Magnet criteria for a Type A Gap Magnet and having a low cost per kg from component elements, the material would appear to be, at first, an ideal candidate [16]. However, the existing issues with developing an industrially viable permanent magnetic material and current solution development pathways are discussed in depth in Chapter 3 but they can be broadly stated as issues of metastability and processing. $\tau - MnAl$ is formed as a heat treated product from a high temperature phase, either by controlled cooling or quenching and annealing and is thus not thermodynamically stable at room temperature and pressure conditions. Above a critical temperature, determined by composition and additional alloying elements, it will undergo a phase change to non-magnetic equilibrium phases. Critically, this temperature is lower than the sintering temperature $(T_{sinter} \approx 0.8T_{melt} \approx 1000^\circ, T(\tau \rightarrow \gamma_2 + \beta Mn) > 300^\circ C$ though it is very dependent on composition), meaning conventional nanocrystalline magnet fabrication techniques of sintering under an aligning field to ensure preferential domain orientation are not possible. Further, it also implies that heat treatments to refine grain structure/texture or as part of net-shape fabrication will lead to non-preferred phase populations, thus reducing magnetic performance.

Therefore, considering the aspects of materials performance, cost and environmental and ethical concerns as well as the challenges of bringing each material to compliance with Gap Magnet specification, the suitable material selected was $\tau - MnAl$. Fundamentally, the other discussed systems are either economically unsuitable, thus failing to displace using NdFeB or hard ferrites from a cost argument, or have intrinsic problems for electric motor applications. Thus, $\tau - MnAl$ and the associated problems of processing and metastability were targeted as the focus of this thesis, having been judged as the most suitable candidate to potentially fulfil this capability gap if these issues can successfully be overcome.

Chapter 2

Theory of Permanent Magnetism and Related Measurement Techniques

2.1 Foreword and a Broad Definition of Ferromagnetic Materials

When investigating new permanent magnetic materials for electric motors, one needs to consider a wide basis of physics and metallurgy. An understanding of the quantum mechanical origins of ferromagnetism are key to the initial design of a compound, micromagnetics for any iterative improvements on magnetic properties and casting/deformation techniques for the actual fabrication of samples and processing to achieve any compositional or microstructural control of the magnets. The analysis, as well, draws on various disciplines of physics and materials science in order to evaluate any experiment. Thus, in the following, an attempt has been made to lay out the chapter by discipline in order to simplify its readability.

With reference to Jiles (2016), a ferromagnetic material can be defined as a material with a high, positive bulk susceptibility, χ where $\chi = \frac{M}{H}$ where M is the magnetisation of a material and H is the externally applied magnetic field, [34], the ability to retain remanent magnetisation, M_R, following exposure to and then removal of an external magnetic field, and a non-zero external magnetic field referred to as a coercivity, H_C, required to reduce magnetisation to zero and a resulting magnetic hysteresis, i.e. path-dependent response of an applied magnetic field to magnetisation or M-H plot. These ferromagnetic materials can be broken down into two categories, soft and hard ferromagnets, which are defined by Jiles as soft ferromagnets having coercivities in the range of $H_C < 10kAm^{-1}$ and hard ferromagnets having coercivities above this value. Distinctly, however, it is H_C and M_R

that are of most interest in motor and generator applications, as together these define the working point where a magnetic material can resist an externally applied field and work against it. This point is referred to as the Maximum Energy Product or BH_{Max} and is expressed as an energy density, representing the maximum magnetic energy that can be stored within a permanent magnetic material as a function of volume. It is this variable and its thermal dependency that is the focus of constant research and improvement in developing candidate ferromagnetic materials to motor applications.

2.2 Origins of Ferromagnetism

2.2.1 Magnetic Moments of Atoms and Non-Interacting Systems

With reference to Spaldin (2003), the origin of ferromagnetic behaviour in a material can be traced back to quantum mechanics [35]. Broadly, an individual free atom in the absence of an applied field has a magnetic moment summing from two components, that of the orbital angular momentum of the electron cloud orbiting the nucleus and that of the individual spin of said electrons and these angular momenta are themselves quantized to certain states as part of a set of quantum numbers. The electrons orbiting the atom in question arrange themselves into energy levels, or shells, due to a requirement to have a mutually exclusive set of quantum numbers, under the Pauli Exclusion principle, and thus each potential position within a shell has two potential states, an up spin and a down spin, Hund's Rule. The orbital and spin angular momenta generate magnetic moment as a result of the electron having a non-zero charge and there are interactions resulting from orbit-orbit, spin-spin and spin-orbit couplings, but upon bonding with other atoms, these orbits further complicate and thus the associated magnetic moment for an atom within a crystallographic unit cell becomes a sum of these individual bonds. This is again further complicated in metallic structures due to "free"-electrons in the material acting as an electron gas.

The effect of this is that a material with atoms of non-zero total angular momentum, a magnetisation vector $\vec{m}$ can form over the atom in response to an applied external magnetic field, referred to as paramagnetism. Using the classical theory of paramagnetism, Langevin theory, to explain this, each atom within a material has a resulting macroscopic moment as derived from the previous explanation but this field can take any orientation in a zero applied field state and across a system would sum to a zero state. In the case of an applied field external to the material, however, these moments would decrease the energy in a system by the equation $\epsilon_z = -\vec{m} \cdot \vec{B} = -\mu_0 mHcos\theta$ where ϵ_z is the Zeeman energy of an individual isolated moment within a system interacting with an external field. Thus, a system minimises its total Zeeman energy by aligning its moments with the external applied magnetic field, giving rise to a field-dependent magnetisation within a material [36].

An important definition resulting for this is that this magnetisation is a fixed value for an atom within a structure, recognising that the bonding of a structure will perturb the calculated magnetic moment for an isolated system with additional coupling interactions, but that in a system of collective magnetic states, $\vec{m}$, of number, n will self assemble such that it minimised energy within the system and that the total magnetic moment for a system, $\vec{M}$, can be expressed as:

$$\vec{M} = \sum_{i}^{n} \vec{m}_i \tag{2.1}$$

By applying an external magnetic field to the collective system such that all $\vec{m}_i$ align across a given volume of material, the total magnetisation for a system will reach Saturation Magnetisation, M_S, such that it can be expressed that

$$M_S = \frac{1}{V} \lim_{H \to \infty} (\sum_{i}^{n} \vec{m}_i) = \frac{nm}{V} \tag{2.2}$$

2.2.2 Ferromagnetic Behaviour and Spontaneous Magnetisation

For ferromagnetic over paramagnetic behaviour to occur , the magnetisation must have a non-zero state in the absence of an applied field. Again, summarising reasoning explained in Spaldin (2003), this was explained by Heisenberg as a consequence of the Pauli Exclusion Principle resulting in an electrostatic term in the Exchange Integral between two neighbouring atoms, such that electron spins favour parallel orientations [35]. To avoid needing to discuss quantum mechanics in depth, this can be mathematically approximated as the Weiss Molecular field:

$$\vec{M} = \frac{\vec{H_W}}{\gamma} \tag{2.3}$$

where $\vec{H_W}$ is the Weiss Molecular field, resulting from this exchange interaction, γ is the molecular field constant and $\vec{M}$ is the spontaneous magnetisation. Comparing this to the Langevin theory of paramagnetism under the understanding that ferromagnetic behaviour is a subset of paramagnetic behaviour, the magnetisation $\vec{M}$ can also be expressed as:

$$\vec{M} = N\vec{m}L(\alpha) \tag{2.4}$$

where N is the number of atoms in a system of magnetic moment $\vec{m}$ and $L(\alpha)$ is the Langevin function expressed by the first two terms of the Taylor series $L(\alpha) = \frac{\alpha}{3} - \frac{\alpha^3}{45} + \ldots$ and $\alpha = mH/k_BT$ (k_B being the Boltzmann constant, T the system temperature, m the magnetic moment magnitude and H the magnetic field vector).

Taking the first term of the Langevin function, vector magnitudes and assuming the condition that the applied field in question is the Weiss field resulting from the exchange integral, it can be stated that the spontaneous magnetisation of a system exists where the Weiss field magnetisation is equal to the Langevin magnetisation. Given that the Weiss field can be rearranged to be a function of α and has a linear dependency, the case where the Weiss field becomes tangential to the Langevin field is the case where the spontaneous magnetisation reaches a zero state. Thus, considering $dM/d\alpha$ for both cases and setting them equal and recognising that the only variable subject to change within a system is T, we can define

$$T_C = \frac{\gamma N m^2}{3k_B} \tag{2.5}$$

where T_C, referred to as the Curie Temperature, the temperature at which a ferromagnet is unable to sustain a spontaneous magnetic field due to the exchange integral and thus transitions to paramagnetic behaviour. Thus, the temperature range at which a ferromagnetic system exists and the relative spontaneous magnetisation a system can achieve is determined by the individual magnetisation of each atom, the density of these atoms and the molecular field constant for the system, which is itself a simplification of the Exchange Integral. This can be seen graphically in Figure 2.1

2.3 Micromagnetics and MAZE Energy

Further expanding on the origins of ferromagnetic behavior, first that atoms have magnetic moments due to electron orbital and electron spin angular momenta which induce magnetic fields, given the electrons' charge, which can self-align due to exchange interactions between atoms to give rise to spontaneous magnetisation, it becomes possible to calculate magnetic moments beyond that of independent atoms. Thus, we can define a system by M_S and T_C, the sum of the magnitude of the magnetic moment per atoms within the system and the temperature at which the energy from self-arrangement of spins resulting in spontaneous magnetisation, mH_W is less than or equal to the thermal energy of the system k_BT; this however does not explain how systems are able to self interact. As such, turning to the field of micromagnetics becomes important to discuss how single

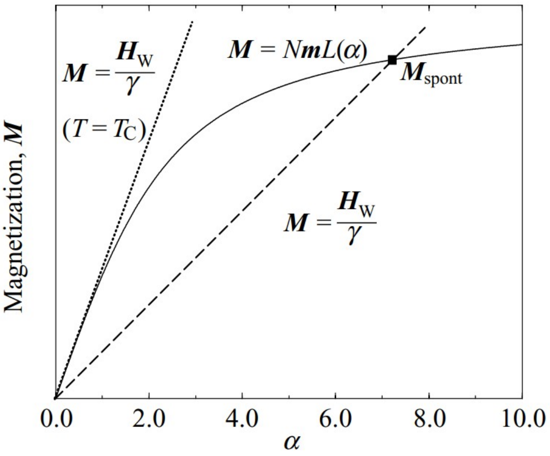

Fig. 2.1 A graphical representation of the Weiss field for a material at both the paramagnetic regime ($T \geq T_C$) and the spontaneous magnetisation regime ($T < T_C$) and the Langevin function, demonstrating that it is possible to express the Curie Tempertaure of a material as a product of the Weiss Molecular Field and the magnetic moment per unit cell of a material. Reproduced from Spaldin [35]

atoms interact with one another to develop models representative of bulk materials such as those discussed within this thesis. The following explanation and discussion is made with reference to Kronmüller and Fähnle (2003) [37].

When considering Brown's theories of micromagnetism and the continuum theory of ferromagnetism, one can define the Gibbs free energy density of a ferromagnet, ϕ'_t as:

$$\phi'_t = U - T \cdot S - \sigma \cdot \epsilon - \mu_0 \vec{\mathbf{M}}_{\mathbf{S}} \cdot \vec{\mathbf{H}}_{\mathbf{ext}} \tag{2.6}$$

where U is defined as the internal energy density, $T \cdot S$ as the energy density from Entropic effects and $\sigma \cdot \epsilon$ the stress-strain energy density term. Discussing the system at zero temperature and stress as well as expanding the internal terms, we can derive the total magnetic Gibbs free energy density at $T = 0K$ as

$$\phi'_t = \phi'_H + \phi'_K + \phi'_s + \phi'_{el} + \phi'_{ex} \tag{2.7}$$

where ϕ'_H is the Zeeman Energy density, ϕ'_K is the Magnetocrystalline Anisotropy Energy density, ϕ'_s is the Magnetostatic Stray Field Energy density, ϕ'_{el} is the Magnetoelastic Potential Energy density and ϕ'_{ex} is the Exchange Energy density. When considering cases where $\sigma, \epsilon \to 0$, we can consider this free energy to be a sum of the four remaining terms, often referred to as the acronym MAZE energies. These terms are expanded upon and put into the context of ferromagnetic alloy development below, again with reference to Kronmüller and Fähnle (2003) [37].

2.3.1 Magnetostatic Energy

With reference to Crangle (1997), one can consider an isolated magnetic system following exposure to a saturating external magnetic field as a system of free magnetic dipoles contained within the surface of the material [38]. These poles are considered to have magnetisations themselves and can be considered to generate magnetic fields, but if one considers the Maxwell Equations and notes that $\nabla \cdot \vec{B} = 0$ (Gauss' Law) and that we define $\vec{B} = \mu_0(\vec{M} + \vec{H})$, one can deduce that the magnetic field between these poles must be orientated antiparallel to the sum magnetisation vector of the ferromagnetic object to satisfy Gauss' Law. Thus, one can express the magnetic field within an isolated ferromagnetic object as:

$$H_{eff} = H_{app} + H_D \tag{2.8}$$

where H_{app} is the applied external field to a material, H_{eff} is the effective applied magnetic field inside the material and H_D is the demagnetising field, defined as $\vec{H_D} = -N_D\vec{M}$ where $0 \leq N_D \leq 1$ and is referred to as the demagnetising factor and is defined by the surface integral of the ferromagnetic material respective to the magnetisation [35].

This corresponds to an energy term

$$\phi_s' = -\frac{\mu_0}{2}(\vec{H_D} \cdot M) \tag{2.9}$$

and thus this mechanism seems to minimise the Gibbs Free Energy by way of either minimising the demagnesation field, a geometric effect, or by minimising the magnetisation of the grain. It is this second variable that is of interest and gives rise to the concept of magnetic domains, intergranular structures of anti-parallel magnetisation regions resulting in a lowered sum magnetisation of the grain where is it energetically favourable to do so. The energy terms around this discussion are not expressed here for the sake of brevity but where appropriate in this these, transition grain dimension limits are discussed where multi-domain states become preferable. Further reading on the topic can be found in Hubert and Schäfer (1998) [39]

When considering bulk cases, H_D becomes an important correction factor for determining bulk material characteristics, recognising that H_{app} is that measured externally by Vibrating Scanning Magnetometry and thus sample geometry is critical to understanding material properties as correction factors for non-saturating fields become important when measuring remanent magnetisation M_R. If one considers that M_R is defined as the field at which a $M_R = M(H = 0)$, there are two differing fields where this can be interpreted from. The first is where $H_{app} = 0 \implies H_{eff} = N_D M$ and the second $H_{eff} = 0 \implies H_{app} = N_D M$. Given that N_D is a geometric property of the material construction rather than an extrinsic magnetic property of the material in question, reporting the latter implies that the resulting M_R calculation is geometrically independent of magnetic material form, and thus is the reported M_R within this thesis. To calculate this, however, the shape factor N_D is required to estimate demagnetising field strengths and as such sample geometry is required. To achieve this calculation, all samples are modelled as cuboid structures under the assumption that from machining, internal angles approximately average to 90° and as such, dimension lengths can be measured and N_D calculated by Magpar software [40]

2.3.2 Anisotropy Energy

Magnetocrystalline Anisotropy energy is defined as the energetic preference for the magnetisation of a repeating crystallographic cell, or unit cell, to lie along specific axis relative to that unit cell. The general equation for this energy density is

$$\phi'_K(\vec{r}) = k_0(\vec{r}) + \sum_i k_{1i}(\vec{r})\gamma_i^2(\vec{r}) + \sum_i k_{2i}(\vec{r})\gamma_i^4(\vec{r}) + \sum_{i \neq j} k_{3ij}(\vec{r})\gamma_i^2(\vec{r}) \cdot \gamma_j^2(\vec{r}) \tag{2.10}$$

where $\vec{r}$ is the direction vector of a potential magnetisation across a unit cell, k_i is a respective energy density of that vector and γ_i are vectors specified by the unit cell system. In this thesis, we consider systems of tetragonal symmetry and as such, this equation can be redefined as:

$$\phi'_{K,\,tetra}(\vec{r}) = K_0(\vec{r}) + K_1 sin^2(\phi)(\vec{r}) + K_2 sin^4(\phi)(\vec{r}) + ... \tag{2.11}$$

where ϕ is the angle between M_S and the c-axis of the unit cell lattice and K_1 are the respective magnetocrystalline anisotropy energy density terms. Depending on the relative magnitude and sign of K_1 and K_2, the easy axis of magnetisation may lie relative to various crystallographic planes but implies that it is is energetically favourable to have domains that lie relative to simple crystallographic directions defined by a unit cell. This can be visualised in single crystal samples by examining magnetisation responses to applied magnetic fields oriented along crystallographic vectors, as can be seen in Figure 2.2. With reference to Coey, the anisotropy field is such that a uniaxial system, such as the Co system in Figure 2.2, is brought to saturation along the hard axis. This can be visualised

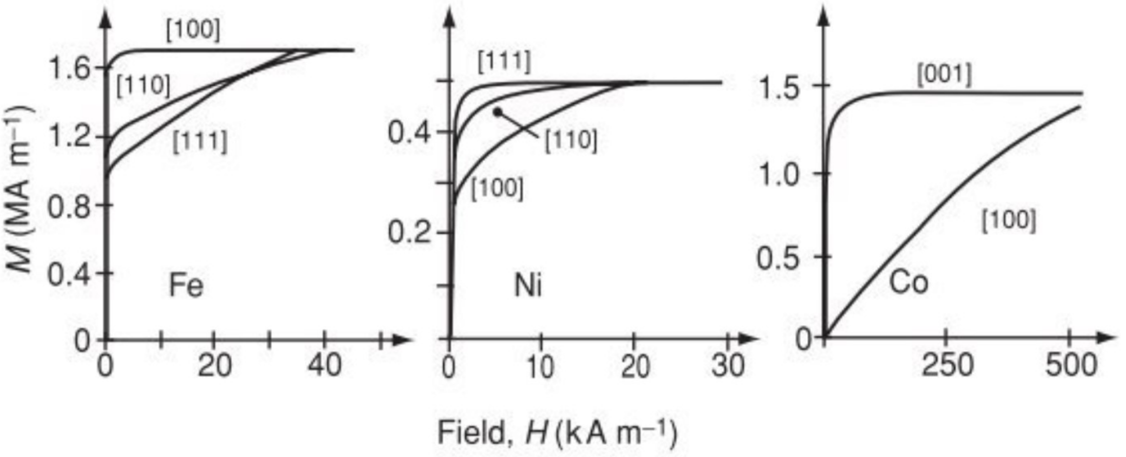

Fig. 2.2 The magnetisation response of single crystals of iron (easy axis: [100], hard axis: [111], cobalt (easy axis: [111], hard axis: [100]) and nickel (easy axis: [001], hard axis: [100]) respectively, showing the difference in required external field to bring the single crystal to saturation magnetisation along each axis. Reproduced from Coey [36].

as the turning point on a magnetic hysteresis loop where the magnetisation response to increased applied field is approximately zero and as expressed as $H_A = 2K_U/\mu_0 M_S$ [36].

When attempting to calculate Magnetocrystalline Anisotropy energy for a polycrystalline, near-isotropic sample, one very quickly runs into the problem of directional isolation. Standard measurement doctrine calls for single crystals to be measured such that lattice vectors can be individually isolated and hysteresis loops across each vector compared for for single crystals/textured samples to be suspended in a rotary system to measure preferential torque and isolate easy directions of magnetisation. In an isotropic system, one does not have a preferential direction of measurement and as such alternative measurement techniques must be utilised.

Single Point Measurement

Several techniques can be adapted for measurement, the first being that of the Single Point Measurement technique, explored by Cabassi [41]. The technique relies on the observation that a single crystal with its easy axis perpendicular to an applied field will experience a discontinuity in its magnetisation at the anisotropy field of the crystal. As the system deviates from this ideal case, the discontinuity disperses into a gradient change but, in theory, the average across the system would tend to an observable discontinuity in higher order differentials of the $M(H)$ relationship, as shown in Figure 2.3.

For this technique to function, either alignment of the grain structure perpendicular to the applied field is necessary in order to increase the discontinuity signal in the data

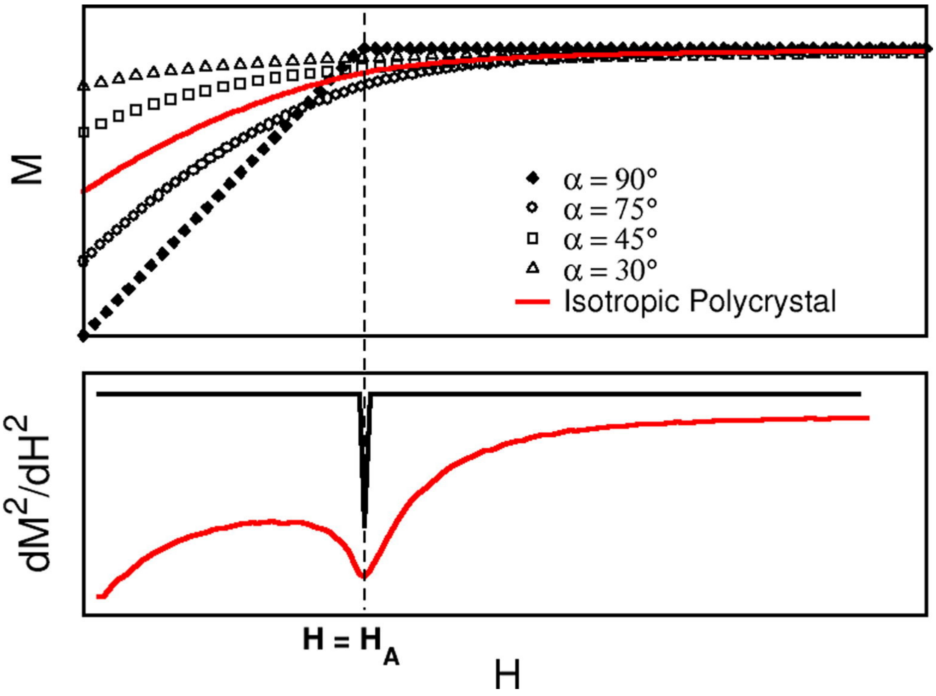

Fig. 2.3 Example magnetisations for a single crystal responding to an applied field H applied at an angle α to the easy axis, along with a polycrystalline estimation representing a sum of those systems. Reproduced from Cabassi [41].

set or for the signal to be generated by a pulsed system capable of generating a ≈ 20T field in millisecond timescales. As the samples in this work are initially created in an untextured state, and developing a texture in the τ phase of MnAl is still a subject of research, preferential alignment during measurement is not yet possible and equipment to fulfil the second criteria was not available during this research. The second technique (that is utilised in this research) uses the Law of Approach to Saturation, defined in Section 2.3.2, which allows an approximation of K_1 to be made as a result of the measurement of hysteresis loop simultaneously with M_S. This method does not require special conditions outside normal operation of a VSM.

Law of Approach to Saturation

The Law of Approach to Saturation as developed by W.F. Brown models the magnetisation of a material near saturation as $M_H = M_S - a_1/H - a_2/H$ where $a_{1,2}$ are system constants that can be derived from unit cell symmetries. As derived in Kronmüller and Fähnle (2003), for a uniaxial system, i.e. where there is a single easy axis of magnetisation, and assuming that $K_1 > K_2$, one can express the magnetisation as:

$$M_S(H) = M_S(1 - \frac{4}{15}\frac{K_1^2}{\mu_0^2 M_S^2}\frac{1}{H^2}) \tag{2.12}$$

where all variables have their previously defined meanings [37]. Thus, it becomes possible to estimate M_S and K_1 from the intercept and gradient of a linear fit of $M(H^{-2})$ plot, assuming that H is sufficiently high. This is the technique used within this thesis to estimate both M_S and K_1, though it is of note that this can be expanded to include K_2 to the same power of H. As such, the reported magnetocrystalline anisotropy term within this thesis is reported as k where $k^2 = 4/15(K_1^2) - 64/105(K_1K_2) - 128/315(K_2^2)$ as from this technique, independent isolation of K_1 and K_2 is not possible and previous literature on τ-MnAl suggests that $K_1 >> K_2$ and thus this approximation may tend towards K_1 [42] .

2.3.3 Zeeman Energy

The Zeeman Energy energy term can be introduced as

$$\phi'_H(\vec{r}) = -\mu_0 \vec{H_{ext}}(\vec{r}) \cdot \vec{M_S}(\vec{r}) \tag{2.13}$$

or broadly the potential energy density of a magnetic object in an applied external field. Whilst this is important in terms of micromagnetic modelling, for the purposes of this thesis it is included for completeness and is less important to control when considering ferromagnetic material design given that it is simply an expression that it is energetically favourable for an isolated domain to be orientated such that the domain magnetisation is parallel with an applied field. Thus, the major consequence from this energy is that there exists some field such that it can be considered that all domains are orientated such that their magnetisations are parallel with said applied field and $M(H \to \infty) \to M_S$.

2.3.4 Exchange Energy

The final micromagnetic energy density to be concerned with with regards to the Gibbs free magnetic energy is that of the Exchange energy. This energy term has been initially introduced in Section 2.2.2 and can be broadly interpreted as that it is energetically favourable for spins, and thus magnetic moments, to align parallel to one another and see long range order in terms of colinearity across a system.

With reference to Coey (2010) and rearranging into an energy density form, one can express the exchange interaction as:

$$\phi'_{ex} = A \cdot \nabla(\frac{M(\vec{r})}{M_S})^2 \tag{2.14}$$

where A is the Exchange stiffness constant and $M(\vec{r})$ is the magnetisation vector oriented in some direction within the material [36]. The Exchange Constant can be defined as the rate of potential increase as magnetic gradients diverge from one another and thus implies that this term is minimised when magnetisation is uniform in a material, in direct opposition to domain formation as driven by the magnetostatic energies.

2.3.5 Effects of MAZE Energies, Domain Formation and Size Limits

When considering micromagnetics and indeed all thermodynamic processes, systems seek minimum energy states. As such, if one considers a zero temperature and strain state, the resulting magnetic structure must seek to minimise Equation 2.7 which then becomes a question of length scale. In systems where length scales are such that magnetostatic effects can win out against exchange effects, regions of antiparallel magnetisation will form within a region of aligned crystallographic axis, i.e that of a grain, single crystal or thin film, referred to as domains. These domains must form within regions of common crystallographic axis, however, and are thus limited to grain structures within that of a bulk, 3D system of low misorientation angle, assuming a uniaxial easy axis such that the magnetisation of each individual grain does not deviate significantly from the respective easy axis, increasing the contribution from magnetocrystalline anisotropy energy as defined by Equation 2.11 in the case of hard magnetic materials.

It is also of consideration as to the minimum size of a grain such that a domain structure can form internally. Given that one can sum Equation 2.7 internally within a grain, there must be a critical length scale such that magnetostatic effects do not dominate those of exchange and the magnetisation of the particle remains coherent. Following reasoning set out in Kronmüller and Fähnle, if one considers an ellipsoidal particle defined by axis a and b, one can define the magnetic energy of the particle for a single and double domain state as a function of those variables[37]. The energy of a single domain state, at zero temperature, is purely expressed as a sum of the demagnetising field contribution for magnetisation parallel along the long axis b as calculated by Equation 2.9 and is thus

$$E_{single} = \frac{1}{2}\mu_0 N_{||} M_S^2 \cdot \frac{4\pi}{3} a^2 b \tag{2.15}$$

and considering a double domain state, one can model the decrease in magnetostatic energy by the coefficient α and add the additional energy of forming a domain wall, a region of rotating magnetisation vectors interfacing the antiparallel magnetic domains with energy $E_{dom.wall} = \pi ab\gamma_B$ where γ_B is the energy of a domain wall formation, one finds the total energy of state 2 is

$$E_{double} = \pi ab\gamma_B + \alpha\frac{1}{2}\mu_0 N_{||} M_S^2 \cdot \frac{4\pi}{3} a^2 b \tag{2.16}$$

thus a critical diameter can be calculated such that it is energetically favourable to be a single domain state. For a spherical particle, where $a = b$, $N_{||} = \frac{1}{3}$ and $\alpha = \frac{1}{2}$, this critical grain diameter reduces to:

$$D_{crit}^{do} = \frac{72}{\mu_0 M_s^2}\sqrt{AK_1} \tag{2.17}$$

though should grain morphology deviate such that $N_{||}$ increases, this critical diameter decreases, thus meaning that morphological control during fabrication is important to determine single domain state size. It is of note though that this calculation is for an isolated grain and does not account for a grain within a continuous medium, thus can only be considered an approximation for the minimum critical grain diameter when assessing grain morphology and domain formation.

When considering the development of permanent magnetic materials, domain structures can be both a hindrance and a benefit. Whilst increasing grain size can improve mechanical properties, increasing toughness and facilitating strengthening through work hardening via plastic deformation, grain size dependence of coercivity and permeability (GSDCP) theory shows us that there is an optimum grain size for coercivity of about the size of Domain Wall widths and that coercivity drops off with a D^{-1} proportionality as a function of grain diameter[43]. Further, single domain grains are beneficial for remanence as the moments undergo intergranular coupling and thus self align, however, there is magnetocrystalline energy to consider and in the case of uniaxial easy axis materials, the grain moment direction will be dominated by crystalline axis orientation. Thus optimum grain size for a magnetic material to optimise extrinsic magnetic properties, Coercivity and Remanence, is in the range of:

$$\pi\sqrt{\frac{A}{K_1}} \leq D_{grain} < \frac{72}{\mu_0 M_s^2}\sqrt{AK_1} \tag{2.18}$$

Remanence, however, is dominated by texture. Given Equation 2.7, one can consider that in a single domain state under no external field, magnetisation direction is determined as a function of exchange and magnetocrystalline energies. Given a uniaxial system, this means that the system remanence will thus be determined by the alignment of the magnetic easy axes and inter-grain coupling.

If one considers a two particle system of single domains, uniaxial easy axes of magnetisation and ignores magnetostatic contributions to the system at zero field, the energy of the system can be considered as

$$\phi'_{2-particle} = A \cdot \nabla(\frac{M(\vec{r})}{M_S})^2 + K_1 sin^2(\phi)(\vec{r_1}) + K_1 sin^2(\phi)(\vec{r_2}) \tag{2.19}$$

where $\vec{r_{1,2}}$ are the respective magnetisation vectors for each particle. One can consider then two cases where easy axes are aligned and misaligned. In the aligned case, all terms minimise when magnetisations are aligned in the same direction, as the $sin^2(\phi)$ functions tend to zero and there is no divergence in magnetisation. In the case of the misaligned state, one must consider the magnitude of both intrinsic variables. In a steady state, Gibbs energy is equal to zero and thus one can consider the ratio between K_1 and A. Given typical units for K_1 for hard magnetic materials are of the order of $(10^5 - 10^6) Jm^{-3}$ and A is of the order of $10pJm^{-1}$, this would imply that magnetisation deviation from easy axis for the two particle system will be slight [37]. Extending this idea to a many body system and considering the sum magnetisation over all the particles, increasing this sum magnetisation, and thus the remanence of the system, can be achieved by axis alignment rather than coupling deviations.

Given that the desired application of the systems developed in this thesis is as permanent magnetic materials, a useful metric to assess the measured composition series is the magnetic hardness parameter, κ, where:

$$\kappa = (\frac{k}{\mu_0 M_S^2})^{0.5} \tag{2.20}$$

using previously defined variables [17]. This metric being proportional to $\frac{H_A}{M_S}$ means that it is a good metric as to whether a material can overcome shape anisotropy and still maintain permanent magnetic poles, or whether it must be magnetised in such a way as to change the demagnetisation field to sustain said poles. Values of $\kappa < 0.1$ are considered soft magnetic systems where MAE is low enough in the system for easy re-magnetisation in any direction but little resistance to a change in magnetisation vector and materials in the range of $0.1 < \kappa < 1$ are considered semi-hard and thus dependent on shape anisotropy. Those above this range are considered hard magnetic materials and may be suitable for permanent magnetic material applications.

2.4 Theory Summary

The origins of ferromagnetism have been introduced along with the basic principles behind micromagnetic theory. The key finding of this survey is that whilst intrinsic magnetic properties are a product of the unit cell level of a material, the atoms themselves and coupling between atom pairs within the unit cell, extrinsic properties are a result of balancing energy terms within the Magnetic Gibbs energy as the magnetisation moments within coherent groupings of unit cells, referred to as grains, interact with one another.

From a permanent magnetic material perspective, it is important to control grain size to improve coercivity, grain morphology to affect demagnetising effects and prevent domain formation and grain alignment (referred to as texture) to improve remanence. Thus the development of a permanent magnetic material with these principles in mind should start from the chemistry of the alloy, building the most appropriate unit cell with regards to site occupation and lattice parameters to optimise intrinsic magnetic properties, and then move to casting and microstructural control to improve extrinsic magnetic properties, recognising that they are functions of intrinsic properties.

Chapter 3

Literature Review

3.1 Ferromagnetic Behaviour in the MnAl Binary System

3.1.1 Emergent Magnetism from $\tau - MnAl$

Investigated in 1958 by Kōno, a composition range within the $MnAl$ binary system that demonstrated the ferromagnetic behaviour, referred to in later work as the $\tau - MnAl$ phase, was defined [44]. Metastability in the phase was discovered, showing that annealing at $T_{anneal} \geq 650°C$ saw a degradation of the magnetic properties on the scale of hours, owing to the decomposition of the magnetic phase to equilibrium phases by the $\tau \rightarrow \gamma_2 + \beta Mn$ transformation. The structure is synthesised by quenching $Mn_x Al_{100-x}$, where $50 < x < 65$, forming the ϵ-phase and annealing to transform the HCP ϵ-phase structure to the BCT $L1_0$ structure of the τ phase. The mechanism for this is that the $\epsilon(HCP) \rightarrow \epsilon'(orthorhombic) \rightarrow \tau(BCT)$ by an ordering reaction between the $A3$ HCP state to the $B19$ orthorhombic state and a martensitic shear reaction from the B19 structure to the desired $L1_0$ state [45].

3.1.2 Annealing and Transformation

The annealing parameters and optimum alloy composition to maximise τ-phase population and maximise the magnetic properties of the alloy are not consistent in literature. The synthesis of $\tau - MnAl$ is non-trivial and a common approach is to cast an ingot of known and targetted composition from melt and cool to room temperature, heat and then quench from $(1000 - 1100)°C$ to room temperature to trap the precursor ϵ-phase and then anneal between $(400 - 600)°C$ as indicated by Figure 3.1 to achieve the τ-phase, either quenching again or cooling naturally to room temperature depending on concerns about

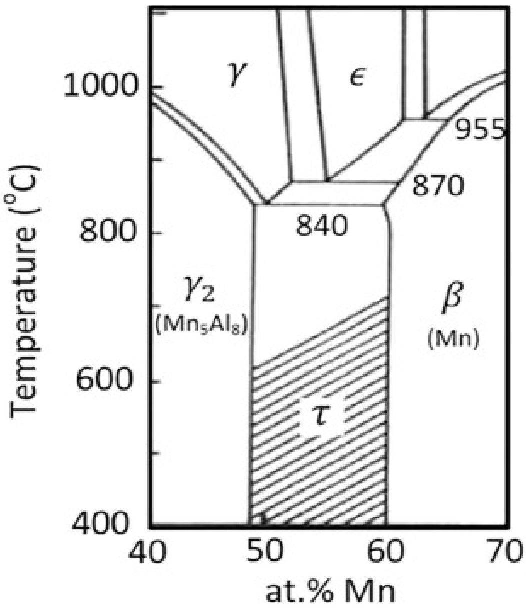

Fig. 3.1 Whilst the composition range that $\tau - MnAl$ exists at is somewhat understood, the material is normally synthesised from the precursor ϵ phase and, as such, it is difficult to create low Mn-concentration material. Reproduced from Tang Nguyen *et. al.*[46]

$\tau \rightarrow \beta Mn + \gamma_2$ transformations. Near-equiatomic MnAl has a longer transformation time than Mn-saturated samples thus it can be interpreted that Mn saturation may destabilise the ϵ'-phase such that it undergoes transformation at lower energies as seen in Figure 3.2 [47]. This figure shows that annealing to ensure homogeneity of the τ-phase results in decomposition to equilibrium γ_2 and βMn phases, both being non-magnetic and detrimental to ferromagnetic properties [45].

As discussed by Crisan *et. al.* , the transformation $\epsilon \rightarrow \tau$ sees a saturation of manganese, with the $L1_0$ symmetry group having an optimal ratio of 1:1 [48]. Whilst both the Mn and Al atoms randomly occupy $(0,0,0)$ and $(\frac{1}{2},\frac{1}{2},\frac{1}{2})$, excess Mn forms substitutional defects, substituting the Al atoms at the $(\frac{1}{2},\frac{1}{2},\frac{1}{2})$ sites. Given bond lengths at this site, the Mn-Mn bond has antiferromagnetic coupling, meaning that higher $Mn\ at.\%$, $\tau - MnAl$ compositions will see a decrease in M_S of the sample following transformation [47]. The alloy synthesis techniques discussed within this Chapter, such as gas atomisation and traditional casting, strive to achieve compositions nominally close to $Mn_{55}Al_{45}$ though an approach to precipitate secondary phases is discussed in Section 3.3.

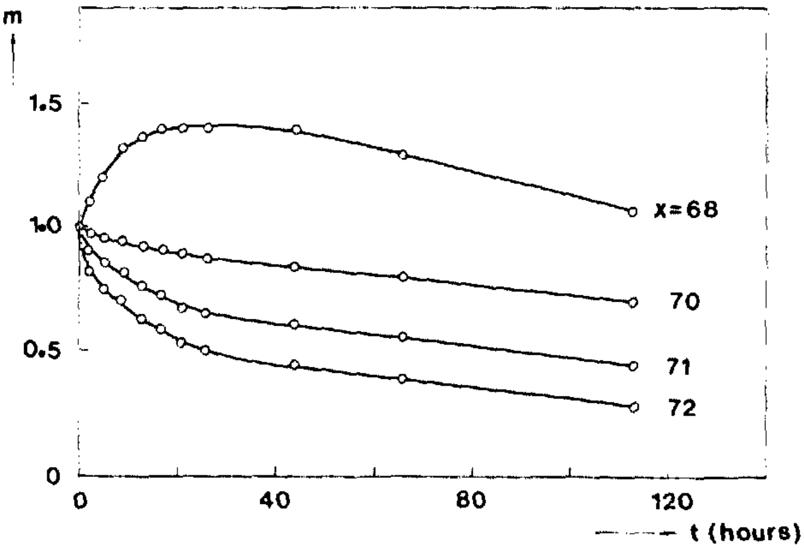

Fig. 3.2 A plot of $M_S(t)/M_S(10min)$ against time. Given that only the near-equiatomic composition shows transformation to $\tau - MnAl$ occurring after 10 minutes, with all other samples showing a decrease in saturation magnetisation and thus decay from metastable to equilibrium states, it can be implied that the excess Mn in solid solution affects the transformation mechanics of $\epsilon \rightarrow \tau$. Reproduced from Pareti, Colzoni, Leccabue and Ermako [47]

3.1.3 The Effect of Interstitial Carbon Doping

A well-established modification of the $\tau - MnAl$ material is of adding $(0 < C\ at.\% < 2)$ to the system. As discussed by Kuo, Yao, Huang and Chen, adding carbon stabilises the formation of $\tau - MnAl$ and sees improvement in magnetic properties [49]. Alloys of MnAl and MnAlC of $(70-72)wt.\%$ Mn were cast and oil quenched from $\approx 1100°C$ to room temperature to trap the ϵ'-phase and annealed at $\approx 525°C$ for 30 minutes to achieve the τ state. Following testing, these samples were ground and sintered to optimise sintering temperatures prior to a repeat of the heat treatments to reestablish the $\tau - MnAl$ within the material. The effect of carbon doping on the magnetic properties can be seen in Figure 3.3 which shows that any addition of carbon within the range leads to an increase in magnetic properties compared to an undoped sample.

Carbon doping discussed by Zhao *et. al.* is that the addition of $(0 < at.\% < 3)$C stabilises $\tau - MnAl$ at higher temperatures for composition $(Mn_{54}Al_{46})_{(100-x)}C_x$, shown in Figure 3.4 [50]. In all three plots, C-doping changes the precipitation of equilibrium phases and in cases of $x > 3at.\%$ prevents $\gamma_2 + \beta Mn$ forming at high temperature. Figures 3.4(b) & (c) suggest that C-doping allows the alloy to be worked at higher temperatures with C-doped alloys showing minimal magnetisation degradation at $500°C$ and less than a 25%

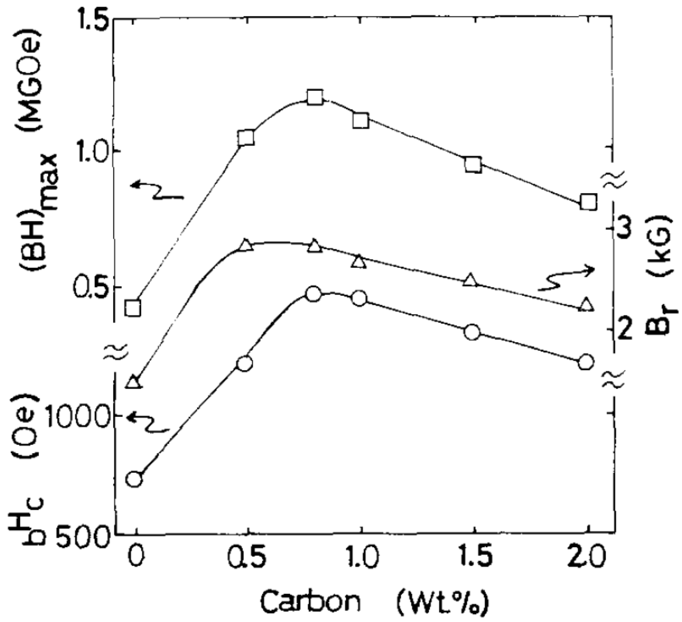

Fig. 3.3 A plot of the effect of carbon doping on the magnetic properties of MnAlC alloys tempered at ≈ $525°C$ for 40 minutes. This figure was reproduced from Kuo, Yao, Huang and Chen (1992). The exact sintering temperature of the MnAlC samples is not published and though a fixed post-sintering heat treatment is discussed, Kuo *et. al.* show that the variation of ≈ $100°C$ of anneal temperatures on a sample of $0.8wt.$%C can lead to a variation of ≈ 50% in BH_{max}, H_C and M_R, thus meaning that this graph should be interpreted as showing a trend and not exact, reproducible data as the exact phase population of the precursor material is not discussed and thus cannot be assumed to be 100% ϵ-phase [49].

decrease of magnetisation at $550°C$. Though these annealing temperatures are above the T_C of $\tau - MnAl$, magnetisation can be used as a metric to determine τ population as it can be postulated that, under the Curie-Weiss law:

$$\chi_{ferro} = \frac{C_f}{T - T_C} \ , \ T > T_C \tag{3.1}$$

, a ferromagnetic material at a temperature, T, above its Curie Temperature, T_C, should have a greater magnetic susceptibility, χ, than a paramagnetic material:

$$\chi_{para} = \frac{C_p}{T} \ \forall \ T \in \mathbb{R}^+ \tag{3.2}$$

, assuming that the Curie Constants, C, of the materials are of the same order of magnitude [51].

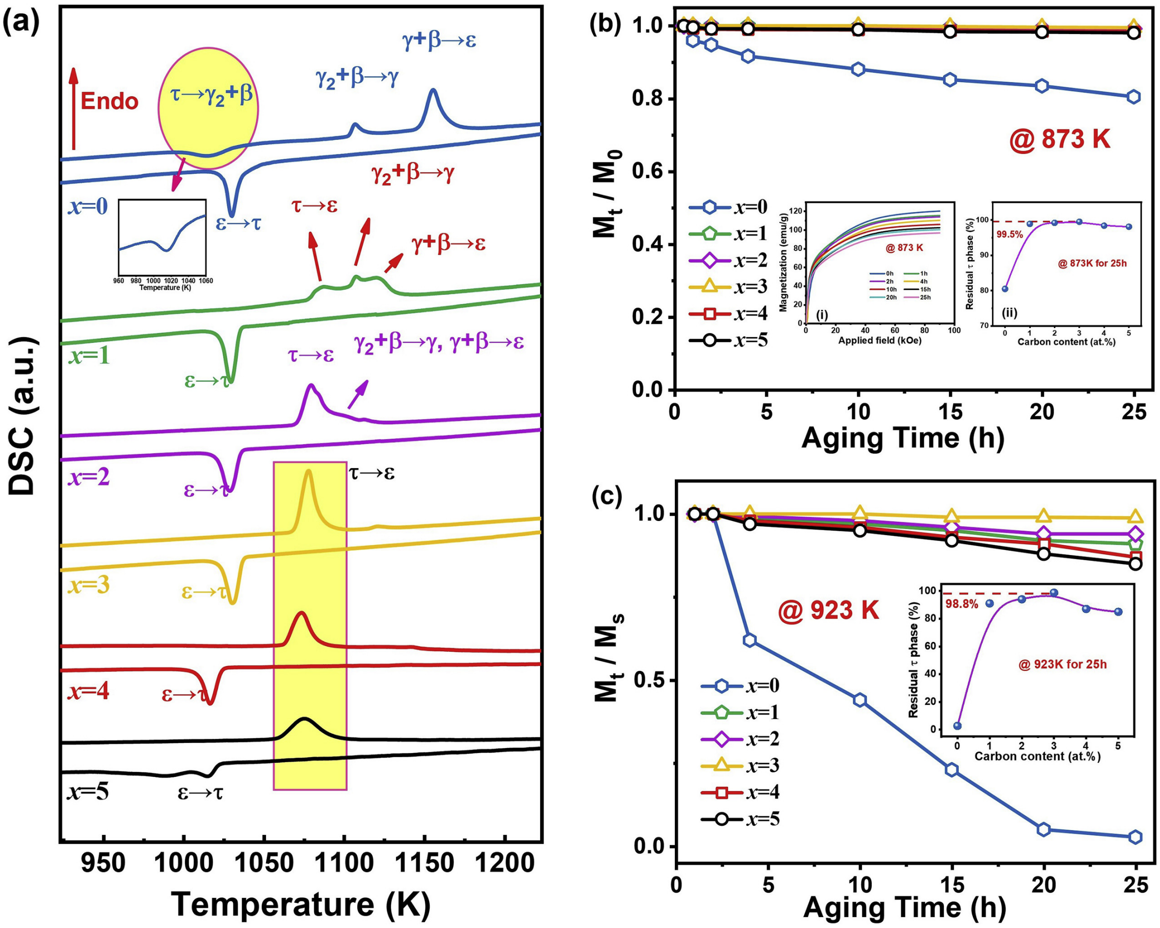

Fig. 3.4 (a) The DSC data for $(Mn_{54}Al_{46})_{(100-x)}C_x$ being heated from the $\tau - MnAl$ phase to study decomposition temperatures. (b) A plot of time-dependent magnetisation at $600^{\circ}C$ over initial magnetisation against time. (c) A plot of time-dependent magnetisation at $650^{\circ}C$ over initial magnetisation against time. No information is published regarding the field applied on the samples undergoing heat treatments in (b) and (c), implying these measurements were undertaken in zero-field conditions. Reproduced from Zhao *et. al.* [50].

3.2 Milling and Sintering of τ MnAl

Annealed-as-bulk $\tau - MnAl$ does not represent the optimum structure for extrinsic magnetic properties. To optimise extrinsic magnetic properties, the microstructure of the ferromagnetic alloy must be textured such that there is alignment of the easy axis of the lattice [17]. The easy axis of the lattice can be defined as the direction along the crystal axis of which it is the lowest energy for the magnetisation to orient itself, expressed by Equation 2.11 the additional energy needed to have a magnetisation oriented θ degrees from the easy axis of magnetisation and is explored in more depth in Section 2.3.2. For tetragonal systems where the anisotropy constant $K_1 > 0$, the easy axis lies along the c-axis. With $K_1 = (1.5 - 1.77) MJm^{-3}$, $\tau - MnAl$ has an easy axis along its c-axis [52].

The anisotropy constant determines the coercivity limit of the material under the following equation:

$$H_C < H_A = 2\frac{K_1}{\mu_0 M_S}, \tag{3.3}$$

where it is assumed that in the case of maximum possible coercivity, a hysteresis loop tends towards a rectangle with vertices on an $M(H)$ plot of $(\pm H_A, \pm M_S)$, and that the alignment of the c-axis sets the remanence of the material [36]. Much work on $\tau - MnAl$ has gone on either improving the anisotropy and saturation magnetisation of the material through doping or improving the texture of the material to see greater alignment of the c-axis.

Generalised states of alignment can be seen in Figure 3.5 by Coey, where either bonding or sintering aligned magnetic powders can fix the texture of the microstructure and improve magnetic properties [17]. Figure 3.5(c) can be considered the formation of annealed as bulk material, with statistical alignment of the magnetisation of each grain but with variance in the exact direction. In an idealised case, powders are aligned and sintered for optimum properties. For $\tau - MnAl$, this introduces additional complications as shown in the papers discussed in the following sections.

3.2.1 Effect of Mechanical Milling and Heat Treatments on Gas Atomized MnAl/MnAlC Alloy Powders

Work by Lee *et. al.* shows precipitation of equilibrium γ_2 & βMn phases detrimental to M_S can occur at lower temperatures by introducing additional strain into the material through milling, evidenced by a broadening of the characteristic XRD peaks of the $\tau - MnAl$ lattice [53]. $\tau - MnAl$ particles were generated using Gas Atomisation techniques and

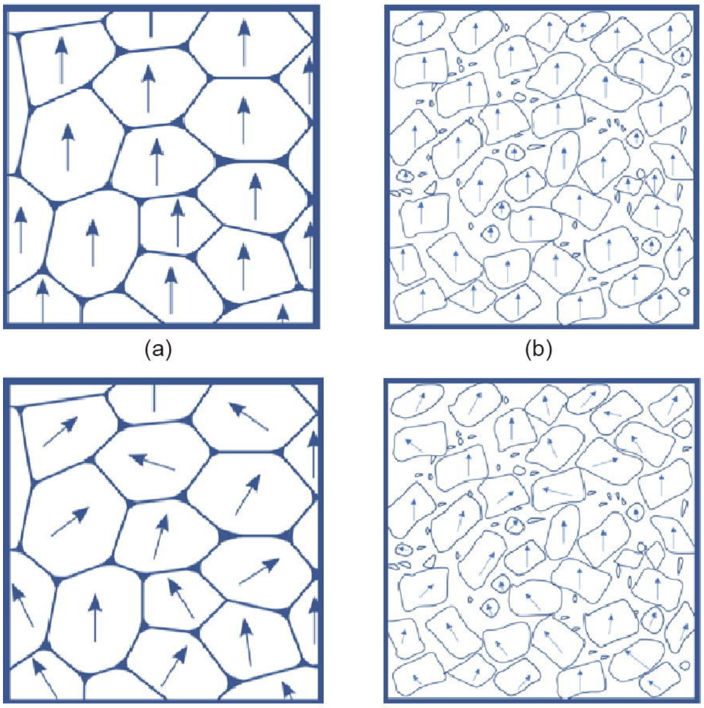
(a) (b)
(c) (d)

Fig. 3.5 Images of idealised structures common to permanent magnets. (a) A sintered, oriented ferromagnet. Efficiency of orientation ≈ 100% (b) A bonded, oriented ferromagnet. Efficiency of orientation ≈ 70% (c) A sintered, non-oriented ferromagnet (or idealised annealed-as-bulk alloy). Efficiency of orientation ≈ 25% (d) A bonded, non-oriented ferromagnet. Efficiency of orientation ≈ 12%. Bonded magnets assume a density of magnetic material of 70%. Reproduced from Coey [17].

annealed at $650°C$ for 20 minutes prior to ball milling for 5, 10, 20 and 26 hours and then a repeat of the annealing process, the results of which can be seen in Figure 3.6, showing the increasing magnitude of $\gamma_2 + \beta Mn$ peaks relative to τ-phase peaks as a function of annealing time. Samples that underwent the same milling process, but not the second annealing, showed no precipitation of γ_2 or βMn peaks, suggesting that the milling decreased both the temperature needed to see $\tau \rightarrow \gamma_2 + \beta Mn$ and the time required to see decomposition when compared to the work of Zhao *et. al.* shown in Figure 3.4.

The effect of the milling process investigated by Lee *et. al.* on the H_C and M_R of the metal powder is significant. Annealing after milling shows a significant decrease in properties compared to the unannealed samples and this difference is proportional to milling time, and thus can be interpreted as proportional to the precipitation of equilibrium phases within the particles. The difference in properties can be seen in Table 3.1 and, whilst there is an increase in H_C as milling time increases, with the annealed material showing an increase of ≈ 40%, the decrease in M_R is significant in comparison,

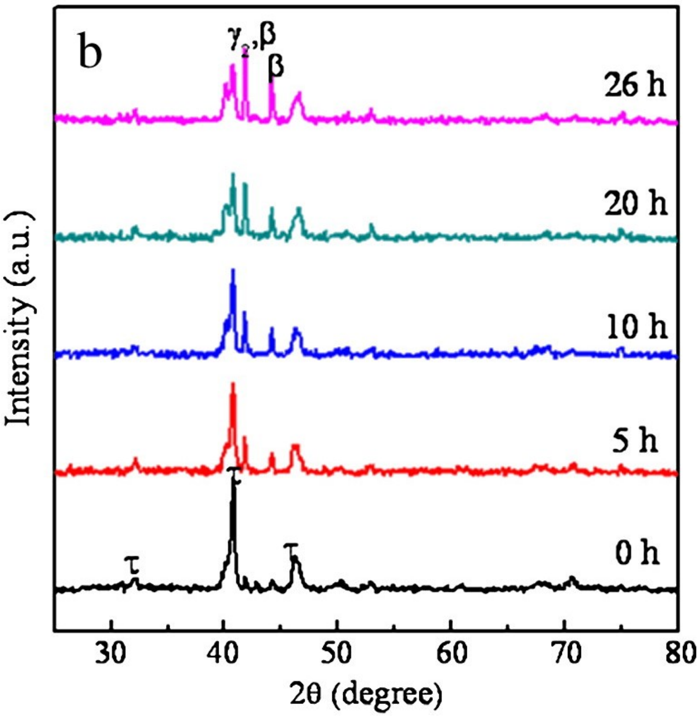

Fig. 3.6 XRD plots of Gas Atomised $\tau - MnAl$ milled for 0, 5, 10, 20 and 26 hours following a 20 minute anneal at $650°C$. The rapid precipitation of the equilibrium states when compared to the work of Zhao *et. al.* is believe to be the result of an increase of strain induced within the material from the milling process, given the correlation of equilibrium state signal and milling time. Reproduced from Lee, Wang, Zhang and Choi [53].

with a $\approx 50\%$ decrease at 26 hours. The increase in H_C is attributed to a decrease in particle size and, in the annealed samples, to the development of equilibrium phases pinning domain walls but given the decrease in M_R, attributed to additional stress within the system, techniques to achieve similar particle sizes without introducing the same levels of stress into the system. Annealing at $280°C$ was shown to increase M_R to values near unmilled powders at low milling times or by significant margin, defined as $\Delta M_R = 10emu/g = 10Am^2/kg = 45.9kAm^{-1}$ within the paper, resolving the concerns regarding M_R degradation.

Following the reasoning by Coey and presented in Figure 3.5, sintered and aligned magnetic materials will provide the best density of domains and thus the best BH_{max}, thus any powdered form of $\tau - MnAl$ would need to be compacted and fused in some fashioned [17]. Given that temperatures at $650°C$ produce a degradation of magnetic properties, sintering would need to take place below this temperature to avoid precipitation of equilibrium phases. With a Liquidus temperature between $(1200 - 1250)°C$ as defined by Jiménez-Villacorta [55], this sets a theoretical limit on the sintering temperature of

Milling Time [hours]	$H_{C,unannealed}$ $[kAm^{-1}]$	$H_{C,annealed}$ $[kAm^{-1}]$	% Change	$M_{R,unannealed}$ $[kAm^{-1}]$	$M_{R,annealed}$ $[kAm^{-1}]$	% Change
0	231	231	0	179	179	0
5	247	263	+6.48	156	147	-5.77
10	263	287	+9.13	133	129	-3.01
20	279	319	+14.34	106	96	-9.43
26	287	327	+13.94	96	92	-4.17

Table 3.1 A table showing the effects of milling time on gas atomised powders of $\tau - MnAl$. Unannealed samples are tested following milling and annealed samples have undergone an anneal at 650°C for 20 minutes. Errors are not provided as these results are interpreted from graphs provided by Lee, Wang, Zhang and Choi [53]. Powder Density was not given so a value of $4590kgm^{-3}$ as quoted by similar studies on milled $\tau - MnAl$ powders by Muñoz-Rodríguez *et. al.* [54]

$T_{sinter} < 0.54T_{liquidus}$, meaning that for higher densities, higher pressures or more novel techniques may be required.

Muñoz-Rodríguez *et. al.* have demonstrated that increases in performance can be made by the controlled precipitation of βMn phases by reducing milling time and increasing milling energy when compared to the work of Lee, Wang, Zhang and Choi [53]. Gas Atomised MnAlC powder was milled for 60 seconds and mill rate of $450rpm$ (the mill rate used by Lee *et. al* is not mentioned in their publication) referred to as flash-milling [54]. They also expanded on the work of Lee, Wang, Zhang and Choi by including the doping of carbon in their alloys, the effect on $\tau - MnAl$ is discussed in Section 3.1.3 but changes the high temperature behaviour of the phase. The study also expands to include sintering and annealing for magnetisation recovery.

SEM was employed to investigate particle morphology following the flash-milling process employed with initially spherical-like particles from the Gas Atomisation process transitioning to irregular, smeared particles, increasing the strain within each particle, evidenced by the broadening of the peaks within the XRD data from the unmilled to the flash-milled powders. This is evident on the ϵ-phase particles but those that would be directly comparable to the work in Lee *et. al.* is difficult as the XRD shown for the $\tau - MnAl$ powder shows that the precursor has equilibrium phases already present [53]. It is evident in the $\tau - MnAl$ peaks that broadening has taken place, indicating additional strain being imparted to the powder and suggesting that strain on the system will occur regardless of milling time.

The magnetic properties for the material are presented in Table 3.2. Similar to Lee *et. al.*, H_C increases with milling time by 12.7% for ϵ-phase powders and when utilising pre-transformed powders in the milling process, though the effect is reduced with only a 5.7% increase in H_C [53]. This may be due to the C doping stabilising the $\tau - MnAl$ structure as work on its high temperature properties have C shown preventing large scale precipitation

Initial Sample Phase		$M_R [kAm^{-1}]$	$H_C [kAm^{-1}]$	$BH_{max} [kJm^{-3}]$
ϵ-phase (gas-atomized)	Hot-pressed	205	229	12.4
	Milled 60s + Hot Pressed	186	258	9.5
τ-phase (gas-atomized + annealed)	Hot-pressed	202	230	11.0
	Milled 60s + Annealed $425°C$ + Hot-pressed	193	243	10.7

Table 3.2 A table of results detailing the effect of milling Gas-Atomized powders of $\epsilon - MnAl$ and $\tau - MnAl$ on magnetic properties of Hot pressed magnets. Units were converted using published densities for the hot pressed magnets though only one value was published for $\tau - MnAl$ magnets and as such, additional error should be assumed on those data points. Data reproduced from Muñoz-Rodríguez *et. al.* [54].

of equilibrium phases responsible for domain pinning increasing the H_C of the sample. The precipitation of Mn_3AlC may also be contributing to this effect, reducing the strain within the system by removing the Mn saturation from the $\tau - MnAl$ phase, conjectured to increase the precipitation of $\gamma_2 + \beta Mn$ phases as evidenced by milling. The effect on the M_R of the samples also is comparable to the work in Lee *et. al.*, decreasing following a milling operation due to the precipitation of equilibrium states. This further suggests that room temperature milling provides a trade-off between H_C and M_R that shows some dependency with time but is apparent even on the scales of seconds, assuming that the energy of milling between the two studies is comparable.

The data in Table 3.2 shows that milling, regardless of whether the powder was composed of ϵ- or τ-phases, is detrimental to the BH_{max} of the magnets when produced by Hot-pressing. Whether Hot-pressing is the most appropriate compaction technique can be debated, having no mechanism to ensure a texture beneficial to magnetic properties and thus falling into a structure similar to Figure 3.5(c), but by direct comparison, the precipitation of equilibrium phases being detrimental to M_R appears to outweigh any increase to H_C by domain pinning and particle size reduction when considering the material for application in a permanent magnet motor.

Work by Fang *et. al.* utilises Drop Synthesis to create $Mn_{55}Al_{45}C_2$ powders consisting of spherical particles before exploring the effects of cryogenic milling and flash heating [56]. The milling operation was undertaken at $\approx 196°C$ with a mill rate of 1800rpm for 2 or 4 hours. This is 4 times the milling speed of the work completed by Muñoz-Rodríguez *et. al.* but with timescales more comparable with Lee, Wang, Zhang and Choi [54] [53].

XRD data shows that there is still significant evidence of peak broadening and thus strain being imparted on to the particles. This study only conducted milling operations on $\tau - MnAl$ powders and, as such, there is no evidence to show if the same stress would be applied to an ϵ-phase powder. The data from the XRD is of low quality, making the identification of minor peaks from the 2 hour and 4 hour milling processes challenging and the patterns from τ, ϵ & βMn phases present many peak convolutions, meaning that the identification of secondary phases is not possible from this data. Flash heating at $900°C$ appears to improve this significantly with a comparison shown in Figure 3.7 and the peaks narrowing in reciprocal space following flash heating, implying that the strain induced in the system has dissipated from the system by inferring a microstrain decrease. This is contrary to Muñoz-Rodríguez *et. al.*, implying shorter anneal times or a hotter anneal temperatures may be superior at removing stress from the particles without precipitating equilibrium phases. Given the level of the background noise, it could be interpreted that the dwell time per angular iteration may have been insufficient to see the ϵ peaks within the data clearly. A better methodology to confirm the presence of epsilon peaks would have been to examine the range between (3.5 – 5)Å with a long dwell time to determine the presence of the ϵ-phase to determine phase population and whether the material had undergone complete $\epsilon \rightarrow \tau$ transformation.

Examining the methodology, a key difference between the two papers is the annealing process. In Muñoz-Rodríguez *et. al.*, the powders were were annealed under N_2 at a $0.167°Cs^{-1}$ heating ramp, whereas the work by Fang *et. al.* utilised an approach where the powders were sealed in ampules then introduced directly into a pre-heated resistance furnace for the anneal. If one assumes that the generally high thermal conductivity of most metals means that a $600°C$ initial temperature gradient would see a higher rate of temperature change in the method utilised by Fang *et. al.* over that of Muñoz-Rodríguez *et. al.*, this may explain why fewer peaks from equilibrium phases are visible in the XRD plots from the former method. If one assumes that the temperature is ramped to and from $300°C$ and annealed for 10 minutes at $425°C$, the total time for the annealing process would be 35 minutes, with 15 minutes spent at or above $400°C$ where transformation has been observed.

The results in Table 3.3 indicate that there is some benefit to the process. If one uses M_S as a metric of ferromagnetic phase population, it is clear that the initial cryomilling operation reduces $\tau - MnAl$ density within the system, likely through the added strain leading to the precipitation of equilibrium phases as seen in other work as M_S decreases as a result of cryomilling and decreases further as a result of extending the cryomilling time. What is of particular interest, however, is the effect of flash heating on the samples. No cryomilled sample returned to the M_S values of the drop synthesised sample, implying a level of irreversible phase transformation inherent to the cryomilling process with $M_{S,DS} = 614kAm^{-1}$ and the maximum value reported for the flash heated samples

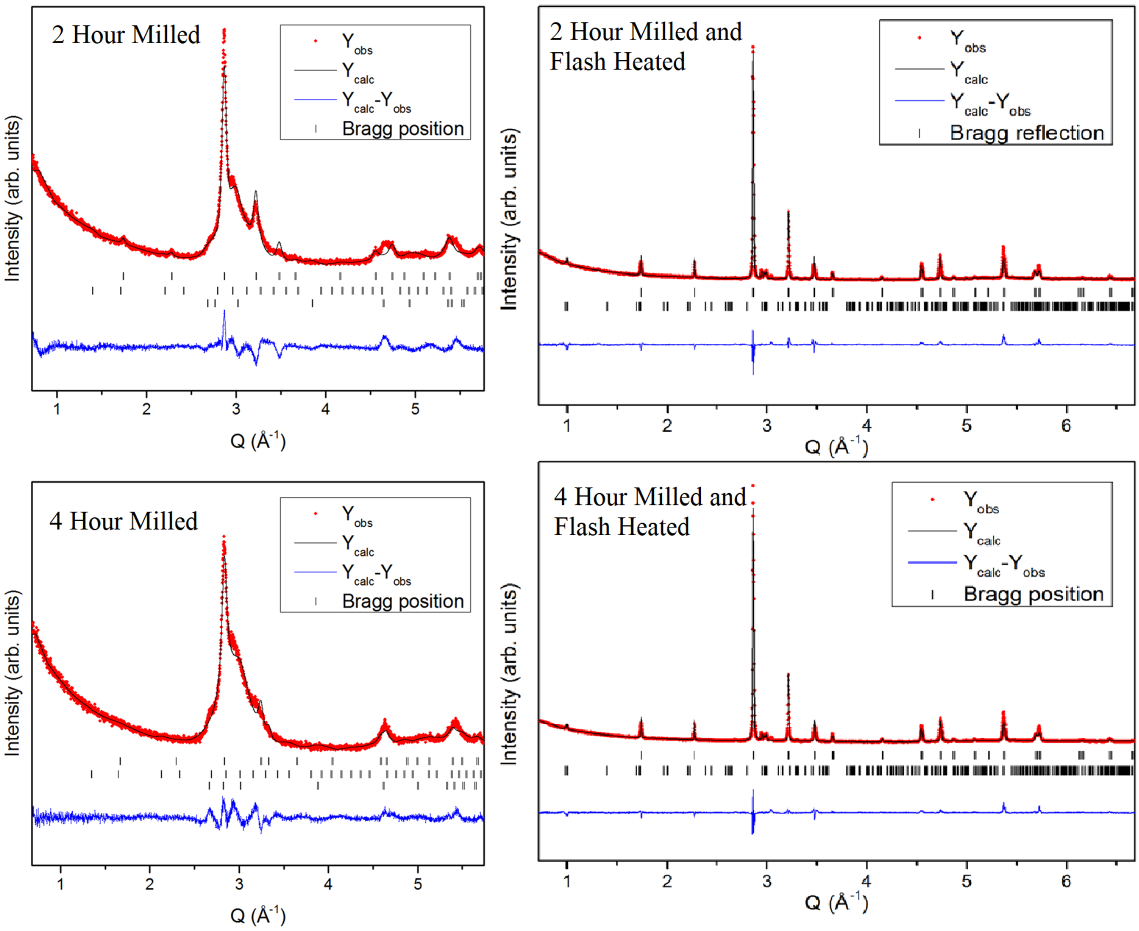

Fig. 3.7 XRD plots of drop-synthesised $\tau - MnAl$ powders cryomilled for 2 and 4 hours on the left hand side followed by XRD plots of the same material following 5 minute Flash Heating at $900^{\circ}C$. Given that there is no mention in the methodology section of the paper these figures were reproduced from of a change in XRD operating parameters, it is assumed that the change in data quality is due to recrystallisation and the removal of strain from the system. Reproduced from Fang *et. al.*

Sample (Drop Synthesized)	$M_R[kAm^{-1}]$	$H_C[kAm^{-1}]$	$M_S[kAm^{-1}]$
$(Mn_{55}Al_{45})_{100}C_2$	120	32	614
cryomilled 2 hours	37	302	104
Flash heated 1 minute	81	183	247
Flash heated 5 minutes	134	95	541
Flash Heated 15 minutes	132	103	527
cryomilled 4 hours	7	176	29
Flash Heated 1 minute	42	270	117
Flash Heated 5 minutes	148	127	515
Flash Heated 15 minutes	142	119	514

Table 3.3 Magnetic data derived from MH hysteresis loops of MnAl powders produced via drop synthesis, cryomilling and Flash Heating. Reproduced from Fang *et. al.* [56].

reported as $M_{S,FH,Max} = 541 kAm^{-1}$ with no indication that the drop-synthesis M_S could be reobtained by flash heating. The values of H_C and M_R exceed that of the drop synthesized powder for samples flash heated for 5 minutes or longer but not for M_R for samples flash heated for 1 minute, implying a minimum heating time for extrinsic magnetic property improvement. This is of particular interest as the work of both Muñoz-Rodríguez *et. al.* and Lee, Wang, Zhang and Choi both saw a decrease in M_R as H_C increased during milling [54] [53]. This implies that the degradation of the $\tau - MnAl$ phase inherent with milling process is clearly being recrystallised during the flash milling, as determined by the increase in M_S but the texture of the cryomilled particles remains aligned as shown in Electron Backscatter Diffraction (EBSD) images shown within Fang *et. al.*. This paper does not consider compaction techniques and so direct comparison with previously outlined work must be carefully considered but the results do suggest that cryomilling and flash heating may be the superior technique to ensure the best texture and phase population for permanent magnet applications.

3.2.2 Spark Plasma Sintering of MnAlC

Spark Plasma Sintering (SPS) was utilised in a study by Pasko *et. al.* where precursor $\epsilon - MnAl$ ribbons produced by melt spinning were heated to $(650-900)°C$ under a pressure of $70MPa$ at a heating ramp of $100°Cmin^{-1}$ to see one-step compaction and transformation from $\epsilon \rightarrow \tau$ [57]. The logic provided behind this approach is that melt spinning can produce nm-scale grains and thus see improved properties as grains approach the length scale of domains, as discussed in Section 2.3.5, thus avoiding excess heating and grain growth/coarsening is imperative to keep these properties whilst seeing full transformation. Two approaches were utilised, the first heating to $650°C$ to attempt transformation

		Phases							
Sample	Heat Treatment	ϵ	τ	γ_2	βMn	Density [%]	$M_S[kAm^{-1}]$	$M_R[kAm^{-1}]$	$H_C[kAm^{-1}]$
$Mn_{54}Al_{44}C_2$	AQ	100							
	$550C$		100				438	247	144
	$650C$		84	6		88	398	207	152
	$850C$		79	21		100	374	127	72
	$950C$		96	4		100	470	111	40
$Mn_{49}Al_{49}C_2$	AQ	59		41					
	$550C$		70	30			302	175	183
	$650C$		25	67		92	119	64	247
	$850C$		35	65		99	175	72	104
	$950C$		46	54		99	191	72	80
$Mn_{55}Al_{45}$	AQ	100							
	$550C$		75		25		342	191	112
	$650C$			33	67	100			

Table 3.4 A table of heat treated As Quenched (AQ) melt spun ribbons of varying compositions, their phase populations (Mn_3AlC was not reported and assumed to make up remained of population) and magnetic properties. Reproduced from Pasko, Lobue, Fazakas, Varga and Mazaleyrat [57]

whilst compacting and the second heating to $(850-950)°C$ where the ϵ-phase is stable to perform compaction and then expecting transformation to occur on cooling.

The results of the SPS study can be seen in Table 3.4 and show clearly that the composition and heat treatment temperature are key variables to one-step transformation in the SPS system, with magnetic properties and their associated trends not showing consistent behaviour across all three systems and heat treatments shown. For reference, As Quenched (AQ) samples have been taken as ribbons from the melt spinning process and those treated at $550°C$ were annealed in a vacuum furnace at $550°C$ with a $0.167Ks^{-1}$ heating ramp rate. When comparing the M_S value of $Mn_{54}Al_{44}C_2$ to that of $(Mn_{55}Al_{45})_{100}C_2$ reported in Fang *et. al.*[56], the difference of $176kAm^{-1}$ would suggest that the geometry of the thin ribbon generated by the melt spinning process was providing a greater demagnetising field than that of the particle, lowering the stray field observed by the Vibrating-Sample Magnetometer (VSM) used to measure the magnetic data for the samples. This would explain the difference given that no mention of correcting for these effects was given in the text when concerned with the melt spun ribbons.

It is evident, however, that this process is not suited to pure $\epsilon - MnAl$ given the total decomposition to equilibrium states following the $650°C$ process. With the C-doped samples, the optimum heat treatment was dependent upon Mn to Al composition ratio but will all samples seeing a degradation of M_R when undergoing SPS. $Mn_{49}Al_{49}C_2$ is broadly invariant in its degradation of M_R of $\approx 60\%$ but the coercivity decreases across the range as sintering temperature increases. $Mn_{54}Al_{44}C_2$ shows similar behaviour with regards to

H_C but also shows a degradation in terms of M_R. Whilst theories have been postulated for the increase in coercivity, including the nucleation of equilibrium states, finer grains and increased porosity, the only composition and heat treatment to be somewhat comparable to a furnace annealed sample is that of $Mn_{54}Al_{44}C_2$ annealed at $650°C$. This clearly indicated that if this technique were to be utilised, significant development is required.

Combining a cryomilling preparation technique as discussed in Fang *et. al* and an SPS compaction approach as discussed in Pasko *et. al.*, Tyrman *et. al.* further evolves the work in SPS for the formation of $\tau - MnAl$ production by the use of a tungsten carbide mold, allowing for a pressure of 400MPa and a sintering temperature between $(500-600)°C$ to be investigated [56][57] [58]. The effects of this sintering process can be seen in Figures 3.8 and 3.9 and it was noted that there was little variance in measurements from either face of the sintered cube perpendicular to the direction of sintering with J_R and $J_{1.9T}$ showing differences in the range of $(0-15)mT$ and $\mu_0 H_C$ showing a directional difference of $\approx 0.02mT$ at $400Pa$ where the difference was greatest. The results show that both H_C and J_R increase as a function of sintering pressure for a sintering temperature of $550°C$ but there is a bias created by the anisotropic application of pressure during annealing. SEM of the sample that underwent SPS at a pressure of 400MPa is reported to show a flake-like structure perpendicular to the direction of pressure. This is reasoned as the primary reason for the relative increase in J_R and decrease of H_C in this direction and given that there is no correlation between βMn formation and the increase in properties, this appears to be the dominant effect. For the ease of readability, it is of note that J is defined here as the magnetic polarisation and that $J_{S/R} = \mu_0 M_{S/R}$

The anisotropic properties of the material produced by high pressure SPS suggest that the process is providing a bridge between previously discussed work, which would fall under a sintered, non-oriented magnet as defined in Figure 3.5(c), to a texture closer to that of a sintered, oriented magnet as shown by Figure 3.5(a). To further explore the limits of this effect, a change in sintering temperature and mold size could be implemented in further work to optimise this anisotropy and maximise the squareness of the MH loops to improve the BH_{max} of the material. Other compositions should also be studied to investigate whether the volume fraction of βMn can be controlled or whether near equatomic ratios of Mn:Al show similar behavior given that excess Mn will occupy Al sites and bond antiferromagneticly, reducing available $\tau - MnAl$ sites contributing to key magnetic variables [47].

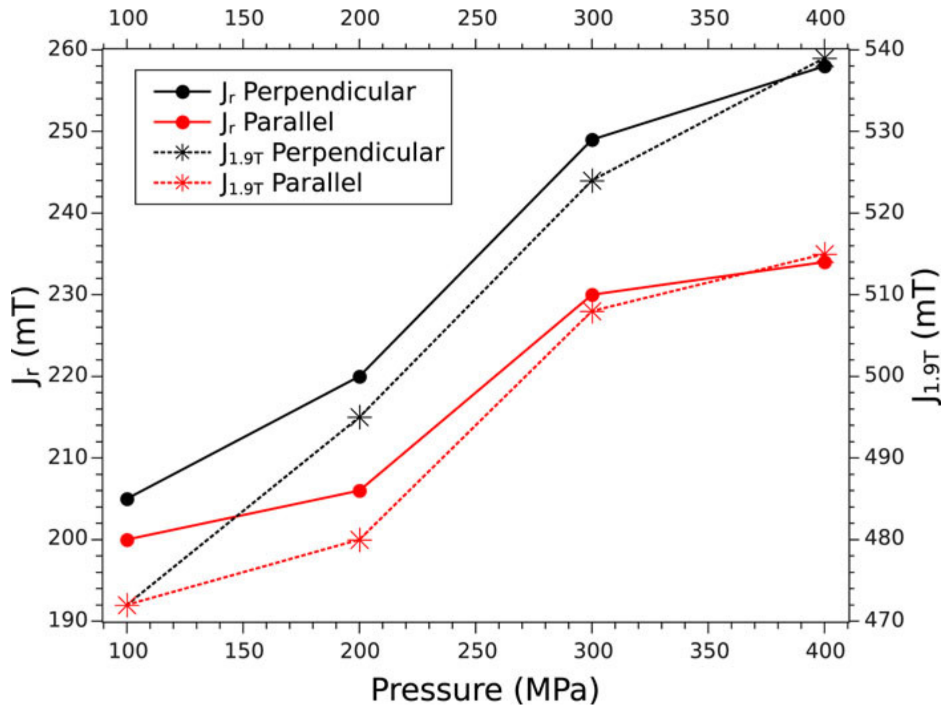

Fig. 3.8 A plot of SPS pressure against J_R and $J_{1.9T}$ in both the parallel and perpendicular directions of sintering. Reproduced from Tyrman *et. al*[58].

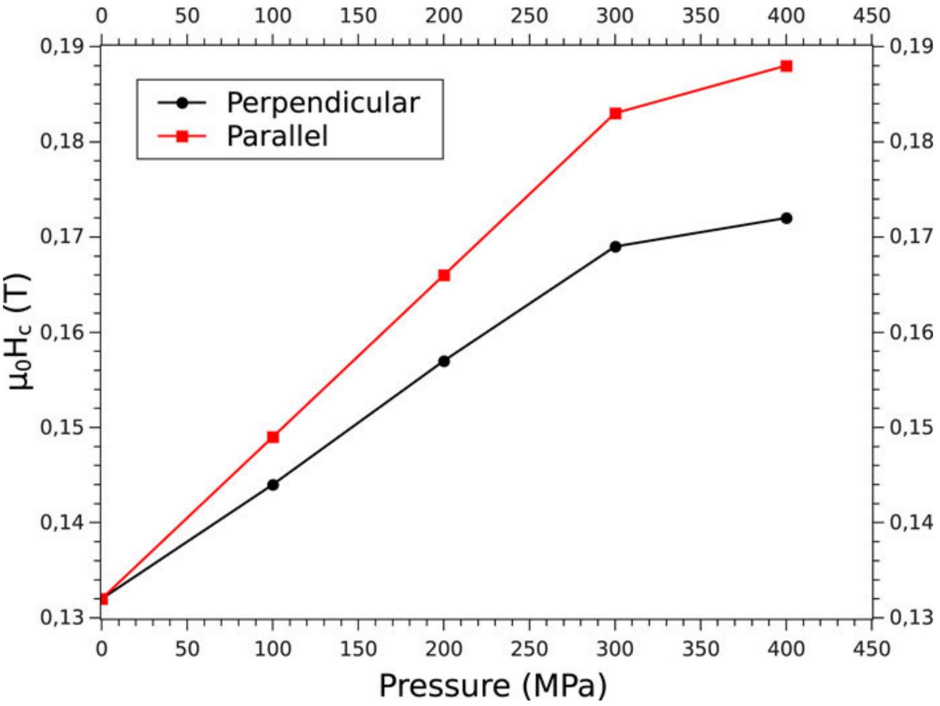

Fig. 3.9 A plot of H_C against sintering pressure in both the parallel and perpendicular directions of sintering. Reproduced from Tyrman *et. al*[58].

3.2.3 Conclusions on the State of Processing

When considering all processing techniques discussed, a common theme can be extracted. Degradation from metastable τ-phase to the equilibrium states $\gamma_2 + \beta Mn$ appears inevitable when changes to the microstructure occur. This transformation can be useful in controlled cases to raise H_C at the expense of M_R with the exception of cryomilling and then flash heating [56] and high temperature SPS processes [58], though the results from these experiments must also be understood as half of a process given that the paper does not discuss any compaction technique and how the particles would behave under sintering and the latter as an area that still needs much investigation to be used as a technique for larger scale development. This suggests that this behaviour and trade-off in properties may be inherent to the material itself and the metastability of $\tau - MnAl$. The work discussed in previous sections has outlined that the addition of C to the alloys has generally favourable results when considering milling, sintering and SPS induced property changes and it can be postulated that this is due to the C-doping stabilising the structure, as outlined in Section 3.1.3.

When milled, these papers show that $\tau - MnAl$ will partially decompose into equilibrium states regardless of milling time or temperature and when sintered, will see a similar decomposition, even in the case of high pressure SPS. As such, there is a need to address the composition of the material itself to increase high temperature transformation temperatures and thus improve the metastability of the material. By finding a ternary system or doping regime that would allow the processes outlined in this section to occur without the precipitation of equilibrium phases, benefits could still be expected to be seen by the reduction of particle size and the texturing of the microstructure as shown by the milling and SPS processes respectively.

3.3 Doping and Dual Phase Investigations

3.3.1 Initial Doping Investigations - Period II, Transition Metals and Rare Earths

The effects of Dy-, Pr- and B-doping of $\tau - MnAl$ ribbons produced by melt spinning were investigated by Liu, Chen, Zheng, Tan & Ramanujan [59]. B was selected as another Period II element to investigate if it has similar stabilising properties as C. Dy and Pr were identified as candidates for their 4f shells and prior application in improving magnetic properties in NdFeB alloys. It can be seen in Figure 3.10 that doping did not prevent the formation of the precursor ϵ-phase by the evidence of ϵ-phase XRD peaks observable in

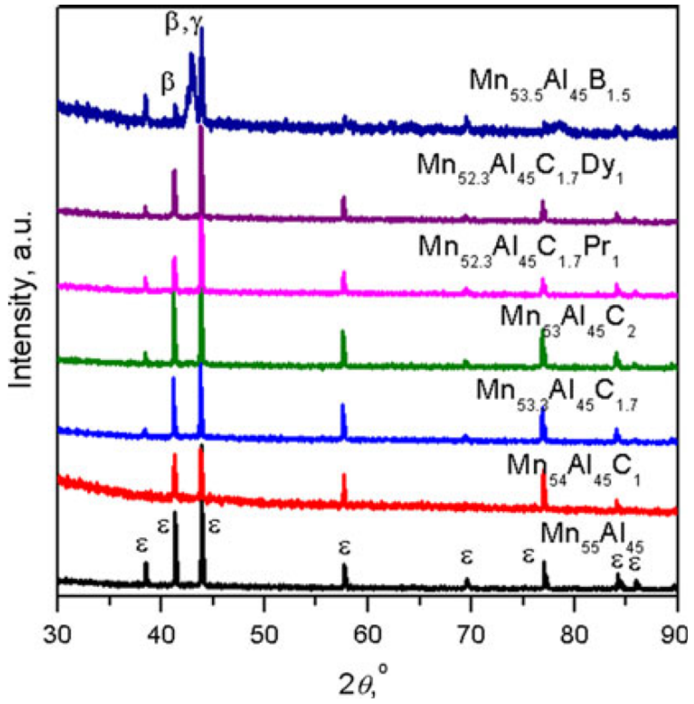

Fig. 3.10 XRD plots for doped $\epsilon - MnAl$ ribbons produced by melt spinning. Reproduced from Liu, Chen, Zheng, Tan & Ramanujan [59]

all data sets shown, though in the case of B-doping, the precipitation of the equilibrium states γ_2 and βMn can be observed, suggesting it may change the stability of the ϵ-phase to induce spontaneous decay.

Using Differential Scanning Calorimetry (DSC) to observe the phase changes in the alloys between $(300 \rightarrow 1000)^{\circ}C$, the effect of the doping on the $\epsilon \rightarrow \tau$ transformation can be observed. No ternary system investigated produced phases previously not discussed though the addition of Dy and Pr had a similar effect as C inclusion does of increasing the $\epsilon \rightarrow \tau$ phase transformation temperature from $484.7^{\circ}C$ to $535.5^{\circ}C$ for Pr and $531.9^{\circ}C$ for Dy. No significant deviation was observed for the high temperature transformation $\tau \rightarrow \epsilon$ for Dy-, Pr-, or C- doping of either $1at.\%$ or $1.7at.\%$. B-doping appears to block the transformation to the τ-phase, having no discernible peaks around expected transformation temperatures for the τ-phase and thus having no further reporting by the authors of this paper.

When considering the magnetic behaviour, the inclusion of Dy or Pr has little effect on the hysteresis loop of samples annealed at $650^{\circ}C$ for 10 minutes when compared to C-doping at a level of $1.7at.\%$, as seen in Figure 3.11 with little variation observed in extrinsic magnetic variables, T_C and minor changes in the gradient of $M(H \rightarrow \infty)$ implying small

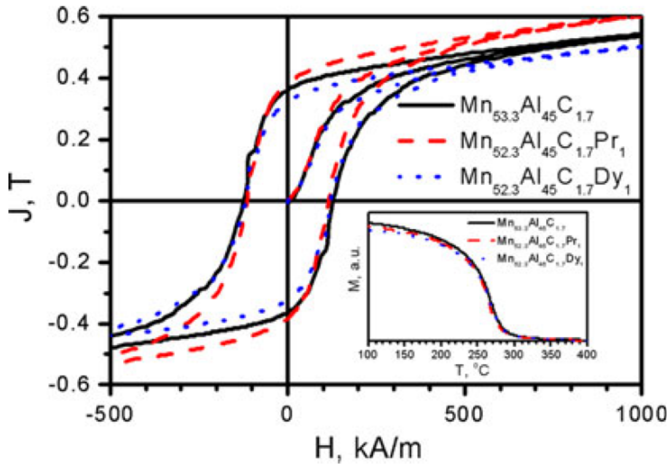

Fig. 3.11 BH hysteresis loops for $Mn_{53.3}Al_{45}C_{1.7}$, $Mn_{52.3}Al_{45}PrC_{1.7}$ and $Mn_{53.3}Al_{45}C_{1.7}$. All samples were annealed from $\epsilon \rightarrow \tau$ via an anneal at $650°C$ for 10 minutes. Reproduced from Liu, Chen, Zheng, Tan and Ramanujan [59]

changes in M_S and k, though accurate calculations are not possible with the provided dataset. In many ways, this observation is fortunate, given that this material is being investigated as a low-cost, Rare-Earth free permanent magnetic alloy. Examining the hysteresis loops presented by Liu, Chen, Zheng, Tan & Ramanujan, it is apparent that the addition of Dy is actually detrimental to magnetic properties and Pr only presents minor improvements, showing that the inclusion of 4f shells into the $\tau - MnAl$ does not affect electron bonding or anisotropy to levels that affect macroscopic properties enough to justify the cost of RE inclusion.

To investigate theoretical predictions that Fe-doping may improve the K_1 and H_C values for $\tau - MnAl$, Qian *et. al* synthesised doped material of composition $(Mn_{54}Al_{46})_{99}Fe$, $(Mn_{54}Al_{46})_{99.5}Si_{0.5}$ and $(Mn_{54}Al_{46})_{99}Si$ [60]. Though it is is not discussed, it can be reasoned that Si was investigated due to being in the same Periodic Group as C. Samples were induction melted to composition and underwent annealing at $1100°C$ for 10 hours for homogeneity and quenched to trap the ϵ phase before a secondary heat treatment at $\approx 500°C$ for 20 minutes to produce the desired τ-phase. Samples then underwent high-energy ball milling for 100min before testing. No compaction or sintering technique was utilised.

Examining the $M(T)$ plots for the initial sweep to annealing temperature present in Figure 3.12(a), it is observable that the addition of Fe and Si changes the $\epsilon \rightarrow \tau$ transformation. The addition of Si raises the critical transformation temperature to $(544 - 562)°C$ but Si $1at.\%$ changes the low temperature behaviour as well, potentially indicating the precipitation of a secondary paramagnetic phase between $(225 - 325)°C$ with a differing magnetic susceptibility. This would explain the formation of equilibrium phases in the XRD patterns visible in Figure 3.12(b) if this change in transformation was indicative of the transformation $\epsilon \rightarrow \gamma_2 + \beta Mn$, implying that Si doping destabilises the desired transformation. Given that a heating rate is not given, however, it cannot be interpreted whether the transformation of $\epsilon \rightarrow \tau$ in $(Mn_{54}Al_{46})_{99}Si$ occurred due to the remaining ϵ-phase population undergoing transformation as in an undoped alloy or whether an equilibrium was reached with the Si precipitating out $\gamma_2 + \beta Mn$.

Fe-doping, however, seems to show more promising results. Though a second transformation inflexion in the dH/dT can be seen, the resultant structure following the secondary heat treatment only shows peaks for the secondary τ-phase has not been generated in great quantity and the Fe dissolves into the lattice during transformation. Examining the effect on the magnetic properties of the materials, all three materials raise the value of H_C over 50% of that of the undoped material reported in the paper for comparison but all doping regimes see a decrease in M_S & M_R, though the the Fe-doped and Si(0.5.at%)-doped material only sees a ≈ 10% decrease in M_R compared to the ≈ 50% reduction from the Si(1at.%)-doped material. The hysteresis for the Fe-doped and Si(0.5.at%)-doped material also sees a greater area swept in the second quadrant, implying that the material would have a greater BH_{max} than that of the undoped powder.

Whilst Fe is shown in this paper to be a beneficial dopant to the system, with a significant increase in H_C from $191kAm^{-1}$ to $335kAm^{-1}$ with a minimal decrease in M_R, the paper does not cover the stabilising properties of Fe to the structure at higher temperatures for annealing and hot working processes nor does it cover compaction or sintering techniques, meaning more work would be required to characterise this system. Further, by decreasing the value of M_S for the system, it can be implied that processing to improve the BH_{max} for the system will see a lower maximum M_R, limiting material optimisation.

3.3.2 Ga Alloying Effects and Methodologies

Due to both the MnAl and MnGa system containing $L1_0$ systems exhibiting ferromagnetic properties and the MnGa phase being thermodynamically stable, Mix, Bittner, Müller, Schultz & Woodcock investigated the ternary $Mn_{55}Al_{45-x}Ga_x$ system for $5 < x(at.\%) \leq 9$ [61]. Samples were produced via arc melting and no reference is made to sample geometry beyond noting that demagnetising factors were corrected for thus it is assumed that methodology ensured a homogeneous alloy and samples were taken from crystallographically similar regions to minimise the effect of contact cooling and nucleation on grain formation.

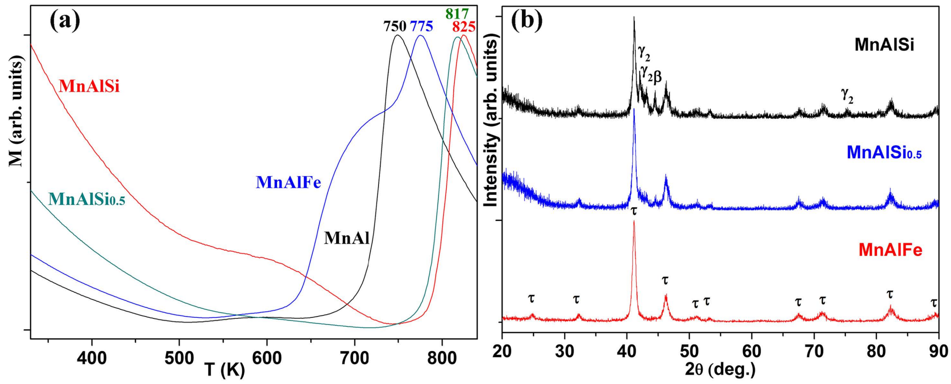

Fig. 3.12 Investigations into Fe- and Si-doped MnAl. (a) Magnetisation vs temperature approaching the transformation heat treatment. (b) XRD plots for the three doped samples following heat treatment. Reproduced from Qian *et. al.* [60]

Following the initial annealing process, ϵ-phase formation was observed along with a secondary Ga-doped γ_2 phase which is observed to transform to an $L1_0$ phase during the secondary anneal. Given that both of these states are ferromagnetic, this results in a value of $M_S = 657kAm^{-1}$, a significant increase in M_S when compared to MnAlC alloys discussed by Fang *et. al.* and Pasko *et. al* and is referenced as higher than the maximum for either binary magnetic system [56] [57]. The justification for this is given by the dispersion of Mn concentration between the two phases, seeing a closer to equiatomic ratio between Mn and Al/Ga such that fewer substitutional defects of Mn existing in Al sites occur, resulting in less antiferromagnetic coupling throughout the material.

The significant finding, however, from this paper is the effect that Ga-doping has on the thermal stability of the alloy. Seen in Figure 3.13 are the XRD plots of $Mn_{55}Al_{45}$ and $Mn_{55}Al_{38.57}Ga_{6.43}$ following an anneal at $700°C$ for two hours, a higher temperature than that observed by Zhao *et. al.* where significant reduction in magnetisation reduction was observed following 4 hours annealing at $650°C$[50]. Whilst decay into equilibrium states can be seen in Figure 3.13(a) for the undoped alloy by the emergence of βMn characteristic XRD peaks, no change can be observed for the dual phase Ga-doped alloy in Figure 3.13(b), showing that the alloy is stable under these conditions and thus presents better prospects for sintering operations than the undoped alloy. What is not discussed and could be considered the next step of investigation for the ternary system are the values of H_C or M_R for the system, nor an optimisation for the system to find the best ratio between the two phases to ensure hard ferromagnetic properties.

Following on from work published by Mix *et. al.*, Jiao *et. al.* investigated the effect of liquid phase sintering to improve densification and magnetic properties of MnAlC magnets by sintering in solidus solution with MnGa [62]. $(Mn_{54}Al_{46})_{98}C_2)$ and $Mn_{65}Ga_{35}$

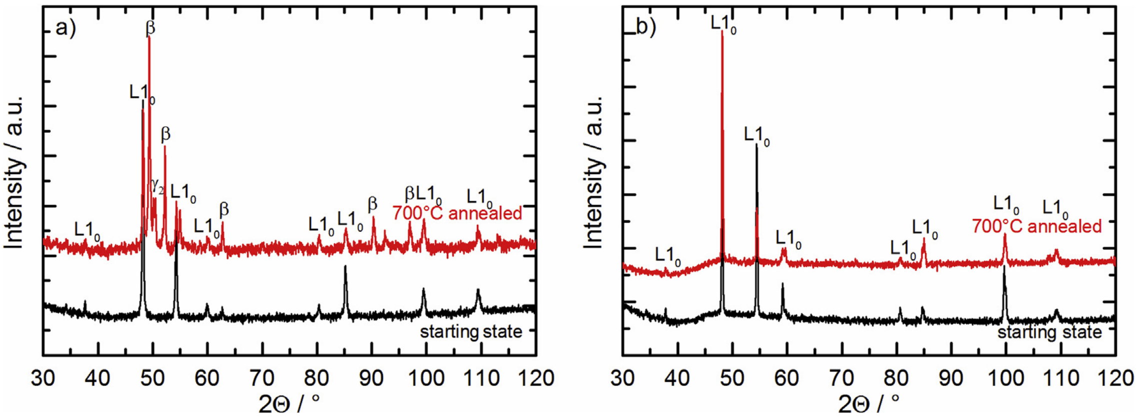

Fig. 3.13 (LHS) XRD patterns for a sample of $Mn_{55}Al_{45}$ in the τ phase before and after an anneal at 700°C, showing the precipitation of the equilibrium phases $\gamma_2 + \beta Mn$. (RHS) XRD patterns for a sample of $Mn_{55}Al_{38.57}Ga_{6.43}$ in dual $L1_0$ structure undergoing the same annealing process but not showing decomposition in the same fashion as the binary system. Reproduced from Mix, Bittner, Müller, Schultz & Woodcock [61]

samples were prepared by arc melting, annealing and quenching to fix the ϵ-phases, melt spinning and ball milling to ensure particle size less than $18\mu m$. Investigated mixtures of (0, 10, 20, 30, 40) $wt.\%$ $Mn_{65}Ga_{35}$ were achieved by ball milling ratios of sieved powders together. Following this, the mixtures were compacted under $600MPa$ and sintered at 1000°C for 2 hours.

It was shown that the increase in $Mn_{65}Ga_{35}$ content decreased porosity in the final sintered material, increasing density from $4.56gcm^{-3}$ for $0wt.\%$ to $5.50gcm^{-3}$ for $40wt.\%$. The inclusion of $Mn_{65}Ga_{35}$ also appears to prevent the formation of the equilibrium βMn phase following sintering. Increasing $Mn_{65}Ga_{35}$ density also increases H_C, M_R, H_A and BH_{Max} though all within the same order of magnitude. Whilst this approach may prove for a novel methodology to overcome many of the disadvantages of sintering processes already discussed in Section 3.2, it explores a Ga heavy composition space such that, much like the work of Mix *et. al.*, the resulting material would still contain Ga $5at.\%$, equating to approximately Ga $7.5wt.\%$. Referencing Figure 1.3, establishing a lower limit to the $Mn_{65}Ga_{35}$ content required to sinter without βMn formation would be critical in achieving Gap Magnet cost criteria as established in Table 1.1 as the relative price of Ga is broadly two orders of magnitude higher than that of Al or Mn by mass, thus significantly increasing MnAlGa alloy cost for small increases in Ga $at.\%$.

3.3.3 Conclusions on Doping Regimes and Gap Within Field

Examining the doping work thus far, two key candidates stand out as areas of further investigation for the development of $\tau - MnAl$ as a permanent magnetic material for electric motor applications, Fe-doping and the MnAlGa ternary system. B-doping and Si-doping both can be discounted as inhibiting the $\epsilon \rightarrow \tau$ transformation and changing the transformation mechanics respectively. RE-doping, in the case of Dy and Pr, is also shown to have minimal effect on the system in terms of improving the magnetic properties and thus is not a desirable area of investigations.

The potentially more advantageous area of investigation is that of the ternary system. In all processing papers discussed, the transformation of $\tau \rightarrow \gamma_2 + \beta Mn$ has been a limiting factor, reducing M_S and M_R. Given that MnAlGa has been shown to be thermodynamically stable at temperatures where $\tau - MnAl$ has been observed, this could potentially be the breakthrough required to optimise this material for bulk production. Given that Ga is considered a costly element by Figure 1.3 at $(100 - 1000)\$ kg^{-1}$, optimisation of Ga content and annealing processes is critical to create a magnetic system that is able to achieve the specifications defined by J.M.D. Coey in Table 1.1 [15].

Further, given the logic of investigation was that MnGa contained a ferromagnetic phase, another potential gap that can be investigated is the MnAlBi ternary system to determine whether similar effects occur. The MnBi system has a well reported ferromagnetic state [63][64][18][19] but the ternary system has not been explored outside of the thin film states as a layered system [65]. As previously discussed in Section 1.3.1, the binary system is inappropriate due to the abundance of Bi but compared to Ga, Bi is considered an order of magnitude cheaper by Coey [15] in Figure 1.3 and thus warrants investigation prior to the optimisation of MnAlGa as a potentially more economic alternative. Following this, work to improve the texture and sintering of the identified and optimised ternary system is imperative for developing a bulk permanent magnet for industrial application, and so testing previously utilised and discussed techniques on the new system will further advance the field, addressing the issue of metastable decay and magnetic property degradation.

3.4 Mechanical Deformation of the τ-MnAl Phase

Considering the previous sections' conclusions on the milling and sintering of τ-MnAl being that any high temperature route to obtain texture, alignment or near-net shape manufacturing can precipitate the $\tau \rightarrow \gamma_2 + \beta$Mn decomposition, alternative pathways to develop domain alignment must be considered to increase the BH_{Max} of the material to any useable value in line with the Gap Magnet criteria laid out by Coey [15]

3.4.1 Cold Working of $\tau - MnAl$

Bittner, Freudenberger, Schults and Woodcock have published work investigating cold working of MnAl and MnAlC produced from both quench and anneal methodologies, normally producing samples with $(95 < H_C < 143) kAm^{-1}$, and from controlled cooling, normally producing samples with $H_C \approx 16 kAm^{-1}$ [66]. Cold swaging of a sample of controlled cooled $Mn_{53}Al_{45}C_c$ to a logarithmic (ot true) strain of $\epsilon_{true} = ln(l_f / l_i) = 1.1$, where l_f and l_i are the final and initial lengths respectively, a showed an increase in coercivity to $H_C = 227 kAm^{-1}$ and achieved a remanence of $M_R = 372 kAm^{-1}$, significantly higher than results published by Fang *et. al.* achieved through cryomilling and flash heating (See Table 3.3 though this does produce a decrease in M_S, attributed to a lattice parameter shift resulting in antiferromagnetic Mn-Mn coupling. The average grain size observed through controlled cooling, however is of the order of $10\mu m$, implying that, by Equation 2.17, the grains are firmly within the multi-domain size range. Using the supplied average Saturation Magnetisation value of $M_S = 613 kAm^{-1}$ and estimating $K_1 = 1.7 MJm^{-3}$ and $A = 12.95 pJm^{-1}$, one can calculate that the critical domain diameter for an idealised spherical grain is $D_{crit} \approx 0.72 \mu m$, recognising that this approximated for $T = 0K \approx -273°C$ [15] [67]. Thus, by GSDCP Theory discussed in Section 2.3.5, this material may not be optimum for studies aimed at increasing H_C due to a $1/D_{grain}$ dependency on H_C. However, given the theory presented within the paper relies on dislocations contained within grain structures as a pinning mechanism for domain motion, the benefits from cold working would not necessarily be seen on single domain particles and the mechanical properties necessary to facilitate cold working, i.e ductility, may be insufficient in nano-grain castings.

Further to this, given the variation in grain size for quench and annealed samples, this may explain the variation in H_C between the two techniques, with the consistent and larger grain sizes of the controlled cooling methodology lowering H_C by way of GSDCP theory and a multi-domain state. It does demonstrate, however, that it is possible to increase extrinsic magnetic properties in a multi-domain grain sample through mechanical deformation processing, presenting a strategy for BH_{Max} increases with better control of as-cast grain structures.

Moving forward with this idea to investigate both cold deformation and the effect of C as an alloying element has on deformation-induced property changes, Si *et al.* deformed a composition series of $Mn_{54}Al_{46}C_x$ where $x = 0, 1, 2, 3, 4, 5$ in a stainless steel tube to engineering strains of $\epsilon_{eng} = (l_f - l_i)/l_i = 6 - 8$ [68]. Given that no reference direction is provided, this is assumed to be an elongation of sample cylinder length rather than a compression strain. The cold rolling was conducted post transformation on τ-phase

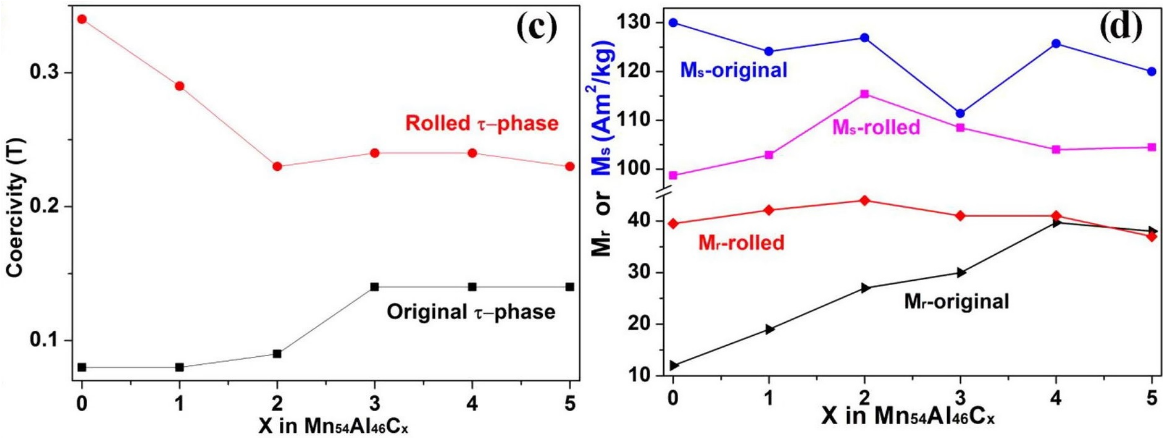

Fig. 3.14 H_C, M_R and M_S variations before and after cold rolling processing on MnAlC group alloys. No comment was made on the final state of the material post-deformation and so it is unclear if this is a bulk or powder sample measurement. Reproduced from Si *et al.*[68].

material and showed an increase in M_R and H_C within the material, which can be seen in Figure 3.14, though this difference decreases as a function of carbon concentration for M_R and H_C and shows a inconsistent decrease for M_S following rolling . The data suggests that C doping to the dual phase concentration of $C > 3at.\%$ leads to a smaller increase in H_C than compositions where C content is fully in solution of the τ-phase.

Of note, however, is an uncertainty in the calculation of M_S against external measurements. Due to a limited applied field of $3400kAm^{-1}$, Law of Approach to Saturation (see Equation 2.12) calculations were taken in from data measured in the applied field range of $(2390 < H_{app} < 3400)kAm^{-1}$, below that of the calculated anisotropy field estimated by data presented by Coey of $H_A = 4510kAm^{-1}$, questioning the validity of those observations as it could be questioned as to whether the material was fully saturated and thus whether the gradient of $M(H^{-2})$ was truly linear in order to fit M_S from. Further, no comment is made to the mechanical state of the rolled $\tau - MnAl$ material and whether it had fractured post deformation. For application on an industrial process level, either the material must survive cold rolling without failure or there must exist a sintering technique to recombine the fractured material without losing the benefit of deformation processing. As the final deformation strain is not expressed within this paper, it suggests that it was not able to be easily measured and that there was some fragmentation of material. Finally, the authors stated that comparisons were made to samples without considering demagnetising effects, which may somewhat explain the change in M_S and M_R.

3.4.2 Conclusions on Mechanical Deformation Processing for Maximum Energy Product Increases in $\tau - MnAl$

Whilst there is evidence of some work having been conducted on mechanically deforming MnAl and MnAlC systems for increased extrinsic magnetic properties, this section of the field still have much in the way of potential research streams to explore. Thus far, most techniques explored have focused on the deformation processing of the τ-phase through novel methodologies, such as swaging or rolling of samples contained within steel jackets. These techniques produce a non-uniform stress field throughout the material and no comment is normally made for the thermomechancal properties or final state of deformation processed material. Whilst there is clear evidence for extrinsic magnetic property changes as a result of mechanical deformation, there has yet to be a paper published on the mechanical properties of $\tau - MnAl$ as a function of temperature and alloying additions.

3.5 Conclusions on the State of Research into $\tau - MnAl$ and Existing Gaps in the Sector

As discussed, various techniques to increase extrinsic magnetic properties, namely M_R and H_C, and thus BH_{Max} have been attempted since the discovery of τ-MnAl. These differing research streams can be broken down into 3 distinct streams: alloying with additional elements to improve intrinsic magnetic properties or metastability, milling and sintering studies to reduce as-cast ingots to optimised particle states and sintering to create an aligned product and hot deformation processing to change the as-cast material microstructure and/or introduce preferred crystallographic orientation to improve extrinsic magnetic properties without requiring sintering operations.

The first stream of research has arguably produced two successful ternary systems, that of MnAlC and MnAlGa. The former increases thermal stability by reducing $\tau \rightarrow \gamma_2 + \beta Mn$ decay rates above $\epsilon \rightarrow \tau$ transformation temperatures and increases M_S at the expense of k and T_C by C occupation in $<\frac{1}{2}\frac{1}{2}\ 0>$ sites of the BCT lattice for $(Mn_{55}Al_{45})_{100-x}C_x$ where $(0 < C \leq 3)$ $at.\%$, causing c/a ratio and volume expansion, or precipitation of a C-rich secondary phase above this concentration reducing the density of desired τ-MnAl phase. The increase in stability is off-set by the decrease in k and T_C, however, showing approximately 10% decrease in both variables and implying only a $15°C$ tolerance between material property and Gap Magnetic Specification [50]. MnAlGa however, showed improved magnetic properties and stability as a result of Ga addition but had prior to this body of work only been investigated in concentrations of $Ga \geq 5\ at.\%$. Given the relative cost of Ga compared to Mn and Al, this would then mean that the resulting ternary alloy would fail the cost Gap Magnet Criteria. Additional alloying studies have investigated the addition of rare-earth elements, Fe, N, B, Si and other ternary systems, producing no additional obvious candidates for advancement to optimisation. At the time of research, the ternary system MnAlBi had not been investigated, meaning that the interaction between τ-MnAl and LTP-MnBi had not been studied to investigate potential benefits for intrinsic or extrinsic properties.

Concerning milling and sintering, various studies show that it is possible to improve extrinsic properties of τ-MnAl(C) by particle reduction, be it through ball milling or gas atomisation as explored in Section 3.2. However, studies focused around the eventual sintering/net-shape manufacturing of prepared powders demonstrate that the sintering or compaction of τ-MnAl particles always results in equilibrium decay to some extent in the former or lower ferromagnetic species density in the latter, meaning that this production route with MnAl(C) feedstock is not optimised for creating bulk systems with maximised intrinsic and extrinsic properties.

The final research stream shows promise for deformation studies as a mechanism to improve extrinsic magnetic properties but there is little published work regarding optimising this process or treating it from a metallurgy perspective. Stress-Strain information is not readily available for $\tau - MnAl$, MnAlC alloys or further alloying additions, especially as a temperature series. As such, it is a worthwhile task to isolate a particular composition of interest and undertake more significant thermomechanical testing in order to best assess an optimum temperature for deformation processing. Further, most existing deformation techniques are conducted either at room temperature, using radial symmetry or a ductile casing. To move forward to near-net shape manufacturing, hot rolling should be investigated to determine the effect of temperature on deformation processing and a consistent stress-field in order to model the effect of plastic deformation on extrinsic magnetic properties. Further, the effect of grain size and heat treatments is rarely discussed and given GSDCP theory, is expected to have a significant effect on H_C if the average grain size is larger than the domain wall thickness.

Thus, the existing gap in literature is percieved as, and the results chapters of this thesis are structured as:

- Investigate MnAlBi to determine whether there exists a beneficial effect from both LTP-MnBi and τ-phases existing simultaneously on extrinsic magnetic properties

- Determine a lower bound on thermal stability effects of Ga inclusion on MnAlGa series alloys. Refine composition and heat treatment to maximise metastable stability enhancement, intrinsic and extrinsic magnetic properties.

- Conduct thermomechanical testing of a targeted MnAlGa alloy, taking advantage of the increase in metastability to determine limits of hot deformation of τ-phase MnAlGa. Hot roll MnAlGa alloy to explore stress and texture relationship to M_R and H_C.

Chapter 4

Experimental Methodologies

4.1 Alloy Fabrication

When concerning alloy fabrication, certain considerations needed to be made when selecting available techniques. Literature research had shown that, whilst possible, powder production for MnAl systems was limited by an inability to sinter in the desired τ state to achieve high densification and domain alignment as it typical of permanent magnet production. Further, given the desire to undertake composition studies, alloy mass needed to be considered leading to a two-stream approach for production. An overview of the casting and testing process for all samples can be seen in Figure 4.1.

4.1.1 Arc Melting

For all initial trials and composition trials, Arc Melting was identified as the most appropriate technique for its high-throughput nature and appropriate production volume. The Arcast Arc 200 was selected as the system of choice as it is able to produce castings in the range of $\approx (100-200)$g of alloys in the MnAl system under a rarefied Ar atmosphere.

Experimental procedures were such that alloy reagents were pre-massed prior to loading and in the case of Ga-containing alloys, the Ga content was massed in the liquid phase and mixed with the Mn content to account for the vastly different melting temperatures of the ternary system's elemental components. The system is then sealed and evacuated to a maximum pressure of the order of $2700 mPa$ before being flooded to room pressure with Ar. The system is then brought to a pressure of $6.7 mPa$ by diffusion pump in order to purge any local atmosphere from the system before again flooding to $\approx 70\%$ room pressure with Ar to facilitate current flow from the electrode.

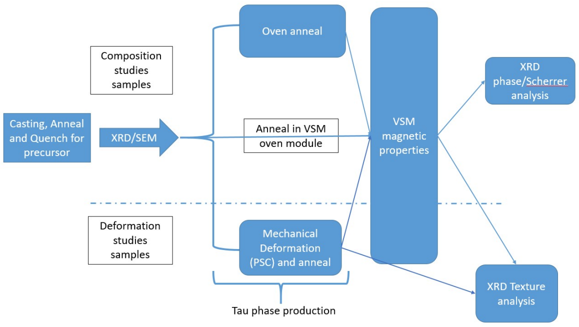

Fig. 4.1 A high-level overview of the manufacturing and testing process for all samples. Whilst additional testing was conducted not contained within this flowchart, this represents the basic characterisation used for both composition, heat treatment and mechanical deformation studies.

The melting procedure was such that a current of 240A was applied through a tungsten electrode to the melt pool contained within a water-cooled copper crucible. Each alloy underwent 5 melts, the first to ensure formation of a semi-stable alloy puck, flipped for the second melt to bring the system close to homogenisation and ensure all reagents were melted, noting that Mn chips were particularly prone to not melting within the bottom of the pool due to Al melting at a lower temperature than Mn and thus having an insulating effect in its liquid state. The subsequent three melts were to ensure complete alloying and were conducted following solidification of the melt pool and flipping to allow the melting process to assist in mixing. Magnetic stirring was also implemented during the later melts, again to assist in mixing, with the solidified matter from the spun pool cooling on the copper being remelted into the pool. All samples were then left to cool within the Ar atmosphere to limit oxide formation. No copper contamination was seen within EDX measurements of alloys, thus confirming that the copper crucible did not contaminate the melt pool.

Imperfections within the Arc Melting Process

It is of note that Arc Melting as described above had noticeable drawbacks to fabrication. Given that both Mn and Bi are volatile when melted under rarefied atmospheres, composition drift from that calculated from reagent masses to measurements taken from EDX meant that several techniques were developed to attempt some accuracy in fabrication. The first was to scale the melt size from 40g to over 100g, noting that the volatile behaviour came from the surface area and thus by increasing melt pool mass, lost material through evaporation would become a smaller fraction of the total mass.

The second technique was to add 1 $at.\%$ Mn to the reagent composition to account for losses. This technique was the most variable in its ability to counter composition drift as it relied on the ability to guess losses through melting. As such, it was more successful in ternary systems than when trying to create binary MnAl alloys due to a lower sensitivity to Mn concentration. As such, it was not refined as a technique and instead used as an assumption that any massed composition would drift towards Mn-lean states, limiting investigations to alloys with compositions in the range $Mn_x(Al, Bi, Ga)_{100-x}$ where $x \geq 55$ $at.\%$.

The third and most successful technique was incremental electrode current increase. By initiating the melting procedures at currents below 220A, it was noted that losses were lower by a lower level of debris forming on the arc melting viewport. As such, the final melting current of 240A was only applied after a melt pool puck had formed to prevent blow-out and evaporation.

It is of note that none of these techniques were particularly useful when considering the ternary system $MnAlBi$. During melts of this system, it was observed that evaporation was so severe that the chamber would quickly be coated with black powder from the Bi content such that forming a contact with the electrode to generate the necessary arc to continue melting became impossible. In such cases, the system was allowed to cool and the melt pool solidify before the chamber was opened to allow for mid-melt cleaning to occur. Pump-down procedures as described above were then performed again before subsequent melting and compositions only confirmed through EDS, with the assumption being that evaporation of Bi content and Mn content meant that it would be impossible to back-load reagents to predict melt compositions to targets.

4.1.2 Vacuum Induction Melting

In order to create geometries such that fabrication of Uniaxial Testing samples and Plane-Strain-Compression (PSC) samples could be cut from homogeneous ingots, Vacuum Induction Melting (VIM) was employed to create ingots of mass in the range of $(3-5)$kg. The composition was predetermined by creating pre-alloyed pucks via the Arc Melting methodology described in Section 4.1.1 prior to loading into a Consarc VIM device. VIM melting was performed by Dr. Yunus Azakli of the Henry Royce Institute, University of Sheffield by way of a $35kW$ medium frequency induction generator. Pieces of pre-cast MnAlGa were loaded into an Al68S one-shot liner (Capital Refractories) and the chamber was evacuated to a pressure of $0.1Pa$ prior to induction power activation on low to dry and heat the crucible in a slow, controlled manner. The melt chamber was then back-filled to $15000Pa$ with Ar to suppress Mn evaporation normal to liquid Mn in a rarefied environment. The charge was taken to liquid state and heated to a temperature of $1280°C$ to then undergo magnetic stirring for 5 minutes and casting into a mould constructed of a copper base and steel plates treated with BN, in a $(100 \times 80) mm^2$ footprint. Cooling was not forced but assumed to be rapid due to metal-metal contacts allowing good thermal conductivity and minimal solidification cavitation was observed.

4.2 Magnetic Data Capture

All magnetic measurements were conducted within a Quantum MPM3 SQUID using the Vibrating-Sample Magnetometer (VSM). Box annealed samples were measured by use of gelatin capsules held within plastic straws and samples annealed within the SQUID were held on a proprietary sample holder with Zircar cement to allow for temperature control between room temperature and $550°C$. All samples measured were centered on within the measurement system to within ±2mm of 66mm, the optimum measuring location within the system and hysteresis measurements were taken with an applied field of up to $5570 kAm^{-1}$.

Where more detailed comparisons between like samples were concerned, i.e. in the case of composition or heat treatment variation, demagnetisation effects were taken into account. This was conducted by assuming cuboidal sample geometry and the associated demagnetsation factor calculated using MAGPAR software [40]. The MAGPAR applet assumes uniform magnetisation across a sample of known cuboidal geometry and calculates the demagnetisation factor analytically assuming that the magnetisation applied is parallel to the defined c-axis of the inputted cuboidal geometry. Thus, using this tool has two approximations when calculating demagnetising factors for experimental samples, that cuboidal geometry is maintained i.e. there is a constant cross section throughout the sample and said cross section is rectangular and that the angle between the applied field and an c-axis of a sample is $\approx 0°$. Both of these criteria are exceptionally challenging to achieve for a high sample throughput on the lengthscale of milimeters and as such, demagnetising factors were only taken to 3 significant figures to reflect experimental uncertainties.

In the case of thermomagnetic measurements, no correction was made for thermal expansion in sample geometry as it was assumed that the expansion is isotropic and that sample mounting had minimal effect on inducing strain across sample length scales during thermal cycling. Further, it was also assumed that sample geometries were such that, along with MPMS sample centring protocols for measurements, that no additional effects for sample size needed to be corrected for during measurements.

For $M(t)$ measurements during the $\epsilon \rightarrow \tau$ transformation anneal within the MPMS3 SQUID VSM, an external magnetic field was applied as to best visualise the change in magnetisation as a function of transformation. However, an external field was not consistently applied during the temperature ramp up to annealing temperature and, as such, this data cannot be used quantitatively to assess the material as there is no consistent external field for the material to respond to and instead these data sets should only be viewed qualitatively for gradient changes and discontinuities to infer phase transformations.

Concerning paramagnetic backgrounds, samples were mounted using either plastic straws and gelatin capsules, for room temperature measurements, proprietary sample holders or 'heat-sticks', for measurements above $127°C$, or quartz rods for mechanically deformed samples. Whilst $M(H)$ data is available for all three sample mounts, corrections were not made as quantitative analyses were only conducted on ferromagnetic samples and thus it was assumed that the resulting magnetisation at field was dominated by the MnAl samples and not the sample holders.

4.3 Mechanical Testing

4.3.1 Dilatometry

In order to calculate thermal expansion coefficients for the ϵ precursor state, a Netzsch Dilatometer DIL 402 Expedis was utilized to investigate the temperature ranges where possible deformation could occur. With a heating ramp of $10Kmin^{-1}$, heating achieved through ambient Ar gas temperature and samples on the length scales of millimeters, it was assumed that any heating saw transitions through metastable to equilibrium states comparable to that of sample treatment for heat treatments, i.e. that any temperature dependent length changes were not time dependent when compared to that of temperature dependent under these conditions. First order discontinuities in thermal expansion represent events that break this assumption and are interpreted as phase changes within the material when accompanied by changes in the first order differential of the relative length against sample temperature. Due to Mn occupying Al sites in non-stoichiometric alloys and Ga theorised to occupy Al sites within the crystallographic structure, this process was both composition and heat treatment dependent and its primary function was to assist in calibrations and corrections of stress-strain measurements taken at temperature.

4.3.2 Mechanical Compression Testing

Equipment and Sample Preparation

A Servotest Thermo-Mechanical Compression (TMC) machine was used for all uniaxial compression and Plane-Strain Compression (PSC) testing whilst Samples for these tests were prepared by the Electric Discharge Machining (EDM) of ≈2kg ingots of target composition. The reason for fabricating from an ingot of this size is to ensure as homogeneous an initial microstructure as possible by maximising the volume of sample away from the micro-grains at the nucleation sites resultant from solidification. The grains within this region were assumed to be equiaxed though due to limited access to microscopy equipment, this was not tested. Further, due to the anneal and quench heat treatment to produce samples in the ϵ-phase precursor, it was assumed that any texture inherent within the sample from casting would become more diffuse as a result of this process.

The TMC machine is capable of conducting compression testing at strain rates starting from $0.1s^{-1}$ and at temperatures from RT to $1100°C$. Samples may either be pre-heated within the furnace as it rises to temperature or entered into the test area under heat.

As a point of deformation with regards to this thesis, commonly stress-strain relationships are considered in the tensile state as opposed to compression. As such, if one considers the definition that strain is defined by $\epsilon = \frac{l-l_0}{l_0}$, this would give a concept of negative strains for the compressive state, where $l \leq l_0$. For the purposes of this thesis, where tensile testing is not considered and thus to save on considering negative strains, strain is redefined as $\epsilon = |\frac{l-l_0}{l_0}|$ such that higher strains indicate greater compressive deformation and that strain is defined as a reduction in initial dimensional length.

Uniaxial Compression Testing

Uniaxial compression testing was first implemented on samples to test whether deformation processing was feasible due to the ease of machining samples. Test samples were machined to a diameter of 10mm and a height of 15mm with a 2mm tap hole in the centre of the longitudinal axis. The geometry of the testing can be seen in Figure 4.2 with the stress applied to the sample parallel to the $\hat{z}$ direction of the sample cylinder. Assuming plastic deformation occurs, two cases can be seen schematically in said figure, that of plastic deformation and barrelling or that of fracture.

In the case of barrelling, the sample has undergone plastic deformation by the activation of slip planes within the microstructure but total volume is conserved, meaning the sample deviates from the idealised cylindrical shape to see a radial increase maximising at an approximately equidistant point on the longitudinal axis. From the perspective of

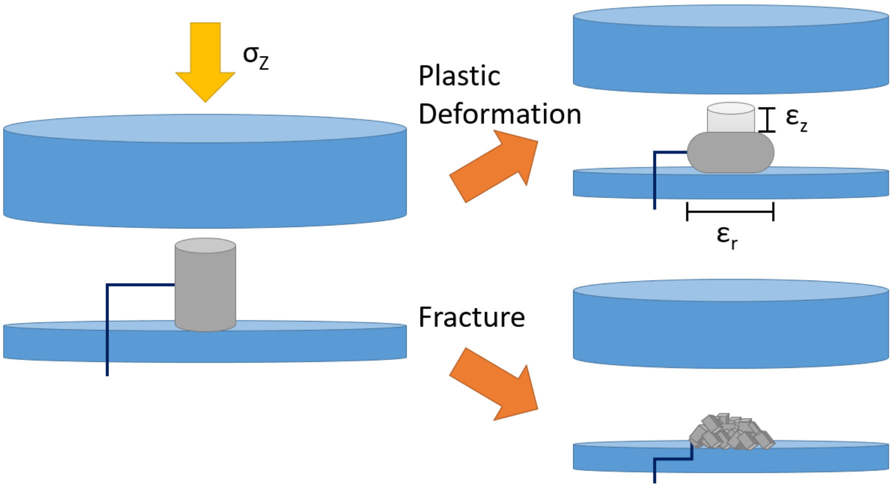

Fig. 4.2 A diagram of the two possible outcomes following uniaxial compression. In the top case, plastic deformation has occurred, the height has reduced and cylindrical radius increased such that material volume is constant, accounting for barrelling behaviour. In the bottom case, fracture has occurred, with the material undergoing mechanical failure and segmenting into multiple objects.

analysis, this then leads to a non-uniform strain on the system. This is explored further as an example in Wang *et. al.* (2017) [69], showing that the core of the samples discussed within were calculated to experience 100% more strain than the outer layers of a barrelled sample, but in terms of experiments discussed within this body of work, it means that one cannot expect to see a uniform texture resulting from deformation, instead predicting both a radial and longitudinal distribution in the resulting microstructural alignment.

In the case of fracture events, no additional mechanical data following the fracture event can be gathered due to the destruction of sample geometry and thus inherent and extreme uncertainty in any resulting stress placed onto the system. Given that the lowest strain rate achievable with the TMC machine is $0.1s^{-1}$, fracture events are assumed to be kinematic and driven by applied stress, with fragments falling from the structure prior to renewed contact with the tool surface and thus the fracture strain being representative for the structure as a whole rather than stacked fragments.

The purpose of this testing, however, is to assess whether a sample can undergo thermomechanical compression without fracture. Further analysis can also take place, such as determining elastic strain limits and plastic flow rates but they are dependent on samples undergoing plastic deformation and not fracture. Given that the ultimate goal of this study is to down-select state variables for Plane-Strain Compression, further analysis of the curves was not completed in lieu of texture analysis.

Plane-Strain Compression Testing

Plane-Strain Compression (PSC) tests can be used to simulate the deformation processes inherent with a hot or cold rolling processing. For the purposes of this body of work, PSC testing was used to simulate hot rolling in order to assess the effect of temperature and deformation plastic strain on microstructural texture.

Samples of dimensions (60x30x10)mm were cut from the VIM cast MnAlGa ingot for PSC testing with a 5mm deep, 2mm diameter thermocouple hole tapped off centre of the sample, with 5mm semi circular recessions milled out of the (10x30)mm cross section faces to facilitate robotic grips for sample manipulation, a wire drawing of which can be seen in Figure 4.3. These samples were treated with BN spray to prevent reaction between the tooling and samples then loaded into the TMC reconfigured into PSC mode with the furnace at testing temperature. A 2 minute dwell time was used to ensure thermal equilibrium between the tested sample and tooling before compression testing took place.

Under PSC testing, a tooling surface of 10mm width is used to compress the sample through the midpoint of the sample geometry, with the direction of compression parallel to that of the 10mm dimension. Across this deformed surface area of (10x30)mm, it is assumed that all stresses on the material surface are constant and that friction forces are ignored. Samples were deformed under a constant strain rate of $0.1s^{-1}$ at temperature before cooling by water jet. Following cooling, extraction was achieved by way of robotic arms with material suspended from tooling by the thermocouple to prevent reheating. Final strain was calculated by thickness reduction measurements taken at room temperature.

Deformation is defined by thickness reduction and not applied stress on the material, though an assumption was made that friction effects on the tooling-sample interface were negligible and thus stress was considered constant across the deformed volume as a function of deformation force. To account both for this friction effect and oxide build up from deformation processes taking place at temperature, during sample preparation surfaces were ground using standard metallurgy preparation techniques until both oxide and BN layers had been visibly removed and a polished surface was visible.

Thermocouple Placement and Effects

Analysis of both uniaxial and PSC testing were undertaken at temperature, with the goal of either understanding the compression deformation properties of the ϵ- or τ-phases of the MnAlGa system or to undertake a specific hot deformation process. As such, thermocouple holes were drilled into the samples, both in the deformation volume for uniaxial testing and off-set from the deformation region for PSC testing. In the case of PSC testing, this should not have had an effect on data validity and in the case of uniaxial testing, the perturbation is deemed such that the mechanical behaviour of the MnAlGa alloy being tested should dominate. Given that the thermocouple hole is placed radially midway through the cylinder and, on observation, there is no axial variation in deformation, it can be assumed that the effect on elastic and plastic deformation is negligible. A wire drawing of the PSC sample can be seen in Figure 4.3 .

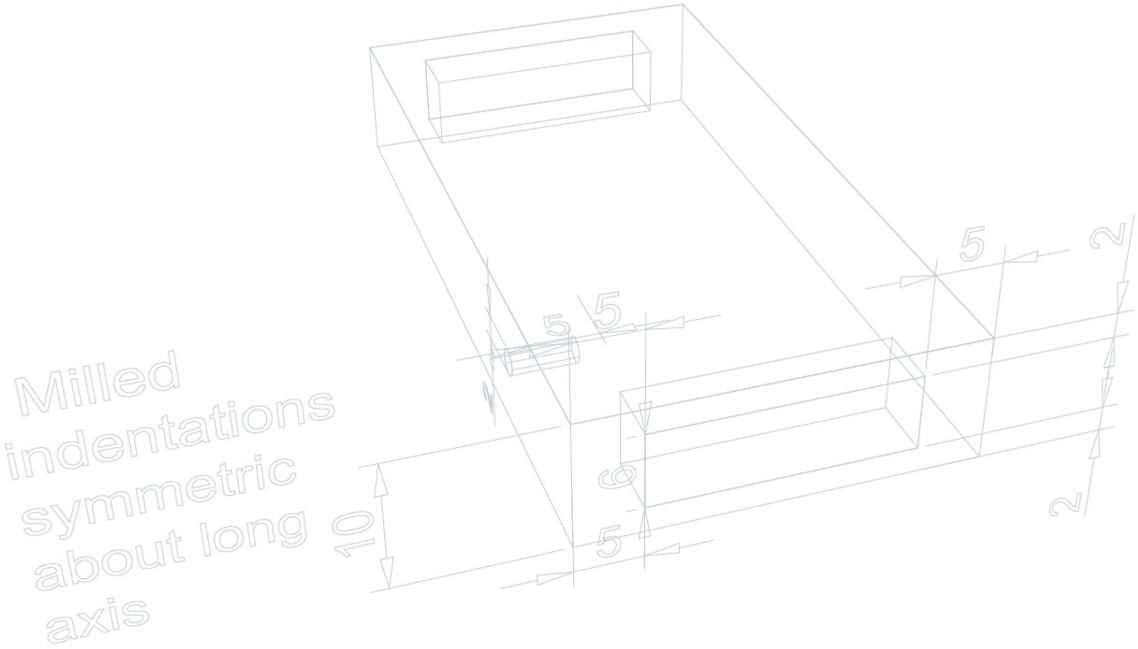

Fig. 4.3 A wire drawing schematic of the PSC sample, demonstrating that the thermocouple hole is offset and not in the expected deformation zone.

4.4 X-Ray Diffraction (XRD) Measurements

4.4.1 Bragg-Brentano XRD Theory

Bragg-Brentano X-Ray Diffraction (XRD) or reflection-mode XRD is a common technique when investigating the structure and phase composition of single crystal or powdered samples. As can be seen in Figure 4.4, the sample is placed in an equidistant mount between a focused x-ray source and detector such that both the source and detector can revolve around the sample by θ degrees respectively, meaning that the resultant reflective

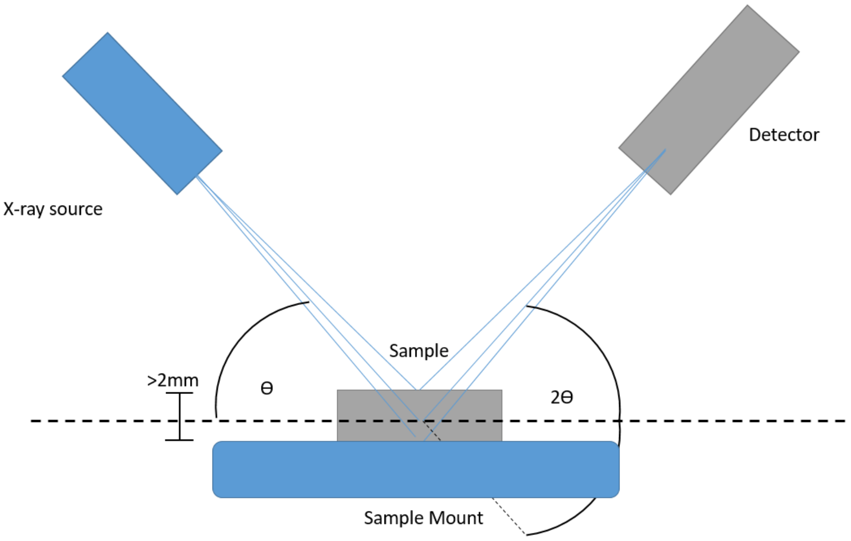

Fig. 4.4 A simplified 2D schematic of a 2θ-XRD measurement set-up, annotated with appropriate angles of measurement inherent to XRD.

angle 2θ can be explored. This is of particular use as it allows a full 180° of angle to be explored.

For a fixed incoming wavelength, lattice planes within a crystalline system can be detected through constructive interference as predicted by Bragg's Law,

$$2dsin\theta = \lambda \tag{4.1}$$

, where θ is the diffraction angle of which the approaching x-ray interacts with the lattice at, λ is the wavelength of the incident x-ray and d is the lattice spacing length. For a known crystallographic lattice, this then gives rise to a series of peaks detectable as the system sweeps through 2θ space corresponding to different lattice planes throughout the lattice. This generated diffraction pattern can then be analysed based off of deviation from this idealised series of peaks expressed by,

$$I(2\theta) = I\delta(2\theta_{hkl}) = I\delta(0.5 * sin^{-1}(\lambda/2d)) \tag{4.2}$$

, where $\delta 2\theta_{hkl}$ is a Dirac-delta function and h, k, l are lattice plane co-ordinates whose spacing result the plane spacing, d, by way of peak shift, spread and intensity deviations.

Grain/Crystallite Size Estimation - Scherrer Equation and Limitations

When considering polycrystalline materials such as metals, microstructural statistics are important parameters to estimate. One key parameter is that of grain size. Whilst this measurement can be performed in 2D by EBSD or SEM of samples, these are limited to both grain counting time, scanned surface area and, in the case of highly textured materials, limited to directions of view, meaning that an average grain size or morphology is limited to scanning parameters. Microscope techniques also require extensive polishing and, in some cases, etching, in order to highlight grain boundaries, destroying surface information in a sample.

Referencing Miranda and Sasaki (2018), one can find an expression for the Scherrer equation:

$$D = \frac{K\lambda}{\Delta_{2\theta} cos(\theta_B)} \tag{4.3}$$

where D is the mean crystallite size, equal to or less than the grain size in a polycrystalline sample, λ is the wavelength of the diffracting X-ray, K is a geometric factor relating the orientation of incoming x-rays to crystallites, taken to be 0.9, $\Delta_{2\theta}$ is the Full Width Half Maximum of an XRD peak and θ_B is the Bragg angle measured for said peak [70]. This equation means that, following a 2θ-XRD scan, it becomes possible to measure crystallite size by diffractive plane, giving rise to a measure of grain morphology and size, both key measurements in understanding microstructure and for micromagnetic understanding of permanent magnetic alloys.

There are limitations to using the Scherrer equation, however, to estimate grain and crystallite size. The first is that the two sizes are not necessarily equivalent. Grains may be monocrystalline, i.e made of a single crystallite structure or polycrystalline whereby a grain is still single crystal but composed of multiple crystallites. Fundamentally, a crystallite measured by the Scherrer equation is a coherent diffraction domain within the kinematic model of X-Ray diffraction. Thus, a crystallite is a lower limit on grain size meaning that the average grain size cannot be lower than the average crystallite size, recognising that any measurement made of either variable is an average modelled by an appropriate distribution, but that grains may be larger than crystallite sizes as a result. For the purposes of this thesis, the two will be assumed to be equivalent unless shown otherwise by BSE-SEM techniques, recognising that crystallite size calculations represent an average across a significantly larger volume than that measured by SEM imaging techniques and thus may be more representative of the material as a whole.

The second is that it is not a grain-specific measurement technique in the same fashion as optical or electron microscopy, measuring and then averaging individual grains by way of detecting grain boundaries and then averaging the sample population, but instead is a measurement of the effect of the average population on XRD peak spread. This means that it cannot account for grain size variation throughout a material and assumes that the grain size is isotropic. Real, as-cast materials are known to have various regions of grain growth depending on initial starting conditions, e.g. nucleation grains formed from surface cooling, columnar grains growing into the melt-pool from initial nucleation in freeze-zones and so on. This means that, in samples where the length-scales of these solidification regions are comparable to sampling geometry, one would be measuring the average of these regions. Given that for material development, one is aiming for consistent grain size and morphology in order to link emergent property changes to microstructure, this average is an idealised case but this technique provides no means of measuring the spread of this average.

Further, the Scherrer equation is only applicable in the case of small, sub-micrometer sized crystallites. Work published by He *et. al.* goes into further mathematical depth on the accuracy of determining crystallite size from this equation, citing limits set by Cullity *et. al.* at $200nm$ in crystallite size and Muniz *et. al.* at crystallite sizes of approximately $1\mu m$ but expressing that the fundamental limit of detection is determined by extinction depth and Bragg angle [71] [72] [73]. Broadly, it was shown that for materials independent of centrosymmetric crystal structures, the limit of applicability is approximately 11.9% of the extinction length of the material for the incident scattering wavelength but generally, the limit is expressed by the equation:

$$S_{Max} = S_0(sin(\theta_B/\mu_0)^{\xi} \tag{4.4}$$

where S_{Max} is the Scherrer limit, θ_B is the Bragg Angle and μ_0 the linear attenuation coefficient for the incident radiation with the fitting constants $S_0 = 1.067 \times 10^7$ and $\xi = 0.87$ [73].

To calculate this limit for MnAl samples, an approximation of the mass-energy absorption coefficient was used by averaging the photon energy attenuation coefficient by alloying element for a given wavelength and then multiplying by alloy density to give an approximation of $S_{Max}(\theta_B)$. Utilising mass-energy linear absorption coefficients from NIST and assuming an incident photon energy of $8 \times 10^{-3} MeV$, one can calculate the Scherrer limit for both $Mn_{55}Al_{45}$ and the later defined MAG-E composition, as shown in Figure 4.5. By the approximation that linear attenuation coefficients are only determined by the mass-energy absorption coefficients and no additional attenuation terms are resultant from other factors, this would set a low angle limit of Scherrer calculations as $\approx 3\mu m$ for a Cu x-ray source, with the limit maximising for peaks measured around $2\theta = 90°$. Broadly, given that nm-scale grains are an objective during casting and heat treatment of magnetic materials for permanent magnet materials in order to optimise

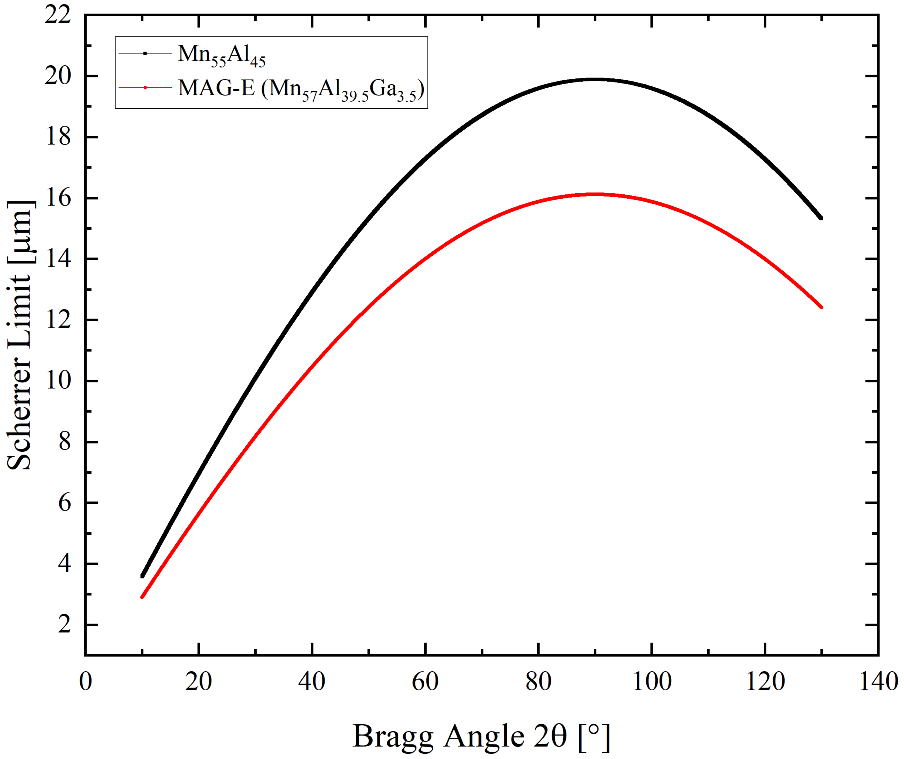

Fig. 4.5 A plot of the maximum sized crystallite observable by means of the Scherrer equation for MnAl group alloys of interest measured by $Cu - K_\alpha$ radiation. These limits were calculated by Equation 4.4 and assume that the linear attenuation coefficient of a material is a linear average of the mass-energy absorption coefficients with no additional arising terms from the unit cell formation.

extrinsic magnetic properties, this limit should be appropriate for measuring crystallites anticipated for the alloy systems under investigation within this thesis.

It is of note that use of the Scherrer equation is not standard practice when determining grain sizes of polycrystalline materials due to the limitations listed above, namely that it is not grain specific and thus cannot provide a distribution of grain sizes as well as having a maximum observable grain size as shown in Figure 4.5, even befor considering additional sources of error reducing this accuracy inherent with benchtop XRD equipment such as surface mounting, surface finish and crystallographic texture affecting the resulting XRD plot used to determine the grain size. However, this technique was utilised in this research as a consequence of the COVID-19 pandemic. In ideal conditions, grain size would have been calculated as a result of Electron Back-Scatter Diffraction (EBSD) measurements, a technique able to measure individual grains and their orientations, thus being able to build up a grain size, morphology and alignment model from samples. However, access to SEM equipment necessary to conduct this analysis was not available during the course of this research due to social distancing preventing training and then the reluctance for centralised facilities to test ferromagnetic samples due to the potential for contact between the sample and the microscope, potentially causing damage to the equipment. Thus, it is acknowledged that the grain sizes presented within this thesis are, at best, estimates and should only be compared on a process-by-process basis as a means of assessing microstructural changes in samples as opposed to an accurate calculation realistically representing a material.

Lattice Parameter calculations

One key aspect of Chapter 7 is the determination of lattice parameters as a function of composition and annealing time. These can be determined through $2\theta - XRD$ measurements by way of peak identification. Assuming a single phase material of known crystallographic space group, one can assign peak positions in 2θ-space to $[hkl]$ plane groups as determined by Equation 4.2. These angles then have a corresponding d-spacing, i.e the space between the diffraction planes. It becomes possible at this point to use geometric arguments to determine lattice spacing by recognising that $[hkl]$ planes intersect with lattice co-ordinates and so d-spacing calculations become geometric measurements. Given the two space groups measured in this body of work are Hexagonal Close-Packed (HCP) and Body-Centred Tetragonal (BCT), it is prudent to express the equations relating the lattice spacing constant to plane indices below

HCP:

$$\frac{1}{d^2} = \frac{4}{3}(\frac{h^2 + hk + k^2}{a^2}) + \frac{l^2}{c^2} \tag{4.5}$$

BCT:

$$\frac{1}{d^2} = \frac{h^2 + k^2}{a^2} + \frac{l^2}{c^2} \tag{4.6}$$

where a and c are lattice constants as defined by unit cell geometry.

When considering the accuracy of determining lattice constants, various factors must be taken into account. The first is the strain state of the material. Should the material have experienced any plastic deformation or contain any residual stress, it stands to reason that lattice parameters would shift as a result of this stress in an analogous form to Hooke's Law. As such, standards used for fitting should be taken from undeformed material as close to equilibrium. Conversely, should a standard be available, it means that it is, in theory, possible to estimate the deviation in lattice parameters for a given composition caused by these stresses, though it is acknowledged that these deviations may be of the order of pm and so at the limits of instrument precision to measure.

A second limit is that of instrument precision itself. When capturing XRD data, all measurements are quantified into discrete steps by detectors and thus a fundamental limit as to measurement precision is set. In the case of lattice parameter determination, this step size determines the diffraction plane spacing precision as a function of Bragg Angle by Equation 4.1. This precision is also wavelength-dependent and allows one to create an associated error function on lattice parameter measurement. If one uses the notion that error on a variable y calculated by a function $f(x)$ on a known measurement with an associated error $x + dx$ is $dy = f'(x)dx$, one can calculate the associated error function for lattice constant observation as

$$d_{error} = \frac{\lambda\theta_{error}}{2\sqrt{(1-\theta^2)}} \tag{4.7}$$

which implies lattice parameter error scales with the Bragg angle of the peak used to measure this. This is visualised for $Cu - K_\alpha$ radiation in Figure 4.6 for various step size choices, showing that the fundamental precision of measurements under $0.0001 nm$ of lattice parameters is in theory possible, assuming no other source of error, at $2\theta \rightarrow 0°$. In practice this is not the case but for measuring lattice parameter shifts as a function of residual stress, it shows that if peak position can be determined to single step accuracy, there is a direct proportionality to calculated lattice constant error.

Phase Population Calculations

One key use of this technique employed for the work in this thesis is that of phase composition determination through Rietfeld refinement. This was conducted using the Malvern Panalytical Highscore software package and GSAS-ii software package [74]. The key principle behind phase composition refinement is that for each plane within a system, there is a multiplicity of which it can be observed when at the correct angle, θ_{hkl}, where in an isotropic system where all planes have an equal probability of being illuminated by the incident X-Ray, the multiplicity of planes with identical d-spacing leads to a calculable intensity distribution, i.e in a cubic system system the [h 0 0] group of planes has a multiplicity factor of 6 and the [h k 0] group of planes has a multiplicity factor of 12 when symmetry arguments are considered. When two or more phases are present in an isotropic powder sample, one can thus use this multiplicity ratio and the relative intensity ratios for distinct phase-dependent peaks to calculate a ratio between the two phases.

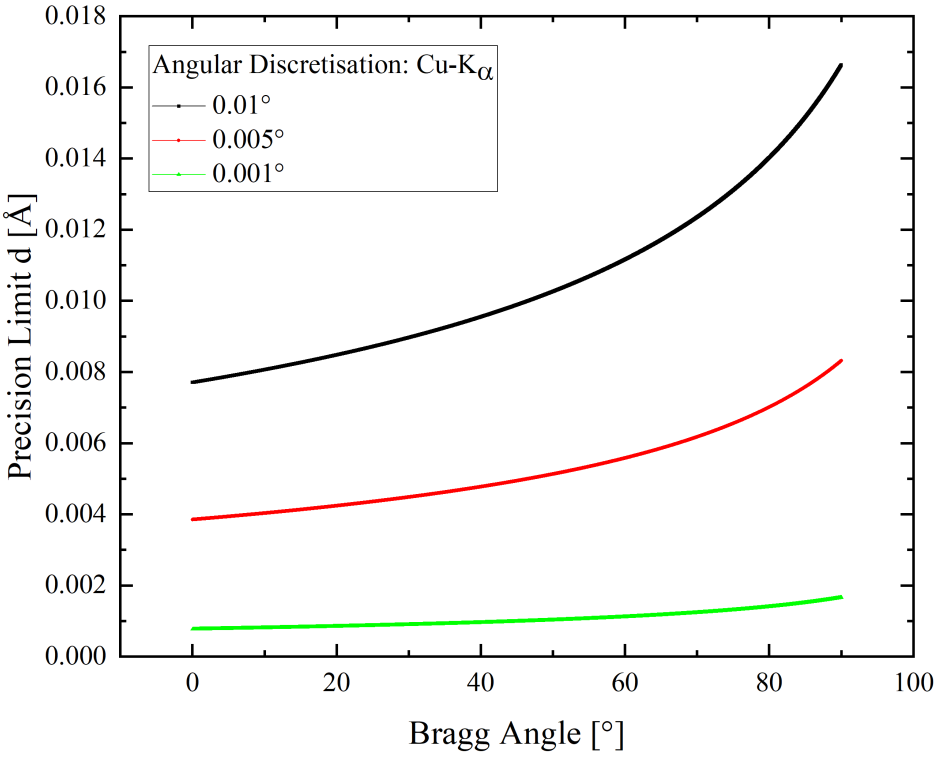

Fig. 4.6 A plot of lattice parameter observation limits as a function of 2θ sensor quantisation for a $Cu - K_\alpha$ x-ray source. This shows that pm shifts in lattice parameters are in theory measurable with benchtop systems providing appropriate measurement quanta are selected and associated scan times sufficient for acceptable signal-to-noise ratios.

In these studies, the data for phase population identification was collected on the Malvern Panalytical XPert system loaded with a Cu x-ray source. Normal procedure for XRD phase analysis would be to measure powdered samples. However, as shown in Section 3.2, milling of solid samples can have an effect on the magnetic properties and potentially the phase composition of the materials through strain-induced $\tau \rightarrow \gamma_2 + \beta Mn$ transformation. As such, all phase population XRD measurements were undertaken on solid, polished surfaces prepared by standard metallurgical methods. A key assumption in the comparison between both powder XRD and in-plane solid state XRD for phase analysis is that the solid samples were near-isotropic in their texture such that there was no orientation to the grain structure, meaning all planes had equal availability to incoming x-rays. As such, only samples produced by arc melting could be considered isotropic and only surfaces from the core of arc melted pucks was used for the scans in an effort to access texture free solidification regions.

Another limitation of the technique is that it is expected that to calculate phase populations, one already knows the lattice parameters of suspected phases within the material. Where this is not the case, known material states would be needed to calibrate lattice parameters for further scans. This would again rely on isotropic samples to ensure all peaks are accessible and in the correct multiplicity for lattice parameter determination.

4.4.2 Texture Measurements

In an effort to characterise the microstructural changes induced by deformation processing, either through Uniaxial compression or PSC, additional XRD techniques were conducted on deformed samples to calculate texture maps and derive residual stress within the material. The adaption to the previously defined technique in terms of geometry is defined in Figure 4.7 but can be summarised by the addition of rotation functions. If one designates that 2θ exists as an angle in the $x-y$ plane of the XRD measurement system, measurements of sample anisotropy require rotation and measurement in the $y-z$ plane, or ϕ vector, and in the $x-z$ plane, or the χ vector. To relate these angles to sample geometry, sample symmetry must be carefully aligned with these measurement planes, such as mounting a rolled sample such that the rolling direction is parallel with the $\hat{x}$ vector and such that the rolling plane lies in the $x-z$ plane. For samples with non-uniform applied stress or more complicated geometry, this becomes challenging and, as such, data gathered against these angles will result in increasing error when translating geometry systems to that of sample-relative co-ordinates.

Texture Measurement Technique

To determine whether crystallographic texture, i.e an anisotropic distribution to orientation of crystallographic planes implying preferential lattice orientation within a material, was present within deformed sample, an adapted Bragg-Brentano geometry was utilised. Utilising known peaks for the composition and phase population determined from known, near-isotropic samples, peaks associated with distinct lattice planes were selected and the source-detector geometry set to the associated 2θ value. The sample is then illuminated by x-rays and set to revolve in both χ and ϕ angles in order to measure if there is angular dependence to the intensity of said peak, creating what is referred to as a Pole Map. In isotropic samples, one would expect a constant signal across $\chi$and ϕ space but in the case of texture, there would be areas of increased intensity corresponding to an increase

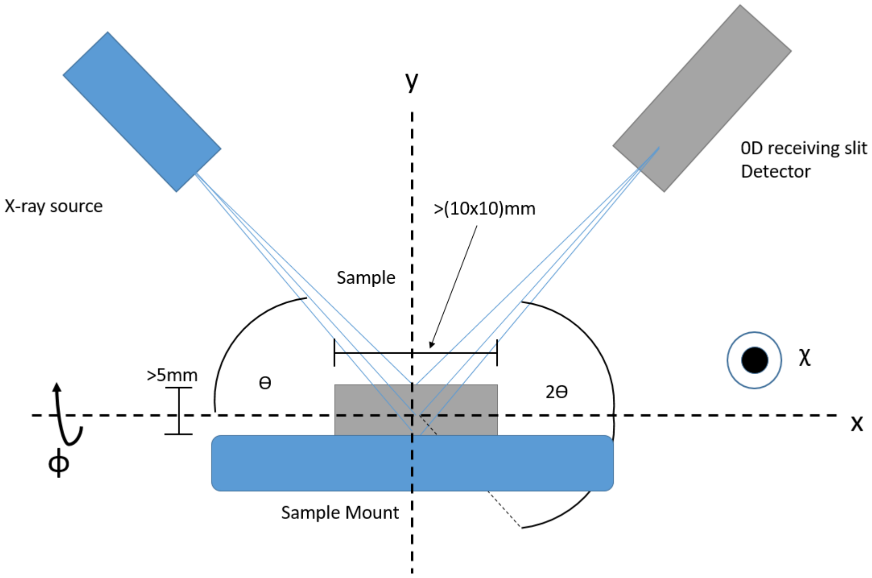

Fig. 4.7 A diagram explaining the geometry of Texture/Residual strain XRD measurements. If one defines a right-handed Cartesian co-ordinate system with the angle θ defined as $\hat{\theta} = \hat{x} \times \hat{y}$, additional rotation angles defined by $\hat{\phi} = \hat{y} \times \hat{z}$ and $\hat{\chi} = \hat{x} \times \hat{z}$ can also be defined to investigate diffraction anisotropy within a sample. This can then be interpreted based on changes in intensity for texture or peak shape and position for residual strain and resolved to a sample-specific co-ordinate system.

in linear plane density in the beam path, implying that the crystallite structure has a preferential orientation. By combining several of these Pole Maps, one can derive an Orientation Distribution Function (ODF) giving a direction dependent cross-section of a material's texture and thus a measure of the anisotropy of said material.

By the alignment of the initial pole figures to sample symmetry planes, the resulting ODF will be similarly oriented to the material. As such, it is possible to then simulate pole figures based on crystalline planes specific the material phase measured and oriented to sample symmetry. From a magnetic property perspective, this can then be used to give a generalised grain alignment of magnetic easy and hard axis and thus either fed into micromagnetic simulations or used to assess or predict changes in extrinsic magnetic variables.

Texture Measurement Quantification

With reference to Kocks, Tomé and Wenk, texture can be assessed by many methods but two were selected for this study: the texture coefficient, t, and fibre occupancy volumes [75]. The first can be defined as

$$t = |ODF|^2 \tag{4.8}$$

or the square of a normalised ODF. It is interpreted as a multiple of resulting preferential orientations against the background measurement of an isotropic model, though it is not without criticism as it expresses nothing about the texture itself, being simply a measure of 'strength', with $t = 1$ interpreted as an ideal isotropic material and $t > 1$ as a material with a preferential orientation. The second variable is such that if one defines an external direction to the sample upon measurement, in the case of this work relative to a deformation stress vector, one can calculate the relative volume of hypothetical grains that would have a plane in question orientated within a misorientation angle respective to said external direction. The higher the volume for two fibres orientated in the same direction of different planes with the same misorientation angle, the greater the degree of preferential orientation for said crystallographic plane.

4.4.3 Texture Measurement Equipment - XRD

With regards to texture measurement of bulk samples within this body of work, a Panalytical Emperyan X-Ray Diffractometer was utilised. The data was generated using an Ag source ($\lambda_{k\alpha 1} = 0.5594075nm$) rather than a Cu or Mo source as the higher energy of an Ag x-ray means a greater penetrative depth, reducing the effects of surface texture when measuring at the trade-off of decreased peak area in 2θ space. A $'0D'$ detector was utilised in combination with an FDS with FASS (Fixed Divergence Slit with Fixed Anti-Scatter Slit) pre-irradiation mount attached to the x-ray source in order to approach a linear x-ray source. Whilst experiments with parallel plate collimators were performed in order to increase the angular resolution of the 0D receiving slit, it was found that the Ag x-rays penetrated and attenuated the collimator, resulting in an increase in noise along with a decrease in signal. As such, a fixed slit anti-scatter slit and soller slit were used to reduce angular divergence to approximately 1°, defining a resolution limit to measurements before convolution dominates data. For bulk measurements and modelling, this was deemed as sufficient to generate calculated ODFs and to allow texture analysis calculations to be performed using the MTEX software package [76].

4.5 Microscopy

Whilst experimental necessities stemming from the Covid-19 lockdown meant that access to Scanning Electron Microscopy (SEM) or Tunnelling Electron Microscopy (TEM) techniques was either limited or non-existent respectively, SEM techniques were used to confirm alloy compositions and estimations of crystallite/grain sizes. The Scanning Electron Microscope used was the FEI Inspect F50, general purpose Field Emission Gun-SEM equipped with Secondary Electron and Back-scatter Election image detectors, Energy Dispersive Spectroscopy and Electron Back-Scatter Diffraction capabilities using a $10keV$ accelerating voltage. The EBSD imaging, however, was not available for use during the work laid out in this thesis due to concerns about ferromagnetic attraction between samples and the microscope causing permanent damage to the equipment, either from the sample as a whole or fragments pulled from fissures in the material. As such, alternative techniques, such as those discussed in Section 4.4.2, were utilised to measure grain size and orientation to understand the microstructure and texture of cast/deformed alloys.

4.5.1 Energy Dispersive Spectroscopy (EDS)

In order to understand the composition of as-cast alloys, EDS was utilised to measure characteristic emissions from alloy surfaces during SEM imaging. The principle behind EDS imaging is that when bombarded by electrons during microscope imaging, electrons in the target material are promoted to higher energy levels within their shell structure. As these electrons decay to ground states, photons are emitted of the energy difference between the two states, characteristic of the element from which the emission occurred. If these photons are measured as a function of 2D mapping locations during scans of a surface, a composition map is able to be constructed.

There are, however, limitations of this technique. If there is overlap between characteristic emissions between two elements within a sample, distinguishing between the two is non-trivial. Further, this is a mass-dependent technique, meaning that lighter elements are, at best, difficult to measure and the detection of their presence within an alloy qualitative rather than quantitative. It is a generally accepted rule that EDS can only quantitatively detect Na and heavier elements within a sample. To overcome this, the Oxford Instruments AZtec software package utilised for EDS mapping was pre-programmed with known or suspected elements within a sample to prevent peak overlap concerns and elements lighter than Na often excluded from quantitative analysis. It is possible to scan points, set 2D areas or 1D vectors to examine composition changes. Scan times were set to several minutes to ensure sufficient data density for both 0D and 2D scans and in the case of 2D scans, element-specific maps were cross referenced to ensure broadly isotropic data density was achieved across the measured surface.

A particular use of this technique is in the detection and identification of minority phases, used specifically in this thesis in Chapter 5 when discussing the detection of

LTP-MnBi during investigations into the MnAlBi ternary system. Rietfeld refinement and calculations of phase populations by XRD has a practical limit of (5 – 10)% phase population for benchtop equipment due to signal to noise ratio limits of diffraction from minority phases. EDS mapping, however, can be used to provide a 2 dimensional sample of a material with concentrations of minority phases estimated from area occupation. Further, it can be used in cases of binary or greater phase alloys for grain size estimation, under the assumption that minority phases within an alloy may only be a single grain in size, though this can also be confirmed with other techniques. Within this body of work, however, EDS is primarily used as a means of composition confirmation and secondary phase identification

4.5.2 Back-Scatter Electron (BSE) Imaging

When measuring signals from SEM measurements, two electron signals can be detected: Secondary Electrons where electrons are generated from the surface of a material by the energy transferred from the incident electron beam during scanning and Back-Scatter Electrons (BSE), where electrons from the incident beam scatter from the sample on impact with the surface. BSE scanning was utilized in this body of work as a means of measuring grain sizes without etching, due to the lack of a clear etchant route for MnAl group alloys. During a BSE measurement, channelling contrast comes from favourable conduction down crystalline planes and, as such, will vary across grains observed on a 2D plane, with a greater contrast variation as the angle of misorientation between two grains increases [77]. Utilising this contrast, it thus becomes possible to resolve grains on a BSE image, though this is only achievable for either high angle grain boundaries or in regions of similar levels of misorientation. However, the ImageJ software package was used with this in mind to take line-scans of BSE images and map changes in the resulting signal intensity, interpreted to be a grain boundary, as a function of scan length. Repeating this for at least 10 random vectors across an image allows for the calculation of an average standard grain diameter and standard error for a material, providing a means of verification in this work for the same average diameter as measured by the Scherrer equation

4.6 Sampling and homogeneity

Throughout the composition, heat treatment and mechanical deformation testing sections of this thesis, a consistent assumption is that of compositional and microstructural homogeneity until proved otherwise. Whilst the former was investigated in the case of MnAlBi samples in order to determine the cause of sample variation, it was assumed to be consistent throughout other samples. In order to best achieve this, all samples from Arc Melted material were taken from the core of the material, with the outer material, approximately $5mm$ deemed as sacrificial due to either potential contamination from the casting surface or non-isotropic microstructures influenced by heterogeneous solidification from the copper crucible walls. Further, the PSC samples were taken from the centre of the deformed material with the outer surface, approximately $(1-2)mm$ ground off the sample in order to account for oxides and reactions with the BN lubricant. Efforts were also made to ensure that samples were of similar mass and dimensional scales, with a goal of cuboidal structures of the order of millimetres and masses in the range of $(10-40)mg$ in order for magnetic measurements within the SQUID to be comparable without needing additional corrections for sample geometry or mass-induced effects

Effort was made in ensuring similar sampling positions relative to cast pucks or deformed material but variations are inevitable within the material and both compositional and microstructural homogeneity are assumptions within the analysis. In an idealised case, EBSD would have been conducted on as-cast puck centres in order to qualify this assumption but between SEM images used to calculate compositions of gallium doped MnAl and texture measurements of undeformed samples shown in Figure 7.14, efforts were made to justify these assumptions.

4.7 Error Calculations

Throughout the results chapters, errors are presented on measured data points and calculated constants and material properties where possible. Magnetic data captured on the MPMS3 SQUID VSM also has associated errors calculated and provided by a min/max measurement when capturing the magnetic induction from the sample. From this and with reference to *"Measurements and their Uncertainties"* by Hase and Hughes, errors propagation equations were calculated using differential error analysis when calculating equations and both means and errors calculated using the weighted mean [78]. Where fits were calculated from data sets, the Origin software package was utilised in order to fit modelled equations to the data set and provide errors on calculated variables, with residuals available for discussion where appropriate.

Chapter 5

MnAl Ternary Systems

5.1 Motivation and Experimental Goals

The goals of the initial experiments presented within this chapter were threefold:

1. The demonstration that tau-MnAl could be manufactured at Sheffield using on-site facilities.
2. To determine whether Bi can alloy with MnAl to form a stable $\tau - MnAl$ derivative phase and measure the effect of Bi concentration on both intrinsic and extrinsic magnetic properties.
3. To assess whether MnAlGa could be manufactured using Quench and Anneal production techniques already in place for MnAlC and measure the property deviation against literature to benchmark future studies.

The relevance of this chapter was to demonstrate that manufacturing techniques available could produce viable samples under experimental timeframes as well as begin limited feasibility studies into two targeted ternary systems in order to begin approaching the material capability gaps established in Section 3.5.

5.2 MnAlC Initial Runs

Two samples were cast of MnAlC in compositions of $Mn_{56.1}Al_{42.2}C_{1.7}$ and $Mn_{55.9}Al_{41.9}C_{2.3}$ using the Arc Melting techniques listed in the Methodology chapter and were transformed to the τ phase using an initial anneal at $1050°C$ for 8 hours, followed by a water quench, then a secondary anneal at $450°C$ for 40 minutes to activate the $\epsilon \rightarrow \tau$ transformation. The

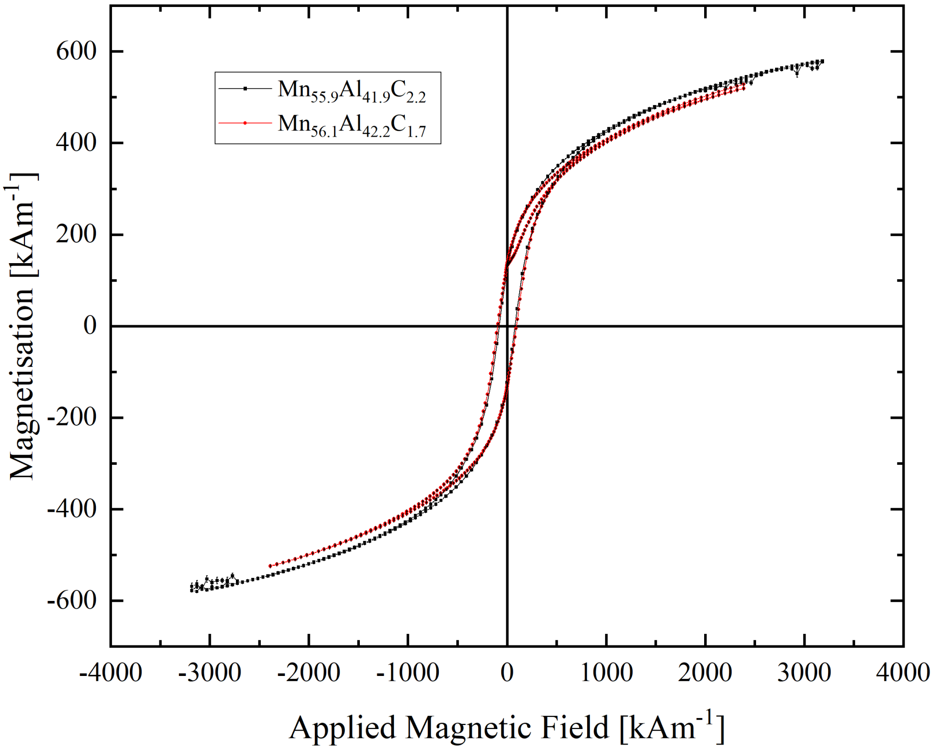

Fig. 5.1 The full 3T sweep of the initial MnAlC test alloys used to proof manufacturing techniques at the University of Sheffield for further research. Whilst saturation is clearly not observable with these alloys, the Law of Approach to Saturation as detailed in the Section 2.3.2 can be used to estimate intrinsic magnetic properties.

resulting magnetic hysteresis loops for these two test compositions can be seen in Figure 5.1 for the full field sweep and Figure 5.2 for the extrinsic magnetic properties of the alloys.

The resulting hysteresis loops for both compositions show that a ferromagnetic state has been achieved, with intrinsic and extrinsic magnetic properties reported in the Table 5.1. Whilst the compositions listed are determined through reagent mass and do not account for composition drift due to the arc melting process, the measured values for M_S, M_R and H_C are within orders of magnitude of reported values, with extrinsic properties compared to data shown in Figure 3.3 and M_S compared to data shown in Figure 3.7. Given that the production process is not directly comparable to any work discussed in the literature review, with extrinsic properties being determined not only by composition but also processing and microstructure, and intrinsic properties being set by composition, which is subject to drift through the Arc Melting production process due to Mn volatility

Composition	M_S $[kAm^{-1}]$	k $[kJm^{-3}]$	M_R $[kAm^{-1}]$	H_C $[kAm^{-1}]$
$Mn_{56.1}Al_{42.2}C_{1.7}$	579.4 ± 0.3	1058 ± 5	132.56 ± 0.03	94 ± 1
$Mn_{55.9}Al_{41.9}C_{2.2}$	631 ± 2	1390 ± 50	112.9 ± 0.1	81.5 ± 0.5

Table 5.1 A table of intrinsic (M_S and k) and extrinsic (M_R and H_C) magnetic variables for MnAlC alloys produced using high temperature quench and anneal processing to achieve an $\epsilon \rightarrow \tau$ transformation for an alloy of target composition $Mn_{56}Al_{42}C_2$. Intrinsic properties are calculated using the Law of Approach to Saturation (see Equation 2.12) and extrinsic by axis intercept.

when melted under a rarefied atmosphere. Comparing the three variables to those of literature and seeing a ferromagnetic hysteresis $M(H)$ curve, however, means that this data demonstrates that τ-MnAl can be manufactured using processes designed in this work.

When considering the calculated values of k, the variation between the two alloys raises some concern about using the Law of Approach to Saturation as a technique to calculate said variable. Given the variation also in M_S, examining $M(t)$ during the $450°C$ anneal seemed prudent to investigate whether the alloys had undergone full transformation or whether they were still in a mixed state at the end of the annealing process. This can be seen in Figure 5.3 which shows that both samples were approaching a steady state value for magnetisation as a function of time, thus it can be inferred that complete $\epsilon \rightarrow \tau$ transformation had occurred within the sample.

Whether this transformation is optimised or not can be assessed by the examination of the behaviour of $M(T)$ during the initial rise to heat treatment within the MPMS3. The thermal response of $Mn_{55.9}Al_{41.9}C_{2.2}$ can be seen in Figure 5.4 as the material is subjected to a $12°Cs^{-1}$ heating ramp from the as-quenched ϵ-phase. The first-order derivative of magnetisation against temperature is also plotted and sign changes can be attributed to a change in magnetic ordering. It can be interpreted that, as the ϵ-phase is paramagnetic, magnetisation should obey Equation 3.2 and decrease with increasing temperature, thus a positive increase in the first order derivative implies that an additional mechanism has been activated to overcome this decrease, namely the precipitation of the τ-MnAl phase. This can be observed to initially take place at $T \approx 100°C$ and this transformation-induced magnetisation increase becomes dominant at $T = (175 \pm 5)°C$, increasing until a steady state decrease in magnetisation is observed at $T \approx 350°C$.

It is of note that this temperature is above the reported value of T_C for MnAlC in the τ-phase. Thus, any decreases in $M(T)$ as temperature increases are again attributed to the time dependent phase population being a combination of paramagnetic states such that the increase of τ-phase does not off-set the magnetisation decrease with temperature

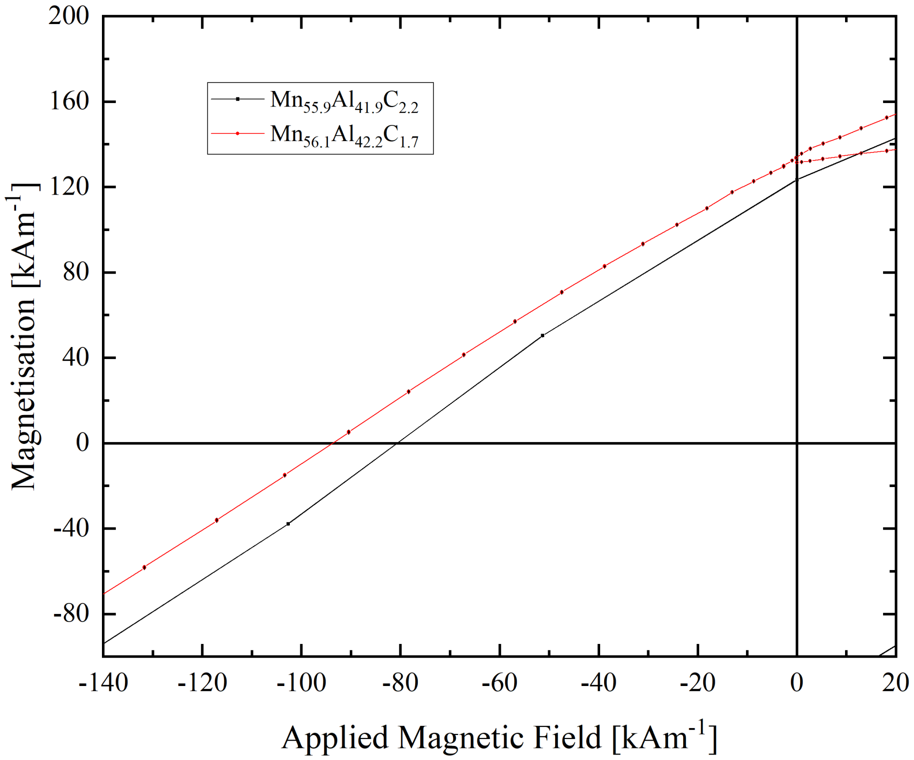

Fig. 5.2 The extrinsic magnetic properties of the initial MnAlC test alloys following a 3T hysteresis sweep as detailed in Section 5.2. Given that these samples have not undergone any alignment or texturing process, the extrinsic properties cannot be considered optimised but can provide a benchmark for comparing assumed-isotropic, as-cast τ-group alloys.

normally observed for paramagnetic materials. As such, it can be judged that the $\epsilon \rightarrow \tau$ transformation is initiated as low as $100°C$, implying high temperature annealing may not be required, nor optimum, for MnAlC systems.

Comparing the recorded values of $Mn_{55.9}Al_{41.9}C_{2.2}$ against published data provided by Pasko *et. al* as discussed in the literature review, we can see that the $450°C$ anneal for 40 minutes produces a value of M_S in excess of that recorded for a 100% τ phase of $M_{S,Pasko} = 438kAm^{-1}$ [57]. $Mn_{56.1}Al_{42.2}C_{1.7}$ as reported in Table 5.1 fails, however, to meet the reported value of M_S for drop synthesized $(Mn_{55}Al_{45})C_2$ as reported by Fang *et. al* of $M_{S,Fang} = 614kAm^{-1}$ [56]. Neither dataset contains data determining the k values of the discussed material and it is of note that, as an as-cast sample free from any deformation

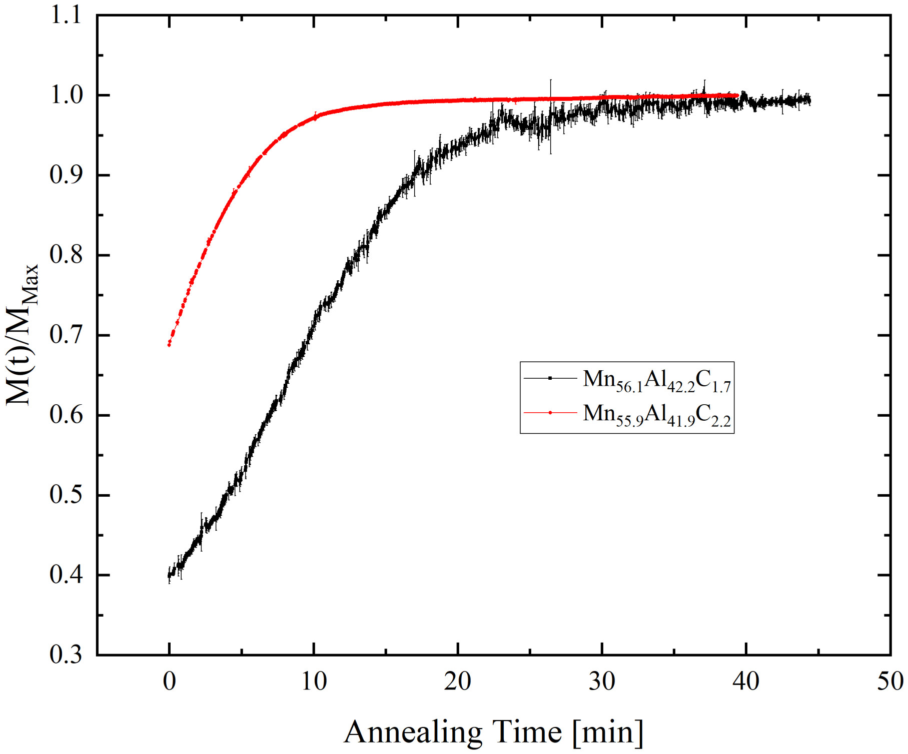

Fig. 5.3 A plot of normalised magnetisation against time for samples of MnAlC annealed at 450°C for 40 minutes under a $1600 kAm^{-1}$ applied magnetic field. Note that due to increased error on the measurements conducted on the $Mn_{56.1}Al_{42.2}C_{1.7}$ sample, an adjacent averaging smoothing algorithm was applied with a bucket size of 1 second in order to compare against that of $Mn_{55.9}Al_{41.9}C_{2.2}$ more effectively.

processing, it is not appropriate to compare values of M_R and H_C given their inherent association with sample microstructure as well as intrinsic magnetic variables.

Looking to the fabrication methodology, several explanations can be posited. The first is that, by producing samples by drop synthesis as compared to arc melting, there is a greater degree of accuracy when targeting a composition, due to having a larger melt pool established and an indirect heating supply, meaning both greater temperature control to prevent Mn vapourisation and lower thermal shock to prevent ejection from the crucible during initial material melting. Further, XRD analysis of the drop synthesized material discussed shows a 100% τ-phase population, whereas this cannot be guaranteed for either of the measured samples here given the use of benchtop XRD equipment, with phase populations below 5% being challenging to capture, especially in the case of ϵ- and

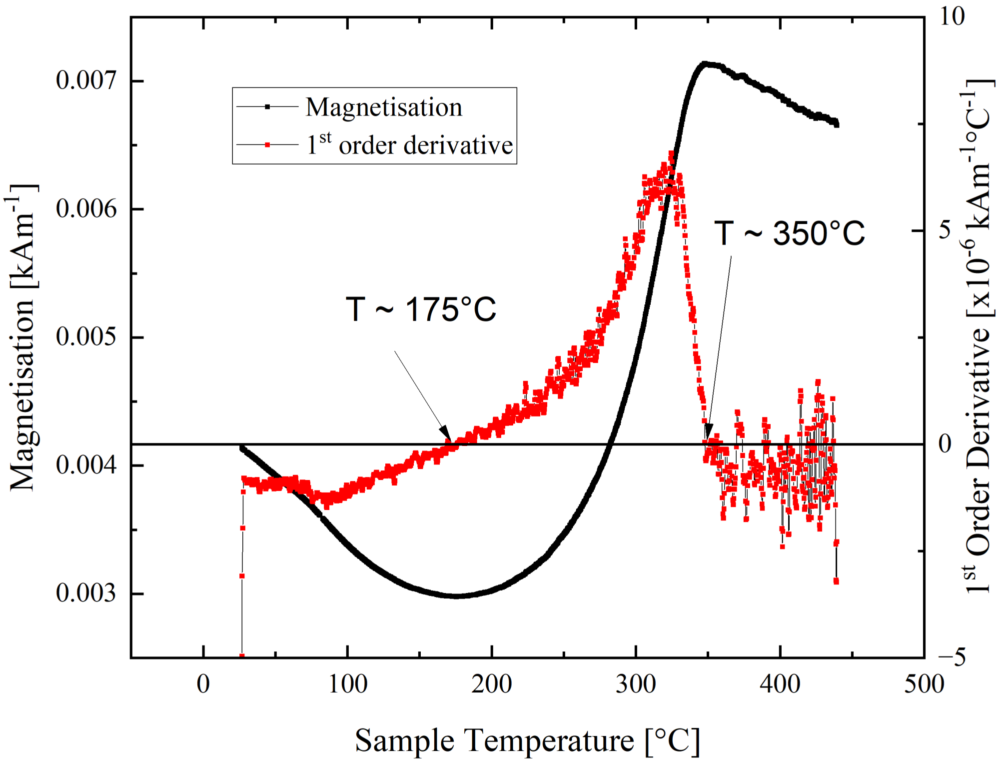

Fig. 5.4 The Magnetisation response of $Mn_{55.9}Al_{41.9}C_{2.2}$ during a temperature sweep from $(30 \rightarrow 450)°C$ from an initial ϵ-phase state at a rate of $12°Cs^{-1}$. The first order differential of $M(T)$ is also plotted to estimate phase precipitation and T_C of emerging ferromagnetic phases.

τ-phases, with peak convolution occurring at low angle principle peaks due to similar lattice parameters and potential texturing effects occurring from in-plane measurements as opposed to powder XRD. As such, Rietfeld refinement was only conducted on composition $Mn_{56.1}Al_{42.2}C_{1.7}$ post transformation in an effort to explore sub-optimal intrinsic magnetic properties when compared to that published by Pareti *et al.*

A final point of comparison is that of deviation from a stochiometric balance. With work published by Pareti *et al.* detailing the M_S variation in τ-phase alloys of Mn_xAl_{100-x} where $(44.2 \leq x[at.\%] \leq 48.9)$ is discussed, showing that the variation between Mn-lean and Mn-rich compositions (a span of around 5 at%) is a difference between approximately $110Am^2kg^{-1}$ and $80Am^2kg^{-1}$ respectively [47]. The actual composition in the work published by Fang *et al.* would be $Mn_{53.9}Al_{44.1}C_2$ and thus closer to an equiatomic ratio than the composition measured in this study of $Mn_{56.1}Al_{42.2}C_{1.7}$. Indeed, if one assumes the variation in C between the two alloys to be negligible when comparing resultant values of M_S, the work by Pareti *et al.* would predict that the drop synthesized alloy would have a saturation magnetisation 17.98% higher. Given that the actual difference between the M_S values is 5.97%, it could be interpreted that even though the C dampens this off-equiatomic effect it is the source of the discrepancy between the two systems.

Looking to the discrepancy in estimated values of k calculated for both compositions, it is a reasonable conclusion that the annealing has not achieved a 100% τ-phase population. k is calculated using the Law of Approach to Saturation, detailed in Section 2.3.2, and thus is determined by the gradient of a high-field plot of $M(H^{-2})$. To determine k for a single phase, two key assumptions must be met: the material must be a single ferromagnetic phase with the inclusion of paramagnetic phases changing the relationship to include an additional term $\chi_{para}H$ to account for the paramagnetic contribution, and it must be measured beyond its anisotropy field to ensure that all domains have been switched and are undergoing alignment to the external field. In Figure 5.5, the Rietfeld refinement fit for $Mn_{56.1}Al_{42.2}C_{1.7}$ can be seen, showing that an incomplete $\epsilon \rightarrow \tau$ transformation has occurred. Whilst the Highscore software utilised predicts a roughly equal phase balance between paramagnetic precursor and ferromagnetic target phase, it is of note that there are several high angle peaks missing for both phases and significant convolution in observed peaks, indicated by the black arrows on the figure. As such, quantitative analysis of the composition is challenging and should be taken more as an indication that incomplete transformation has occurred.

If one takes the measured anisotropy field, H_A, for a binary MnAl alloy of Mn 72 wt.% as expressed in Pareti, Bolzoni, Leccabue and Ermakov as $H_{A,72wt.\%} \approx 65kOe = 5170kAm^{-1}$ (3sf) and compares it to the associated anisotropy field calculated for $Mn_{56.1}Al_{42.2}C_{1.7}$

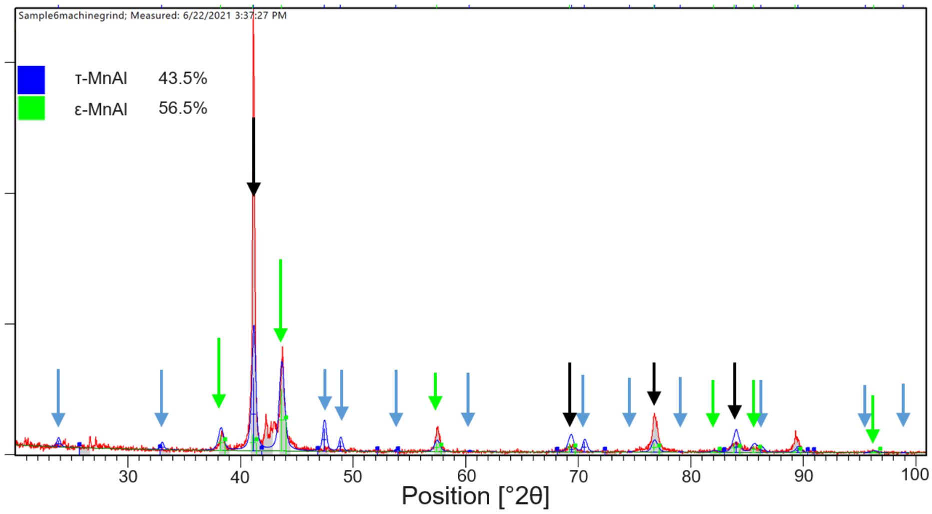

Fig. 5.5 An XRD-2θ scan of composition $Mn_{56.1}Al_{42.2}C_{1.7}$ following a 40 minute anneal at $450°C$ to induce the $\epsilon \to \tau$ phase transition. Blue arrows indicate characteristic lines associated with the BCT τ-phase, green with the HCP ϵ-phase and black indicated lines convoluted between the two phases. Attached is also the calculated phase population by Rietfeld fitting through the Panalytical Highscore+ software package.

using the equation $H_A = 2 \times \frac{k}{\mu_0 M_S}$, we find that $H_{A,(56.1,42.2,1.7)} = (2910 \pm 10)kAm^{-1}$. The calculated anisotropy field for the measured sample is greater than the maximum applied field and, as such, the Law of Approach to Saturation is not truly applicable in this case, as the domains cannot be described as fully switched throughout the system, meaning any extrapolation to $H \to \infty$ would not represent the sum of all domains in a coherent polarisation within the system. Given that the system is in agreement with other published data regarding its associated M_S, it shows that it is only the measurement of k that is not a true comparison of the system.

As a final check as to whether $Mn_{56.1}Al_{42.2}C_{1.7}$ is truly a representative of the system when annealed under these conditions, a comparison of the Curie temperature of the alloy is necessary. Using Pareti, Bolzoni, Leccabue and Ermakov as a reference for the behaviour of T_C against manganese and carbon concentrations within the alloy, it can be seen that manganese concentration increases lead to an increase in T_C within the ranges of approximately $(330-360)°C$ for the binary alloy range defined by $(68 \leq Mn\ wt.\% \leq 72)$ and this is broadly constant for carbon increases over $0.4wt.\%$ when investigated in the composition range $Mn_{70.5}Al_{29.5}C_x$ $[wt.\%]$. To determine the Curie temperature, the Curie-Weiss Law was utilised to form the linear equation

$$\frac{1}{M} = \frac{1}{CH}(T - T_C) \tag{5.1}$$

where C is the Curie constant for the material. Using this fitting equation, one can calculate that $T_C = (270 \pm 10)°C$ for the measured composition. This is in agreement with the carbon-doped material discussed by Pareti *et al.* in the range of $T_{C,Pareti} = (260-280)°C$, thus adding further evidence that this composition and annealing treatment can be used as a standard internally for the fabrication results of τ-MnAl group alloys, despite having lesser intrinsic magnetic properties than those of $Mn_{55.9}Al_{41.9}C_{2.2}$ annealed under the same conditions, which has a value of $T_C = (256 \pm 4)°C$ when measured by the same technique.

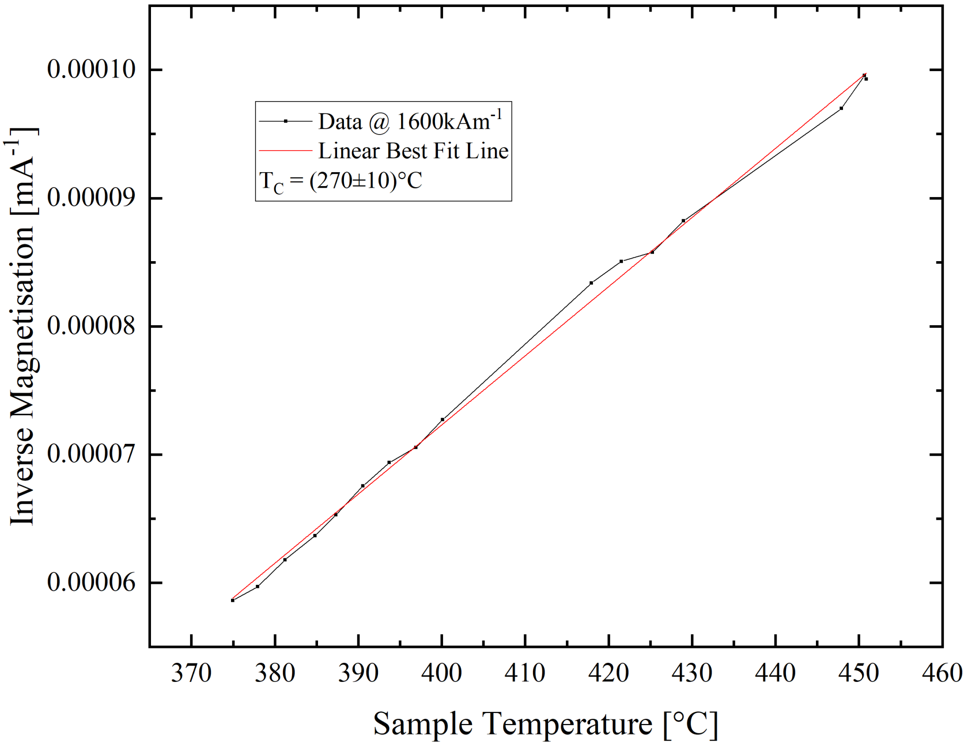

Fig. 5.6 Inverse Magnetisation against temperature data for composition $Mn_{56.1}Al_{42.2}C_{1.7}$ following $\epsilon \rightarrow \tau$ transformation. This data was captured 100°C above the predicted Curie temperature to ensure a linear response for calculations.

On consideration of the optimal properties displayed by composition $Mn_{55.9}Al_{41.9}C_{2.2}$, it is of note that extrinsic magnetic variables, M_R and H_C, are of the same order of magnitude as those displayed by $Mn_{56.1}Al_{42.2}C_{1.7}$ but that the increase in intrinsic properties is off-set by the decrease in extrinsic properties. Given that the extrinsic properties are set by the quantum mechanics of the lattice structure of the ferromagnetic phase and the microstructure of the material, owed to the micromagnetic interactions of the domain structure within the grains and the grain to grain interaction, it is difficult to compare composition to composition extrinsically due to microstructural variations determined by composition variation. As such, only intrinsic properties can be truly compared and measurements taken from the sample of composition $Mn_{55.9}Al_{41.9}C_{2.2}$ shall be used as an internal standard for comparisons with explored ternary systems.

5.3 Ternary System Investigations - MnAlBi

Satisfied that MnAlC can be manufactured using facilities at the University of Sheffield by Arc Melting, with an 8 hour anneal at $1050°C$ followed by a water quench to trap the ϵ-phase and then a 40 minute anneal at $450°C$ to precipitate the transformation to the τ-MnAl phase, two additional lines of experimentation were pursued to satisfy the research goals of this chapter. Ternary samples of MnAlGa and MnAlBi were cast to compare to MnAlC, produced initially by identical heat treatment to that of the reference sample $Mn_{55.9}Al_{41.9}C_{2.2}$.

The logic surrounding the investigation into the MnAlBi system was derived from the success regarding the MnAlGa system. There exists a ferromagnetic phase within the MnBi phase diagram, namely a room temperature stable equiatomic HCP phase referred to as LTP MnBi that forms in equilibrium with Mn and it could be theorised that this intermetallic compound could form in an alloy of MnAlBi [18] [79]. Given the lack of intermetallic compounds formed in the Al-Bi system, it is predicted that the Bi will either exist as a grain-boundary phase of MnAl-based intermetallic or react with Mn in the system to additionally form the LTP phase under near-equilibrium conditions [80]. There also exists the possibility that Bi may be soluble in the τ-MnAl phase, potentially increasing intrinsic magnetic properties.

The first case could potentially increase extrinsic magnetic properties through similar mechanisms to grain boundary diffusion as developed for NdFeB by the precipitation of LTP as an inter-granular phase, disrupting the intergrain exchange coupling reaction at the expense of potentially insoluble, intergranular and diamagnetic Bi ($\chi_{Bi} = -1.34\ cm^3 g^{-1}$ [81]) existing simultaneously [82]. This intergranular coupling is discussed in detail in Schrefl, Fidler and Kronmüller (1994) but can be summarised by being beneficial for H_C at the expense of M_R, though the discussion is limited to the addition of soft magnetic material as opposed to diamagnetic materials [83]. This trade in extrinsic magnetic properties could be beneficial when developing a τ-MnAl system for permanent magnet

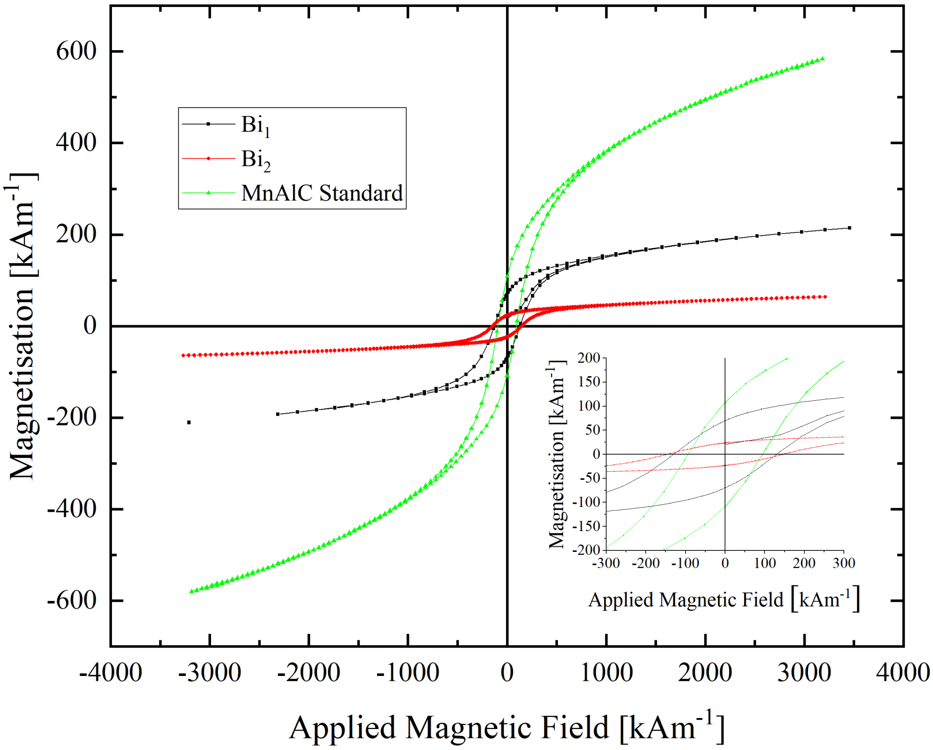

Fig. 5.7 $M(H)$ plots for $Mn_{60.3}Al_{36.7}Bi_3$ (Bi_1), $Mn_{59.7}Al_{36.4}Bi_{3.9}$ (Bi_2) and $Mn_{55.9}Al_{41.9}C_{2.2}$ (MnAlC standard) post $\epsilon \rightarrow \tau$ transformation. The inset graph is the same data centred around axis cross points to display M_R and H_C as a function of composition

applications as in the simulated cases, the majority of simulated dual-phase compositions showed an increase of BH_{Max}.

The other case for which Bi additions may prove beneficial for developing τ-MnAl for a permanent magnetic material is that of countering Mn saturation within the alloy. Work previously discussed by Pareti, Bolzoni, Leccabue and Ermakov states that an increase of Mn in the system can lead to a decrease in M_S of approximately $27kAm^{-1}(at.\%)^{-1}$ above a stochiometric ratio [47]. If Bi doping precipitates a reaction to create the LTP phase in an intergranular state, it could reduce the saturated Mn atoms occupying Al sites within the τ-MnAl lattice and thus allow for the easier to cast Mn-rich alloys to compete with Mn-leaner counterparts.

Composition	M_S $[kAm^{-1}]$	k $[kJm^{-3}]$	T_C $[°C]$
Bi_1	241.9 ± 0.2	685 ± 4	370 ± 30
Bi_2	76.86 ± 0.01	268.4 ± 0.7	400 ± 10
MnAlC Standard	631 ± 2	1390 ± 50	256 ± 4

Table 5.2 A table of intrinsic magnetic property results for the initial Bi-doped MnAl sample run compared to the generated MnAlC standard. Errors on intrinsic magnetic properties are generated from linear fitting statistical errors and observation magnetisation errors provided by the MPMS3 system.

5.3.1 Initial Studies

To this end, two alloys of MnAlBi were cast of reagent compositions $Mn_{60.3}Al_{36.7}Bi_3$, referred to as Bi_1, and $Mn_{59.7}Al_{36.4}Bi_{3.9}$, referred to as Bi_2 using the methodology laid out in Section 4.1.1. As explained in that section, Bi evaporation during the melt process was sufficient to reduce visibility within the chamber to none. Whilst efforts were made to ensure that the chamber and ingot were at or close to room temperature before breaking atmospheric control to remove deposited soot, it was anticipated that Bi concentration in both alloys would be lower than the reagent compositions. Oxide formation was not anticipated, however, due to the lower temperature and the removal from the system of Bi and Mn powder formed from the evaporated reagents. Further outgassing of Bi was also observed during the 8 hour anneal at $1050°C$, depositing throughout the tube furnace, but no oxide was predicted to form due to this taking place under an Ar atmosphere.

The hysteresis curves for Bi_1 and Bi_2 can be seen in Figure 5.7 and show that the addition of Bi as a doping agent decreases M_S when compared to C doping, following the previously outlined heat treatment method. However, looking to the inset, one can see that the addition of Bi does increase H_C in as-cast samples when transformation is induced by the previously defined heat treatment. Given that a goal of development is to improve extrinsic properties of τ-MnAl, this increase could potentially represent an avenue of further exploration for the τ-MnAl system as it moves to an industrially viable product.

In order to better understand the effects of Bi doping on the τ-MnAl system, it is important to consider the effect of its inclusion on the intrinsic magnetic properties and τ-MnAl phase population following the standard heat treatment process. These results can be seen in Table 5.2 and show that the addition of even a few percent Bi can have a significant effect on extrinsic properties when annealed from the supposed ϵ-phase at $450°C$ for 40 minutes.

The consequences of the decrease in intrinsic magnetic variables by Bi addition on the desired extrinsic variables can be estimated by examining theoretical maximum values derived from said variables. Though H_C is observed to be increased by the addition of Bi into the alloy, the resulting value for H_A increases by 30% and 60% for Bi_1 and Bi_2 respectively when determined by the ratio of k to M_S. As a mechanism to harden τ-MnAl alloys at the expense of decreasing stray field, further understanding of the behaviour of Bi within the alloy must be derived in order to explain the process behind this increase and the considerable variation between both samples, despite only 1 $at.$% composition variance in Bi content at casting.

Also of note is the change in sample shape between the MnAlC and MnAlBi samples. Looking to the MnAlBi samples, both approach a lower gradient of $M(H)$ beyond the divergence point observed within the hysteresis loop, interpreted to be H_A for this sample. Comparing this to Figure 2.2, this result either implies that the addition of Bi has lowered H_A in the materials or induced a textural response within the material such that the samples measured were had a greater degree of easy-axis alignment with the applied field. Given that rotation and texture measurements were not made during this investigation, this remains speculation as to the shape change in the hysteresis between the MnAlC and MnAlBi species.

Further, it must be noted that whilst T_C and H_A increase as a product of Bi additions into MnAl alloys as tested, the decrease in M_S is sufficient that applicability for this alloy in a Gap magnet state under these heat treatment conditions is not as appropriate as existing compositions. If one assumes a completely square hysteresis loop, the maximum energy product achievable is $BH_{Max} = \frac{\mu_0 M_S^2}{4}$ which for Bi_1 would mean $BH_{Max}^{Bi1} = (18.4 \pm 0.1) kJm^{-3}$ which falls well below the Gap Magnet criteria for a Type A material as defined by Table 1.1. If the preferential ferromagnetic phase grown could be optimised to increase M_S without decreasing the resulting anisotropy field, the hardening mechanism could prove beneficial as a non-mechanical technique to improve coercivity. In order to investigate this, further studies were done into the microstructure and phase composition of the various heat treatment steps in order to better understand the role Bi plays as an alloying element.

5.3.2 Bi Solubility and its Effects on Alloy Composition

The over 50% decrease in M_S in the Bi_x alloy series cannot be attributed to the increase in Mn within the alloy. The as-cast state was subject to EDX mapping prior to initial heat treatment to verify melt composition. The spectrum testing points can be seen in Figure 5.8 and individual spectra are shown in Appendix A.1. shows that the resultant composition for the alloy as a whole for Bi_1 is $Mn_{58.9}Al_{37.9}Bi_{3.2}$. Not only does this show that there was insignificant composition drift from the reagent composition of Bi_1, but also that in the as-cast state, there was no alloying of the Bi with the bulk MnAl structures. Whilst there is some variation in measured distributions of MnAl and Bi between sampling sites and compositions, Figure 5.8 is broadly representative of observations, albeit with the exact dimensions of Bi inclusions varying dependent on sampling, and thus the density of Bi inclusions within samples taken for magnetic measurements.

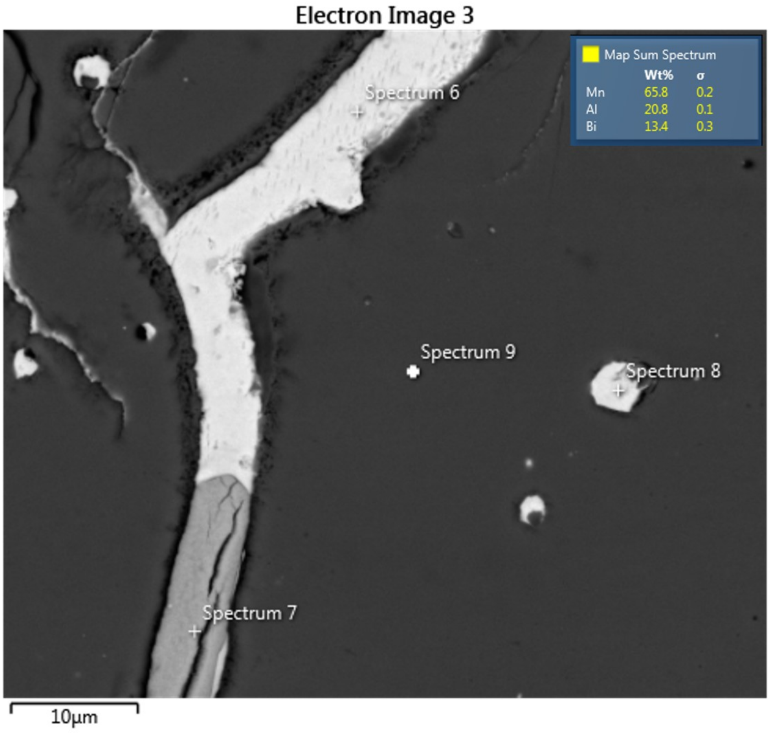

Fig. 5.8 An SEM image of Composition Bi_1 utilised for EDS measurements using the Oxford Instruments AZtec software package. A target area of $(50 \times 50)\mu m$ was selected in order to best capture the ternary phase system present within the material and demonstrate the length scales of the intergranular Bi phase forming post-heat treatment.

Each of the 4 points of interest on the SEM image underwent point EDS analysis in order to determine the composition of the forming structures, with the respective Spectra available in Appendix A.1. Spectra 6 and 8 have a composition of $Mn_{11.8}Bi_{88.2}$ and referencing the MnBi phase diagram, this does not correspond to a known equilibrium phase [84]. There is not enough material present to make an assessment of the structure by XRD alone, however measurements indicate the presence of room temperature state Bi, implying that under the conditions present within casting, Mn absorption within the Bi content may be preferable to Mn saturation within the MnAl mixed phases. This hypothesis is further corroborated by the measured composition of the other majority system within the SEM image of Spectrum 9, having a composition of $Mn_{59.4}Al_{40.6}$. If one assumes negligible composition drift from the as-cast state, the decrease of 1 at% from the bulk composition of Bi_1 at melt represents a potential pathway for alloy fabrication via powder processing to ensure an ease of Mn-lean alloy fabrication by the casting of Mn-rich alloys above Mn 55 at% with dopant Bi followed by an $\epsilon \rightarrow \tau$ transformation and a melting process to remove the resultant Mn-doped Bi, though further investigation would be required to test the validity of this hypothesis.

The composition of Spectrum 7 is $Mn_{52.7}Bi_{47.2}$ implies that, considering errors and the phase diagram of the MnBi system, the equiatomic LTP MnBi compound has been synthesised within this alloy. The validity of this conclusion can be corroborated by the lack of existence of any additional low temperature intermetallic phase comprised of equiatomic Mn and Bi, the $106°C$ range of stability for the high temperature $Mn_{53}Bi_{50}$ phase and the magnetic moment associated with the as-cast state of the alloy that is not present in MnAlC alloys. Assuming an as-cast MnAlC alloy forms an equilibrium ternary alloy of ϵ-phase, βMn and Mn_5Al_8 and that βMn is not ferromagnetic, one can assume that as-cast MnAlC alloys will not demonstrate ferromagnetic behaviour. Rather, it would exhibit paramagnetic behaviour, i.e no permanent magnetisation in the absence of an applied field, no hysteresis throughout a measurement range and a roughly linear magnetisation response to an applied magnetic field, accounting for a slight off-set due to a contribution from the low M_S of approximately $10kAm^{-1}$ from pure Mn_5Al_8 and near-zero M_R [85]. Figure 5.9 shows composition Bi_1 exhibiting a hysteresis response when swept under an applied magnetic field in the as-cast state. If one assumes that the paramagnetic contribution at saturation fields is negligible compared to that of the ferromagnetic LTP MnBi phase and that the ratio of observed M_S to that published for a pure sample of the same phase by Cui *et al.* is equal to the phase population of LTP MnBi within the alloy, it becomes possible to investigate whether this population may increase as a result of varying Bi concentration within tested MnAlBi compositions [84].

Using this hypothesis, it could be estimated that the LTP concentration within the Bi_1 concentration as-cast is (2.30 ± 0.03)%. This would explain how it was impossible to detect this phase by means of laboratory based XRD techniques due to its low concentration but how, when compared to the paramagnetic background of other phases, it is clearly detectable by means of hysteresis presence. This would imply that, for at least the concentration of Bi present in Bi_1, XRD phase population calculations are insufficient in the estimation of minority LTP phase formation.

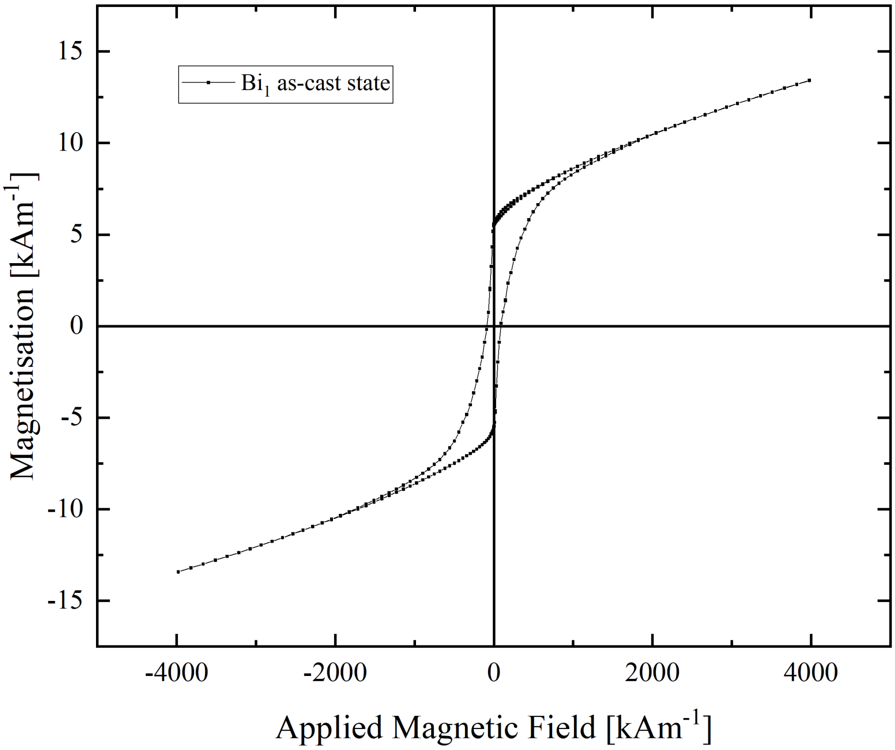

Fig. 5.9 $M(H)$ for as-cast Bi_1, providing evidence for the existence of LTP-MnBi formation within the cast alloy. Given that one would expect a quaternary system upon casting of βMn, Bi, ϵ-phase and Mn_5Al_8, only Mn_5Al_8 exhibits ferromagnetic behaviour with $M_S \approx 10kAm^{-1}$. Given that $M_R \approx 7kAm^{-1}$, this would imply that either there is a significant Mn_5Al_8 population with a high M_R/M_S ratio or there is an additional ferromagnetic phase present.

This ferromagnetic behaviour dissipates, however, when the sample compositions are put through the first phase of the heat treatment to facilitate the $\epsilon \rightarrow \tau$ transformation, namely that of the 8 hour anneal at $1050°C$ and water quench. As previously stated, this anneal saw the outgassing of Bi fumes from the sample, despite being conducted under an Ar atmosphere broadly equal in pressure to that of ambient conditions. No oxide formation was expected or measured from this process, however, and so it is not interpreted that this behaviour derived from oxidation of the LTP phase, but rather that at $1050°C$, no stable intermetallic compound exists in the MnBi or AlBi phase diagram and it is well above the melting temperature for Bi, implying that the sample ingot may be acting in a sponge-like capacity during the annealing process and containing the liquid Bi within

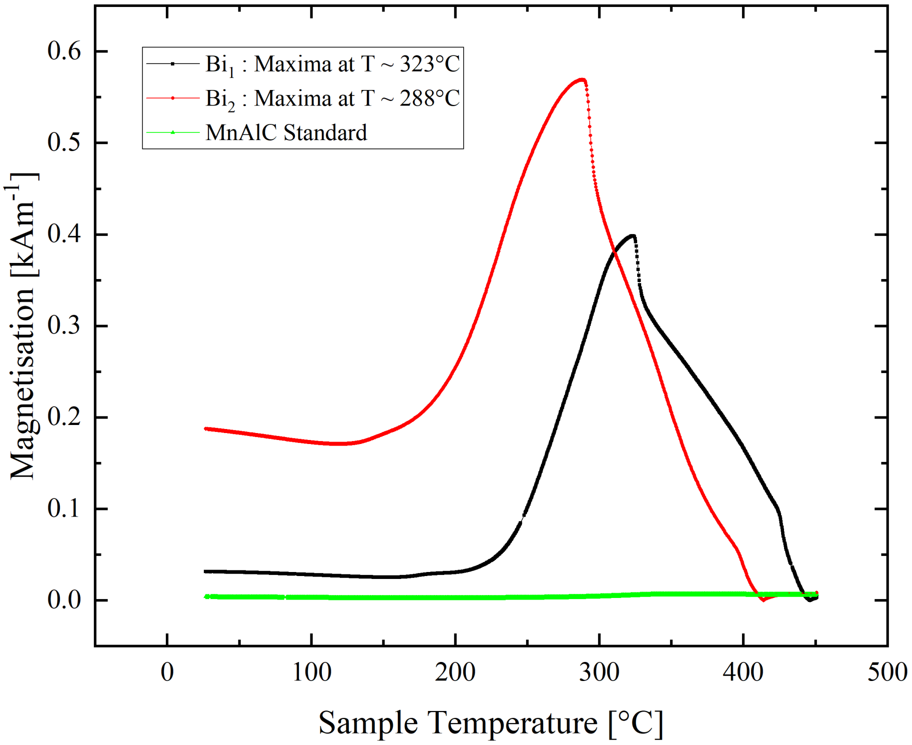

Fig. 5.10 $M(T)$ at $H \approx 0kAm^{-1}$ for compositions Bi_1, Bi_2 and the MnAlC standard capturing the magnetic behaviour of the onset of the $\epsilon \rightarrow \tau$ transition as well as the formation and decay of the suspected LTP-MnBi phase in Bi-containing compositions.

the intergranular structure. Following the water quench, the two components for the alloy do not interact, forming an $\epsilon + Bi$ mixed phase state, though again in Bi concentrations low enough such that XRD would be ineffective to estimate phase concentration.

This hypothesis is explored by Figure 5.10 which shows the magnetisation response to increasing temperature for water quenched samples of Bi_1 and Bi_2 following the initial heat treatment to set the alloy into the ϵ-phase. When compared to the M_R of the LTP-MnBi phase seen in Figure 5.9, it can be seen that the observed magnetisation is an order of magnitude lower than the as-cast state, suggesting that less than 0.1% of the phase population is surviving LTP-MnBi from the initial casting. The increase in magnetisation maximising at $(323.4 \pm 0.2)°C$ can be attributed to the precipitation of LTP MnBi from an interface reaction. A similar maxima can be observed for Bi_2 at $(287.9 \pm 0.2)°C$ with the increase in initial magnetisation observed attributed to minor variations in the decay of residual LTP MnBi or precipitation of the $\epsilon \rightarrow \tau$ reaction during the cooling cycle.

Composition	MnAl [%]	MnBi [%]	Bi [%]	M_S $[kAm^{-1}]$
$Mn_{57.5}Al_{38}Bi_{4.5}$	90 ± 1	3 ± 1	7 ± 1	15.81 ± 0.02
$Mn_{61.1}Al_{32}Bi_{6.9}$	91 ± 1	3 ± 1	6 ± 1	12.81 ± 0.03
$Mn_{58.5}Al_{36.3}Bi_{5.2}$	87 ± 1	4 ± 1	9 ± 1	8.55 ± 0.02

Table 5.3 A table of phase population estimated from BSE-SEM contrast images taken for MnAlBi as-cast samples. ImageJ was the software package used to analyse images taken on the Oxford Instruments AZtex software package with errors estimated as an uncertainty on image repeatability, recognising that feature-to-pixel ratios set scale lengths for image capture and thus phase identification.

5.3.3 Optimisation of Bi Composition and Annealing Temperatures to Maximise Intrinsic and Extrinsic Magnetic Properties

The precipitation of this secondary ferromagnetic phase during the annealing process represents a potential point of optimisation for Bi-doped alloys given that this initial increase in magnetisation is not present in the MnAlC standard behaviour during the initial temperature rise to annealing. In order to fully explore whether this dopant has a beneficial effect on the system, two parameters were varied. The first parameter was the proportion of Bi added into the system and, in theory, the final ratios of Bi, τ-MnAl and LTP MnBi. Given that the Bi has not been shown to sit in solution within the MnAl phases by EDS, assessments can be made as to the increase of LTP-MnBi formation by the hysteresis of as-cast samples. It is not assumed that an $\epsilon \rightarrow \tau$ transformation would occur within the material during solidification despite the alloy temperature transitioning through the metastable transformation temperature range during cooling as the samples were cooled from melt in a water-cooled copper crucible, meaning a cooling rate for the melt pool to room temperature could be assumed to be of the order of approximately $100°Cmin^{-1}$ and thus outside of the 'controlled cooling' transformation conditions expressed in literature for one step τ-MnAl formation [61].

Counter to initial expectations, as-cast hysteresis did not increase as a function of Bi content within alloy composition. Figure 5.11 shows the hysteresis loops for as-cast alloys of $Mn_{60.3}Al_{36.7}Bi_3$, $Mn_{57.5}Al_{38}Bi_{4.5}$ and $Mn_{58.5}Al_{36.3}Bi_{5.2}$ and show that both M_R and M_S decrease as Bi concentration increases in the ternary system. Examinations of EDS mapping of all three alloys show that LTP-MnBi formation occurs, as seen in Figure 5.8 but that as Bi concentrations increase, no relationship between intergranular Bi feature thickness and concentration is apparent. The Bi feature thickness for the three alloys was measured as $(24 \pm 1)\mu m$, $(42 \pm 2)\mu m$ and $(32 \pm 2)\mu m$ respectively.

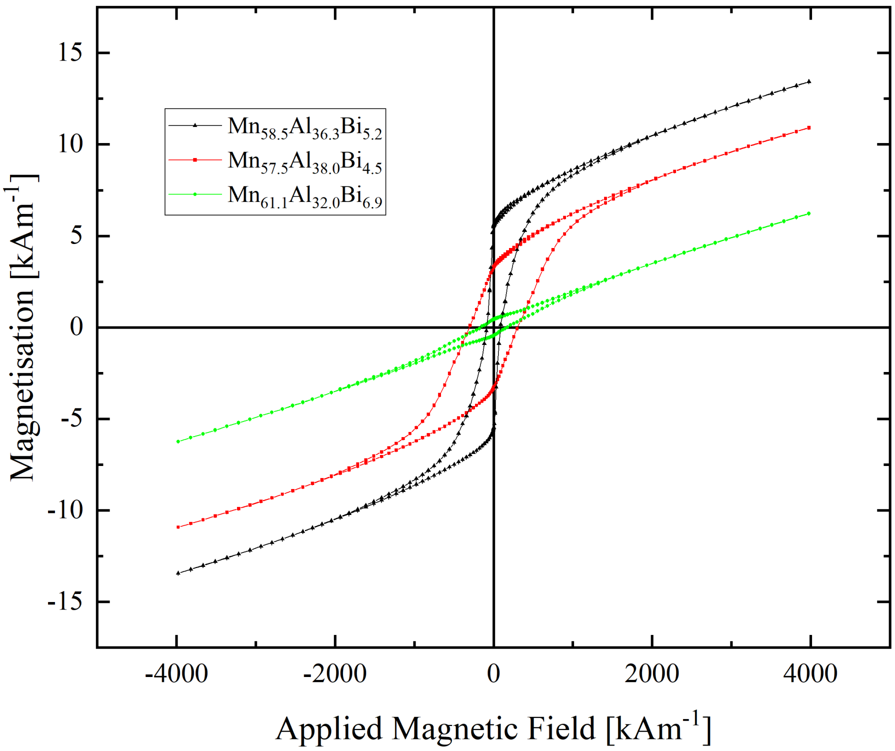

Fig. 5.11 $M(H)$ for as-cast MnAlBi alloys. Ferromagnetic behaviour is attributed to the LTP-MnBi phase present from Bi-MnAl interface reactions and does not appear to increase as a result of increasing Bi concentration due to a lack of trend between M_S and Bi $at.\%$.

In an attempt to correlate LTP-MnBi concentration to magnetic behaviour, BSE-SEM was used to identify phase contents within the alloy. Given that the variation in Figure 5.8 corresponded to differing phase compositions, histograms were calculated from pixel grey-scale values taken from BSE images of areas over $(300 \times 300)\mu m^2$ and histogram ratios calculated as an approximation of phase population. This technique was chosen over phase identification by XRD due to the trace population of the LTP-MnBi phase within the systems and the associated difficulty of accurate phase population calculation of minority phases by Rietfeld refinement. These calculated populations can be seen in Table 5.3 and show that, although there is significant error on measurement owing to the statistical technique used for phase population, all three compositions show similar estimated phase populations of LTP-MnBi, despite measurable variation in associated saturation magnetisation values. Whilst error on phase population could be decreased with an increased measurement area or multi-layer imaging of the same area achieved by surface ablation to build a 3D model of the phase population, these initial results do not suggest that an increase in Bi concentration within the MnAlBi ternary alloy causes a greater precipitation of LTP-MnBi but does have a negative effect on as-cast saturation magnetisation due to decreasing the overall density of the interface-precipitated intermetallic phase.

Further experimentation on the effects of increasing Bi content in the MnAlBi system were suspended following this investigation due to Bi outgassing. After initial attempts to anneal into the ϵ-phase, it was found that all three samples saw significant Bi vapour produced and the experiment was abandoned to prevent damage to heat treatment systems. Should further work be attempted on Bi-heavy compositions, additional measures would need to be taken to prevent damage from occurring due to Bi surface deposition. Further, anecdotal evidence from handling the three samples was an increase in the brittle behaviour of the samples, with all three being able to be broken by hand and exhibiting pores within the structure. All samples appeared solid and dense when segmented post-casting, implying that the porosity was generated from unalloyed Bi vapourising during heat treatment.

The second series of measurements was conducted on Sample Bi_1. Recognising that the sample showed the greater intrinsic magnetic properties of the two initial MnAlBi systems, work was conducted to optimise the heat treatment in order to precipitate both τ-MnAl and LTP MnBi in a dual magnetic phase system. Observing from Figure 5.4, it can be seen that the $\epsilon \rightarrow \tau$ transformation can initiate as low as $100°C$ in MnAlC alloys and that there is a differing magnetisation response when Bi is introduced into the system. As such, in order to assess whether a cooler annealing temperature in the range of the observed magnetisation peak induces greater intrinsic or extrinsic magnetic properties, additional heat treatments were undertaken on as-quenched samples for 40 minutes at temperature intervals of $50°C$ in the range of $(200 \leq T \leq 450)°C$ before being subject to a water quench.

The intrinsic and extrinsic magnetic properties of the heat treatment study can be seen in Table 5.4 and Figure 5.12. These show that two distinct regimes develop across the study, that of paramagnetic-like material with low energy products and those with sufficient hysteresis loops to generate meaningful energy products. The previously stated hypothesis that $\epsilon \rightarrow \tau$ transformation may begin occurring as low as $100°C$ and that LTP-MnBi precipitation may increase at lower temperatures proved to be not an effective way of increasing intrinsic magnetic variables under the MnAlC standard heat treatment conditions.

In the stable range that LTP-MnBi exists within the MnBi phase diagram, namely $(0-262)°C$, any hysteresis developed within the material is small [84]. Assuming under

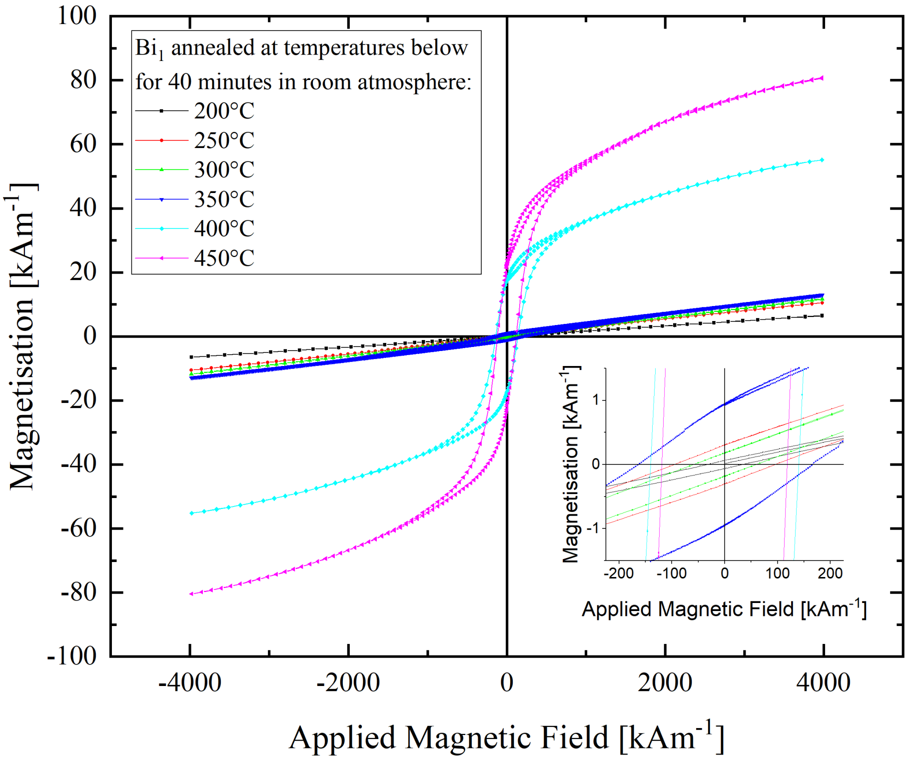

Fig. 5.12 $M(H)$ for composition Bi_1 as a function of annealing temperatures $(200 \leq T \leq 450)^{\circ}C$ for 40 minutes to precipitate an $\epsilon + Bi \rightarrow \tau + MnBi$ transformation.

these conditions a complete phase transformation within the segregated Bi content to the Bi + LTP-MnBi mixed phase group, a lever-rule phase population calculation would predict a phase balance of 6% LTP-MnBi and 94% Bi or a phase population of 0.18% LTP-MnBi with respect to the alloy as a whole. Using the published M_S for LTP-MnBi, this would predict an observed M_S for samples annealed at $(200, 250)°C$ of approximately $0.7 kAm^{-1}$. This would imply that additional transformation to the ϵ-state is occurring to provide the increase in M_S and that increasing the annealing time may yield high M_S values.

Of the samples that underwent sufficient transformation to yield energy products over $10 Jm^{-3}$, a trade-off occurs between H_C and M_R with increasing heat treatment temperature increasing both the saturation magnetisation and ratio between saturation magnetisation and remanence at the expense of coercivity. If one looks at the extrinsic magnetic properties normalised by their theoretical maxima calculated from intrinsic variables, i.e $\frac{H_C}{H_A}$ and $\frac{M_R}{M_S}$, one can see that an increase in annealing temperature improves both ratios though neither approaches commonly accepted engineering maxima of 0.25 and 0.7 respectively. This implies that, when considering a 40 minute annealing time, using a cooler annealing temperature to reduce the decomposition of the LTP-MnBi phase does not appear to have a beneficial effect on intrinsic magnetic variables or normalised extrinsic variables.

Finally, it is of note that the investigation of the MnAlBi system is is for a permanent magnetic material and as such, assessing the magnetic hardness of each sample by Equation 2.20 is a useful metric to assess the heat treatment. Given that the MnAlC standard has a hardness of $\kappa_{standard} = (1.67 \pm 0.06)$, it is of note that hardness decreases as a function of annealing temperature, with $\kappa_{200°C} = (21.3 \pm 0.3)$ and $\kappa_{450°C} = (7 \pm 1)$. Whilst this might imply that the cooler annealing temperatures may produce harder materials, the Law of Approach to Saturation used to calculate k may be inappropriate in cases where the ferromagnetic phase is a minority phase in the system as at high fields, the magnetic moment associated with the paramagnetic phase may lead to non-linear behaviour observed at high-fields when attempting to fit $M(1/H^2)$ as a linear relationship.

Concerning the measurements taken from Bi_1 annealed at $450°C$, it is of note that the errors associated with said measurements can be of the same order of magnitude as the measurements themselves, and differ from the previous measurements taken for composition Bi_1 by an order of magnitude. Of the 4 measured samples, significant variability was seen in the intrinsic magnetic variables, with M_S and k measured in the ranges $(26.5 - 88.1) kAm^{-1}$ and $(118 - 250) kJm^{-3}$ respectively. All samples were taken from the same heat treated material and were of masses in the range of $(55.6 - 97.0) mg$ with no correlation between sample mass and intrinsic magnetic properties. An explanation

T_{anneal} [°C]	200	250	300	350	400	450
M_S [kAm^{-1}]]	8.55±0.04	15.01±0.03	15.67±0.06	17.60±0.03	39.49±0.03	60±10
k [kJm^{-3}]	41.7±0.6	79.5±0.6	78±1	88.2±0.6	116.3±0.7	180±30
H_C [kAm^{-1}]	33.09±0.02	95.13±0.08	59.48±0.02	165.4±0.7	141.3±0.2	126±3
M_R [kAm^{-1}]	0.06362±0.00006	0.30499±0.00003	0.18197±0.00001	0.94697±0.00006	6.6812±0.0004	16±4
M_R/M_S	0.00744±0.00003	0.02029±0.00005	0.01161±0.00005	0.0054±0.0001	0.2845±0.0002	0.27±0.08
BH_{Max} [Jm^{-3}]	0.6047±0.0005	9.005±0.004	3.188±0.002	50.37±0.03	334.2±0.2	700±200

Table 5.4 A table of intrinsic and extrinsic magnetic properties for composition Bi_1 as a function of annealing temperatures $(200 \leq T \leq 450)^{\circ}C$ for 40 minutes to precipitate an $\epsilon + Bi \rightarrow \tau + MnBi$ transformation. Intrinsic properties were calculated

for this phenomenon is variability in Bi content within each sample. Given that the dimensions of the samples were on the scale of a few millimeters and Figure 5.9 shows unalloyed Bi features on the length scale of approximately $(10 \times 50)\mu m$ with smaller features, it is possible that over the samples, the length scales are not sufficient such that Bi dispersion can be considered isotropic and pseudo-homogeneous. This could lead to a varying phase population between each sample cut for magnetic characterisation and in turn to varying intrinsic magnetic properties derived from the local volume fraction of ferromagnetic phases as opposed to the global population for the alloy. As such, this is further evidence that under the MnAlC standard heat treatment conditions to precipitate the $\epsilon \rightarrow \tau$ transformation, the inclusion of Bi into the alloy is inappropriate to optimise the material for applications as a permanent magnetic material. Homogeneity in magnetic properties cannot be guaranteed for magnets fashioned from the same casting below a critical length scale which is greater than that of several millimeters, providing a lower size limit to any potential application of an optimised MnAlBi alloy.

5.3.4 XRD of MnAlBi Alloys in ϵ and τ States

Due to the outgassing of Bi during the initial annealing process to achieve the ϵ-MnAl phase, fabrication was limited to a few grams of material in order to prevent damage to the tube furnace utilised. As such, insufficient volume of material could be manufactured to produce either an in-plane XRD sample or powder samples. Given the determined material properties of the MnAlBi series of alloys, however, sufficient promise is not shown for further development as a ternary system for applications in permanent magnetic materials.

5.4 Ternary System Investigations - MnAlGa by Annealing

In order to assess the potential industrial applicability of Ga-doped $\tau - MnAl$ material as discovered by Mix *et.al.*, the production of a τ-MnAl magnet by the Quench and Anneal method was undertaken and its intrinsic magnetic properties determined [61]. The purpose of this is that previous work forced the $\epsilon \rightarrow \tau$ transformation by means of a Controlled Cooling . No parameters are given for this process but should production of this alloy be scaled from kilograms to tonnes, controlling the phase population by controlling the cooling rate creates additional challenges that a quench and heat treatment, a very common metallurgy technique already in near ubiquitous usage across industry, does not. As such, a sample of composition $Mn_{58.7}Al_{34.8}Ga_{6.5}$, referred to as MnAlGa, was cast by Arc melting and subjected to a $1050°C$ heat treatment for 8 hours followed by a water quench to precipitate the ϵ-phase.

When compared to production of MnAlC or MnAlBi, arc melting of the MnAlGa sample showed a lesser degree of Mn vapourisation when transitioning from reagent materials to melt pool. This can be attributed to the Ga within the crucible melting first and providing a greater local pressure to encapsulate material, as well as better heat dispersion from the arc rather than direct contact onto Mn flakes or Al beads within the pool. As such, there was a lesser degree of material blow out from the crucible and a greater degree of composition control during casting.

5.4.1 Precursor State of MnAlGa($6.5\ at.\%$)

The initial work on this ternary system produced by Mix *et. al* showed the presence of both the ϵ-phase as well as a γ_2 phase either inherent to the MnGa phase diagram as the room temperature, equilibrium phase or the MnAl phase diagram as a high temperature phase, with both being part of the $R3m$ space group and difficult to distinguish [61]. As such, given the differing annealing conditions between the published study, 48 hours at $1100°C$, and the comparable study conducted for the MnAlC standard sample of 8 hours at $1050°C$, as well as the unknown effects that the addition of Ga into the ternary system may have on the phase space at these temperatures, it was deemed important to confirm the state of the precursor material.

An easy test for this was the quantification of the paramagnetic behaviour and susceptibility on the MnAlGa sample against that of the MnAlC and the magnetisation of the samples when annealed. In Figure 5.13 the initial behavior of the as-quenched MnAlGa sample and MnAlC following identical initial heat treatments can be seen and both show paramagnetic behaviour with no observable hysteresis in the $M(H)$ measurements. Whilst

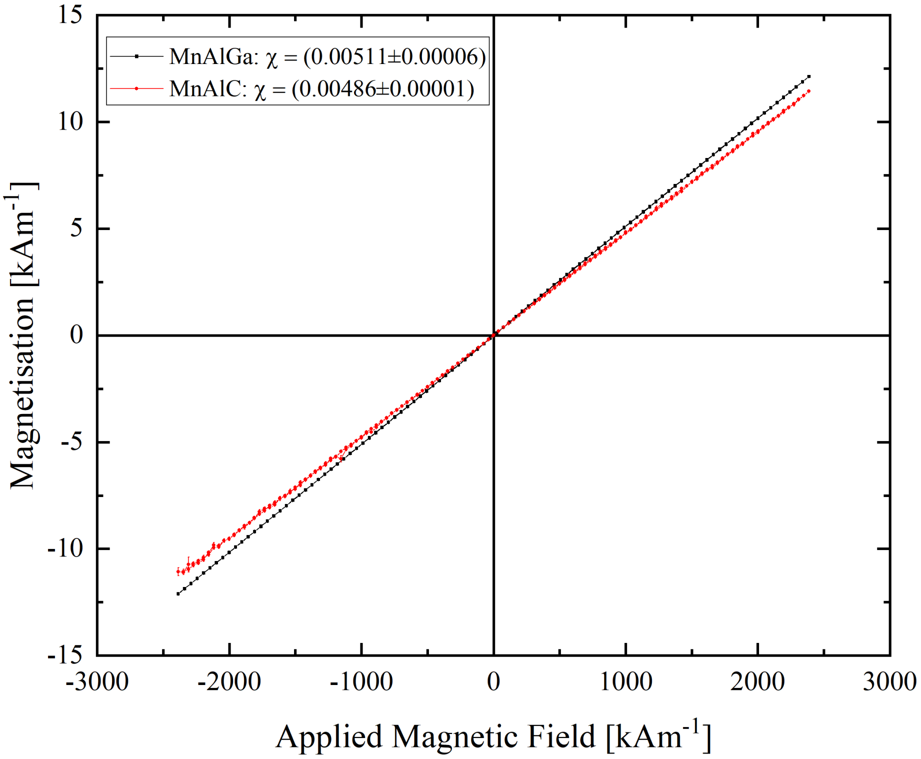

Fig. 5.13 A plot of magnetisation against applied magnetic field for MnAlGa and MnAlC samples following heat treatments at 1050°C for 8 hours followed by a water quench, precipitating the ϵ-precursor state. No variation in zero-field magnetisation can be observed for either sample.

there is a measurable variation in paramagnetic susceptibility between both samples, $\chi_{MnAlGa} = (5.11 \pm 0.06) \times 10^{-3}$ and $\chi_{MnAlC} = (4.86 \pm 0.01) \times 10^{-3}$, this $(5 \pm 1)\%$ increase in susceptibility cannot be necessarily determined by the addition of Ga into the system as the variation in Mn, previously discussed to change magnetic properties in the τ-state, as the difference between Mn concentrations of 58.9 $at\%$ and 55.9 $at\%$ may have contributed to this effect [47]. Further evidence for this observation can be given as the calculated susceptibility for the composition $Mn_{56.1}Al_{42.2}C_{1.7}$ was $\chi_{C=1.7at.\%} = (5.03 \pm 0.07) \times 10^{-3}$, suggesting that variations in composition concentration under 1 $at\%$ can cause variation in this parameter.

In an effort to better understand this variation in paramagnetic susceptibility, a 2θ-XRD scan on a Cu-source was undertaken on an annealed sample of MnAlGa and peak positions mapped. This annotated XRD pattern can be seen in Figure 5.14 and show that all peaks

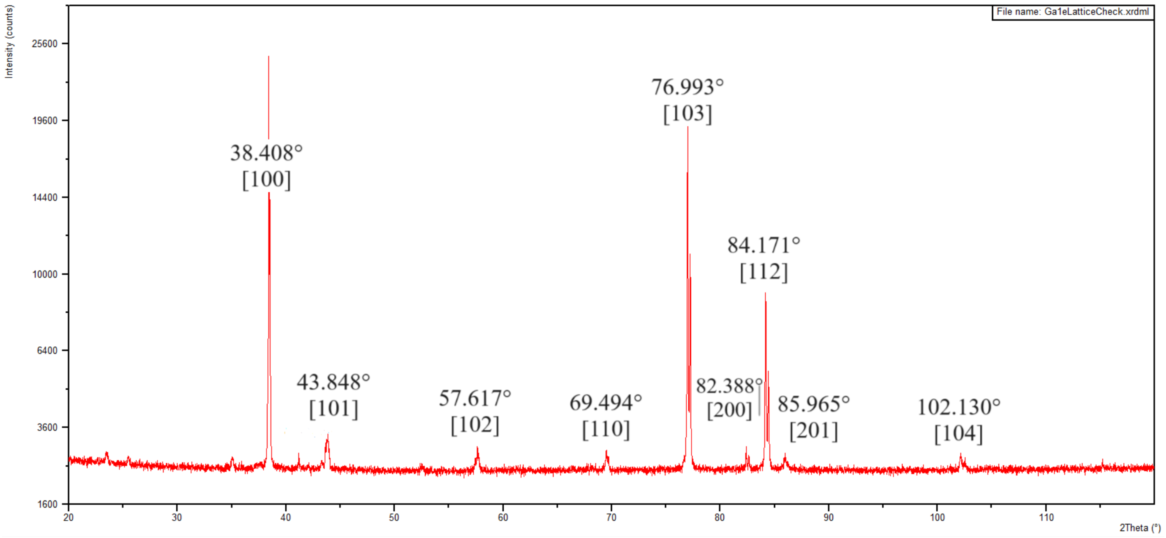

Fig. 5.14 A 2θ-scan with a Cu source on a polished MnAlGa surface to confirm a single phase state and calculate lattice parameters. The isolated structure is HCP with lattice parameters $a = (0.27027 \pm 0.00007)\,nm$ and $c = (0.4368 \pm 0.0005)\,nm$.

listed by Ellner are all present in this sample, showing that any degree of texture present in the cast sample is insufficient for low-intensity peak elimination when compared to noise on measurements, referencing the intensity calculations cited alongside the associated ICDD entry (04-013-9962) and the broad intensity compliance demonstrated by the sample, suggesting that the texture within the casting is broadly isotropic [86]. Given the deviation in 2θ position was not constant however when considering the values measured from the MnAlGa sample and no additional phase could be detected from peak identification, the fitting of lattice parameters was deemed appropriate. It is of note that the lack of γ_2 peaks that are present in data presented by Mix *et al.* suggests that either these low intensity, low population peaks are indistinguishable from noise in this sample or the γ_2 phase did not form from the initial anneal and quench to produce the ϵ-precursor phase.

The measured lattice parameters from this phase were $a = (0.27027 \pm 0.00007)\,nm$ and $c = (0.4368 \pm 0.0005)\,nm$ with errors calculated from the statistical variation across peak position rather than from measurement bin quantisation due to the statistical variation being the greater source. Modelling the lattice parameters for $Mn_{58.7}Al_{34.8}Ga_{6.5}$ under the assumption that the Ga had no effect on the structure against the trends shown by Ellner, we find that the alloy measured in this body of work shows significant deviation from existing trends in the binary alloy system, as shown in Figure 5.15. The addition of Ga, which due to the lack of visible secondary phase peaks within the XRD data is assumed

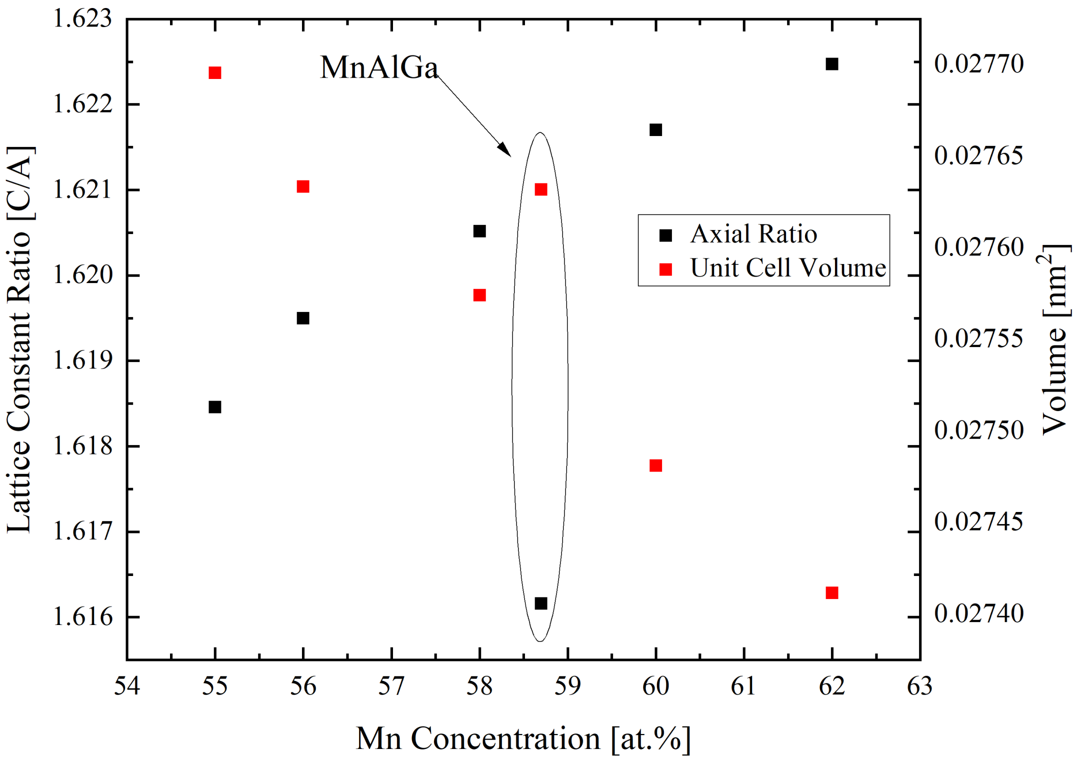

Fig. 5.15 Axial ratios and unit cell volumes of the ϵ-phase for the Mn_xAl_{100-x} system taken from Ellner compared to data captured for synthesised $Mn_{58.7}Al_{34.8}Ga_{6.5}$, implying the addition of soluble Ga into the lattice reduces diagonalisation and increases cell volume when compared to undoped systems [86].

to occupy the Al site within the hexagonal structure, leads to the increase of cell volume by the decrease of lattice diagonalisation.

5.4.2 Magnetisation during Heat Treatment of MnAlGa(6.5 $at.$%)

Satisfied that the precursor state had been achieved by way of paramagnetic state identification by susceptibility within 5% variation, explainable by error in sample mass measurements with a range of approximately 1%, convoluted with linear best fit data from magnetisation measurements with an associated error in the range of $(1-2)$% due to low magnetisation values to be measured by a VSM system, annealing was undertaken within the MPMS3 system. Looking to the time-dependent magnetisation of both MnAlC and MnAlGa during the 450°C heat treatment, further divergence in behaviour can be observed in Figure 5.16. Whereas MnAlC reaches 95% full transformation (7 ± 1)min, MnAlGa appears to be still undergoing transformation at 40 minutes if assessed by dM/dT. Averaging the differential magnetisation with respect to time for both samples between 35 and 40 minutes of annealing time, it is found that $dM/dt\ (MnAlC) = (0.5 \pm 0.7)\% min^{-1}$ which implies a steady state has been reached, with individual fluctuations in magnetisation averaging out to a greater error than any perceivable change in magnetisation when compared to that of $dM/dt\ (MnAlGa) = (0.24 \pm 0.05)\% min^{-1}$ where a distinctive increase in magnetisation as a function of annealing time at $450°C$ can be observed.

In an effort to account for this change in magnetisation increase between MnAlC and MnAlGa, reference to Pareti *et al.* is once again made, where the annealing behaviour for Mn-heavy alloys is discussed. Given that the data range only covers $(51 < Mn\ at.\% < 56)$ extrapolation must be made to assess both alloys given they contain 55.9 $at.\%$ and 58.7 $at.\%$ respectively. Pareti *et al.* report that for undoped MnAl alloys annealed at $580°C$, magnetisation decreases as a function of annealing time following 10 minutes for compositions with Mn content in excess of 53.5 $at\%$ with this rate increasing as a function of time [47]. Si *et al.* observe that for annealing at $400°C$ under an applied field of $3600 kAm^{-1}$, a maxima in magnetisation achieved for a composition of $Mn_{54}Al_{46}$ following $100 mins$ of annealing. Most published work on MnAlC alloys previously discussed in the literature review utilises a higher annealing temperature to instigate the $\epsilon \rightarrow \tau$ phase transformation [49][50] [53] [54]. Work by Zhao *et al.* (2018) states that optimum annealing conditions for MnAlC alloys with C content below 3 $at.\%$ are $500°C$ for 30 minutes [50]. With the assumption that lower annealing temperatures lead to lower transformation rates through the diffusion arguments set by Lu *et al.*, it can be concluded that the addition of Ga in replacement of C lowers the diffusion rate such that longer annealing times are required to facilitate equivalent τ-phase fractions when compared to MnAlC alloys [87]. As such, one can conclude that the final intrinsic magnetic properties discussed in Figure 5.18 do not represent optimum material properties and further optimisation work would need to be conducted in order to maximise these properties. This is under the assumption that the paramagnetic magnetisation increase at temperature is directly proportional to τ-phase population increase.

As previously discussed, a $(125 \pm 5)°C$ difference in T_C can be observed between the MnAlC standard and the MnAlGa material following a 40 minute anneal at $450°C$. Figure 5.17 shows the magnetisation behaviour of both materials upon cooling from the anneal normalised by final magnetisation. Given that this cooling is conducted at zero applied field, the resultant magnetisation direction is random and requires alignment under sufficient applied magnetic field to achieve true material remanence, thus meaning only

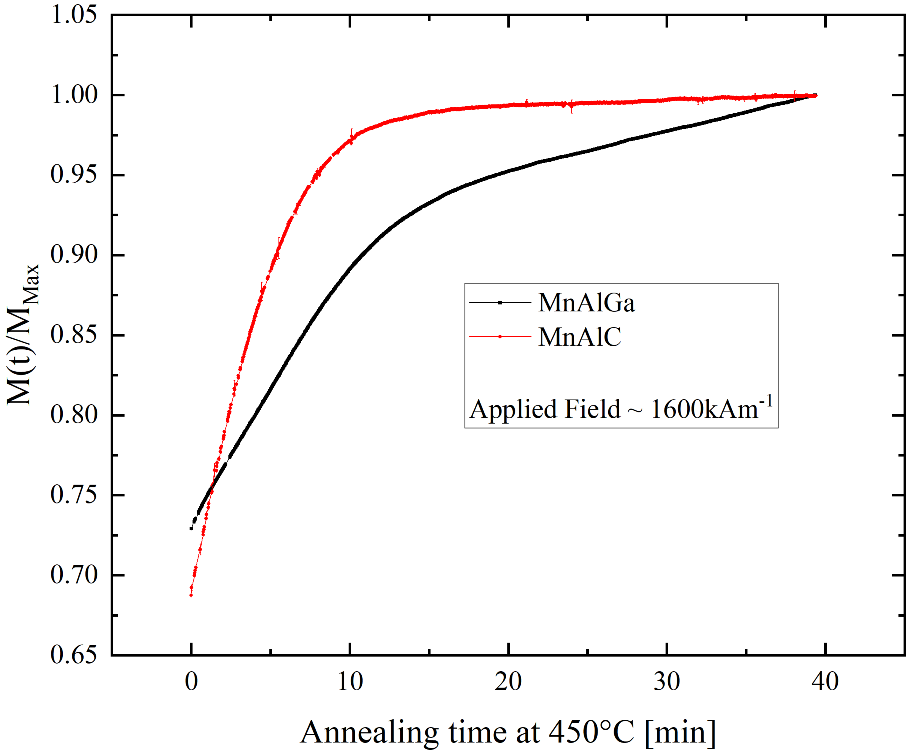

Fig. 5.16 $M(t)$ at an annealing temperature of $T = 450°C$, capturing the magnetic behaviour for the $\epsilon \rightarrow \tau$ transformation for MnAlGa and MnAlC alloys. This shows that for transformation rate is sensitive to composition, with MnAlGa still showing positive differential behaviour at 40 minutes and MnAlC having reached a steady state .

relative behaviour between the two materials can be directly compared. Whilst the effects of C doping on T_C are well understood and discussed within previous chapters, it is of note that the Ga doping causes an inflection within the magnetisation response in the region of $(340-360)°C$ [47]. This does not correspond to the two-phase system shown in Mix *et al.* showing distinct inflection points which indicate two ferromagnetic systems transitioning to paramagnetic states at distinct temperatures [61]. This suggests that annealing at $450°C$ for 40 minutes is insufficient to precipitate the secondary $L1_0$ phase discussed in literature. Further, the increased T_C observed, measured by fitting the Curie-Weiss law above T_C as discussed in Equation 3.1, is greater than the reported values of T_C for any of the alloys discussed in Mix *et al.* (supplementary material) but is closer to that reported for undoped MnAl by Pareti *et al.* [47]. The $22°C$ increase of T_C between the reported results for $Mn_{55}Al_{38.57}Ga_{6.43}$ and the alloy $Mn_{58.7}Al_{34.8}Ga_{6.5}$ synthesised for this work can thus

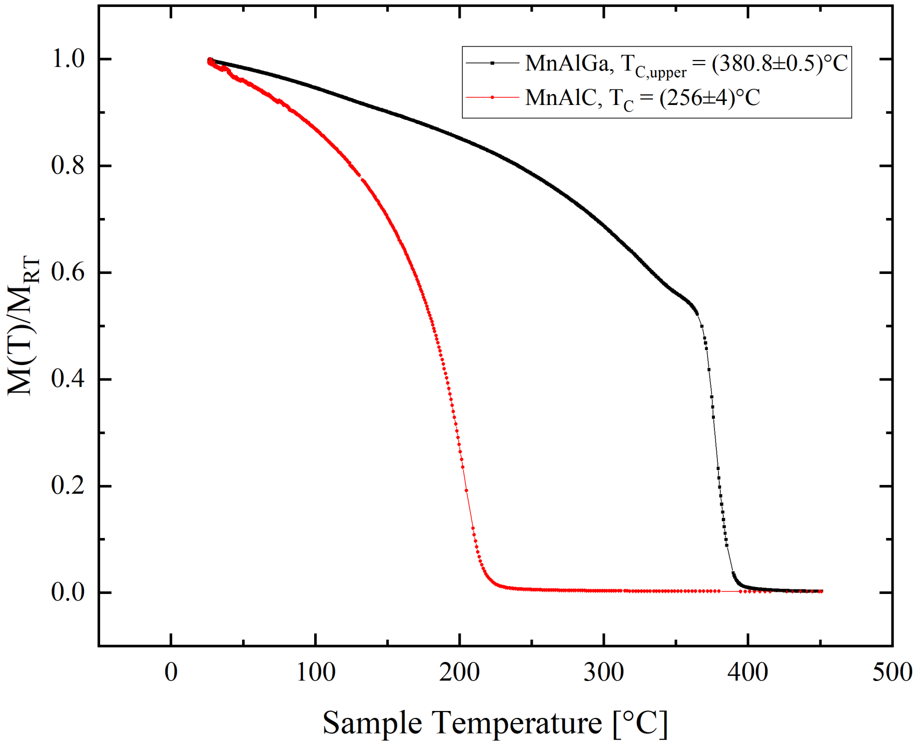

Fig. 5.17 $M(T)$ for both MnAlGa and MnAlC compositions following a 40 minute anneal at $450°C$ with both samples undergoing the metastable $\epsilon \rightarrow \tau$ transformation. Given a cooling rate of approximately $12°Cs^{-1}$, the low data density near T_C for each alloy is reflective of dM/dT as both samples enter ferromagnetic behaviour regimes.

be explained by the same observation that the Mn rich composition sees an increase in T_C as a function of Mn content due to Mn-Mn exchanges from the saturated Mn atoms occupying Al sites within the $L1_0$ structure.

5.4.3 Hysteresis of τ-state of MnAlGa(6.5 $at.$%)

Following the heat treatment process and recognising that said heat treatment is not an optimised process for the material, with $dM/dt\,(T = 450°C) > 0\% min^{-1}$ for MnAlGa at 40 minutes, the end of the heat treatment time, Figure 5.18 shows the magnetic hysteresis of the resultant ferromagnetic material. From the inset graph highlighting low applied field behaviour, we can gather that for identical heat treatment conditions, the addition of Ga in replacement of C in the system can lead to an increase of $(27 \pm 3)\%$ in coercivity

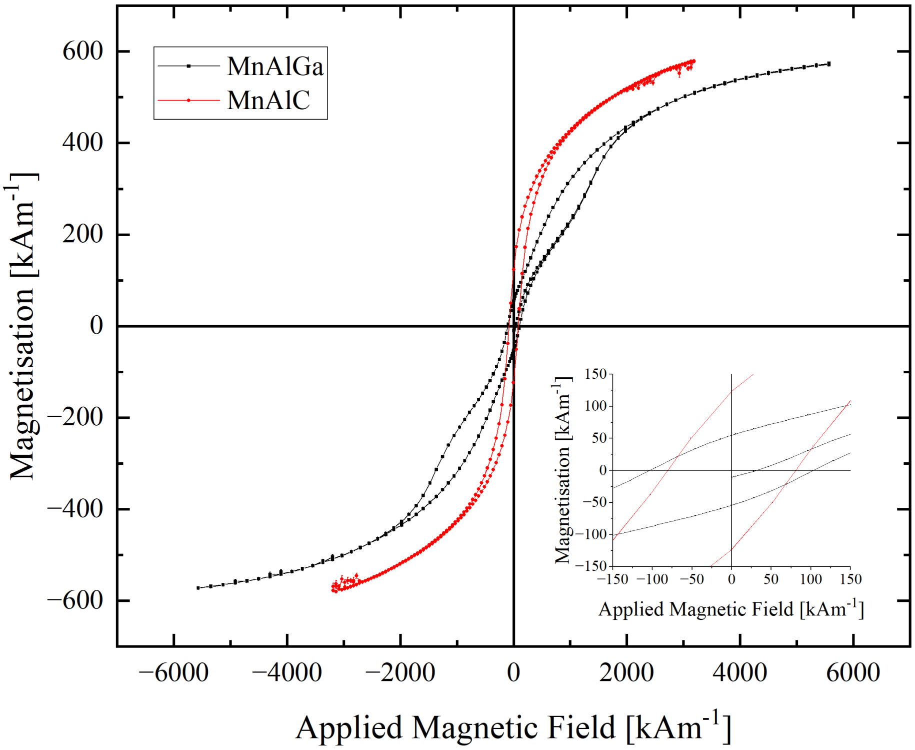

Fig. 5.18 Magnetic hysteresis measurements of MnAlGa and MnAlC samples following a 40 minute anneal at 450°C to activate the metastable $\epsilon \rightarrow \tau$ transformation. Inset: M(H) for both samples at low fields, displaying variation in M_R and H_C.

with $H_C(Ga) = (103 \pm 1)kAm^{-1}$ and $H_C(C) = (82 \pm 2)kAm^{-1}$ at the expense of a decrease in remanent magnetisation of (55.92 ± 0.05)% given final remanence values of $M_R(Ga) = (54.41 \pm 0.06)kAm^{-1}$ and $M_R(C) = (123.42 \pm 0.04)kAm^{-1}$. The non-uniform hysteresis loop observed for MnAlGa demonstrates an interesting phenomena, that there are two distinct switching fields from saturation, potentially indicating that there are two ferromagnetic phases present within the sample interacting with one another and switching domain polarity distinct from one another. It also implies that if this is the case, in the zero field case, the two phases align ferrimagnetically, thus lowering M_R for the material as a whole and lowering magnetic performance as a permanent magnetic material, thus presenting as an undesirable material property.

In order to better understand these variations in extrinsic magnetic properties as a result of Ga addition into the alloy and make better comparisons to the work of Mix *et al.*, where extrinsic magnetic properties following saturation are not published, examination of the intrinsic magnetic variables calculated by Equation 2.12 is needed. These results are published in Table 5.5 and show that, despite an incomplete transformation occurring by the prescribed heat treatment for the MnAlGa alloy, the saturation magnetisation values are broadly comparable, with only a $(2.2 \pm 0.3)\%$ difference between the two systems. The significant change between the systems, however, is the increase in magnetocrystalline anisotropy energy, estimated LAS and expressed as the variable k. Recognising that this approach is an averaging effect as opposed to specific axis measurements accessible in thin film techniques but that the system is uniaxial in its easy axis, the significant increase in the system is clear when examining the hysteresis loops but results in an increase of $(45 \pm 5)\%$ by way of substituting Ga for C. Both samples were measured to maximum applied magnetic fields under that of the calculated anisotropy field, H_A, however. It could thus be inferred that the values of M_S, k and M_R may vary slightly from reported values but testing beyond $5570kAm^{-1}$ was not possible using the MPMS3 system and as such, there were few data points between $H_{A,\,Ga}$ and $M_{S,\,Ga}$ to fit under an LAS approach, meaning that points measured under the anisotropy field were also used and linear behaviour assumed within this region for linear fitting purposes.

Using the commonly understood maxima of $M_R \to 0.7M_S$ and that, by Brown's paradox, $H_C \to 0.2H_A$, we can calculate that the maximum extrinsic magnetic properties achievable for composition MnAlGa when transformed under the prescribed heat treatment of this chapter [88]. These maxima would thus be $M_{R,Max,Ga} = (356 \pm 1)kAm^{-1} = (6.34 \pm 0.02)M_R$ and $H_{C,Max,Ga} = (1056 \pm 8)kAm^{-1} = (10.24 \pm 0.08)H_C$. Whilst referencing the as-cast state as inefficient in terms of microstructural refinement to increase H_C and easy axis alignment to increase M_R, calculating these measurement to engineering maxima ratios allows one to assess the starting point for both systems. Comparing this ratio to that of the MnAlC standard, we find that $H_{C,Max,Carbon} = (8.6 \pm 0.2)H_{C,Carbon}$ meaning that the inclusion of Ga into the MnAl alloying system not only increases coercivity in the as-cast state but also increases the maximum achievable coercivity by $(51 \pm 1)\%$. Additional processing steps will be needed to achieve this increase but given the additional thermal stability demonstrated by Mix *et al.* for this ternary alloy in the τ-phase, hot deformation processing or aligned sintering operations may be possible, as may be grain refinement heat treatments in the τ-state without significant $\tau \to \beta Mn + \gamma_2$ decomposition.

Looking to remanence differences between the two systems, it is of note that the ratio between the two maxima achievable by the alloys is $(Ga/C)_{M_R} = (2.3 \pm 0.4)\%$, far less than the observed ratio between the two systems as previously stated. Given that both systems underwent similar casting and heat treatment processes, this implies that the replacement of C with Ga into the ternary system, decreases relative as-cast M_R. Referencing Schrefl

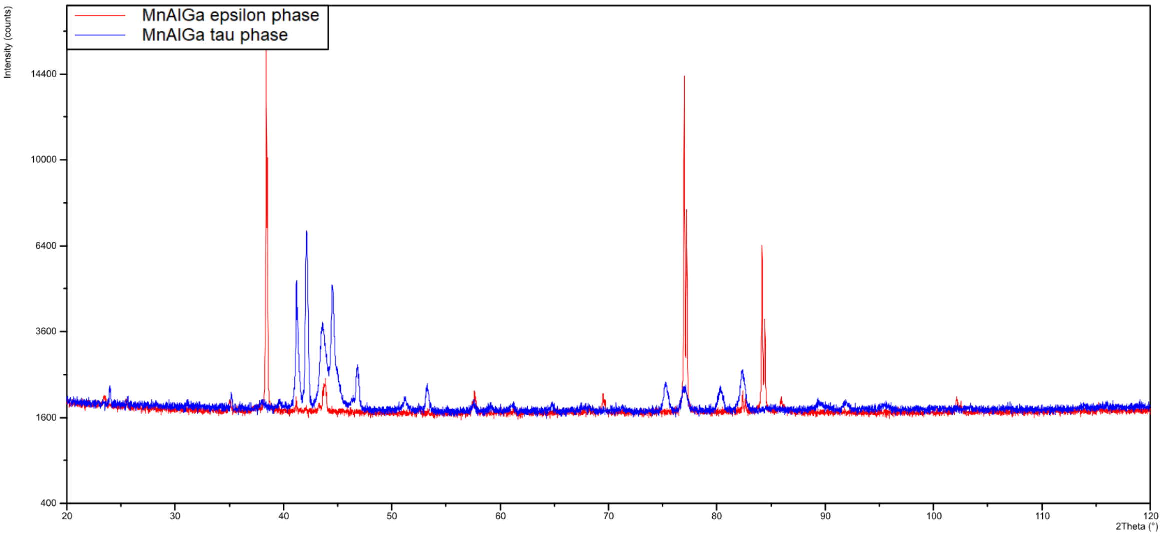

Fig. 5.19 2θ-XRD scans of MnAlGa before (red) and after (blue) the $450°C$ heat treatment for 40 minutes to induce the $\epsilon \rightarrow \tau$ transformation. The significant decrease in relative intensity for principle peak associated with the ϵ-phase in post-heat treatment data suggests that a significant phase fraction underwent transformation but given the presence of ϵ-phase peaks, peak convolution and the limitation of benchtop XRD for phase fraction analysis below 10% occupation, accurate phase composition calculations are significantly challenging.

and Fidler and Kronmüller (1994), this decrease in remanence and increase in coercivity could be attributed to an increase in grain size within the alloy suggesting that, given identical thermal histories between the two alloys and the variation between engineering maxima and observed extrinsic magnetic properties, that the difference between alloying with Ga rather than C can lead to an increase in grain growth during heat treatment [89]. Using the Scherrer equation as an estimation of grain size in recognition that nano-sized grains are expected and that an etching route for optical microscopy has not been published, one finds that the average grain size for MnAlGa and MnAlC is $(40 \pm 10)nm$ and $(30 \pm 2)nm$ respectively, assuming a spherical grain morphology approximation and that crystallite size is equal to grain size. The high relative error on the grain size of MnAlGa is related to the XRD data shown in Figure 5.19 and that, due to the incomplete transformation, not all τ-XRD peaks are measurable and there is overlap between ϵ and τ peaks. This data, however, does suggest that the Ga increases grain growth rates during heat treatment, leading to larger grains and thus a change in extrinsic magnetic variables.

Looking to explain the change in behaviour between the two states, Pareti *et al.* is once again consulted to investigate the effects of C addition on k. Whilst direct reporting on k is not made for the composition spectrum, M_S and H_A is reported, allowing one to

Alloy	$M_S\ [kAm^{-1}]$	$k\ [kJm^{-3}]$	$H_A\ [kAm^{-1}]$
MnAlGa	617 ± 1	2020 ± 20	5280 ± 40
MnAlC	631 ± 2	1390 ± 50	3500 ± 10

Table 5.5 Intrinsic magnetic properties for MnAlC and MnAlGa following an $\epsilon \rightarrow \tau$ transformation conducted by an anneal at $450°C$ for 40 minutes. M_S and k were extrapolated using Equation 2.12 with the associated errors derived from statistical variations from a linear best fit.

estimate k by Equation 3.3, assuming a constant density for MnAlC alloys as 4.3 $g\ cm^{-3}$ as measured experimentally for the MnAlC standard and assuming that minor fluctuations in composition do not create significant drift from this figure. Combining results published from Pareti *et al.*, Zhao *et. al* and Mix *et al.*, it is possible to build up a database to check these results against [47][50] [61]. The results of this database approach can be seen in Figure 5.20 and show that both samples outperform the material from at least one database. The MnAlC standard outperforms the work of Pareti *et al.* and is equal to that of Mix *et al.*, suggesting that the fabrication methodology in Mix *et al.* does not lead to a comparable advantage to that of magnetocrystalline anisotropy energies derived from the MnAlC system in this study.

It is clear, however that the MnAlGa sample outperforms all comparable samples and is only comparable to that of $Mn_{55}Al_{45}$ from the Mix *et al.* study. Given that the transformation is considered incomplete, it suggests that when compared to the transformation pathway suggested by Mix *et al.* shorter transformation times or cooler transformation temperatures may be considered better optimised in terms of inducing greater magnetocrystalline anisotropy in the structure. Following logic laid out in Zhao *et al.*, this increase in k could be interpreted as a more favourable lattice diagonalisation. i.e the c/a ratio decreases [50]. Given the production route employed by Mix *et al.* was to induce transformation by means of a controlled cool to an initial τ state with minority γ_2 phase present to then anneal at $500°C$ for 24 hours, one can infer that there is both greater activation energy and a longer time for slip systems within the MnAlGa alloy to activate, implying that any residual stress from the $\epsilon \rightarrow \tau$ transformation would be able to dissipate and the crystal structure able to relax to a local equilibrium state. In the case of the material discussed in this study, it is clear from the magnetisation as a function of time at constant applied field that the paramagnetic response of the MnAlGa alloy tested in this body of work was still increasing. Following the reasoning that paramagnetic response increases are proportional to saturation magnetisation increases in the system, this suggests that the system is still evolving at this time. Work discussed in Chapter 6.3.1 discusses further the optimisation of this process, but this may be corroborated by Figure

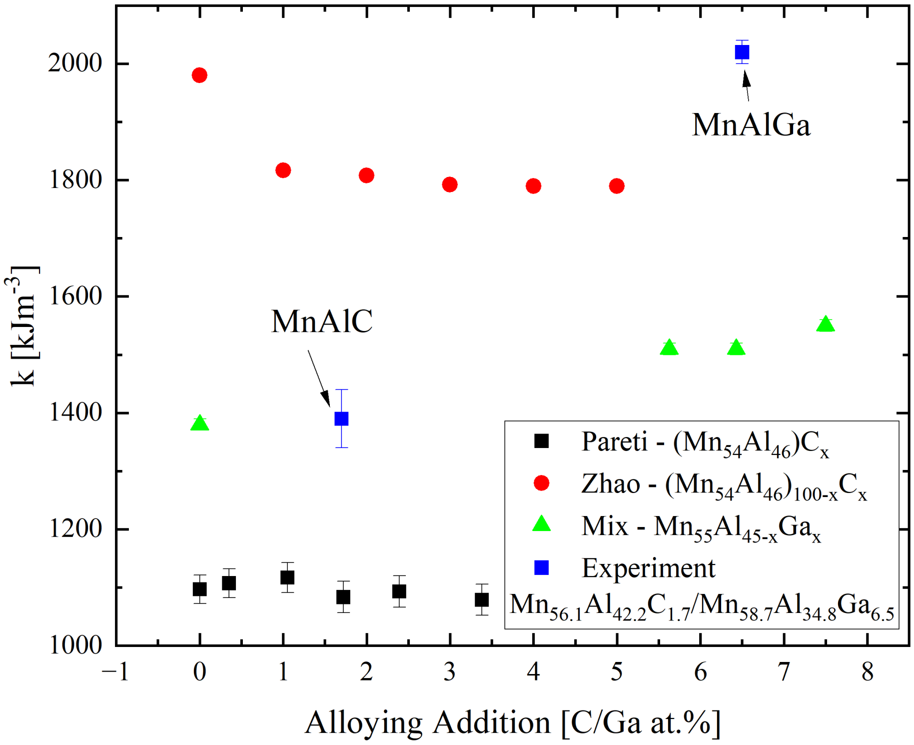

Fig. 5.20 Alloying addition percentage against estimated Magnetocrystalline Anisotropy Energy density for MnAlC/Ga group alloys, both from literature and experiment [47][50][61]

5.21 whereby a decrease in M_S is observed for the MnAlGa sample produced in this body of work when compared to that of Mix *et al.*.

Efforts were made to determine whether the MnAlGa sample annealed at 450$^\circ C$ for 40 minutes was in a strained state in a similar fashion to that of the ϵ-phase discussed in Figure 5.15 but it was found that the phase population had not yet reached a uniform state, with ϵ-phase peaks still measurable within the data. As such, peak identification from the XRD data displayed in Figure 5.19 proves challenging and any strain identified within the system would not be simply due to dislocations inherent from the metastable transformation but also due to the system being in a mixed phase state. As such, it is necessary to conclude that the intrinsic magnetic properties of MnAlGa as discussed in this body of work are not optimised for the composition, as a 100% τ-phase material cannot be confirmed to have been synthesised, with evidence from magnetisation behaviour during annealing suggesting that there is still further potential for τ-phase population increase.

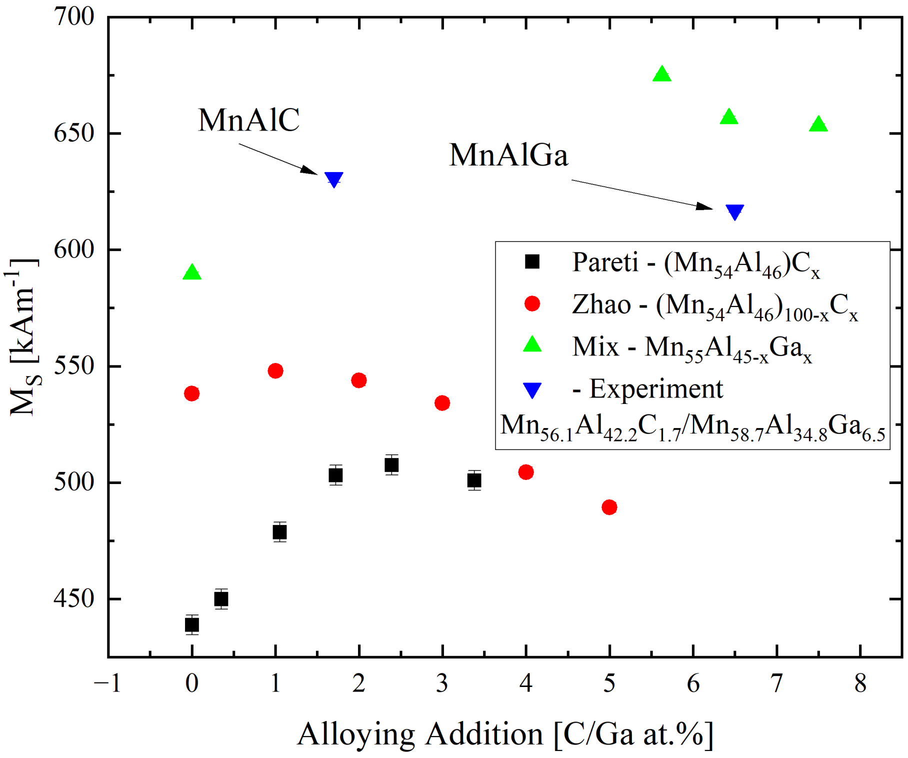

Fig. 5.21 Alloying addition percentage against estimated Saturation Magnetisations for MnAlC/Ga group alloys, both from literature and experiment [47][50][61]. This shows that both systems measured in this Chapter are outliers but whether this is due to Mn concentration or heat treatment conditions is challenging to determine.

Instead, longer annealing times and optimisation of this material must be conducted to ensure maximum properties are achieved.

5.4.4 Reflections on MnAlGa Alloys against MnAlC when using Short Heat Treatments

In conclusion, regarding the testing of cooler and shorter annealing times of MnAlGa alloys to that of Mix *et al.* it can be shown by this study that the $\epsilon \rightarrow \tau$ transformation is still precipitated from a quenched high temperature state by annealing at $450°C$ for 40 minutes [61]. Initial comparison between MnAlGa and the previously measured MnAlC standard show that there is little variation in the precursor state from a paramagnetic frame of reference, with only a variation of $(5 \pm 1)\%$ between the paramagnetic states of the two alloys. This variation is attributed to the variation in Mn content between the two alloys, with the MnAlGa alloy containing Mn concentrations of 58.7 $at.\%$ and the MnAlC standard containing Mn concentration of 55.9 $at\%$. No ferromagnetic behaviour indicative of MnGa intermetallic phase formation is present, implying that the initial phase population is 100% ϵ-phase to the accuracy of Rietfeld refinement software and benchtop XRD equipment. Further, it was shown that the addition of soluble Ga into the HCP lattice structure caused a lattice parameter change, with a decrease in diagonalisation relative to a binary MnAl alloy of the same Mn concentration and an expanded cell volume. This is interpreted as being the reason behind the variation in paramagnetic susceptibilities observed in Figure 5.13.

Moving to the annealing behaviour, two deviations from the MnAlC standard were observed. The first is that the $M(T)_{\epsilon-phase}$ behaviour of the MnAlGa alloy varied when compared to either explored MnAlC alloy within this body of work. MnAlC alloys explored in this work see an initiation of the $\epsilon \rightarrow \tau$ transformation at approximately $100°C$ with an increasing magnetisation until reaching a maxima, interpreted to be a phase-dependent T_C, between $(250-350)°C$ and the commencement of a new paramagnetic $M(T)$ relationship relative to that discontinuity. MnAlGa does not reflect this behaviour when measured, instead seeing transformation induced at approximately $60°C$ and two magnetic behaviour transition points visible between $(400-450)°C$. This variation is further expanded when moving to the annealing behaviour at $450°C$, with the increase in paramagnetic magnetisation as a function of annealing time being greater for MnAlGa when compared to MnAlC. At 40 minutes, both MnAlC alloys investigated in this study had reached near steady state magnetisations where as there was still a positive differential observed for MnAlGa.

On cooling, the increased T_C was observed for addition of Ga over C, but this increased temperature was greater than that observed for similar alloys by Mix *et al.* [61]. Further, intrinsic magnetic properties deviated from those observed from Mix *et al.* in a beneficial manner, namely the increase in magnetocrystalline anisotropy energy as the detriment to saturation magnetisation. This was interpreted as an increase in microstrain within the lattice for material produced experimentally, which would have been removed in the reference due to the transformation in longer and higher temperature heat treatments. As such, it may prove optimum to develop heat treatments such that microstrain is present within MnAlGa ingots to increase k and decrease M_S as a mechanism to increase H_C and thus BH_{Max}, bringing the MnAlGa system closer to fulfilling the Gap Magnet Criteria listed in Table 1.1 and becoming an industrially viable product for permanent magnetic material application specifications.

5.5 Conclusions

In conclusion for this chapter, three key experimental goals were achieved. The first was in-house fabrication of an MnAlC standard utilising cooler and shorter annealing methodology than stated in literature. The reasoning behind this is that there was a desire to reduce heat treatment time and temperature both from an industrial perspective and to limit potential grain growth. The MnAlC standard was shown to reach a steady state in terms of ferromagnetic population by (15 ± 1)min if one assumes that paramagnetic response in the $\epsilon + \tau$ system is dominated by the τ phase given the temperature of measurement is $\approx 70°C$ higher than the measured T_C for the resulting system of $(270 \pm 10)°C$. This would imply that for MnAlC systems, the longer and higher temperature heat treatments prescribed in literature may be unnecessary to ensure maximal transformation and intrinsic magnetic properties. The benefits of reducing this transformation time is that it becomes possible to maintain microstrain in the crystallographic system resultant from the metastable transformation or any deformation of the parent state prior to heat treatment as well as minimising time spent at temperature that could precipitate grain growth and thus a reduction in extrinsic magnetic properties. Thus, it can be considered that this first objective was achieved and that it has been successfully been demonstrated that $\tau - MnAl$ can be manufactured at the University of Sheffield using non-specialised laboratory equipment.

The second experimental goal was the investigation of the MnAlBi system to see whether Bi would alloy with either the ϵ or τ phases, potentially increasing intrinsic magnetic properties. The results of this investigation were that at no point during the casting or heat treatment cycle taken from the cycle derived for the MnAlC standard does Bi alloying with the majority MnAl phases occur. Instead, intergranular Bi forms with a reaction between the supersaturated Mn and Bi forming LTP-MnBi occurring at Bi-MnAl interfaces. It was then found through a composition study that, assuming the as-cast state is representative of interface phase formation, that LTP-MnBi phase formation is broadly invariant with Bi concentration within the tested doping range of $(4.5 < Bi\ at.\% < 6.9)$ with the phase population theorised to be related instead to MnAl particle size and thus total reactant surface area between the two majority phases needed for the intermetallic reaction. Therefore, whilst it can be assessed that the second objective of this chapter has been met, the measured results are such that explored Bi concentrations do not provide a practically usable benefit for $\tau - MnAl$ applications. Further work may be orientated at measuring lower concentrations to determine a maximum Bi concentration such that the decrease intrinsic magnetic variables is tolerable compared to the increase in H_C.

As an emergent stretch goal for the second objective of this chapter, an alloy of $Mn_{60.3}Al_{36.7}Bi_3$ was investigated further to determine whether LTP-MnAl formation could occur and lead to hysteresis at lower annealing temperatures or whether Bi inclusion in the alloy would change $\epsilon \rightarrow \tau$ transformation rates. It was found that significant transformation occurred at annealing temperatures at or above $400°C$ but that multiple samples taken from material annealed at $450°C$ demonstrated intrinsic magnetic properties over such a range that the highest recorded measurement of M_S was approximately 330% greater than the lowest. Examination with BSE-SEM showed that Bi-induced features were on the scale $(10 - 100)\mu m$ and as such, the density of these features may not be considered isotropic on the millimetre length-scale for samples measured by VSM, explaining the significant variability for material exposed to the same heat treatments from the same casting. Whilst this does not provide any direct material development benefits, improving magnetic performance, it does increase understanding of the MnAl and Bi interactions during alloying and annealing, showing that even at concentrations of Bi $3at.\%$, homogeneous compositions across samples, and thus reproducible properties, cannot be maintained and so an upper alloying limit must be determined in order to assess at what point the material can be considered consistent across samples.

The final objective of this chapter was to assess the repeatability of results surrounding the MnAlGa ternary system discussed by Mix *et al.* when produced by a shorter and cooler heat treatment [61]. The previously published work induced the $\epsilon \rightarrow \tau$ transformation by means of a $500°C$ anneal for 24 hours. Whilst this anneal demonstrates that full transformation can occur in the material, it does not investigate whether this annealing time is a minimum required heat treatment. As such, using a 40 minute heat treatment at $450^{\circ}C$ shown to work for the MnAlC standard as the heat treatment for MnAlGa, the ternary system was investigated in comparison to MnAl, MnAlC and MnAlGa results in literature.

It was found that the initial precursor state for MnAlGa shows variation against that of MnAl ϵ-phases of similar Mn concentrations, with a reduction in diagonalisation occurring with the inclusion of Ga. Further, in contrast to work published by Mix *et al.* no secondary phase is detectable in Figure 5.14 from peak identification [61], implying that the Ga is occupying lattice sites within the HCP ϵ-phase. $M(t)$ during the $\epsilon \rightarrow \tau$ transformation heat treatment for MnAlGa varies from that of MnAlC, with a positive magnetisation differential being observed for MnAlGa at the end of the heat treatment, implying that transformation was still occurring, corroborated by the precursor peak presence in XRD scans of quenched material visible in 5.19.

Extrinsic magnetic properties of MnAlGa following this heat treatment were greater than those reported for MnAlC alloys and the magnetocrystalline anisotropy energy measured was greater than that reported by Mix *et al.* at $k_{MnAlGa} = (2020 \pm 20) kJm^{-3}$ though the M_S was lower than similar compositions reported in literature. Whilst this can be contributed to a decrease in overall ferromagnetic phase population, the increase in k may also be interpreted as a change in lattice parameters for the τ phase should the Ga be in solid solution and occupying sites within the $L1_0$ structure. Refined measurements of this lattice shift require accuracy within the XRD peak data that must be derived from fully transformed materials due to the corroboration of the ϵ-phase <002> peak and τ-phase <110> peak leading to overlap and uncertainty in peak position. And so, it can be confirmed that the third objective was also met, demonstrating that MnAlGa could be manufactured using shorter and cooler transformation heat treatments than literature though that there is optimisation work to be completed to ensure optimum intrinsic magnetic properties for future microstructural refinement studies to improve extrinsic magnetic properties and develop MnAlGa into an industrially viable low cost permanent magnetic material.

In conclusion for the three systems, it was demonstrated that current annealing approaches for MnAlC utilise heat treatments that are both unnecessarily high temperature and longer than required to see equilibrium phase transformation, with approximately 15 minutes at $450^{\circ}C$ leading to stabilisation of paramagnetic response to applied field, interpreted to be a stabilisation of phase structure and dislocation transport at temperature such that both maximum τ-population had been achieved and residual stress from metastable transformation dissipated through dislocation transport. The same methodology applied to MnAlBi samples showed that Bi is not a suitable alloying additive at concentrations of 3 $at.\%$ or above, due to it not alloying with any MnAl phase, instead forming interface-driven intermetallics with supersaturated Mn. MnAlGa is shown to undergo transformation at temperatures lower than that published by Mix *et. al* and still retain extrinsic magnetic properties greater than that of MnAlC systems, though work must be conducted to further refine heat treatment times to maximise τ-phase yield and internal stress reduction.

In terms of fulfilling the overall research goal of designing a rare-earth free permanent magnetic material that can fulfill the gap magnet criteria, the major learning points from the work shown in this chapter are: current heat treatment practices for MnAlC systems are longer and higher temperature than necessary, leading potentially to a decrease in extrinsic magnetic properties as a result; the inclusion of intergranular Bi may increase H_C at the expense of M_S and M_R and that MnAlGa can be produced by a quench and anneal process but that it must undergo potentially longer heat treatments than MnAlC alloys in order to fully complete the $\epsilon \rightarrow \tau$ transformation. The two streams of work that stem out of this research are the development of the MnAlGa alloy system and further investigations into low-Bi content MnAl alloys.

Chapter 6

Composition and Processing Optimisation

6.1 Motivation and Experimental Goals

Following on from the previous chapter, where the manufacture of tau-phase MnAlGa was demonstrated for cooler temperatures than literature, the research goals of this chapter were defined as:

1. Measure the composition space $Mn_{50-60}Al_{balance}Ga_{0-10}$ to compare against data published by Mix *et. al.* to assess the optimum Ga alloying content for intrinsic magnetic property increase [61].
2. Determine the dependency of intrinsic and extrinsic magnetic properties of an optimised MnAlGa system on transformation heat treatment time and temperature
3. Develop an optimised transformation heat treatment for a targeted MnAlGa composition such that M_R and H_C are maximised

The first objective is motivated by economics. At the time of writing, the cost of materials to manufacture a kilogram of $Mn_{55}Al_{45}$ is approximately 0.66$\$kg^{-1}$ where as a kilogram of $Mn_{55}Al_{39}Ga_6$, a composition near that reported by Mix *et. al.* when first discussions of the ternary system were published, would cost approximately 22.45$\$kg^{-1}$, estimated by referencing stock exchanges for high purity reagents per kilo, understanding that this is subject to market changes [61]. When referencing Table 1.1, this would price said ternary alloy as a Type C Gap Magnet. Whilst reported values of T_C and k for the system are sufficient to meet the material requirements, the required minimum value of $M_S^C = 800kAm^{-1}$ is approximately 22% higher than the reported value for the ternary system as a single phase material, thus meaning that it cannot qualify as a Type C Magnet. As such, it is useful to investigate whether Ga-lean compositions can achieve similar intrinsic magnetic properties as to fulfil the Gap magnet requirements whilst reducing material costs, becoming an industrially viable permanent magnetic material from a cost perspective.

To fulfil the second objective, it is of note to recognise that as a metastable system, it is insufficient to only optimise the composition of the alloy to maximise intrinsic magnetic properties. An optimum annealing temperature must be determined to ensure the activation of appropriate transformation systems, without leading to equilibrium transformations within the material. An ideal system would not see significant change in intrinsic magnetic properties due to the thermodynamic stabilising effects of Ga additions into the system. As such, rate of change of magnetisation under annealing conditions can be considered a sufficient metric for assessment, with ideal annealing temperatures tending to $\frac{dM}{dt} \rightarrow 0$ over time and a limit determined by temperatures over which where this differential becomes negative, indicative of the undesirable $\epsilon \rightarrow \gamma_2 + \beta$Mn transformation.

Concerning the third objective, although the system is reported to be thermodynamically stable below expected annealing temperatures, it is well understood that extrinsic magnetic properties are largely influenced by the microstructure of the magnetic material, as discussed in Section 2.3. As such, an optimum annealing time at a given temperature should exist where maximum intrinsic properties have been established through the $\epsilon \rightarrow \tau$ transformation, but also extrinsic properties have been set by the associated grain growth, re-crystallisation and dislocation transport through the system under anneal, changing grain-grain interactions and thus affecting H_C and M_R as a result. Investigations into M_S and k changes as a result will also be of interest, as microstrain is removed from the system by dislocation transport, thereby causing changes in lattice parameters and bond lengths, though this is not the primary motivation behind this work.

This work will not address optimisation of the as-cast to ϵ-phase material processing, nor will it go into the optimisation of the casting process of the material ingots. Whilst the initial conditions for the material such as grain size and homogeneity of dopant elements will affect the final extrinsic and intrinsic magnetic variables respectively, it is assumed that all as-cast alloys in the tested MnAlGa series have similar grain sizes such that it does not drastically affect intrinsic magnetic variables, and SEM/EDX imaging shows that Ga is evenly dispersed throughout the material, not forming secondary phases within the alloy. As such, these points of investigation are considered only appropriate after initial investigations and proof-of-concept work has been completed as goals for potential industrialisation of any resultant compositions that meet Gap Magnet requirements, as established in Table 1.1.

6.2 Composition Opimisation of MnAlGa Alloys for Low Ga Content and Fixed Heat Treatment

To investigate the effect of Ga content on the intrinsic magnetic properties of $Mn_{50-60}Al_{balance}Ga_{0-10}$, 8 compositions were cast across this range in accordance with methodology laid out in Section 4.1.1. The reagents used were Mn flakes at 99.95% purity, Al shot at 99.95% purity and liquid Ga at 99.995% purity. Samples were combined prior to melting by liquid Ga and the Ga content specifically targeted to liquefy and encapsulate the Mn and Al material. This was intended to provide a more even heating to the Mn and Al reagents, attempting to prevent Mn evaporation from overheating or Al ejection from thermal shock though composition drift was still observed in all samples.

When examining the composition drift of the 8 samples, it is worth noting that only one of the three elements exhibits volatility under the conditions present within the arc melter; manganese. It can be assumed that any composition drift in Ga or Al can be attributed to material leaving the crucible during the melting procedure alongside Mn composition drift. The compositions can be seen in Table 6.1 and show that significant drift took place within the system, with each element varying by $\approx (1-2)at.\%$ from the intended composition. Whilst this could partly be explained by the production of surface oxide reducing the mass of available alloying elements within the system when comparing reagent to puck, the dominating factor in the system does not seem to be Mn evaporation during the melt procedure. This can be shown when examining the resulting alloy ratios, where the majority of the alloys see an increase in the proportion of Mn in the system, suggesting that Al ejection from the melt pool is the primary factor around composition drift.

It can also be noted that in all alloy cases, barring G_0 where Ga is not present, the concentration of Ga in the system increases. This can be explained by the low melting point of Ga, $29.770°C$ [90], being near room temperature. Therefore Ga would be rendered into its liquid state early in the alloying process, reducing the chances of its ejection from the crucible. Thus, the increase in Ga concentration is a product of the reduction of the quantity of all other alloying elements within the system (which is in turn implied to have taken place during the heating stage, while these elements are still in the solid state, due to ejection of unmelted material from the crucible under the action of the arc).

	Pre Melt [at.%]			Post Melt [at.%]		
Sample composition #	Mn	Al	Ga	Mn	Al	Ga
Ga_0	59.8	40.2	0	52.58	47.42	0
Ga_1	57.5	41.4	1.1	58.8	39.9	1.3
Ga_2	57.1	40.9	2.0	57.9	39.7	2.4
Ga_3	56.0	39.8	4.2	58.2	37.3	4.5
Ga_4	57.3	36.7	6	59.9	33.6	6.5
Ga_6	56.4	40.7	2.9	57.1	39.5	3.4
Ga_7	57.9	37.7	4.5	60.2	34.9	4.9
Ga_8	58.3	32.0	9.7	57.0	31.4	11.6

Table 6.1 Atomic mass calculations derived from reagent mass at melt and EDS measurements respectively. It is of note that a $\approx (1-2)\%$ drift can be observed in all elements within each alloy when compared to compositions calculated from reagent mass. The mass of the reagents do not count for the mass of oxide layers lost in the melt process, however.

When considering the distribution of concentrations within the alloying system, composition drift saw the distribution of Mn and Ga in the system skew to Mn heavy compositions, as shown in Figure 6.1. The impact of this is discussed later in this section, but shows that optimising this composition is less trivial than anticipated, owing to the challenge of achieving exact compositions through arc melting. It also shows that compositions doped with Ga under Mn 57 at.% have yet to be explored and could represent an area of further investigation into the system.

6.2.1 Transformation

Using the MPMS3 Oven module, it was possible to measure the magnetisation of samples as they underwent annealing. As defined in Equation 3.1, an increase in magnetisation can be interpreted as the $\epsilon \rightarrow \tau$ transformation taking place asuming similar Curie constants for both materials as the paramagnetic susceptibility for the τ-phase near T_C is assumed to be greater than that of the ϵ-phase at the same temperature. As seen in Figure 6.2, the addition of Ga clearly has an effect on the rate of this change, and thus by inference, this transformation. Looking at the undoped sample, observed magnetisation appears to peak after approximately 20 minutes, before undergoing decay, interpreted to be the $\tau \rightarrow \beta Mn + \gamma_2$ transformation to equilibrium states, though this is in disagreement with Section 5.2 but given the differing Mn concentration in both alloys, this can be accounted for as an Mn dependent metastability feature. It is of note that other compositions vary wildly in their apex of magnetisation throughout the transformation, with $Mn_{57.9}Al_{39.7}Ga_{2.4}$,

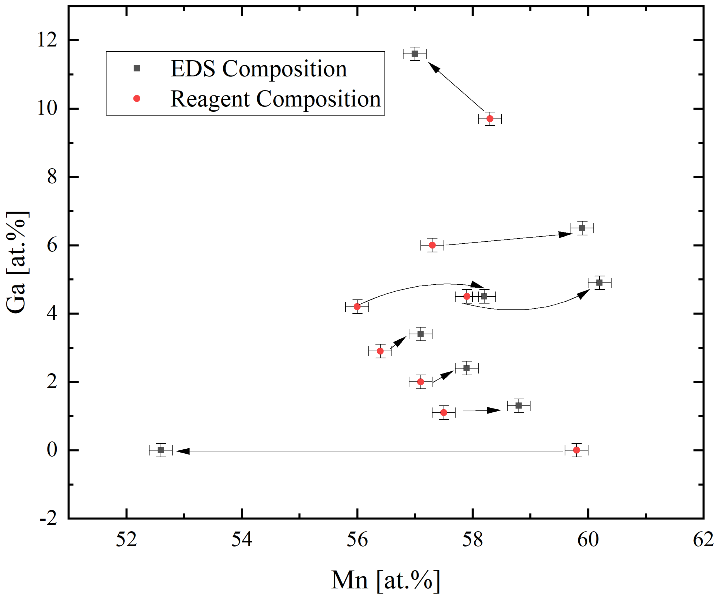

Fig. 6.1 The compositions of the 8 alloys investigated within thus study plotted by Mn and Ga concentrations. The variation in concentrations allows an investigation into which species is dominant in improving magnetic behaviour.

$Mn_{57.1}Al_{39.5}Ga_{3.5}$ and $Mn_{57}Al_{31.4}Ga_{11.6}$ not reaching a maximum within the annealing time. No pattern emerges when sorting by any element concentration against magnetisation apex, implying that the change in behaviour is more complex than the change of one of the alloying elements at this temperature but specifically that the addition of Ga can slow the rate of $\epsilon \rightarrow \tau$ transformation as evidenced by only 5 of the 8 measured compositions reaching maxima by 120 minutes of annealing at $430°C$.

6.2.2 Saturation Magnetisation and Magnetocrystalline Anisotropy Energy as a Function of Composition

Using the Law of Approach to Saturation theory and fitting by Equation 2.12, the M_S and k values for each composition were calculated and can be seen in Table 6.2. When compared to the Coey criteria in Table 1.1, it is clear that there is a disparity in how well different compositions meet the intrinsic magnetic criteria. All compositions except Compositions Ga_7 and Ga_8 can be classified as Type A gap magnets as defined by both M_S and k. Individual cases measured approached within 10% of the M_S criteria for a Type B candidate, though these cases were sporadic and considered to be outliers. When

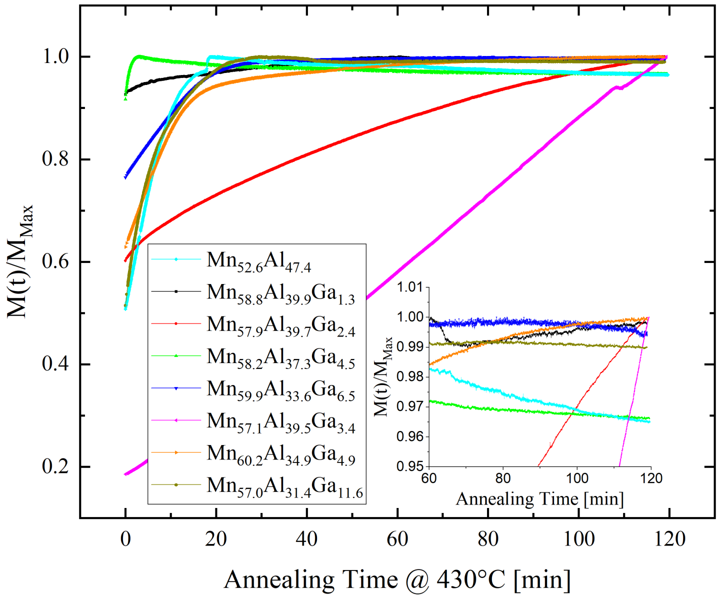

Fig. 6.2 A plot of magnetisation normalised against the maximum observed value for each composition against time for samples undergoing $\epsilon \rightarrow \tau$ transformations at $430°C$. It is clear that the change in composition and addition of Ga changes this transformation, with only 5 of the compositions reaching a maxima within the annealing time at this temperature and the apex of each transformation being measured within a range of approximately 5 to 115 minutes. The Inset is the same data, focused on the interval between 60 to 120 minutes

considering k distributions across the composition series, it is clear that all measured candidates surpass even the Type C criteria for Gap Magnets, implying that the measured systems have sufficient anisotropy energy to be engineered into hard magnets. This is reflected in the calculated anisotropy fields H_A, as determined by Equation 3.3, and the resulting high values.

Given that all samples included in this section underwent transformation via a 2 hour anneal at $430°C$, this suggests that there is room to optimise this process by composition to maximise values of M_S to approach criteria for Type B & C materials. All compositions have the potential to qualify as Type C when assessed using k as a criteria and M_S can be assessed as an expression on ferromagnetic phase population and thus is dependent on the annealing process. For many compositions, measurements taken during the annealing process indicate that beneficial transformations were still occurring within the alloy at the end of the heating window. The $L1_0$ phase population for each alloy was

Sample composition #	$M_S\,[kAm^{-1}]$	$k\,[kJm^{-3}]$	$H_A[kAm^{-1}]$
Ga_0	590.6 ± 0.3	1976.3 ± 0.3	5326 ± 3
Ga_1	570.4 ± 0.1	2025.6 ± 0.1	5651 ± 1
Ga_2	606.6 ± 0.1	1790.5 ± 0.1	4698 ± 1
Ga_3	572.0 ± 0.1	1697.6 ± 0.1	4723 ± 1
Ga_4	587.5 ± 0.1	1810.8 ± 0.1	4905.1 ± 0.6
Ga_6	600.5 ± 0.1	1861.1 ± 0.1	4933.0 ± 0.5
Ga_7	548.4 ± 0.1	1878.6 ± 0.1	5452 ± 1
Ga_8	360.1 ± 0.1	1123.7 ± 0.1	4966 ± 1

Table 6.2 A table of intrinsic magnetic properties for τ-phase MnAlGa group alloys. H_A is interpreted as a theoretical maximum coercivity for a Stoner-Wohlfarth particle comprised of each composition with geometry such that $\mathcal{N} = \frac{1}{3}$ as defined by Equation 3.3. As set by Brown's Paradox, achieving 20% of this value is considered a practical maximum for engineering coercivity in a bulk material.

calculated post anneal by Pawley Refinement through the GSAS-ii software package and can be seen in Figure 6.3 [74]. The accuracy of phase population calculations should be interpreted to ±3% given the use of benchtop equipment and in-plane scans but secondary phases where observed were seen to be the remaining ϵ-phase, indicating incomplete transformation. When compared to Figure 6.4, some correlation can be seen between areas of higher observed M_S and that of more complete transformation. This then suggests that alloys of higher Ga saturation may achieve Type A criteria following optimisation of the Time-Temperature-Transformation process.

In order to assess whether variations in Ga or Mn content within the alloy dominated changes in observed M_S, a contour plot of the three variables was generated, as seen in Figure 6.4. It can be seen that for a 2 hour anneal at $430°C$, the addition of Ga has a measurable effect in lowering the observed value of M_S when compared to the effect of varying Mn concentrations. The black line on the figure is to denote compositions with sufficiently high M_S such that they would qualify as Type A Gap Magnets and suggests that, whilst there is some observed dependence on Mn concentrations, the Ga component of a potential alloy must not exceed 4 $at.$% for Mn-rich compositions or 1 $at.$% for Mn-lean compositions. Given previously published work on Ga-heavy compositions by Mix *et. al*, this might suggest that either the annealing process for Ga_8 needs significant optimisation work to bring to reported measurements for a Quench and Anneal production process or that it may not be possible to achieve a single phase $L1_0$ composition using this technique, with it only possible using the 'controlled cooling' technique, which presents significant engineering challenges for scale up beyond laboratory sample sizes [61].

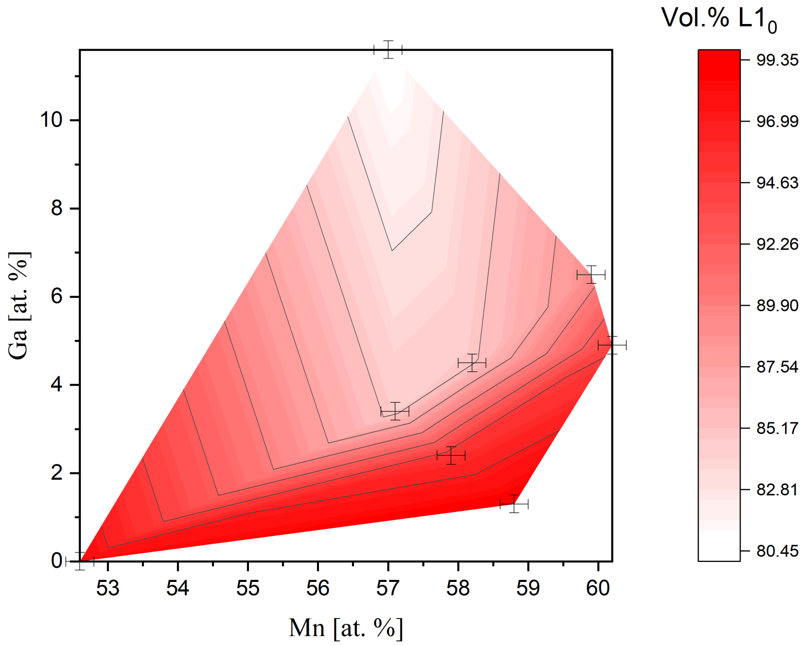

Fig. 6.3 A colour map of $L1_0$ phase population against composition for samples annealed at 430°C for 2 hours. The general trend in the dataset suggests that the addition of Ga into the system retards the $\epsilon \rightarrow \tau$ transformation under these conditions, implying a change in temperature or anneal duration is necessary to approach single phase states.

Whilst these figures could be adjusted for $L1_0$ population and scaled accordingly, uncertainty in the phase population calculations would increase the noise in this data set. Given the non-ferromagnetic phase population measured was in the range of approximately $(1-20)\%$, the error on said corrections would be significant on measurements made on $L1_0$-rich compositions. Further, given over-annealing would lead to stress reduction in the system, lattice parameter changes as a reduction of microstrain and thus shifted intrinsic properties, each alloy would need to be optimised individually for a total comparison which is beyond the scope of this body of work.

An example of this transformation time not being optimised can be seen in the behaviour of composition Ga_2, which saw an increase of $(11.53 \pm 0.04)\%$ in observed M_S between initial measurements following a 2 hour anneal at 430°C and measurements taken following Zero-Field Cooling and Field Cooling measurements, resulting in 2 heating cycles from $(27-527)°C$ lasting 160 minutes. Using this observed value for composition Ga_2, $M_S = (605.0 \pm 0.1) kAm^{-1}$ and $k = (1779 \pm 8) kJm^{-3}$, the composition would have transitioned into a Type A Gap Magnet, albeit with a decrease in observed anisotropy. Whilst other samples that did not undergo this measurement range outperformed this specific

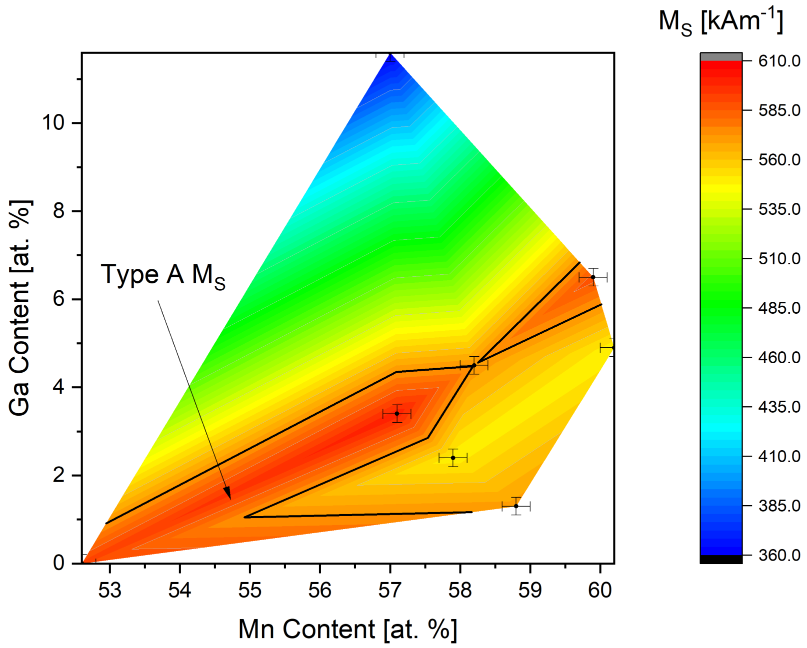

Fig. 6.4 A contour plot of M_S against Mn and Ga alloy composition. Whilst the contour plot was only plotted using 8 compositions, it does predict an island of potential exploitation in the range $Mn_{(59-60)}Al_{(34-36)}Ga_{(5-6)}$. The error on the boundaries of this region, however, is uncertain and this does not represent an necessarily optimised transformation for the composition. Type A M_S criteria is defined as $M_S^A \geq 570 kAm^{-1}$.

sample, this behaviour was observed across all samples doped with Ga to varying degrees. This further demonstrates that targeted compositions need separate Time-Temperature-Transformation optimisations, implying that as well as the Mn the Ga content affects the $\epsilon \rightarrow \tau$ transformation mechanics when considering single phase formation.

When considering the distribution of k values across the measured composition space shown in Figure 6.5, one can begin to theorise maxima for extrinsic magnetic material properties by composition. M_R is always less than M_S but fundamentally derived from said variable, with an upper engineering limit, there is potential for a $(200-300)\%$ increase in M_R. When considering H_C increases, the micromagnetic-derived, microstructure approximation Kronmüller equation

$$H_C = \alpha H_A - N_D M_S = \alpha \frac{2k}{\mu_0 M_S} - N_D M_S \tag{6.1}$$

can be used to assess theoretical limits, using previously defined variables, with $(0 < \alpha < 1)$ defined as an H_A-dependent coupling constant and $(0 < N_{eff} \lessapprox 1)$ as an

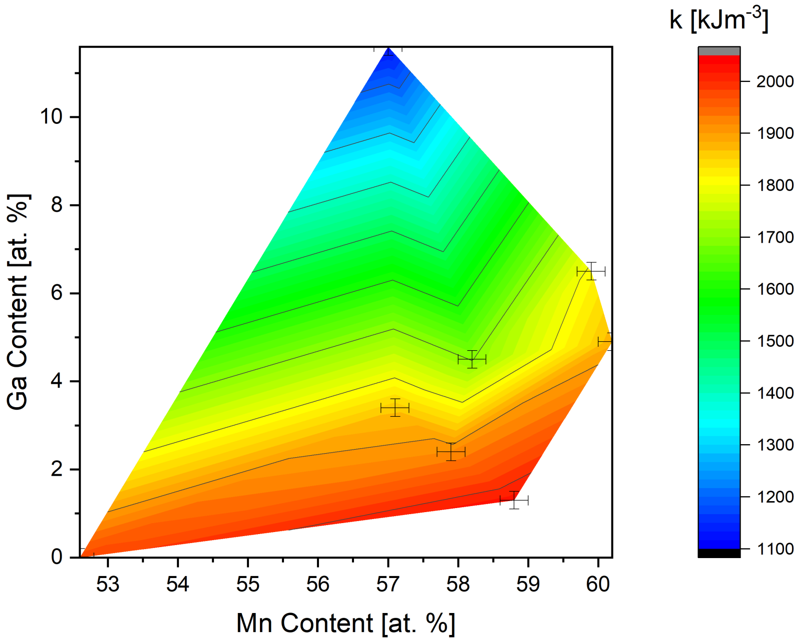

Fig. 6.5 A contour plot of k against Mn and Ga alloy composition. All tested compositions exceeded the Type C Gap Magnet k criteria of $k_C \geq 1000 kJm^{-3}$.

effective demagnetising shape factor. Using these constant limits, one can make a general estimation that an order of magnitude of growth in coercivity can be expected following sufficient development [91]. In practice, Brown's paradox implies $\alpha < 0.01$ in as-cast metals and only approaching $\alpha \rightarrow 0.3$ from sophisticated processing of certain alloys, significantly limiting development [92]. As a result, a general engineering limit of $H_C = 0.2H_A$ is assumed to be a goal for developing permanent magnetic systems [88]. With this in mind, it could be expected that the MnAlGa system could achieve values of H_C in excess of $1000kAm^{-1}$, which is within the range of NdFeB or SmCo systems and an order of magnitude higher than observed for the as-cast samples discussed. This is further discussed in Section 6.2.2.

In Figure 6.6, one can see the calculated hardness values, κ, for the MnAlGa range tested in this body of work. All tested compositions show $\kappa > 2$, and thus all compositions can be considered hard materials. When compared to material parameters published in "*Perspective and Prospects for Rare Earth Permanent Magnets*", Coey (2020), the addition of Ga into the system increases the calculated values of k against an undoped system and thus increases the magnetic hardness of the alloy [17]. Further, when compared to the data for $Mn_{55}Al_{38.57}Ga_{6.43}$ as published by Mix *et. al.*, it can be seen that all

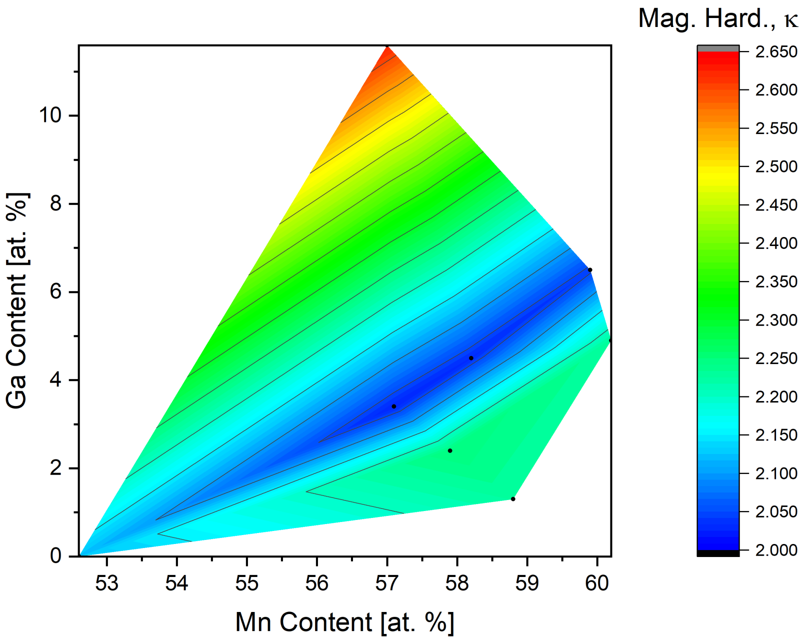

Fig. 6.6 A contour plot of the magnetic hardness parameter κ, as defined by Equation 2.20, against Mn and Ga alloy composition. All measured compositions can be considered 'hard' ferromagnetic materials given that $\kappa > 2$.

measured compositions except Ga_8 see a $(20-30)\%$ increase against the reported value of MAE for the system of $K_1^{eff} = 1.51MJm^{-3}$ if one assumes that similar corrections for uniaxial symmetry have been made when the data was calculated using the Law of Approach to Saturation [61]. Further, looking at the calculated value of H_A for said reported composition of $\mu_0 H_A^{Ga=6.4} = 4.58T$, it can be reported that all measured compositions in this series of experiments are in the range of $(5.935 \pm 0.001 \leq \mu_0 H_A^{MnAlGa} \leq 7.102 \pm 0.001)T$ and thus suggest a greater anisotropy field can be generated across the τ-phase structure for lower Ga doping levels when produced through a Quench and Anneal technique.

It is of note, however, that these calculations are not corrected for phase population and are treated as a material average due to associated errors with phase population calculations on these alloys as previously explained. This is highlighted when comparing calculated M_S values for the MnAlGa composition series explored in this work against that published by Mix *et. al.*. $Mn_{55}Al_{38.57}Ga_{6.43}$ in said body of work had an associated value of $M_S = 796kAm^{-1}$ (3s.f.) where as observations for the explored series were in the range of $(360.1 \pm 0.1 \leq M_S^{MnAlGa} \leq 600.6 \pm 0.1)kAm^{-1}$. Treating the lowest value, resultant from measurements of Ga_8 which showed significant secondary phase production when examining peaks in the 2θ-XRD patterns of the transformed system, these resulting measurements of M_S are approximately 75% of that reported by Mix *et. al.* for a ternary system but also within range of or exceeding measurements for $Mn_{55}Al_{45}$ in the same paper of $M_S^{MnAl} = 590kAm^{-1}$ (3 s.f.). Work referenced in Section 3.1.2 shows that moving away from a stoichiometric balance within the alloy has a negative effect on the M_S of the resultant material, as Mn occupying the $(\frac{1}{2}, \frac{1}{2}, \frac{1}{2})$ site within the lattice causes an anti-ferromagnetic bond length and thus decrease in unit cell magnetisation [47]. Given that all samples examined here apart from the undoped composition, which is in agreement with the published value for M_S^{MnAl} are Mn-heavy by comparison, it can be said that even $(1-5)$% Ga-doping can have a positive effect on the M_S of the ternary system following transformation when compared to that of the binary MnAl system.

Stoner-Wohlfarth Limit of Coercivity by Composition

Whilst the optimisation of the annealing process is not discussed, from the values reported one can make an estimation to the material coercivity the compositions could achieve given the theory outlined in Equation 3.3 defined as $H_A = H_{C,S-W}$. This theory is limited as it assumes that the particle in question is a mono-domain particle of geometry such that $\mathcal{N} = \frac{1}{3}$ (i.e a perfect sphere [93]) but if one assumes that any increase in size to a multi-domain state will see a decrease in H_C and recognises that $\mathcal{N} = \frac{1}{3}$ represents an optimum geometry for coercivity given $0 \leq \mathcal{N} \leq 1$, this can be interpreted as a limit to which optimisation could approach for a material, recognising that any value for a bulk material would never reach this value. For a sample to reach this value, it would need to be a geometrically perfect sphere and single crystal, which does not reflect the polycrystalline samples cast in these experiments not the sample geometry measured. In the case of gas atomisation, it may be possible to create such particles morphologically and of the correct dimensions but in the case of cast samples, this calculation is simply to provide a theoretical upper limit that is in no way intended to be a practically achievable result.

All calculated values of $H_{C,S-W}$ exceed that of approximately $4500kAm^{-1}$ which is an order of magnitude in excess of the observed values in the range of $\approx (80-110)kAm^{-1}$, as can be seen in Figure 6.7. This suggests that there is scope to increase the H_C through additional processing and production refinement. This would increase the BH_{Max} of the material and thus its potential as a permanent magnet material as graded by Table 1.1. Further work to investigate possible techniques to improve H_C are discussed in later chapters.

Though the coercivities presented in Figure 6.7 are considerably above values considered feasible by Brown's Paradox ($H_C \to 0.2H_A$), as a fundamental limit, it is dependent on grain morphology tending to that of a sphere and of particles being single domain [88]. To

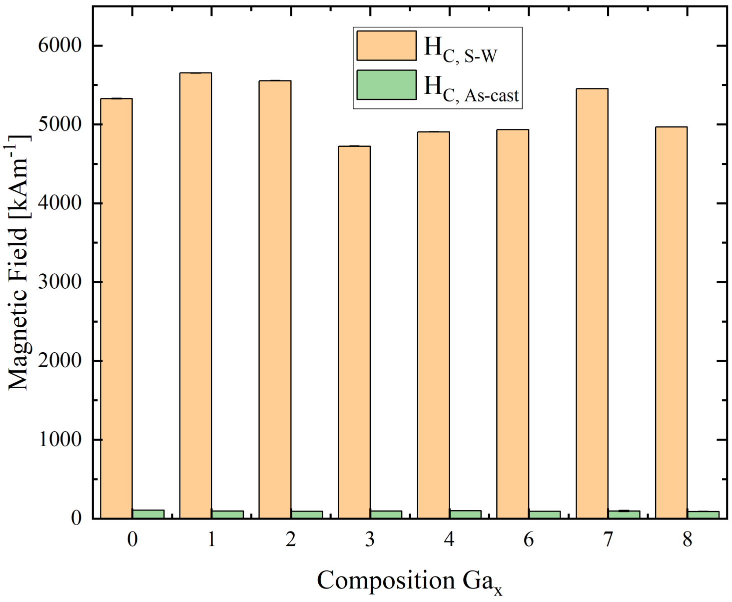

Fig. 6.7 A comparison of calculated anisotropy fields against observed coercivities for as-cast compositions. This demonstrates the significant scope for improvement of H_C in this ternary system by engineering of the microstructure.

investigate the limits of this comparison and evaluate the grain size of each composition, Back-Scatter Electron (BSE) imaging was undertaken on composition Ga_1, following a 2 hour anneal at $430°C$. BSE imaging is particularly sensitive compared to Secondary Electron (SE) imaging to both atomic mass of imaged materials and grain orientation differences from materials with a polished surface due to channelling contrast, as discussed in Section 4.5.2. BSE was selected over Electron Back-Scatter Diffraction (EBSD) for imaging as a faster technique to understand both transformation mechanics and provide an estimation of grain size following casting and annealing free of the risks of accidental short-circuiting components due to magnetic attraction of samples overcoming mounting restraints and seeing contact between sample material and microscope. SE and optical techniques were also not selected as imaging techniques due to the lack of a clear etching pathway for this alloy system in literature making grain recognition impossible by these techniques.

In Figure 6.8, one can see a BSE image of composition Ga_1 following metallographic grind and polish. Attached to the image are the results from EDX scanning of the surface in order to distinguish if BSE contrast is induced by channelling current or elemental variation. As is visible in the EDX plots, Mn and Al distributions through the alloy are

Spectrum number	Mn (± 0.1)[$wt.\%$]	Al (± 0.1)[$wt.\%$]	Ga (± 0.1)[$wt.\%$]
1	73.5	25.0	1.6
2	73.2	25.2	1.7
3	73.3	25.0	1.6
4	72.6	25.7	1.7
5	73.0	25.2	1.8
6	73.3	25.1	1.6
7	73.4	24.9	1.6
8	73.0	25.3	1.7
9	73.0	25.5	1.5
10	73.2	25.5	1.7

Table 6.3 A Table of EDX spectrum calculations for the sampling points shown in Figure 6.8. Error values were generalised across the entire set as the highest machine error calculated by the analysis software used, showing all spectra were in agreement to an precision of $1\,wt.\%$, commonly understood as a general precision limit of EDX on polished metallic samples.

near homogeneous and do not correspond to the contrast changes within the BSE image, especially when considering the larger features at the top and bottom of the SEM image. Further, the spectra analysed by EDX marked on the BSE image show that all compositions measured had standard deviations of $\sigma(Mn, Al, Ga) = (0.2, 0.2, 0.1)at.\%$ with no discernible relation between contrast and deviation in any three of the measured elements. The inclusion of the carbon EDX map is for completeness due to the inclusion of carbon within the incoming X-ray signal, but this is not assumed to be a component of the alloy but instead derived from the polishing process using diamond solutions. It is a generally accepted notion that quantitative EDX cannot accurately calculate carbon concentrations without very careful calibrations, which were not performed during these experiments, due to the low atomic mass of carbon and as such, this quantitative data was ignored for any calculations. Further, given the purity of the reagent materials used in the fabrication of each alloy sample for this study and decontamination procedures implemented in the cleaning of the Arcast Arc 200, it is considered highly unlikely that carbon contamination would produce a measurable or meaningful effect on any of the manufactured alloys in this series of work. The associated spectral information can be seen in Table 6.3.

By the above discussion, it can be inferred that the contrast differences shown in Figure 6.8 are due to orientation mismatching between the grains of the sample. This produces distinguishable features, which can be used for an estimation of grain size as each grain will have a unique crystallographic orientation and thus the boundaries can be determined by grey-scale changes within the image. This is only an estimation, however,

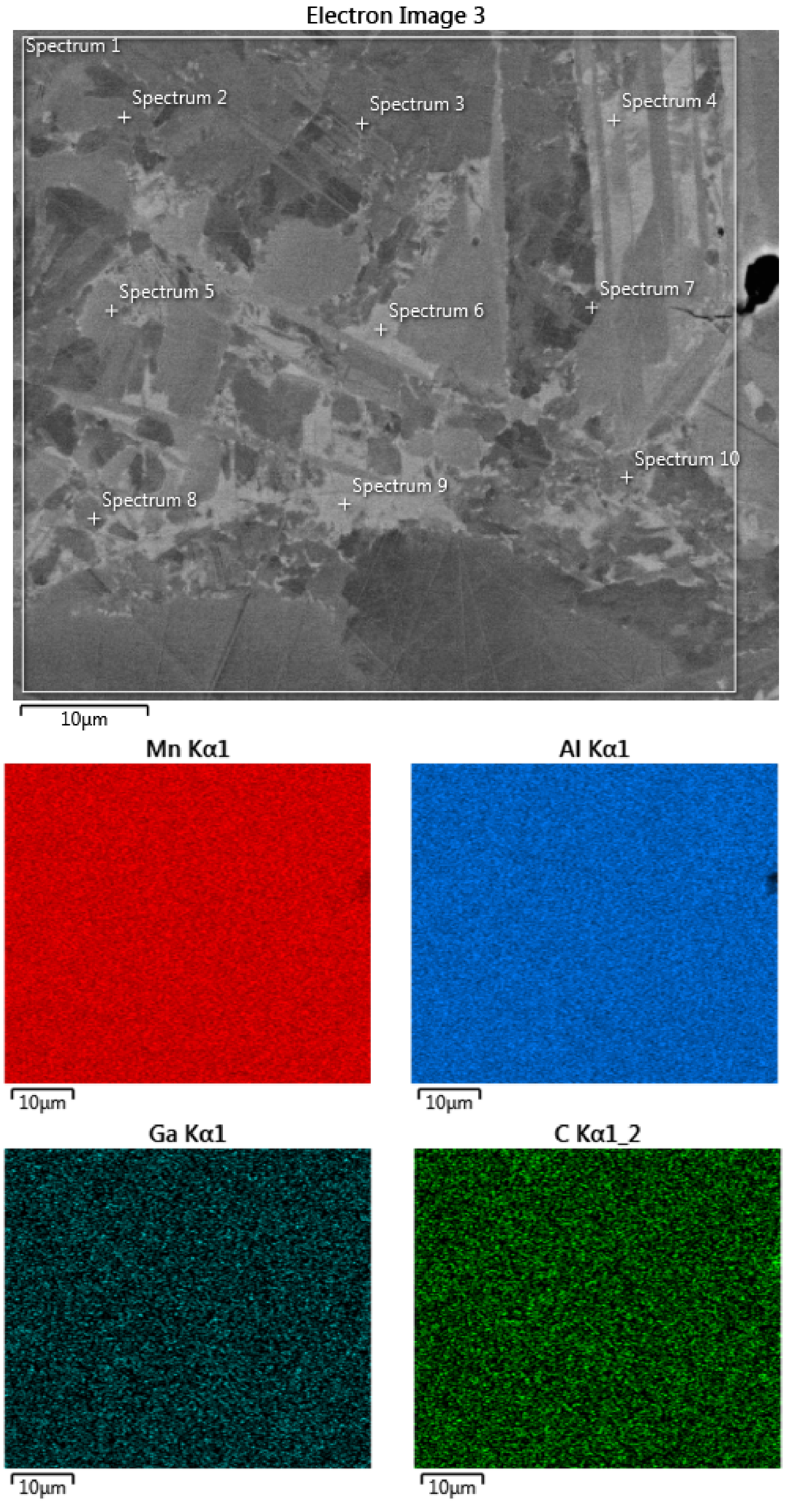

Fig. 6.8 Top image: A BSE image of composition Ga_1 following the $\epsilon \rightarrow \tau$ transformation at magnification 5000x. Spectrum points are overlaid to show locations for EDX point mapping to confirm whether contrast is due to orientation mismatch or composition variation. Bottom Figures: EDX maps of the highlighted square Spectrum 1, showing homogeneity within the material despite contrast differences.

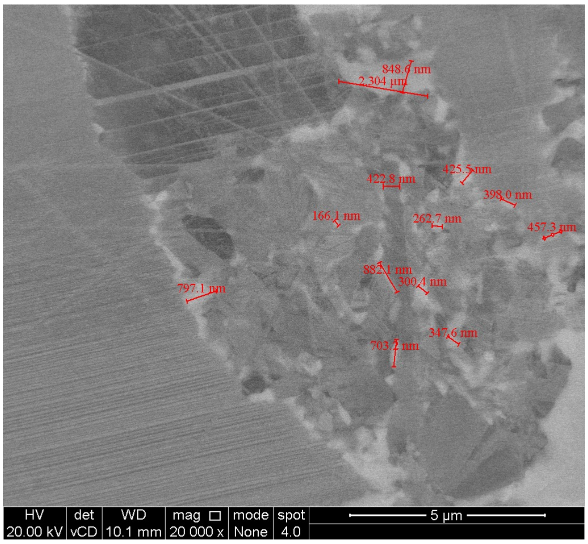

Fig. 6.9 A BSE image of composition Ga_1 following the $\epsilon \rightarrow \tau$ transformation at magnification 20000x. The annotated red lines are individual measurements of contrast features in the BSE image interpreted to be different grains.

as low angle grain boundaries will be less visible by this technique. This calculation can be made by repeatedly marking lines over a processed BSE image and averaging the length of the line divided by the number of contrast changes observed, the linear intercept method for grain size determination discussed in Section 4.5.2. This is limited, however, by the pixel size of an SEM image as the smallest unit of measure and in practice is also limited by the contrast noise of the image. This can be somewhat mitigated by image smoothing to reduce intra-grain noise but, taking Figure 6.8 as an example, the fundamental size observable would be approximately 58nm per pixel and this would thus set a resolution limit of approximately 500nm in order to distinguish the feature. From this figure, the average grain size for Ga_1 following the previously laid out casting and transformation mechanics would be $(1.44 \pm 0.06)\mu$m, under 3 times the realistic error limit for this technique and thus higher magnification should be utilised. When this calculation is repeated on a BSE image captured at a magnification of $20,000\times$ as seen in Figure 6.9 compared to the $5,000\times$ of Figure 6.8, one finds that the average grain size drops to $(0.39 \pm 0.02)\mu$m, a $(73 \pm 5)\%$ decrease in grain size. Thus, resolution limits determine calculable grain size and given that Scherrer Equation calculations on the XRD data used to calculate phase populations estimate crystallite size at (23 ± 2)nm, the diffraction method is deemed a more reasonable determination of the minimum grain size of the material.

The purpose of determining the grain size of composition Ga_1 was two-fold. Firstly, given all compositions underwent identical heat treatments in this study, it is assumed that all compositions see grain sizes of the ferromagnetic $L1_0$ phase within similar orders of magnitude. Secondly, it allows comparison of grain size to Stoner-Wohlfarth particles in order to assess the optimisation of grain size, and thus comment on whether the initial 3 hour anneal at $1050°C$ is appropriate when setting the compositions to the ϵ-phase. Following equations set out by Kronmüller and Fähnle in Equation 2.17, it is possible to calculate the maximum diameter of a spherical single-domain particle, D^{do}_{crit}. Using $A = 2.69pJm^{-1}$, one can calculate the maximum diameter for a spherical particle of composition Ga_1 to be $D^{Ga1}_{crit} = (411.01 \pm 0.08)$nm, comparable to that of MnBi [94][37]. When assessing this against grain size calculated for Ga_1, it can be assumed that there are several single domain particles within the microstructure when assessed by the sizes calculated via the Scherrer equation and through BSE at a magnification of 20,000x, but it can also be said that many particles are significantly over this size if using the value calculated at 5,000x. As such, it can be considered that the grains within the alloy are at or over the single domain particle size if modelled as a perfectly spherical grain, or all over if modelled as a prolate ellipsoid given that $D^{do}_{crit}(sphere) = 3D^{do}_{crit}(prol.ell)$.

Given the fabrication route used was Arc Melting, thus the sample was rapidly cooled via a water cooled copper jacket from melt and has undergone heat treatment and phase changes, it is reasonable to assume that a measured surface will contain a variety of grain sizes from nucleation on cooling, grain growth during heat treatment and τ-phase growth. Thus, it can be expected that a significant volume fraction of the grains are multi-domain, seeing a decrease in extrinsic magnetic properties when compared to engineering estimates of maximum possible properties and a further step in refinement of production would be to see a consistent, fine grain size of the compositions, thus seeing more predictable behaviour from GSDCP theory discussed in Section 2.3.5. Further exploration of this is, however, considered beyond the scope of this chapter as the primary assessment criteria of the compositions are the intrinsic magnetic properties.

6.2.3 Curie Temperature as a Function of Composition

Tracking trends on a contour map of composition against T_C, as seen in Figure 6.10, it is observable that a local minima for T_C does appear. With 8 data points and error on the compositions determined by EDS, this trend should be taken as qualitative rather than quantitative but it does suggest that a composition of $Mn_{58}Al_{37.5}Ga_{4.5}$ represents a minima for the system for T_C. Comparisons of samples on near constant Mn contours show a decrease in T_C as Ga concentration increases within the alloy. Whilst all samples demonstrate values of T_C over the requirement laid out in Table 1.1, the plot does show that Ga doping benefits may come with a decrease in T_C and thus M_S and M_R at higher

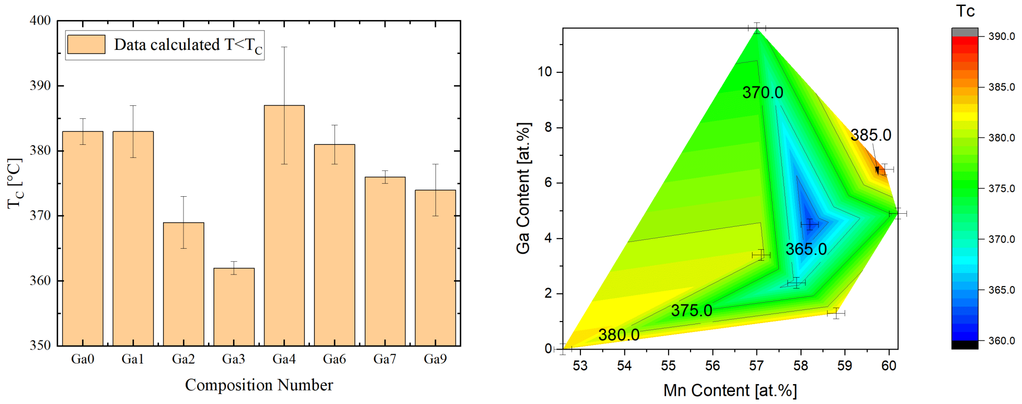

Fig. 6.10 LHS: A bar chart showing the average calculated value of T_C by composition, with associated errors using a linear fit for a zero-field heating measurement of $T \rightarrow T_C$. RHS: A contour plot of T_C against Mn and Ga alloy composition. All compositions tested pass the minimum criteria of $T_C > 275°C$ as required in Table1.1.

temperatures but that all compositions show an increase in T_C when compared to that of the MnAlC standard, seen in Figure 5.6. It is, however, challenging to estimate T_C to within an accuracy of $\pm 1°C$ and so the contour plot is seen as qualitative rather than quantitative evidence. When compared to values for the T_C of MnAlC(3at.%), however, it can be seen that the dual phase ternary system has a $T_C = 297°C$ which, whilst above the Gap Magnet criteria, is still over $70°C$ lower than the lowest T_C found for the Ga_x series as shown in the LHS of Figure 6.10 [50].

Thermal Hysteresis Behaviour

In reference to the previous section, the associated variation and error in calculating T_C may be that the alloys demonstrate a hysteresis when transitioning between ferromagnetic and paramagentic regimes. This can be clearly observed in the Field Heating/Cooling curve captured for composition Ga_7 shown in Figure 6.11. This phenomenon is explained in by Bozorth [95] as a change in the metallurgical state of a material, ranging from a phase change to an appreciable difference in solid solubility of a constituent element of an alloy. This implies that Differential Scanning Calorimetry (DSC) may be required to fully investigate this temperature range to observe any potential change in state but that the error associated with measuring T_C may be in part due to averaging between these two measurements, with a difference of $(5-6)°C$ between T_C calculated from cooling and heating measurements. Whilst further work would be needed to fully characterise this

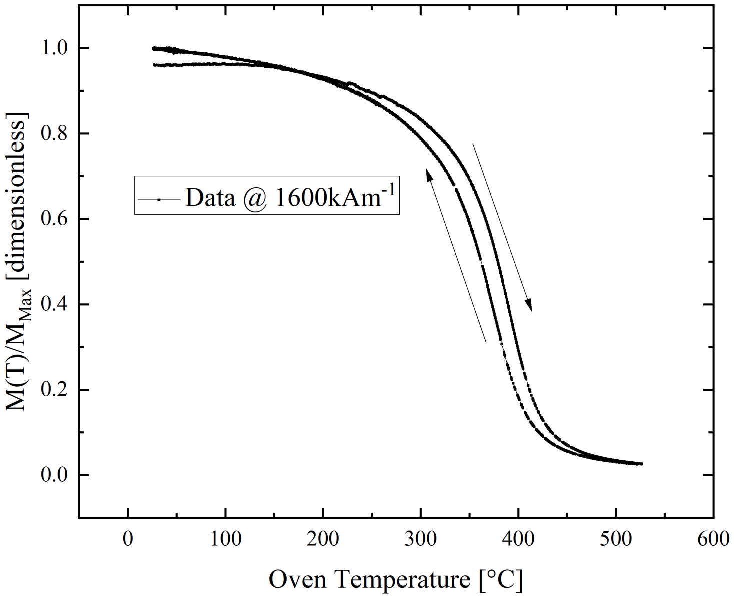

Fig. 6.11 A plot of Magnetisation vs. Temperature of composition Ga_7 under a field of $1600kAm^{-1}$, showing a clear difference in behaviour on the top curve being the Field Heating Curve and the bottom the field cooling, showing a cooler transition to ferromagnetic behaviour. and as distinguished by the arrows superimposed over the graph.

behaviour, measurements estimated in Figure 6.10 show that even predicted minima fall above the criteria laid out for a Gap Magnet by Coey in Table 1.1.

6.3 Processing and Transformation Optimisation of Target Alloy Composition

When designing a permanent magnet, both intrinsic and extrinsic magnetic properties must be controlled through manufacture. Intrinsic properties are derived from the composition and phase of material selected and its inherent quantum mechanical properties whereas the extrinsic properties are a product of the intrinsic properties and the system itself, its microstructure and overall geometry. In the case of developing the MnAlGa system for applications as a permanent magnetic material, the control of heat treatments is doubly important during the $\epsilon \rightarrow \tau$ transformation step as it both controls the phase population, thus intrinsic magnetic properties of the final material, and also the extrinsic properties by way of grain growth, dislocation transport and internal stress reduction within the alloy. As such, the optimisation of the transformation process is not a trivial task.

6.3.1 Annealing Temperature Determination for Target Composition

To optimise the first variable, that of maximising phase population, a time temperature transformation study was conducted and evaluated by the change in relative magnetisation as a function of annealing time. The logic behind this was that both the precursor ϵ-phase and equilibrium γ_2 and βMn phases are paramagnetic at room temperature and thus an increase in magnetisation under a fixed field and annealing temperature is attributed to an increase in the τ-phase population as determined by the logic established in Section 3.1.3. The alloy targeted for this study was Composition Ga_6 as shown in Table 6.1 due to the high M_S and k calculated for that alloy, expressed in Table 6.2. This alloy was cast via the Arc Melting technique laid out in Section 4.1.1 and was subjected to the reduced 3 hour 1050$^{\circ}C$ anneal and water quench to set the precursor ϵ-phase but attempt to reduce the grain size disparity compared that of the initial MnAlGa studies shown in this chapter.

5 samples of recast Ga_3, hereby referred to as MAG-E (Manganese Aluminium Gallium - Electrical to reference targeted applications in electric motors and generators), were extracted and treated to a 2 hour anneal at $(400, 420, 430, 450, 500)^{\circ}C$ within the MPMS3 VSM's oven unit mounted to the associated heat stick holder. Given the low susceptibility of the heat stick compared to mass of sample, the associated magnetisation response was not corrected for in the data sets. Figure 6.12 shows that the $\epsilon \rightarrow \tau$ transformation is sensitive to the transformation temperature, with a temperature range of $(420-430)^{\circ}C$ where transformation can occur within manageable timescales for large volume production. Measurements taken at 400$^{\circ}C$ are not displayed here as it was seen that this temperature was too cool to precipitate transformation of Ga_6 under a 120min time frame. Instead, a general decrease in magnetisation as a function of time was observed, suggesting that at this temperature, an $\epsilon \rightarrow \gamma_2 + \beta Mn$ transformation occurs.

Overall, the transformation at 430$^{\circ}C$ was selected moving forward for composition Ga_6 as an optimum annealing temperature for annealing time refinement experiments. Whilst there was little variation in the resulting values of k and M_S between the two engineering temperatures, the increase in initial rate of transformation may suggest that an optimum transformation time may be shorter than that of 420$^{\circ}C$.

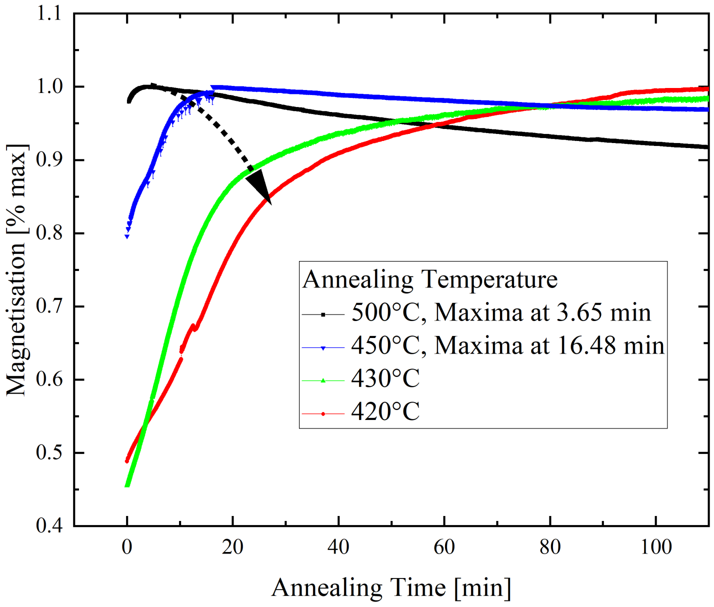

Fig. 6.12 A plot of magnetisation against annealing time under a constant $1600kAm^{-1}$ applied magnetic field at differing temperatures. The superimposed black line highlights the behaviour change in all four measured samples. The first two see an inflection in magnetisation whilst cooler temperatures see continuing growth as a function of annealing time with a positive gradient at 120min.

Thermal behaviour of Intrinsic Magnetic Properties

Work by Bance *et. al* (2014) shows that in the NdFeB system, there is grain size and morphology dependence on the coercivity of the overall magnetic material, with the coercivity estimated by the Kronmüller equation:

$$H_C(T) = \alpha H_A(T) - N_{eff} M_S(T) - H_{th}(T) \tag{6.2}$$

where $H_C(T)$ is the coercivity of a ferromagnetic material at a given temperature, T, $H_A(T)$ is the anisotropy field of the material for a given temperature, α is the parameter relating microstructure to coercivity and N_{eff} is an effective demagnetising factor for the reduction of H_C by local magnetostatic effects [96]. As such, an investigation into the behaviour of a target composition over a varied annealing time was developed to investigate whether transformation time would significantly affect either of these coefficients.

Following the data shown in Figure 6.12, an annealing temperature of 430°C was selected and samples cut from the alloy ingot were annealed at this temperature within a box

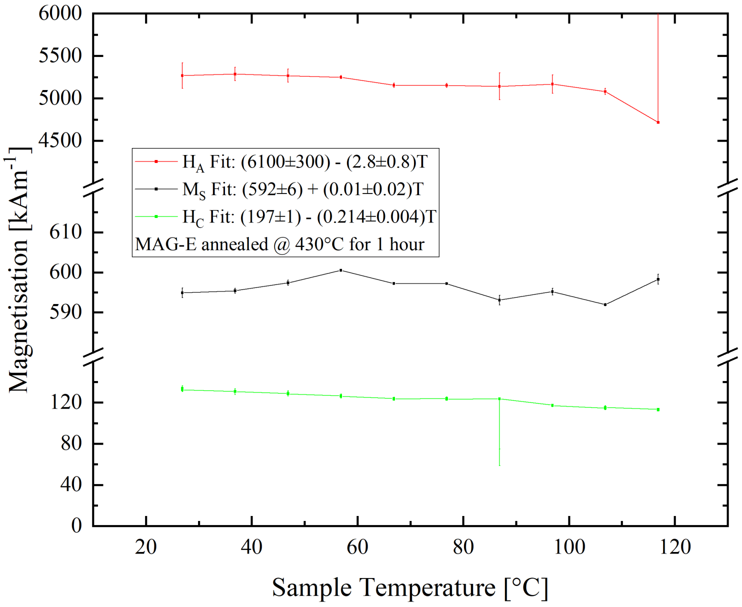

Fig. 6.13 A plot of the temperature variation of H_A, M_S and H_C of MAG-E following a 1 hour anneal, precipitating the $\epsilon \rightarrow \tau$ transformation. Despite near 100% τ-phase population, the thermal trends of intrinsic properties are unstable and measurement errors were at points significant despite averaging. This is attributed to dislocation transport activation leading to lattice microstrain changes during measurement.

furnace and normal atmosphere for 1, 2, 3, 4, 6 and 24 hours followed by a water quench. In order to assess the effect of annealing time on α and N_{eff}, each sample was measured using a Quantum design MPMS3 SQUID with attached oven module to investigate the material response to a ±7T applied field in a temperature range of $(26.85-226.85)^{\circ}C$. By measuring how the anisotropy field, coercivity and saturation magnetisation vary as a function of temperature, estimations can be made for annealing time dependencies of α and N_{eff}. This discussion can be found in Section 6.3.1

For MAG-E to be implemented within motor designs, the thermal behaviour of the intrinsic and extrinsic magnetic properties will need to be determined. As this is a product of phase population and microstructure, it is expected that the thermal dependency of these properties will vary as a function of annealing time.

A plot of H_A and H_C for the sample of MAG-E annealed for 1 hour can be seen in Figure 6.13. The data sets show that, much like the samples discussed in the composition variation experiments earlier in the chapter, there is a significant discrepancy between the calculated values for H_A and H_C. Of particular interest, however is the thermal

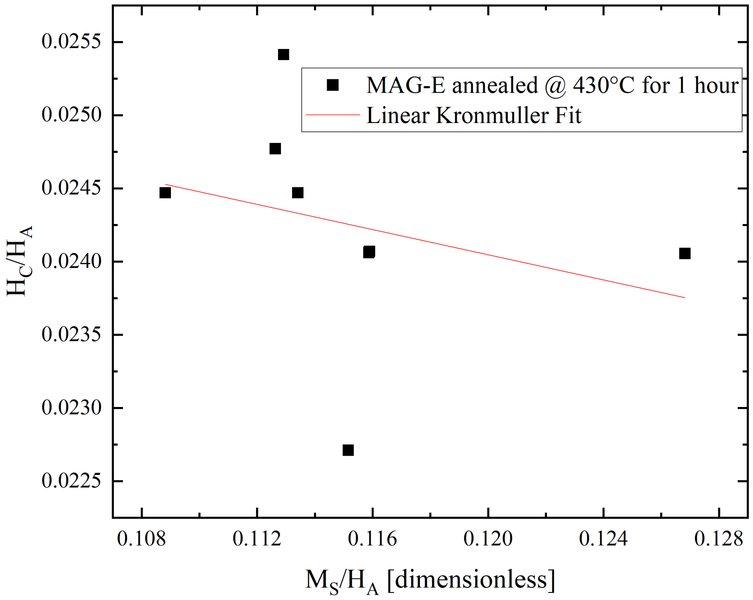

Fig. 6.14 A Kronüller plot of MAG-E following a 1 hour anneal, precipitating the $\epsilon \rightarrow \tau$ transformation. From the applied linear fit, it is clear that the linear relationship predicted by Equation 6.2 does not apply and that either the microstructure is changing as a function of measurement conditions or the intrinsic magnetic properties are unstable as a function of temperature.

dependency of both parameters. If one assumes a linear decay model for both H_A and H_C within the measured temperature range, it is of note that the standard deviation for the normalised residuals for each fit are $\hat{\sigma_A} = 0.02321$ and $\hat{\sigma_C} = 0.01033$. Thus, it can be stated that the linear fit is less appropriate for the thermal dependency of H_A in this case, with error propagation such that the thermal coefficient of Anisotropy Field decrease with temperature is $\alpha_A = -(3.3 \pm 0.2) kAm^{-1} {}^{\circ}C^{-1}$.

Looking to the Kronmüller plot for the sample annealed at 1 hour, it can be seen that the relationship expressed in Equation 6.2 does not apply in this case. The data shown in Figure 6.14 shows no linear proportionality between H_C and M_S when normalised by H_A as one would expect. Instead, it would suggest that if this equation holds, both α and N_{eff} have a dependency on the measurement temperature or a time dependency throughout the experiment. Given that the 2θ measurements across the entire annealing study show a phase population of $\approx 100\%$ as shown in Figure 6.15, it can be concluded that this effect is due to the internal stress caused by the $\epsilon \rightarrow \tau$ transformation within the system. Magnetisation against time for this composition as shown in Figure 6.12

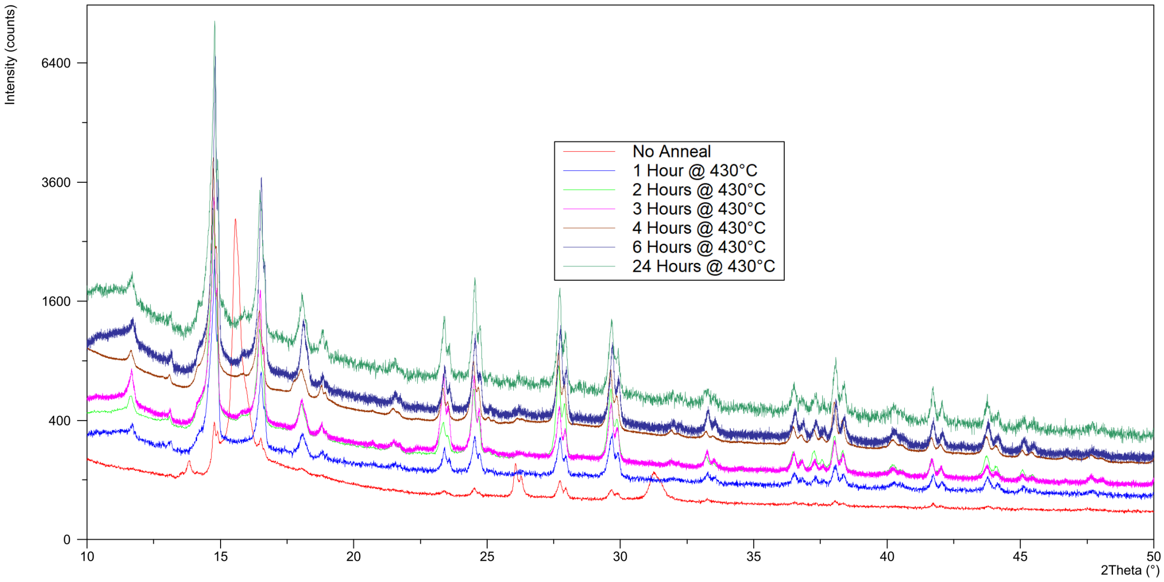

Fig. 6.15 2θ-XRD scans of MAG-E as a function of annealing time. In order to reduce background noise from Mn fluorescence under a Cu x-ray source, an Ag source was selected instead, explaining the factor of ≈3 decrease in 2θ-diffraction peak position.

shows that $dM(430°C)/dt > 0$ at this time, implying that whilst the phase population may be $\approx 100\%$, lattice parameters may still be changing as a result of dislocations resulting from the metastable transformation moving via activated slip systems and allowing the system to relax into a more energetically favourable lattice scale. As such, when the system is quenched during this anneal, these slip systems are deactivated and the system remains in a nonequilibrium state. It could, therefore, be hypothesised that as the system is brought to temperature, the activation energies for these hypothetical systems are reached, allowing for microstructural changes to occur and explaining the instability in the measurements for both H_A and M_S.

Focusing on the two hour anneal, it can be seen that the instability in the saturation magnetisation as a function of sample temperature observable in the 1 hour annealed sample is no longer present, with a smooth, non-linear trend being observable for $M_S(T)$ in Figure 6.16. Looking to the Anisotropy Field, however, it can be seen that this has both decreased at room temperature and decreased as a function of temperature when compared to that of the 1 hour annealed sample as well as maintaining a degree of instability not seen in the measurements of M_S. This is due to instabilities when measuring k, with low temperature measurements when approaching an applied field of $5570 kAm^{-1}$ and an almost 10% increase in M_S at $27°C$ or Room Temperature. Looking to discussion on the origins of ferromagnetic behaviour in the τ-MnAl system, this developed stability between 1 and 2 hours of annealing would suggest that dislocation transport and thus lattice parameter change by way of residual stress reduction will have ceased to negligible levels for all slip systems that could activate below $200°C$ and see meaningful change within the time-frame of measurement, given the total magnetisation of a unit cell, which is proportional to the saturation magnetisation of the system, is a product of Mn-Mn coupling throughout the superlattice structure and thus that of lattice parameters [97].

This hypothesis is not further corroborated, however, by the increased stability of H_C as a function of temperature. Though H_C as a function of Anneal Time at RT is broadly a random variable, with each sample having a random, pseudo-isotropic microstructure from casting and heat treatment not creating anisotropic directions within the material, the relative decrease as a function of temperature appears to be constant and proportional. However, looking to Table 6.4 and normalising the thermal decay values for the 1 and 2 hour annealed samples by the RT coercivity, one can find that the relative error on the 2 hour sample is higher, implying that this normalised linear decay is less appropriate and the relative error on each coercivity measurement is higher. This may be partly explained, however, by H_C measurements within a VSM being an indirect measurement, with the independent variable being that of the applied field and difficulty in estimating required data density for observing switching events following shape factor corrections. Further testing into the residual strain reduction by the annealing process when compared to other microstructural variable sensitivity is discussed in Section 6.3.1.

Moving to the 3 hour annealed sample, it can be seen that there is a greater compliance with linear dependency models when considering intrinsic and extrinsic magnetic variables. Figure 6.17 shows the behaviour of k, M_S and H_C as a function of increasing sample temperature. All three variables show a decrease with increasing temperature, with the figure containing the linear fit information for each associated variable. The increased error in observation on the thermal dependency of H_A can be attributed to its method of calculation from the Law of Approach to Saturation, by Equation 3.3, meaning the error on both observations compounds leading to percentage errors on the thermal dependency of each variable of $Err(H_A) = 2.31\%$, $Err(M_S) = 1.47\%$ and $Err(H_C) = 1.42\%$.

Using these thermal decay models, however, it becomes possible to assess the potential performance of MAG-E annealed at $430°C$ for 3 hours at motor operating temperatures. If one assumes that a hypothetical electric car motor operates at approximately $200°C$, one can predict $M_{S,200°C} = (630 \pm 10) kAm^{-1}$ and $H_{A,200°C} = (4100 \pm 100) kAm^{-1}$ from the linear fits, broadly in agreement with observations. Taking the Coey criteria from Table 1.1 and calculating that the associated minimum anisotropy field from the magnetocrystalline anisotropy energy and saturation magnetisation requirements for a Type B Gap Magnet is

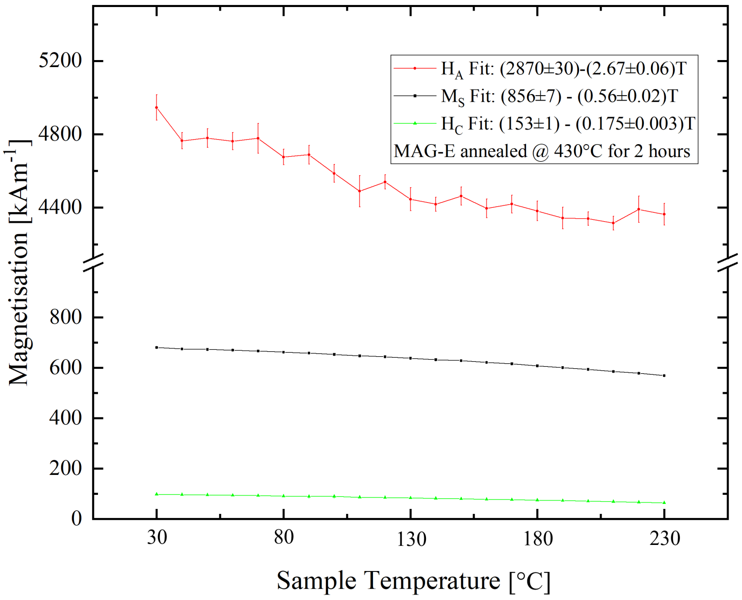

Fig. 6.16 A plot of key magnetic variables as a function of temperature for a sample of MAG-E annealed from a quenched ϵ-phase at $430°C$ for 2 hours. It is of note that the instability in the observation of H_A arises from instability in calculation and observation of k given its calculation from Equation 3.3

$H_{A,Coey} = 1730kAm^{-1}(3s.f.)$, implying that whilst M_S is within 5% of Type B criteria at RT, H_A is above criteria even at operating temperatures. If one also assumes that the maximum energy product achievable for a permanent magnetic material is $BH_{Max,theory} = \frac{\mu_0 M_S^2}{4}$, MAG-E annealed at $430°C$ for 3 hours would have a theoretical maximum energy product at engine operating temperatures of $BH_{Max} = (123 \pm 2)kJm^{-3}$. Whilst this is above the Type A criteria at temperature, the Gap Magnet criteria make no mention of temperature dependence beyond that of T_C and at RT, one finds that the theoretical limit of the maximum energy product is $BH_{Max,RT} = (146 \pm 2)kJm^{-3}$, meaning that MAG-E following this heat treatment and composition would fulfill all criteria for a Type A system but not that of a Type B due to low M_S. It is of note that systems will never in practice reach this limit, as this is a condition of a perfectly square loop [15]. As such, it is a better approximation that this material, when considered for operations at the working temperature of hypothetical electric motors, is a high performing Type A material with a unit cost of approximately £$6.63kg^{-1}$ at the time of writing.

Annealing for 4 and 6 hours sees a general decrease in properties when compared to that of shorter annealing times. Figures 6.18 and 6.19 show a decrease in both intrinsic

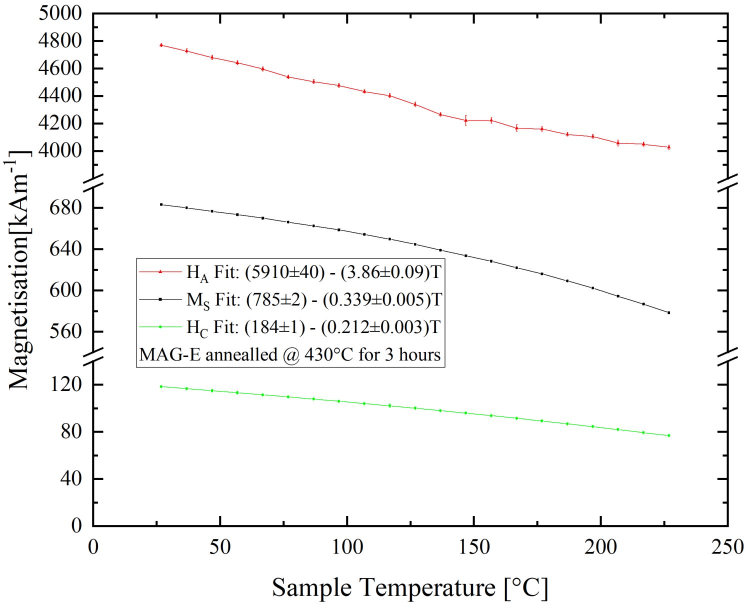

Fig. 6.17 A plot of the temperature variation of H_A, M_S and H_C of MAG-E following a 3 hour anneal, precipitating the $\epsilon \rightarrow \tau$ transformation. The increased variation and error in high temperature measurements of H_A are attributed to its measurement as a ratio of k and M_S by Equation 6.2 and thus compounding the error on both a gradient and intercept of a linear best fit, thus doubly dependent on the applicability of said model.

variables as a function of temperature and at RT when compared to lower annealing temperatures. Following through with the hypothesis that lattice parameter shift is a result from residual stress relaxation and assuming that no additional dislocations are generated as a result of the heat treatment such that microstrain is apparent in the lattice and parameters shift in an unexpected response, this would suggest that there is an optimum stress within the system to shift to magnetically favourable lattice parameters such that intrinsic magnetic properties are maximised. Given that further processing of the as-cast material would be necessary to increase extrinsic magnetic variables and thus increase the BH_{Max} of the material as a result, this hypothesis may not hold true for a system where additional, anisotropic stress has been build into the system, either by differential cooling or through deformation processing, but it may suggest a way of maximising theoretical limits on these variables should there be a processing route that does not sacrifice the optimum values achievable from the as-cast state or seeks to incorporate the heat treatment in the process whilst achieving the desired microstructural refinement and texturing.

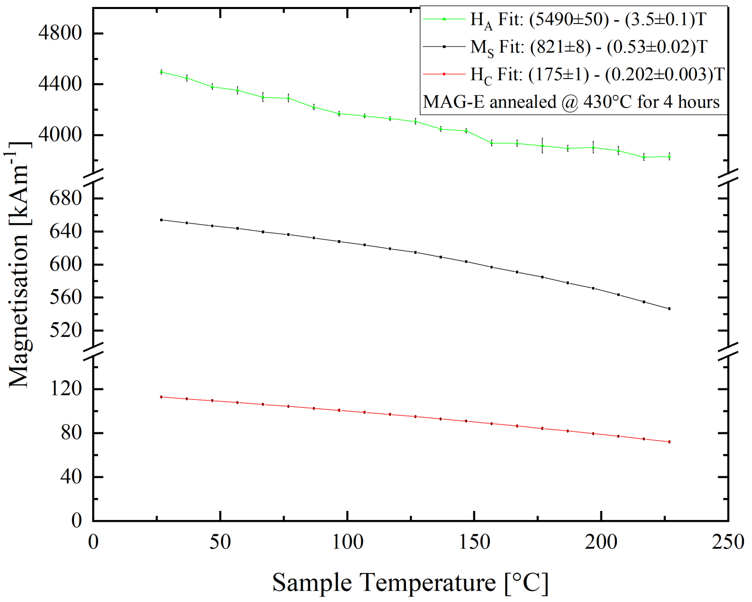

Fig. 6.18 A plot of the temperature variation of H_A, M_S and H_C of MAG-E following a 4 hour anneal, precipitating the $\epsilon \rightarrow \tau$ transformation. The instability and increased error in the H_A data points and trend is derived from it being measured as a ratio between M_S and k.

Of particular note is the discontinuity in measurement of intrinsic magnetic variables for the sample annealed for 6 hours, as seen in Figure 6.19. When measuring this sample, due to unreliability in the MPMS3 oven module, the low temperature measurements were recorded first, i.e. $(27 \rightarrow 127)°C$ before measuring T_C for the sample. Following this, the high temperature measurements were captured. Given that the temperature range reached to test for the Curie point of a sample in these experiments it set to reach $526.85°C$ ($800K$), this temperature may see additional dislocation transport/lattice parameter shift in the same fashion as this annealing study shows for heat treatments at $430°C$. Referencing heat treatment data for the paramagnetic response of MAG-E in Figure 6.12, it can be seen that a maximum response for heat treatments of MAG-E at $500°C$ is observed at approximately $3.65min$, which when compared to the maxima of the response for heat treating at $450°C$ suggests that this maxima is achieved faster as temperature increases. Given that the Curie point test exposed the sample to temperatures above $500°C$ for $(7.25 \pm 0.01)min$, it can be assumed that, if the material response is comparable to the heat treatment of the ϵ-phase given that by $3.65min$, it is theoretically in the τ-phase, the material has entered into a 'decay regime' such that $M_S(RT)$ is decreasing if one assumes

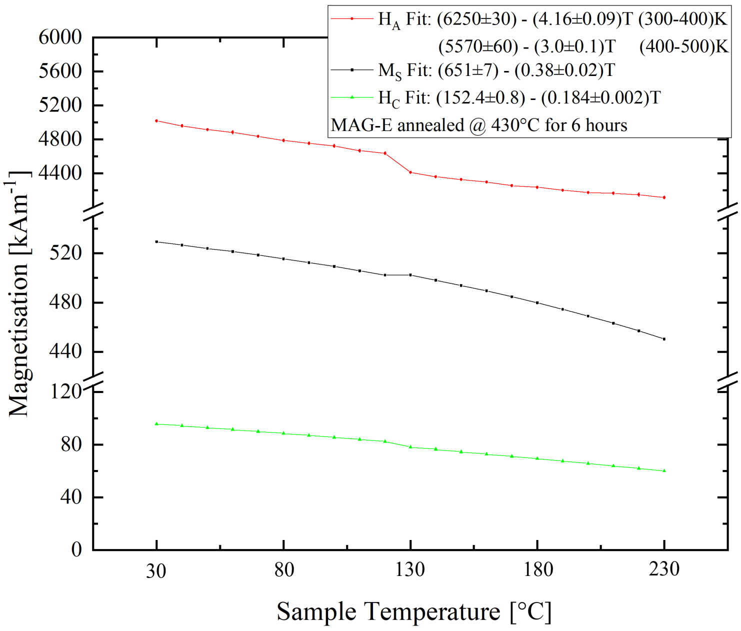

Fig. 6.19 A plot of the temperature variation of H_A, M_S and H_C of MAG-E following a 6 hour anneal, precipitating the $\epsilon \rightarrow \tau$ transformation. The discontinuity observed at $127^{\circ}C$ in intrinsic magnetic properties is attributed to a change in sample measurement ordering, resulting in additional heat treatment above the targeted annealing temperature, demonstrating that MAG-E is sensitive to operating temperature, even on the timescale of minutes.

the proportionality between paramagnetic response to ferromagnetic saturation. As such, one can conclude that this further places an operational window on permanent magnetic material applications for MAG-E such that in overheat instances where the material moves into the paramagnetic regime, not only will the material lose polarisation on cooling, thus lowering M_R but should the material reach $450^{\circ}C$ or higher for longer than the observed maxima shown in Figure 6.12, irreversible losses to intrinsic magnetic properties may also occur.

The purpose of the 24 hour annealing process was also an additional method of testing the temperature stability of the MnAlGa system in the τ-phase. Mix *et. al.* had previously tested the thermal stability of $Mn_{55}Al_{38.57}Ga_{6.43}$ in the τ phase by subjecting the sample to [61] to heat treatment of $700^{\circ}C$ for 2 hours but only discussion around phase formation is present in the literature, with observation of βMn precipitates forming in BSE-SEM images for Ga containing compositions. No discussion was made from a magnetic perspective and so, whilst $L1_0$ phase stability was anticipated, the decreasing intrinsic magnetic properties trend with increasing annealing time motivated investigating samples with significantly longer annealing times to determine pseudo-equilibrium properties.

A 24 hour anneal sees comparably lower values of M_S when compared to that of the shorter annealing times. The thermal behaviour of $M_{S,24h}$, $H_{A,24h}$ and $H_{C,24h}$ can be seen in Figure 6.20 and shows similarities to the data captured for a 3 hour annealed sample. Crucially, the additional 21 hours annealing has minimal effect on the calculated anisotropy field, with only an increase of $(1.69 \pm 0.01)\%$ observed between both estimated fields at $-273°C$. It is of note, however, that the thermal dependency of H_A, M_S and H_C appears to vary considerably following the additional annealing time, with a change of $(24.1 \pm 0.7)\%$, $(18.0 \pm 0.5)\%$ and $-(59 \pm 1)\%$ respectively. Though the purpose of the annealing process was to optimise the extrinsic magnetic properties and intrinsic magnetic properties, it can be seen that the annealing can also affect the thermal dependency of the magnetic properties of MAG-E. Given that the material is being developed for permanent magnetic material applications in electric motors, this dependency is also important to optimise to ensure appropriate extrinsic magnetic properties at a given systems operating temperature, and thus an optimised BH_{Max} at a given operating temperature. Given that some systems may operate across greater temperature ranges, it may not necessarily be optimised to simply maximise a given variable but rather to minimise the reversible decrease of said variable as a function of temperature.

The measured values for M_S, k and H_C across the annealing range can be seen in Table 6.4 and shows that continued annealing does not asymptotically tend towards a maximum value for any of the three variables, with values captured from a sample annealed for 24 hours being the lowest in the set for all three variables. Indeed, it appears that an idealised annealing time exists between 2-4 hours though with only three measured data points in this range, it is difficult to speculate further as to an exact optimum annealing time, especially when considering k and M_S would see independent maxima in this data set. Given that all 2θ-XRD scans and resulting phase population calculations show no measurable precipitation of equilibrium phases, it can be deduced that this change in properties is inherently linked with stress reduction and grain morphology change within the system. By this logic, it can be inferred that there is a desirable residual stress within the system from the $\epsilon \rightarrow \tau$ transformation that can distort the BCT lattice such that optimum intrinsic magnetic properties can occur.

When considering the thermal dependency of MAG-E as a function of annealing time, it can be seen that the biggest change in the response of $d(M_S)/dt$ is between that measured for a sample annealed for one hour and resulting measurements, which show a broad consistency of (3-5)x the rate of sensitivity to temperature. Whilst this might

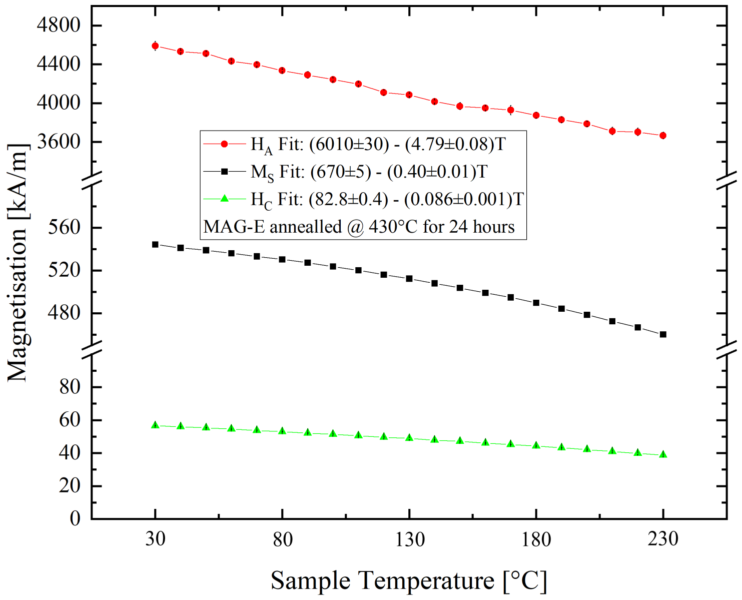

Fig. 6.20 A plot of the temperature variation of H_A, M_S and H_C of MAG-E following a 24 hour anneal, precipitating the $\epsilon \rightarrow \tau$ transformation.

suggest that a 1 hour anneal is an optimised process for higher temperature applications of MAG-E, with k within the acceptable range for for even a Type C gap magnet as defined by Table 1.1 when at hypothetical electric motor operating temperatures of $\approx 200°C$, the variability in M_S as a function of temperature and thus the resultant M_R as shown in Figure 6.13 shows that this would make for a poor engineering material due to an inability to predict its behaviour above room temperature as the system evolves under temperature. As such, if one once again assumes a motor operating temperature of $200°C$, the optimum annealing time at $430°C$ is 3 hours given it would maintain the highest extrinsic magnetic properties both at room and operating temperatures, overcoming the increased temperature sensitivities measured.

Further, following the hysteresis measurements across the measured temperature range, a further measurement was taken at room temperature to ensure that the system could function at a maximum operating temperature of $220°C$ or a 10% overheat condition. It was found that following this operating cycle of $0 \rightarrow 220°C$ in 48 hours, increasing in temperature approximately every 3 hours by $10°C$ and cycling through a $7T$ applied magnetic field at every interval, the percentage change for the extrinsic magnetic variables M_S, k and H_A was $(0.10 \pm 0.03)\%$, $-(4.1 \pm 0.5)\%$ and $-(4.2 \pm 0.5)\%$ respectively. Whilst

Time [h]	M_S at 27°C [kAm^{-1}]	k at 27°C [kJm^{-3}]	H_C at 27°C [kAm^{-1}]
1	(595 ± 1)	(1970 ± 60)	(134 ± 2)
2	(680.9 ± 0.6)	(2120 ± 30)	(99 ± 1)
3	(683.3 ± 0.1)	(2048 ± 5)	(118.4 ± 0.8)
4	(654.0 ± 0.1)	(1848 ± 8)	(112.8 ± 0.7)
6	(529.3 ± 0.1)	(1670 ± 5)	(96.0 ± 0.4)
24	(544.3 ± 0.3)	(1570 ± 20)	(56.6 ± 0.2)
	$d(M_S)/dT$ [kAm^{-1} °C^{-1}]	$d(k)/dT$ [kJm^{-3}°C^{-1}]	$d(H_C)/dT$ [kAm^{-1}°C^{-1}]
1	(-0.12 ± 0.03)*	$(-1.7 \pm 0.3)*$	(-0.214 ± 0.004)
2	(-0.56 ± 0.02)	(-2.67 ± 0.06)	(-0.162 ± 0.005)
3	(-0.52 ± 0.02)	(-2.95 ± 0.02)	(-0.212 ± 0.003)
4	(-0.53 ± 0.02)	(-2.65 ± 0.03)	(-0.202 ± 0.003)
6	(-0.38 ± 0.02)	(-2.61 ± 0.05)	(-0.148 ± 0.002)
24	(-0.40 ± 0.01)	(-2.56 ± 0.02)	(-0.087 ± 0.001)

Table 6.4 A Table of results to determine the effects of annealing at 430°C on samples of MAG-E for 1, 2, 3, 4, 6 and 24 hours. Thermal dependencies are calculated as linear fits for measurements taken from 27°C and higher. *It is of note that the data for the sample annealed for 1 hour showed no discernible trend over the measured temperature range, with data variation leading to significant error in the calculation of an appropriate thermal dependency constant.

the decrease in H_A might be cause for concern when considering the application of MAG-E in a permanent magnetic material application, where BH_{Max} and thus H_C are of concern and H_C being intrinsically linked to H_A by Equation 6.2, it was found that there was no measurable change in H_C for the 3 hour annealed sample before and after the operating cycle, thus implying that that any shift in intrinsic properties was counteracted by favourable changes in the Kronmüller coefficients within the microstructure of the material. Further, the observed M_R value for the sample increased by $(25.03 \pm 0.02)\%$, implying that although the 3 hour anneal may be optimum for the intrinsic magnetic properties, the extrinsic may benefit from additional annealing time.

To further investigate this, one can see a plot of M_R normalised by M_S across the annealing time spectrum in Figure 6.21 and can see that there is no distinct proportionality between annealing time and the resultant M_R values. $M_{R,1h}$ shows similar behaviour to that of the saturation magnetisation of that sample, with significant fluctuations between each measurement under heating, present in both the normalised and direct measurements. During the 6 hour measurement, oven module instability in the MPMS3 resulted in the measurement cycle being split in two, leading to a discontinuity in the resultant remanence in the material and showing that in the as-cast annealed state, remanence is not fixed by an initial state seemingly cast into the material but can be re-magnetised into

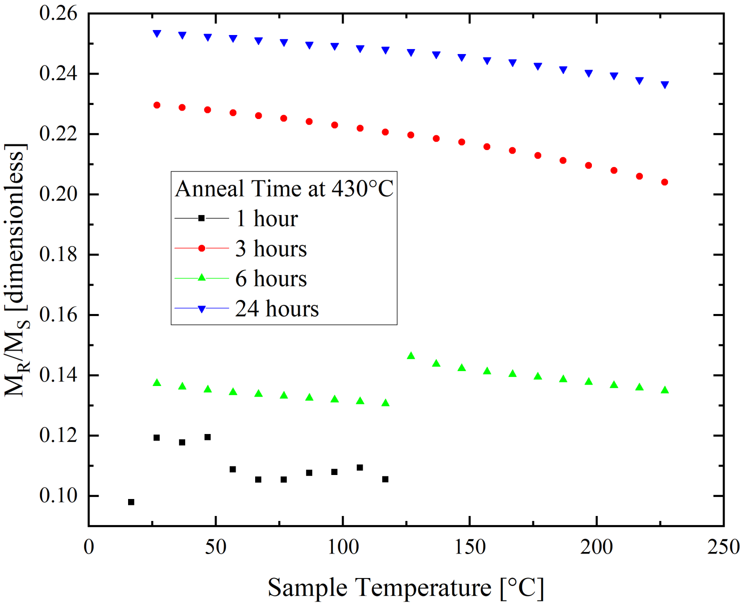

Fig. 6.21 A plot of M_R/M_S against sample temperature for MAG-E samples annealed from the ϵ-phase for 1, 3, 6 and 24 hours. Whilst the initial ratio is a pseudo random property resultant from the initial microstructure of the samples, the behaviour demonstrates that 1 hour of annealing at $430°C$ is insufficient for predictable behaviour and that overheat events, as in the case of the 6 hour sample, can result in this ratio changing from the RT state irreversibly.

the material, leading to the observed value of M_R at $126.85°C$ being greater than that of the value observed at $36.85°C$. Thus, it can be concluded that in the isotropic, as-cast state, annealing is not a suitable method to control the remanence behaviour of the material and no self-ordering behaviour can be observed leading to an increased remanence, with it seemingly being a random property of the sample. However, the relationship between M_R and the annealing time does corroborate the notion that 1 hour annealing at $430°C$ is insufficient time for a feasible material for applications, due to the unstable response to temperature observed for the sample.

This random behaviour can be rationalised by considering that the domain structure is inherently linked to the texture of the sample as τ-MnAl has an easy axis along the c-axis of its BCT structure. As the sample is as-cast, one would assume a near-isotropic texture to form within the sample. This is explored in Chapter 7 further but would imply that each grain is near randomly oriented to one another during the casting process from arc melting. If one assumes the solidification mechanics are dominated by a large equiaxed region and that any resultant texture from the chill and columnar zones around the surface of the melt pools are not dominant of the overall texture, any sample taken from the system would have an inherently random overall texture and thus magnetic polarisation. As such, given all samples taken for this study were taken from a different location within the cast sample, they would all have a random texture associated with them, which would be further affected as the heat treatments necessary were implemented on the sample. As such, they cannot be comparable when considering the behaviour of M_R within this study and a consistent texture must be imparted onto a sample before the affects of annealing on both the remanence and thermal dependency of the remanence for MAG-E can be truly discussed

Kronmüller Magnetic Microstructure Constants Approximations by Annealing Time

In an effort to understand the changing intrinsic variables and coercivity, it becomes important to compare the Kronmüller coefficients as a function of annealing time to investigate whether they dominate the decreasing coercivity as a function of temperature and, if so, whether it is a shape or coupling dependent effect, i.e does α or N_{eff} vary more as a function of annealing time.

Using Equation 6.2, it becomes possible to determine the Kronmüller coefficients from temperature dependent measurements of H_C, M_S and H_A by way of calculation from k, hence the interest in the temperature performance of the alloy system as a function of annealing time and somewhat explaining the change in extrinsic magnetic performance as a function of heat treatment conditions. Figure 6.22 shows the calculated Kronmüller coefficients for MAG-E as a function of annealing time. It is of note that statistics for material annealed for 1 hour at 430°C were not included due to non-physical constant calculation from the data shown in Figure 6.14, such as negative magnetostatic interactions and high error on observation ratios.

Looking to Figure 6.22, it is of note that there is proportionality between the observed Kronmüller coefficients calculated from data captured between and that of $H_C(T = -273°C)$ modelled from coercivities measured in the $(27 \leq T \leq 127)°C$ range. The reason this comparison is made with modelled zero-temperature coercivities is to attempt to minimise the contribution of the unmodelled H_{th} term in comparison. At 24 hours of annealing, however, it can be seen the overall trend in Kronmüller coefficient evolution with annealing time diverge, with N_{eff} increasing from the observed value at 6 hours, with errors small enough that there is no agreement in mutual observation to suggest an accuracy sampling error of a constant value, and α decreasing as a function of time, again obeying the same error argument such that the two measurements are not in agreement

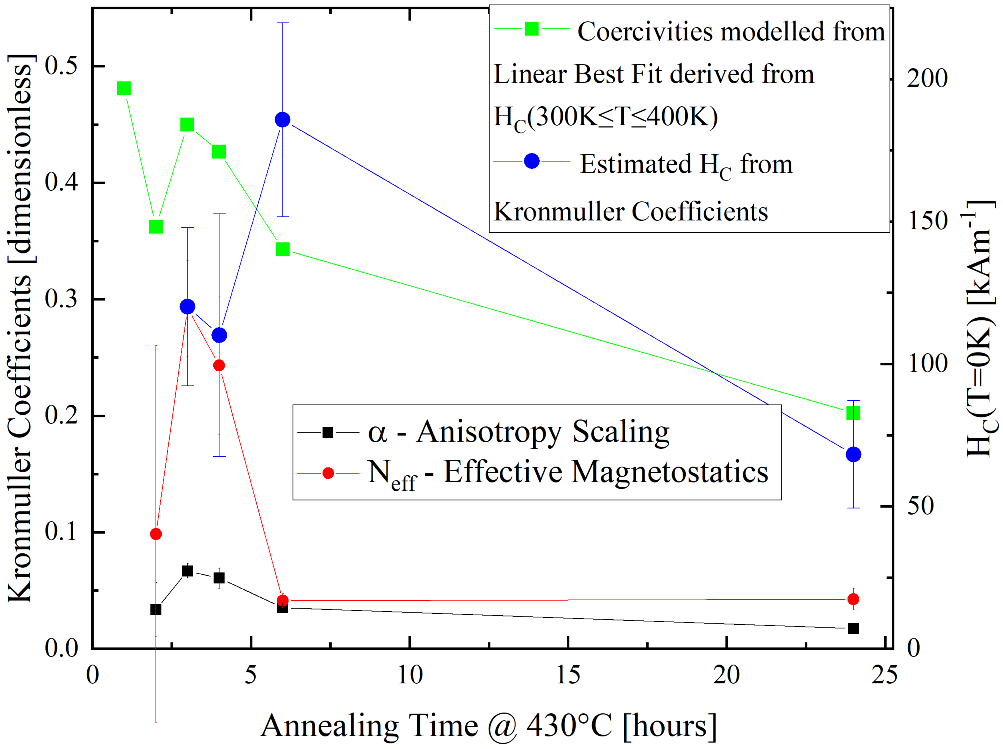

Fig. 6.22 A plot of the calculated Kronmüller coefficients for MAG-E as a function of annealing time at 430°C to facilitate the $\epsilon \rightarrow \tau$ transformation alongside both observed and predicted values of H_C. showing that whilst the calculated variables are of the right order of magnitude, Equation 6.2 does not accurately predict H_C, implying that the ignored H_{th} term is important in determining accurate H_C behaviour.

and represent measurable change in the system. Given this, it would suggest that the coercivity of the system is more sensitive to α variation than that of N_{eff} variation, i.e the coupling between grains dominates over the effective coupling interactions derived from grain morphology when determining coercivity in this case as discussed in Sections 2.3.1 and 2.3.4 . Further, Kronmüller coefficients were fit in the data range $(27 \leq T \leq 127)°C$ rather than the fully measured data range as above this temperature, inflection is observed such that N_{eff} and α becomes negative. Given that all intrinsic magnetic variables and H_C are positive by definition, this cannot be explained at the time of writing and thus this data was discarded for the purposes of fitting.

However, it cannot be said that this model is accurate at predicting the coercive behaviour of the transformed τ-state MAG-E. Looking to the right hand axis of Figure 6.22, one can compare the difference between $T = -273°C$ calculations of coercivity by Equation 6.2 and that of extrapolated data from measured H_C data. Comparing the two data sets, it can be seen that for all but the sample annealed for 6 hours with the non-standard thermal history previously discussed, the estimated zero-temperature coercivity is less than that of that extrapolated by a linear best fit line. Recognising that it is unlikely that this model is representative of zero temperature coercivity approximations as it was initially intended as an engineering estimate for applications in electric motors, the coercivity was remodelled using a logarithmic decay using the equation $b\,ln((T_C - x)/a)$ under the assumption that coercivity decays to zero at T_C with an assumption that $dH_c/dT \propto T^{-1}$. This fit can be seen in Figure 6.23 and shows that by modelling H_C with a logarithmic model, the Kronmüller-derived coercivity is in agreement for 3 of the 4 published calculations shown, if only due to large error on derivation. It is of note that the derived coercivitiy for the 2 hour annealed sample is not included as the propagated error was such that impossible negative coercivities were predicted, meaning any resulting calculation could not be treated with confidence.

In assessment of Figures 6.22 and 6.23, whilst agreement can be derived for some data points for derived Kronmüller coefficients, they do not capture wholly extrapolated behaviour or thermal trends of the coercivity of the heat treated samples. It is of note that samples measured such that the heat treatment was less than 3 hours had associated errors on coefficient calculation that comparison to extrapolated coercivity fits is impossible. Further, it is of note that, despite fitting only data collected prior to overheating, the 6 hour heat treated sample remains anomalous in its Kronmüller coefficient calculations and thus estimated value of $H_C(T = -273°C)$. Further testing below $27°C$ may increase the accuracy of coefficient calculation by providing further data points given the inflection

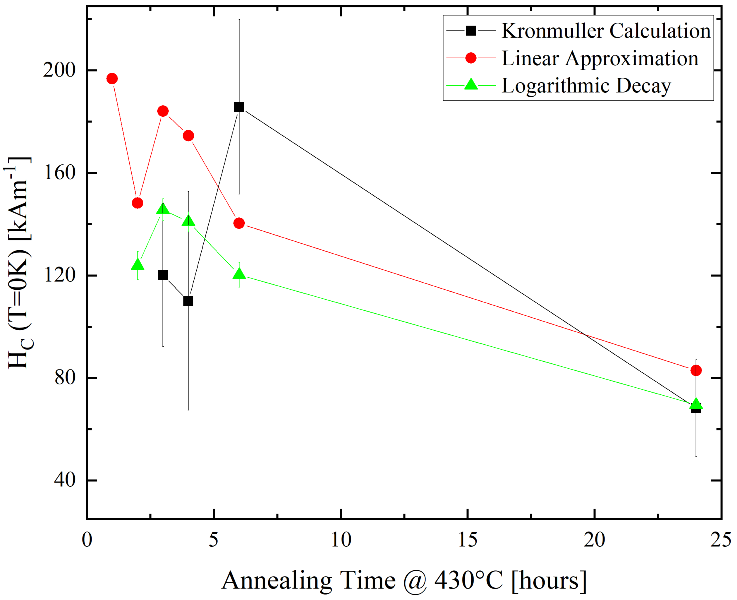

Fig. 6.23 $H_C(T=0K=-273°C)$ as a function of annealing time, estimated by calculated Kronmüller coefficients for MAG-E and extrapolated values of H_C from measurements in the range of $(27-127)°C$ by both linear and logarithmic decay models.

observed at approximately $127°C$, reducing contributions from H_{th} as it is assumed that this term has a temperature dependency.

Should these calculated coefficients be taken as representative rather than that of an anomalous sample, however, it can be interpreted by the change in Kronmüller coefficients that α variation dominates $H_C(t_{anneal})$ at $430°C$. Thus, it can be inferred that from a microstructural perspective, it is more important to manage inter-grain coupling effects rather than grain morphology such that the effective magnetostatic field across the grain is minimised. The form that this structure would take, however, is not put forward, recognising that this would be the subject of micromagnetic simulation and mechanisms to increase α would be process specific.

Grain Growth and Lattice Parameter Change through Annealing at $430°C$

Given that $430°C$ is a temperature already shown to precipitate the metastable $\epsilon \rightarrow \tau$ phase change and that room temperature intrinsic and extrinsic magnetic variables are changing as a result of annealing time, it suggests that not only are grain morphology and coupling a function of annealing time as determined by the Kronmüller equation, Equation 6.2, but also that grain size and lattice parameters may change as a result of annealing conditions given this would change exchange interaction lengths. Referencing theoretical first-principle calculations for an off-stochiometric MnAl binary alloy by Anand, Pulikkotil and Auluck (2014), theory suggests that increasing unit cell volume for a fixed c/a axis ratio of $c/a = 1.298$ sees an increase in unit cell magnetisation, with the Mn on **[000]** sites increasing in magnetisation with a greater response than the antiferromagnetically aligned Al-site occupying Mn atoms increasing in magnetisation [97]. The converse being true for volume compression with a fixed lattice ratio. Looking to Zhao *et. al.* and assuming that C doped alloy behaviour is comparable to that of Ga doped alloy when considering diagonalisation, it can be interpreted that an increase in c/a ratio leads to a decrease in T_C and k with no clear relationship to M_S from the data set, which when compared to Anand, Pulikkotil and Auluck would agree, given the comparability of the 7 nearest neighbour calculations and orientations resulting from Mn-Mn coupling as the crystallographic axes vary.

Looking to the XRD data shown in Figure 6.15, it is clear that by 1 hour, annealing at $430°C$ tends towards an equilibrium phase population, with no peak emergence or elimination occurring as a function of annealing time that can be clearly discerned from background data. However, the lattice parameters can be fit from the datasets and seen in Table 6.5. This data was captured using a Cu source rather than an Ag source as the data displayed in Figure 6.15 in order to maximise the $d(2\theta)$ sensitivity of the experiment with the understanding that the FWHM of the peak profile determines crystallite size by Equation 4.3 and that peak position determines lattice parameter lengths. Given that the expected lattice parameter shifts were anticipated to be of the order of previously discussed work in Chapter 5.4.1 or less, diagonalisation ratios changes of the order of 0.001 were anticipated during experimental design.

In order to best capture the exact peak positions, as many corrective factors as possible must have been understood in order to ensure consistent lattice parameter site identification. Given manual loading into the diffractometer using a bulk background holder with the diffraction plan and z height set by means of a raised lip and glass slide, corrective measures were taken during data analysis. The shift in the z axis caused by mounting results in a systematic shifting of all lattice parameters and, as such, initial peak positions were measured against that of a known standard from the International Crystal Diffraction Database entry (00-030-0028) for τ-MnAl ($M_{55.5}Al_{44.5}$). Recognising that there would be differences also inherent to composition, averages between observed angle and reported angle in 2θ, an average was taken from all deviated peaks and applied as a zero correction to the anneal-specific XRD measurements. Further, following general peak identification,

Annealing Time	a [Å]	c [Å]	c/a	Volume [Å^2]	Crystallite Size [nm]
1	2.75890±0.00009	3.5623±0.0004	1.2919±0.0002	9.834±0.001	39±5
2	2.7585±0.0001	3.5626±0.0005	1.2915±0.0002	9.828±0.001	21±2
3	2.75854±0.00009	3.5626±0.0004	1.2915±0.0001	9.828±0.001	26±2
4	2.76016±0.00007	3.5626±0.0003	1.2907±0.0001	9.8334±0.0008	27±2
6	2.75905±0.00009	3.5645±0.0003	1.2919±0.0001	9.8345±0.0009	27±2
24	2.7605±0.0001	3.5664±0.0004	1.2916±0.0001	9.843±0.001	40±6

Table 6.5 A table of lattice parameters and Scherrer-derived (see Equation 4.3) crystallite sizes for samples of MAG-E annealed at $430°C$ to precipitate the $\epsilon \rightarrow \tau$ transformation.

the [002] and [110] peaks were isolated for each sample to fit the c and a lattice parameters respectively. Using data collection bin errors calculated in Figure 4.6, a Gaussian peak model can be constructed from the $I(2\theta)$ data and the planar spacing, with associated fitting error, calculated to derive lattice parameters.

Table 6.5 shows that with annealing time, lattice parameters are not constant but do show minor variation. Initially it can be seen that the unit cell is in a strained state, greater than that achieved for longer annealing times, implying that the lattice mismatch between the parent ϵ-phase and resulting τ-phase may result in lattice distortions that, as annealing time increases, decay to an equilibrium lengths of $a = (2.7858 \pm 0.0001)$Å and $c = (3.5626 \pm 0.0004)$Å, though there appears to be an outlier data $t_{anneal} = 4h$ for the calculated a lattice parameter. Looking to examine the change of behaviour in the 6 and 24 hours annealed samples, it is of note that the c axis shows an expansion of $(0.05 \pm 0.01)\%$ and $(0.08 \pm 0.01)\%$ respectively against what is interpreted to be the local equilibrium value for the c-axis in a single phase state shown for samples annealed for 3 to 4 hours at $430°C$. An explanation of this phenomena comes upon closer examination of the XRD pattern for the 24 hour annealed sample when compared to that for a 6 hour or the interpreted as near-equilibrium 4 hour anneal, shown in Figure 6.24 where the two principle peaks of the βMn phase become detectable at 42.2549° for [221] and 44.6218° for [310] referencing the International Crystal Diffraction Database entry (04-003-1750) for β-Mn ($M_{75}Al_{25}$), allowing for minor shifts in peak position caused by misalignment and composition variation. Thus, it can be theorised that this increase in c axis length is caused by a strain to the grain structure caused by βMn precipitation under the heat treatment conditions and thus a shift away from local equilibrium conditions, rather than continued dislocation movement and system relaxation from reducing residual stress.

The impact of these lattice constant changes can be seen more clearly in Figure 6.25 where a decrease in lattice parameters corresponds to an increase in M_S. Given that no additional phases can be detected by XRD for any sample annealed for less than 24 hours, it can be concluded that either phase precipitation is less than the detectable limit of

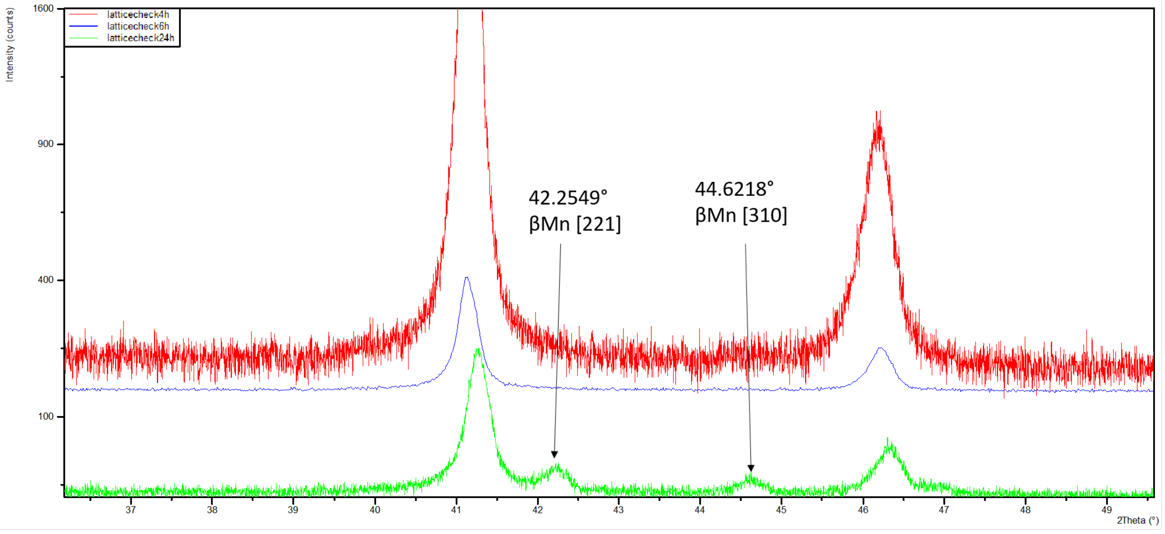

Fig. 6.24 2θ-XRD data for MAG-E samples annealed from the ϵ-phase at $430°C$ for 4, 6 and 24 hours. This plot highlights that MAG-E is not truly stable at $430°C$, showing the emergence of βMn XRD peaks as annotated onto the plot.

approximately 5% phase population and this is causing this change in properties or that the change in lattice structure is causing a change in intrinsic magnetic properties, i.e. residual stress from the $\epsilon \rightarrow \tau$ transformation has an effect on the magnetic state of the τ phase as it is in an excited, strained state. If one assumes that M_S is a linear sum of the phase population of ferromagnetic states in the system, the change between the 3 hour annealed sample and the 6 hour annealed sample sees a decrease in M_S such that $M_{S,6h} = (0.7746 \pm 0.0002) M_{S,3h}$ with no detectable secondary phase precipitation. If one assumed that the sum magnetic moment per unit cell was constant when considering observed lattice parameter changes, this would imply a measurable phase population change not present in the XRD measurements. Thus, referencing Anand, Pulikkotil and Auluck (2014), it can be inferred that changes in the c-axis lattice parameter of less than 0.01Å can have a measurable effect on intrinsic magnetic properties and it has been presented that it is in theory possible to control this parameter change by heat treatment [97].

Exchange Constants and Spin Wave Stiffness Constants of MAG-E by Annealing Time

It is of note that exchange constants and spin wave stiffnesses are not usually measured from such complex samples and as such, the data presented in this subsection could be considered inaccurate. Its inclusion in this discussion is limited to determining if any trend with annealing time is observable against intrinsic magnetic property variation and

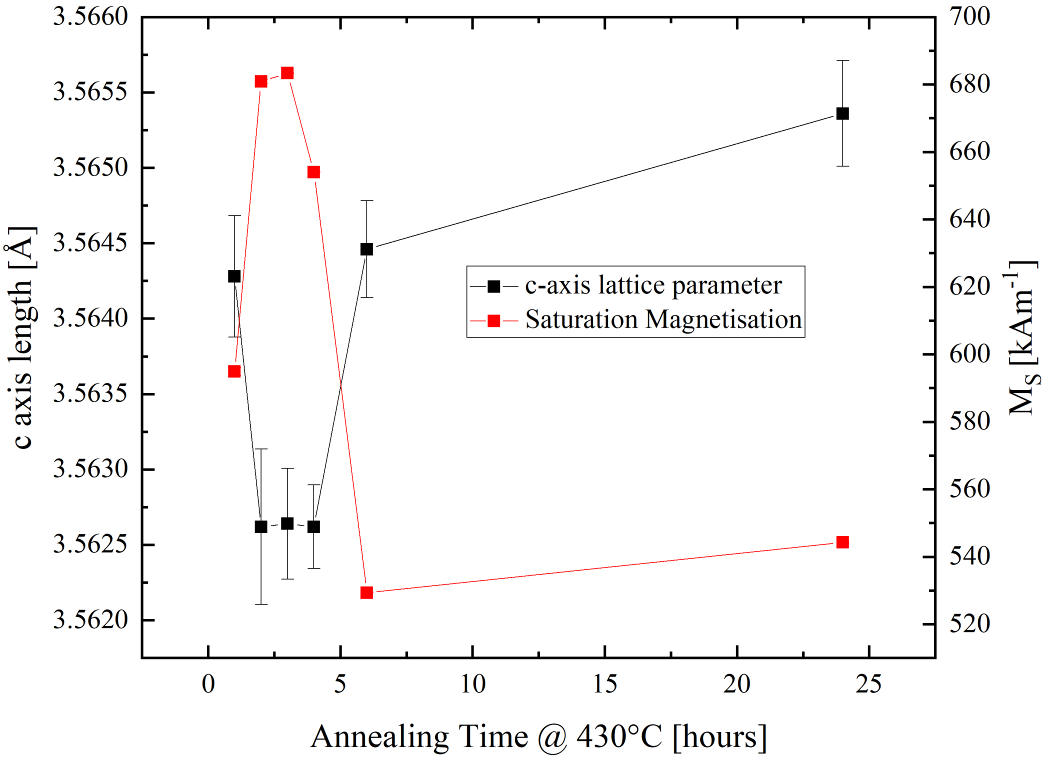

Fig. 6.25 M_S and c-axis lattice parameters plotted against annealing time for samples of MAG-E annealed at 430°C to precipitate the $\epsilon \rightarrow \tau$ transformation. From this, it becomes possible to infer that there is a relationship between the two variables and it may be possible to tune intrinsic magnetic properties with heat treatments.

should not be considered an accurate source of these constants for modelling applications or further calculations as there may be influence from additional material properties not considered in this subsection.

Following logic laid out in "Micromagnetism and the Microstructure of Ferromagnetic Solids" by Kronmüller and Fähnle [37], one can express the Bloch equation as:

$$J_S(T,0) = J_{S,0}(1-(\frac{T}{T_0})^{\frac{3}{2}}) \tag{6.3}$$

where $J_{S,0} = \mu_0 M_{S,0}$ and $J_S(T,0) = J_{S,0}$ at zero applied magnetic field and temperature, i.e is the full saturation magnetisation response of a material once all paramagnetic contributions have been removed. This is known as Bloch's $T^{\frac{3}{2}}$ law. Under the assumption that the energy dispersion of a spin wave in a ferromagnetic material follows the equation $\epsilon_k = D_{sp}k^2$ where ϵ_k is the energy dispersion term, k is the wave number and D_{sp} is the spin wave stiffness constant, it becomes possible to determine the characteristic temperature of Bloch's law. From this, it becomes possible to formulate the following equations:

$$T_0 = (\frac{M_{S,0}}{0.117\mu_B})^{\frac{2}{3}}\frac{D_{sp}}{k_B} \tag{6.4}$$

$$J_S(T,0) = \mu_0 M_{S,0} - \Phi T^{\frac{3}{2}}, \tag{6.5}$$

where

$$\Phi = (\frac{k_B}{D_{sp}})^{\frac{3}{2}} 0.117\mu_B\mu_0 \tag{6.6}$$

where μ_B is the Bohr Magneton and k_B is Boltzmann's Constant. This means that fitting the Saturation Magnetisation against Temperature can derive Spin Wave Stiffness Constants by annealing process and be used to determine the Exchange Constant, A, for the material as a function of annealing time and material temperature by the relationship:

$$A(T) = \frac{M_S(T,0)D_{sp}}{2g\mu_B} \tag{6.7}$$

where g is the Lande factor [37]. The determination of this exchange constant is useful as it firstly determines whether this is affected by the annealing process and secondly is used in micromagnetic research to understand the potential effects and dimensions of domain wall effects.

Looking to Figure 6.26, one can see that the data may not comply with the Bloch $T^{\frac{3}{2}}$ model given a deviation from a linear best fit applied to the data. This is further compounded by a quadratic-like dependency emerging within the residuals from the fit,

Annealing Time [h]	D_{sp} $[meV\AA^2]$	A $[pJm^{-1}]$	$J_{S,0}$ $[T]$
1	340 ± 60	9 ± 2	0.787 ± 0.009
2	153 ± 3	4.98 ± 0.1	0.951 ± 0.004
3	160 ± 2	5.22 ± 0.06	0.948 ± 0.002
4	157 ± 1	4.94 ± 0.04	0.913 ± 0.001
6	187 ± 1	4.72 ± 0.04	0.736 ± 0.001
24	180 ± 2	5.7 ± 0.1	0.759 ± 0.002

Table 6.6 A table of micromagnetic constants derived from the application of Bloch's $T^{\frac{3}{2}}$ law on the magnetic hysteresis data for each heat treatment. It is of note that the exponent of said law did not truly reflect the data trend, instead showing variations in this exponent across each sample.

observable in Figure 6.27 implying that this model does not fully capture the behaviour of the system. However, if one uses this model to calculate these micromagnetic variables for the sample annealed at 430°C for 3 hours, it can be calculated that the Spin Wave Stiffness Constant $D_{(sp,3h)} = (160 \pm 2)$meVÅ, which at room temperature would lead to an Exchange Constant $A_{3h} = (5.22 \pm 0.06) pJm^{-1}$, in the same order of magnitude as $Nd_2Fe_{14}B$ and $BaFe_{12}O_{19}$. The calculated values for D_{sp} and A across the annealing spectrum can be seen in Table 6.6

In a similar fashion to Kronmüller calculations, this initial run at calculating D_{sp} and A as a function of annealing time by use of the Bloch equation was limited to data captured in the temperature range $(27 \leq T \leq 127)°C$ to account for the unique measurement conditions of the 6 hour annealed sample as well as limit the deviation from the temperature power dependency observable in the residuals from full fits shown in Figure 6.27. However, from these fits it can be seen in Table 6.6 that the Bloch equation fits produce similar proportionality in determination of $J_{S,0}$ as observed in M_S at room temperature shown in Figure 6.25. Further, given that it has been previously shown that lattice parameter change can precipitate intrinsic magnetic variable changes in the $\tau - MnAl$ system by Anand, Pulikkotil and Auluck (2014) and measured in Figure 6.25, it can be inferred that the relaxation of the unit cell during annealing and resultant change in lattice parameters precipitates a change in Exchange Constant, A, and Spin Wave Stiffness Constant, D_{sp}. Further, as crystallite size is broadly invariant following 'complete-transformation' at some point between 1 and 2 hours annealing as shown by Table 6.5 as determined by the Scherrer equation, it can be inferred that annealing at 430°C can be used to not only tune extrinsic magnetic variables by way of grain coupling and morphology changes determined by the Kronmüller coefficients but also exchange behaviour to change intrinsic magnetic properties. It is of note, however, that the calculated Exchange Constants are approximately twice that expressed in Bance (2017), implying that either the deviation from a $T^{\frac{3}{2}}$ dependency and forcing a local fit causes a significant overestimation in this parameter or the addition of a few percent Ga into the system has a measurably significant effect in changing exchange behaviour [94].

An application of this tuning is that of single domain particle size and GSDCP theory, discussed in Section 2.3.5. The Stoner-Wohlfarth model is that of a single domain particle and thus is more appropriate to modelling a bulk system with grains of single domain size. Further, if a material has grains of below the critical size 2.17 for domains to form, coercivity mechanisms reliant on domain wall motion no longer exist, meaning that bulk coercivity for a material consisting of these particles will increase as the magnetisation of all particles must be switched to an opposite polarisation to see a change in bulk magnetisation direction as opposed to a change in the average orientation of the sum of the magnetic domains in the system. As a result, being able to tune this critical domain size without changing the grain size presents the opportunity to create a sample with suboptimal grain size and anneal such that this critical diameter increases as a result of unit cell relaxation to force existing grains into a single domain state or increases theoretical domain wall thickness such that H_C increases due to the $1/D$ dependency theorised by GSDCP theory.

Considering the deviation from a linear fit observable in Figure 6.26 and the non-random distribution of residuals observable by fit in all but the 1 hour annealed sample, previously discussed to be unstable in temperature-dependent magnetic measurements, it can be concluded that the $\frac{3}{2}$ power of temperature dependency does not apply in this case and that there is a variation from this. Instead, expanding the model stated in Equation 6.5 to

$$J_S(T,0) = \mu_0 M_{S,0} - \Phi T^{\xi}, \tag{6.8}$$

where ξ captures this change in temperature dependency. By calculating $M_{S,0}$ using the same non-linear fitting technique used to calculate $H_{C,0}$ by fixing a zero state at T_C and allowing a free fitting of the data under the equation form $M_S \approx b\ ln((T_C - x)/a)$ under the same assumptions expressed in previous subsection assuming a general inverse temperature dependence for M_S. By using this as an approximation of $M_{S,0}$, recognising that it is an arbitrary fit, one can rewrite Equation 6.8 as

$$ln(J_{S,0} - J_S) = ln(\Phi) + \xi ln(T) \tag{6.9}$$

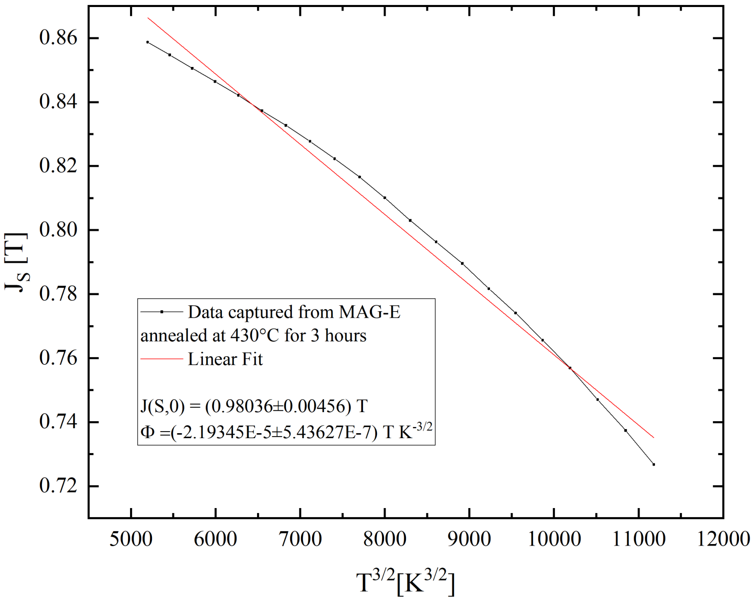

Fig. 6.26 A Bloch equation fit following Equation 6.5 for a MAG-E sample annealed at $430°C$ for 3 hours, forcing the $\epsilon \rightarrow \tau$ transformation. It is clear from the distribution of observational data points against the best fit line and examination of the residuals (shown in Figure 6.27) that the $T^{\frac{3}{2}}$ behaviour predicted may not be the most appropriate model to explain observations.

allowing independent determination of both the temperature dependence of the Bloch model and the micromagnetic spin constants as a function of annealing.

Utilising this fit, it can be found that the average exponent for all annealed samples excluding the outlier 1 hour annealed sample is $\xi = (1.77 \pm 0.02)$, implying that the temperature dependence of the material is actually closer to a $T^{\frac{7}{4}}$ relationship for $\tau - MnAl$ rather than the stated $T^{\frac{3}{2}}$ relationship derived from Bloch's equations. At the time of writing, it is unknown why this deviation occurs, recognising that this would be an area of investigation at a computational quantum mechanical level to derive this deviation in this system and it is well beyond the scope of this study, also recognising that additional datasets to confirm this observation for additional castings may also be appropriate to confirm observations. Using the refitted data to calculate both adjusted Exchange Constant values and Single Domain Critical Grain Sizes, Figure 6.28 was generated and it can be seen that the changes in model used to calculate the Exchange Constant, A, result in a ratio of approximately (2.79 ± 0.03) between free-fit calculations and those fitted to a $T^{\frac{3}{2}}$ relationship. Both models compute that the single domain grain radius is of the

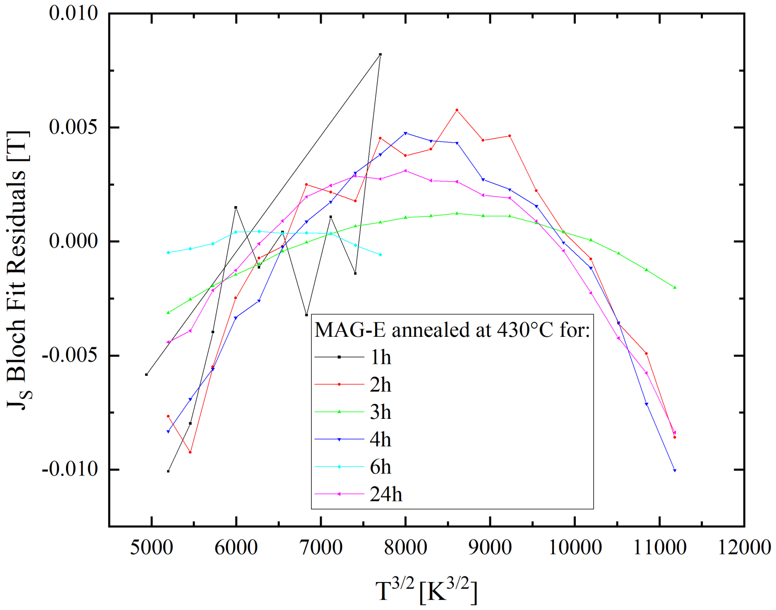

Fig. 6.27 A plot of Bloch equation fit residuals following Equation 6.5 for a MAG-E sample annealed at $430°C$ for 3 hours, forcing the $\epsilon \rightarrow \tau$ transformation. The quadratic-like trend in these residuals suggest that the $J_S(T)$ proportionality has not been best captured by Equation 6.5.

order of hundreds of nanometres and that it may be possible to tune this size depending on annealing time if one interprets the change in behaviour between 2-4 and 6 hours as relaxation of the lattice rather than initial precipitation of the βMn present in the 24 hour annealed sample. Given that average grain size is shown to not deviate during this anneal in Table 6.5 and is below either calculated limit, it can be interpreted that the materials discussed in this section are on average composed of single domain grains and that the casting route used can produce sufficiently small grains as to prevent domain formation occurring on average throughout the system, recognising that the Scherrer equation measures the system average and does not provide a standard deviation for the distribution in the system.

Dominant Coefficient of Change Resulting from Heat Treatment at $430°C$

Concluding this subsection discussing the effects of annealing ϵ-MAG-E at $430°C$, it can be concluded that, whilst 1 hour is sufficient to precipitate the $\epsilon \rightarrow \tau$ transformation such that the remaining ϵ-phase population is undetectable by XRD refinement, intrinsic and

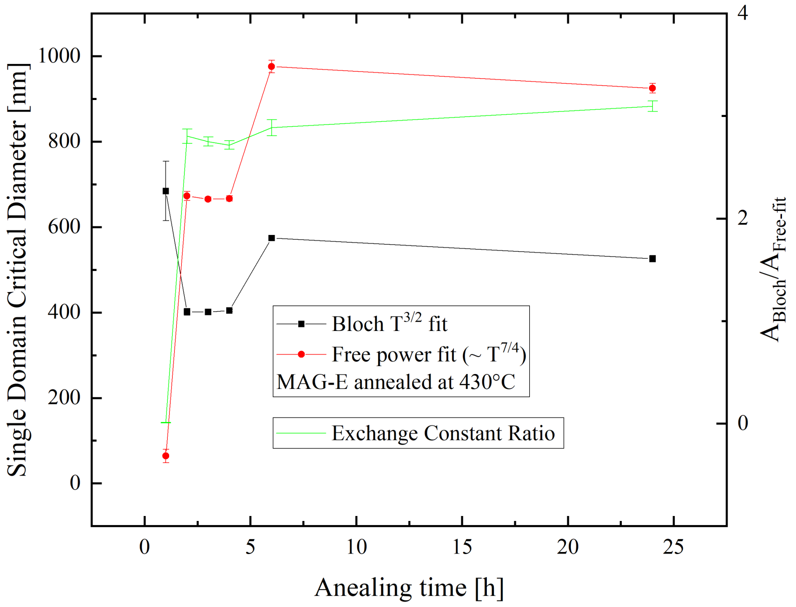

Fig. 6.28 Single Domain Critical Diameters as calculated by Equation 2.17 using A as calculated by $T^{\frac{3}{2}}$ and $T^{\frac{7}{4}}$ fits, with the ratio between these two Exchange constants plotted against the RHS y-axis. This demonstrates that increased annealing time for a stable structure may not increase this diameter but the precipitation of βMn may.

extrinsic magnetic properties are not constant as a function of annealing time and phase population. Whilst extrinsic magnetic properties are anticipated to change as a result of heat treatment due to changes in the microstructure of the system, intrinsic properties are not due to their origin in the crystallography and exchange interactions at the unit cell scale, resulting in the interactions of electron shells within the structure of the unit cell.

Looking first to the extrinsic changes, it can be seen that the optimum annealing time for maximum H_C is that of 3 hours as measured, with decay observed in room temperature values for longer annealed samples. Attempting to model this behaviour with Kronmüller coefficients to investigate if it was a grain interaction/morphology change as a function of annealing time, it was found that both the anisotropy scaling coefficient, α, and the effective magnetostatic contribution N_{eff}, as defined by Equation 6.2 saw maxima at 3 hours annealing time but that the relative variation in N_{eff} being greater than that of α. Given that the calculated anisotropy is an order of magnitude greater than that of the saturation magnetisation and that both α and N_{eff} are approximately bound in the range of $0 \lessapprox \alpha,\ N_{eff} \lessapprox 1$, and with N_{eff} being measured to be an order of magnitudes greater than α, there is greater scope to take advantage of the higher anisotropy field and increase

α to increase coercivity rather than attempting to change grain morphology to reduce the magnetostatic interactions and thus reduce N_{eff} [94]. Whilst it is shown that the annealing process has an effect on both variables, it is also of note that neither intrinsic magnetic variable linked to α and N_{eff}, namely H_A and M_S, are constant as a function of annealing time. This coupled effect between the 4 variables as a function of annealing time implies that there is a lesser degree of control in annealing at $430°C$ to influence microstructure such that preferential states can be reached to increase coercivity without also changing lattice parameters of the ferromagnetic state or precipitating equilibrium states. As such, it can be concluded that, whilst annealing to achieve a change in microstructure may be possible at this temperature, it should not be considered an optimum route with post- or pre-anneal processing utilised to set a preferential microstructure to maximise coercivity.

Further examining the microstructural dynamics of MAG-E during the $\epsilon \rightarrow \tau$ annealing process, three key findings can be determined from XRD. The first is that for the composition $Mn_{57.1}Al_{39.5}Ga_{3.4}$, 24 hours annealing at $430°C$ is sufficient for initial precipitation of the equilibrium, paramagnetic βMn phase. This is somewhat contradictory to the work of Mix *et. al.* but given the lower Ga concentration in the alloys, suggests that the equilibrium $L1_0$ phase may not be forming in sufficient ratios to maintain stability [61]. However, it is of note that intrinsic magnetic properties did not see significant decrease at the precipitation of the βMn phase, implying that as other studies have shown, βMn precipitation may be beneficial. It is, however, not beneficial for the coercivity of the material, with room temperature $H_C(t_{anneal} = 24h) = (56.6 \pm 0.2)kAm^{-1}$ compared to the optimum value of $H_C(t_{anneal} = 3h) = (118.4 \pm 0.8)kAm^{-1}$ suggesting that in the as-annealed state, the inclusion of βMn precipitates is detrimental to BH_{max} improvement and thus achieving Gap Magnet criteria (see Table 1.1 without additional processing, with the precipitation offering no increase in M_R over single phase samples.

The second observation from XRD techniques is that, as determined by the Scherrer Equation, average crystallite size, interpreted to be analogous to grain size, does not deviate as a result of annealing time in single phase samples. This implies that annealing at $430°C$ to facilitate a complete $\epsilon \rightarrow \tau$ transformation does not risk grain growth and a transition from a single domain grain size to a grain diameter above the calculable diameter from Stoner-Wohlfarth theories in which a multi-domain state will form. This technique does not provide information about the distribution of grain sizes, only the average grain illuminated in the exposed material volume during the XRD experiment, namely approximately $(5 \times 5 \times 0.002)mm$ which is believed to be be representative of the material given that samples were not taken in a geometrically specific methodology and that surface layers potentially contaminated with oxide formation were intentionally excluded from XRD experiments. As such, it can be concluded that for quench and anneal production methods for τ-MAG-E, the initial casting and annealing time to set the precursor ϵ-phase are dominant in determining average grain size, with the transformation anneal having little effect prior to equilibrium phase formation.

The third and arguably most important observation is that of lattice parameter variation in single phase samples. It was observed that from the initial single phase sample measured, namely material annealed for 1 hour, compared to that annealed for 2, 3 and 4 hours, there is a measurable shift of the c/a-axis ratio, namely that at 1 hour of annealing $(c/a)_{1h} = (1.2919 \pm 0.0002)$, at 2-3 hours of annealing $(c/a)_{2,3h} = (1.2915 \pm 0.0002)$ and 4 hours $(c/a)_{4h} = (1.2907 \pm 0.0001)$. Whilst these results were obtained using techniques zeroing lattice parameters from an undoped sample and accounting for z-axis shift, the variation in lattice parameters indicate that a c/a-axis ratio is optimum for this system. Referencing calculations performed by Ananad *et. al.* it is shown that for a constant c/a-axis ratio, volume changes can have an effect on the overall magnetisation of the unit cell, as such it could be hypothesised that by instead changing this ratio, similar effects may be observed due to changing the relative distance and thus exchange integral between Mn nearest-neighbour pairs in the system [97]. A mechanism for this lattice parameter shift is hypothesised, suggesting that the precipitation of the τ-phase causes internal residual stress due to initial lattice mismatch between the parent ϵ-phase and τ-phase, which is removed through the system through thermally activated dislocation transport mechanisms. This would also explain the instability in the thermal dependency of the intrinsic magnetic properties of the 1 hour annealed sample, as lower energy dislocation transport mechanisms may be activated to reduce residual stress that has already dissipated in samples that have undergone longer anneals.

Assuming composition homogeneity between all measured samples, the variation in lattice parameters explains the change in intrinsic magnetic properties, namely the saturation magnetisation, magnetocrystalline anisotropy and exchange stiffness constant. This potentially allows the exploitation of this relaxation to tune these parameters to maximise M_R, H_A or D_{crit} depending on engineering requirements. Further work to develop numerical predictions on this behaviour and understand better the effects of temperature would be required to develop this technique, but it does suggest an alternative to composition variation to change intrinsic magnetic properties for this material as well as confirming the limits of the assumption around the homogenous composition on measured sample lengthscales.

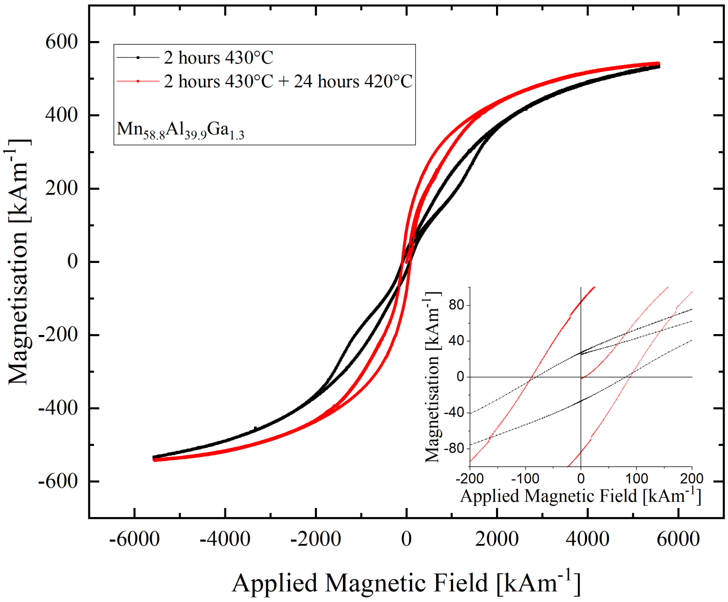

Fig. 6.29 The MH curve of composition Ga_1 after a 2 hour anneal at 430°C and then a subsequent anneal at 420°C. The inset is a zoomed section of the same plot to highlight the extrinsic properties of the composition before and after the annealing process.

6.3.2 Composition Effects on Optimum Annealing at (420, 430)°C

As an aside, it can be seen from Figure 3.2 that each composition responds differently to annealing with no clear trend to any of the specific elements within the ternary system dominating the effect. As such, it was deemed of interest to look at the long-term annealing behaviour of three target compositions to see if an optimum M_S was achieved. Given the thermal stability demonstrated by Mix *et. al* for the MnAlGa system, thermal decay into equilibrium phases was not anticipated for this study [61]. The three selected compositions for testing were Ga_1, Ga_3 and Ga_4 (see Table 6.1 for exact compositions) in order to assess the annealing behaviour across both phase precipitation space as shown in Figure 6.3 and resultant sample M_S space as shown in Figure 6.4.

The experiment was such that the samples underwent the same 2 hour anneal of the water quenched ϵ-state to precipitate the $\epsilon \rightarrow \tau$ transformation as the previously discussed work and then a subsequent anneal at 420°C for 24 hours in a room atmosphere box furnace to ensure comparability between the two states. The samples were water quenched following this 24 hour anneal to ensure consistent cooling behaviour between compositions. The results of this process for Ga_1 can be seen in Figure 6.29 and show that the additional annealing time can show significant improvement for k as demonstrated by the gradient. The calculated variables from both plots as well as the percentage change following the 24 hour anneal can be found in Table 6.7. The shape change between the two hysteresis loops may be attributed to sample measurement orientation against inherent texture and thus average easy/hard magnetic direction within the material as a result of annealing and thus microstructural changes in the metastable system, meaning that any assessment on the increase in M_r would require additional testing with sample orientation against casting heat flow directions controlled and for the samples to be measured on a rotating sample holder in order to ensure consistent average easy/hard axis measurement within the system. Overall, the additional annealing time can be seen to have a positive effect on composition Ga_1 with neither intrinsic nor extrinsic variable seeing a decrease.

Further, looking at Figure 6.29, the non-uniform shape present in the 2 hour annealed sample, interpreted to be the interaction of a secondary ferromagnetic phase arranged ferrimagnetically, is not present in the hysteresis from the longer anneal. Either this implies that the secondary phase is no longer present within the sample or that it has aligned itself such that the two domains across the two phases are aligned constructively but this presents an increase in magnetic performance, significantly increasing M_R as a result of a lack of ferrimagnetic coupling.

Given the small change in M_S following the anneal of Ga_1, it could be concluded that the phase population of the τ-phase has not changed significantly. As the τ-phase is metastable, transforming from the ϵ-phase, it can also be assumed that the main mechanism of property change through annealing is through dislocation transport and stress-relaxation throughout the system. Given the significant negative change in k, an estimation of the Magnetocrystalline Anisotropy Energy (MAE) for the material and thus derived from the crystalline structure, it can be assumed that the annealing process has led to a change in lattice parameters, thus changing this potential across the unit cell but in such a fashion that it was insufficient to significantly change the average exchange lengths, and thus the Mn-Mn interactions where the magnetisation of the system is derived from [97].

Looking to composition Ga_3, one can see the results in Figure 6.30. Unlike the behaviour observed for composition Ga_1, the opposite is the case in this example with both intrinsic and extrinsic variables seeing a decrease as a result of the annealing process. Much like composition Ga_1, the change in M_S is small enough such that metastable decay into the equilibrium phases is not suspected to be the dominating factor but rather that the removal of stress from the system by thermally activated dislocation transport has seen a shift of lattice parameters to a less favourable state for magnetic properties. Indeed,

	Ga_1	Ga_3	Ga_4
	Before		
M_S $[kAm^{-1}]$	589±0.8	588±5	535±2
k $[kJm^{-3}]$	2470±30	2000±200	1840±80
M_R $[kAm^{-1}]$	27.0±0.2	131.29±0.02	77.69±0.01
H_C $[kAm^{-1}]$	80.5±0.4	99.2±0.2	86±1
	After		
M_S $[kAm{-}1]$	564.2±0.5	569.3±0.8	540.9±1
k $[kJm^{-3}]$	2330±20	1710±40	1610±70
M_R $[kAm^{-1}]$	83.9±0.3	123.61±0.01	98.33±0.02
H_C $[kAm^{-1}]$	88.5±0.1	84.7±0.5	75.0±0.2
	Percent Change		
M_S [%]	-3.18±0.02	-3.11±0.03	1.150±0.005
k [%]	-29±3	-15±1	-12.2±0.7
M_R [%]	211±1	-5.849±0.001	26.572±0.007
H_C [%]	9.98±0.05	-14.6±0.1	-12.7±0.2

Table 6.7 A table displaying the effects of a 24 hour anneal on MnAlGa compositions Ga_1, Ga_3 and Ga_4 at $420°C$ already transformed to the τ state by a 2 hour anneal at $430°C$. The percent change in each variable demonstrates that slight composition changes by a few atomic percent can completely change the material response to annealing.

it suggests that composition sees variable improvement in a stressed state, such that the non-equilibrium environment following $\epsilon \rightarrow \tau$ transformation may provide a beneficial stress state for magnetic properties and further investigation for a Time-Temperature-Transformation study evaluating these properties may be in order.

Finally, examining the plot for Ga_4 shown in Figure 6.31 and associated variables in Table 6.7, one can see a trade-off between variables following the anneal. M_S and M_R increase as a result and k and H_C decrease. Given that M_R can be understood as a percentage of M_S where average domain polarity is orientated in the direction of measurement resulting in an observable stray-field, this effect can be understood as being influenced by the shift in M_S. Indeed, all three compositions show correlation between the intrinsic variables, M_S and k, and extrinsic variables, M_R and H_C but not a directly observable relationship. This thus implies that microstructure is evolving during the annealing process such that it is also affecting these variables.

Taking the variation in H_C across all three samples and using Equation 6.2, the Kronmüller equation, as well as the equation for H_A from Equation 3.3, one can see that the coercivity from a material can be directly compared to its intrinsic magnetic variables by arbitrary material constants previously discussed. Dropping the temperature dependent factor, H_{th} and rearranging, one can formulate the following:

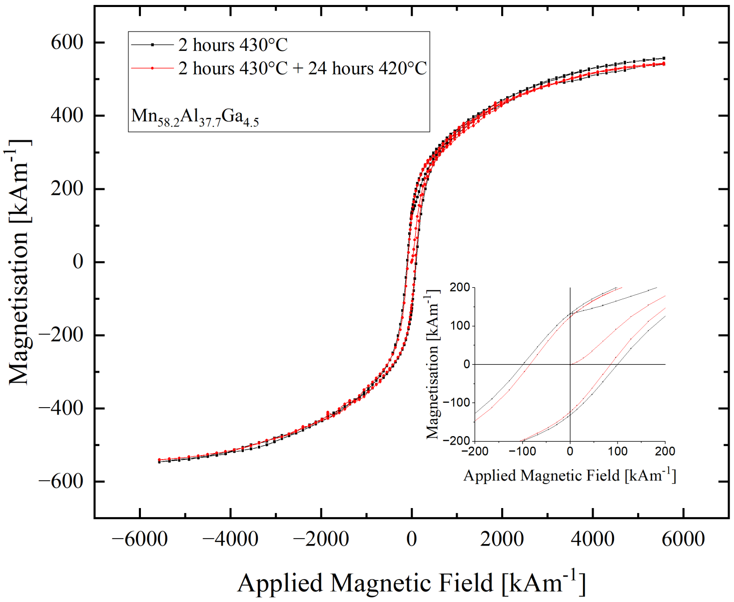

Fig. 6.30 The MH curve of composition Ga_3 after a 2 hour anneal at $430°C$ and then a subsequent anneal at $420°C$. The inset is a zoomed section of the same plot to highlight the extrinsic properties of the composition before and after the annealing process.

$$H_C = \alpha \frac{2k}{\mu_0 M_S} - N_{eff} M_S, \;\; T = const. \tag{6.10}$$

Examining the trend across the three compositions, one can create a variable space plot for α and N_{eff} based upon the observations in Table 6.7. This plot is shown in Figure 6.32 and shows the effect of the annealing on the microstructure from a micromagnetics perspective. In the case where there was no microstructural change, i.e. no grain growth or internal stress reduction in the system, one would expect these plots to remain constant as the system does not change its self-interaction parameters but as is observable, this is not the case. Both Ga_1, Ga_3 and Ga_4 see a decrease in the linear relationship between N_{eff} and α as a result of the additional heat treatment. When plotted in this format, the gradient of the straight line plot modelled with a $y = mx + c$ relationship is $m = \frac{2k}{\mu_0 M_S^2}$ which, referencing Equation 2.20, means $m = 2\kappa^2$. Using this metric, one can say that this heat treatment has magnetically softened compositions Ga_1, Ga_3 and Ga_4 but consistent extrinsic variable change between the three compositions is not present. Thus, any heat treatment designed to improve extrinsic properties in a MnAlGa alloy will need to be individually investigated but system softening is to be expected as a result.

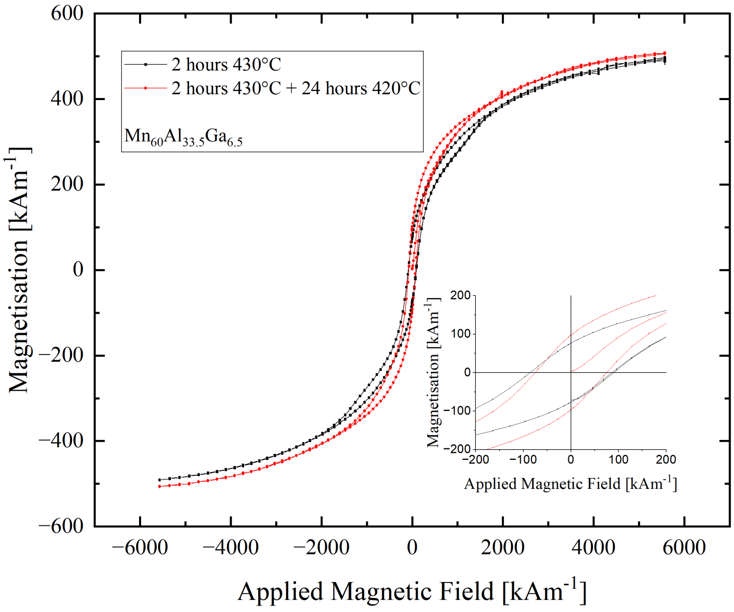

Fig. 6.31 The MH curve of composition Ga_4 after a 2 hour anneal at $430°C$ and then a subsequent anneal at $420°C$. The inset is a zoomed section of the same plot to highlight the extrinsic properties of the composition before and after the annealing process.

6.4 Conclusions

Evidence laid out shows that the addition of Ga into the τ-MnAl system has an effect on a number of variables, both magnetic and crystallographic. Whilst the efficacy of Ga has been outlined in previous work, efforts to optimise the composition at low Ga levels had not previously taken place. These studies show that the addition of Ga changes the metastable $\epsilon \rightarrow \tau$ transformation, but that the change in transformation rate is not trivial. Analysis of nearest composition pairs with respect to Mn concentration shows that the increase of Ga in the alloy increases the transformation rate but that it varies wildly over the composition space explored. This suggests that further work will be able to optimise the transformation time and temperature for a chosen composition to maximise phase population and M_S.

When examining the composition space explored across a standardised annealing parameter space, it can be shown that all compositions meet the required T_C defined within Table 1.1 by Coey [15]. 5 of the 8 compositions also match the requirements for a Type A gap magnet, with one approaching the requirements for a Type B when assessed on observed M_S. Given that the composition underwent observed magnetisation decay

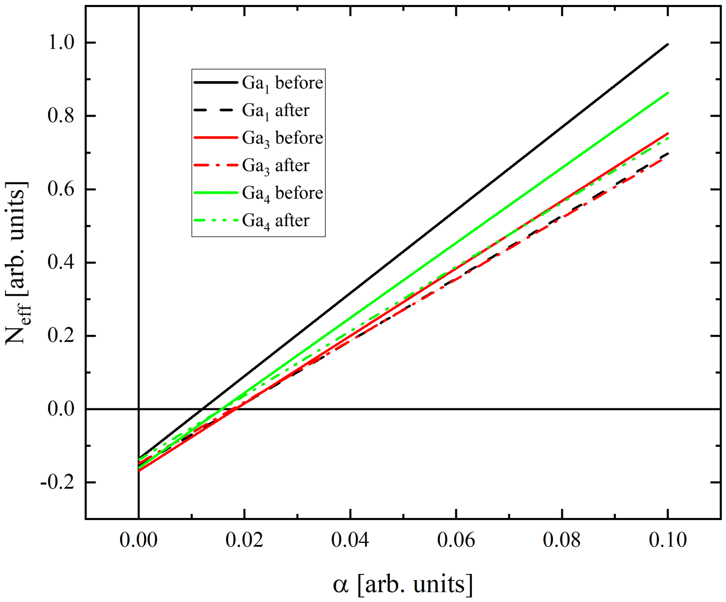

Fig. 6.32 A plot of the micromagnetic variables relating H_C to k and M_S as described by Equation 6.2 for compositions Ga_1, Ga_3 and Ga_4 before and after a 24 hour heat treatment at 420°C. Note that the gradient of these line can be interpreted as proportional to the magnetic hardness parameter, κ, showing that the annealing process is affecting said parameter.

within the annealing time, as seen in Figure 6.2, it could be postulated that this composition could meet the requirements for a Type B magnet by fine-tuning this transformation time. All compositions sampled show k values above the Type C criteria.

When considering the composition space against the key variables defined within Table 1.1, it is clear that the addition of low levels of Ga into the alloy is beneficial for permanent magnetic behaviour. Whilst further work is needed to explore the optimised annealing process and decay rates of the compositions when held at operational temperatures, MnAlGa as a system may represent a potential avenue of further exploration for the τ-MnAl system to become an industrially viable material. Thus, it can be considered that the first objective for this chapter was achieved with a composition selected for optimisation though recognising that further work to explore other compositions would not be inappropriate.

The heat treatment optimisation of the selected composition, $Mn_{57}Al_{39.5}Ga_{3.5}$ or MAG-E, showed that an optimum heat treatment temperature was 430°C. This was deduced by considering whether the observed magnetisation at the annealing temperature reached a maxima within a 60 minute time-frame and whether magnetisation increased or decreased as a function of annealing time at 2 hours, to represent realistic engineering conditions prohibiting annealing times on the scale of a few minutes, anticipating scale-up of production. It was found that $450°C$ or hotter induced a maxima in observed magnetisation during this time-frame, with a negative $M(t)$ gradient observed afterwards and that annealing temperatures of $400°C$ or cooler did not initiate the necessary $\epsilon \rightarrow \tau$ transformation necessary to increase sample magnetisation.

When then seeking to optimise the annealing time at $430°C$, it was noted that the annealing process controlled both the phase population and microstructure, thus determining both intrinsic and extrinsic magnetic properties. It was determined that, although the phase population was determined to be 100% τ-phase by one hour of annealing, intrinsic properties continued to change as a function of annealing time. Thus, it was inferred that this change was resultant from dislocation transport through thermally activated slip systems and stress inherent to the $\epsilon \rightarrow \tau$ transformation being removed from the grains, resulting in lattice parameter shifts throughout the system. It can be seen that the annealing time also affects the thermal dependency of intrinsic magnetic variables, meaning that the annealing optimisation must also consider this. Therefore, the second objective can be considered explored but not fully achieved, recognising that the system is more complex than initially theorized and whilst maxima have been theorised, there is more work in understanding and measuring the lattice shift phenomena to create a truly tunable permanent magnetic material to match engineering specifications in industrial applications.

To better understand whether the change in intrinsic magnetic variables or grain morphology dominated the changing coercivity as a function of annealing time, each sample was analysed according to the Kronmüller Equation and Bloch's $T^{\frac{3}{2}}$ law to investigate whether micromagnetic coefficients or Spin Wave Stiffness Coefficients and Exchange Constants saw greater change which could be attributed to the change in H_C. Overall, it was found that the dominant change in behaviour for MAG-E under these annealing conditions was not a change in microstructure resulting in a change in Kronmüller coefficients but a change in intrinsic magnetic properties resulting from a change in lattice constants and thus Mn-Mn bond lengths. As such, additional techniques will be required to improve extrinsic magnetic properties on an optimally annealed MAG-E sample by way of microstructural refinement. It can be, however, concluded that a 3 hour anneal at $430°C$ is the optimum annealing time and temperature explored in this body of work to maximise intrinsic magnetic properties for use in a permanent magnetic material application by way of lattice parameter relaxation to magnetically favourable bond lengths. Therefore, the third objective can be understood as complete from a measurement perspective, with an optimised heat treatment time devised but that specific understanding as to the underpinning mechanisms behind the magnetic property changes require significant further work in order to develop working models to predict behaviour.

Chapter 7

Mechanical Processing Investigations for Extrinsic Magnetic Property Improvement

7.1 Motivation

Following the work of the previous chapter, where optimised composition $Mn_{57}Al_{39.5}Ga_{3.5}$ (referred to as *MAG-E* (Manganese Aluminium Gallium - Electrical)) displayed the highest M_S and T_C for the measured range and underwent heat treatment optimisation, the research goals for this chapter were themed around mechanical processing of this alloy and can be expressed as the following

1. Identify ductile behaviour regions for both ϵ-phase and τ-phase MAG-E as a function of temperature.
2. Measure the crystallographic texture before and after uniaxial compression of a ductile temperature to assess alignment effects of deformation.
3. Extend deformation to PSC, a hot rolling simulation technique, to determine directional texture effects of deformation and the resulting changes in extrinsic magnetic properties.

When considering the normal bulk formation of hard ferromagnets, the production route is such that a powder is formed of the target composition to a desired particle size, and then this powder is sintered to near net shape under an applied external field to ensure domain alignment, low porosity and thus desirably high extrinsic magnetic properties. As referenced in Chapter 3, the $\tau - MnAl$ system is not suited to this manufacturing technique due to its metastable nature. Given that the lowest temperature one can effectively sinter a system at is estimated as, $T_{Sinter} \approx (0.66-0.75)T_{Liquid}$ [98], with an approximate melting temperature of $1250°C$, this implies a sintering temperature in the range of $(825-940)°C$ would be required, over $100°C$ above temperatures at which Mix *et. al* demonstrated that even the MnAlGa system is stable [61].

As a consequence of this inability to use sintering to form a desirable microstructure and texture to improve extrinsic magnetic properties, a different approach to achieve this is required. Taking inspiration from the treatment of electrical steels to achieve a Goss Texture [99] and the increase in properties shown by Tyrman *et. al.* through use of Spark Plasma Sintering [58], deformation processing of bulk cast samples was identified as a potential methodology for introducing texture and anisotropy into the system to increase properties, without causing a decrease in τ-MnAl phase population. Further, whilst mechanical deformation of the MnAl and MnAlC systems has been investigated in the past, no deformation work on the MnAlGa system has been published at the time of writing, presenting an opportunity for the inclusion of Ga to further improve previously observed results on the material group.

7.2 Mechanical Response of MAG-E

In order to investigate the potential for deformation-induced anisotropy and texture within the the MAG-E system, it was deemed important to first examine how the system deforms under compression stress as a function of temperature. As the system is metastable and must undergo the $\epsilon \rightarrow \tau$ transformation to be useful, the mechanical response of both systems were investigated with the assumption that texture generated in the precursor state may thus lead to texture in the final state.

Measurement ranges for the two species were not identical as it was shown in the previous chapter that the τ state shows decomposition through a decay in M_S at $500°C$ and so the system was not measured above this temperature. The ϵ-phase, however, is thermodynamically stable from $870°C$ as shown in Figure 7.1, meaning higher temperature deformations can be explored without risk of metastable decay to undesirable phases.

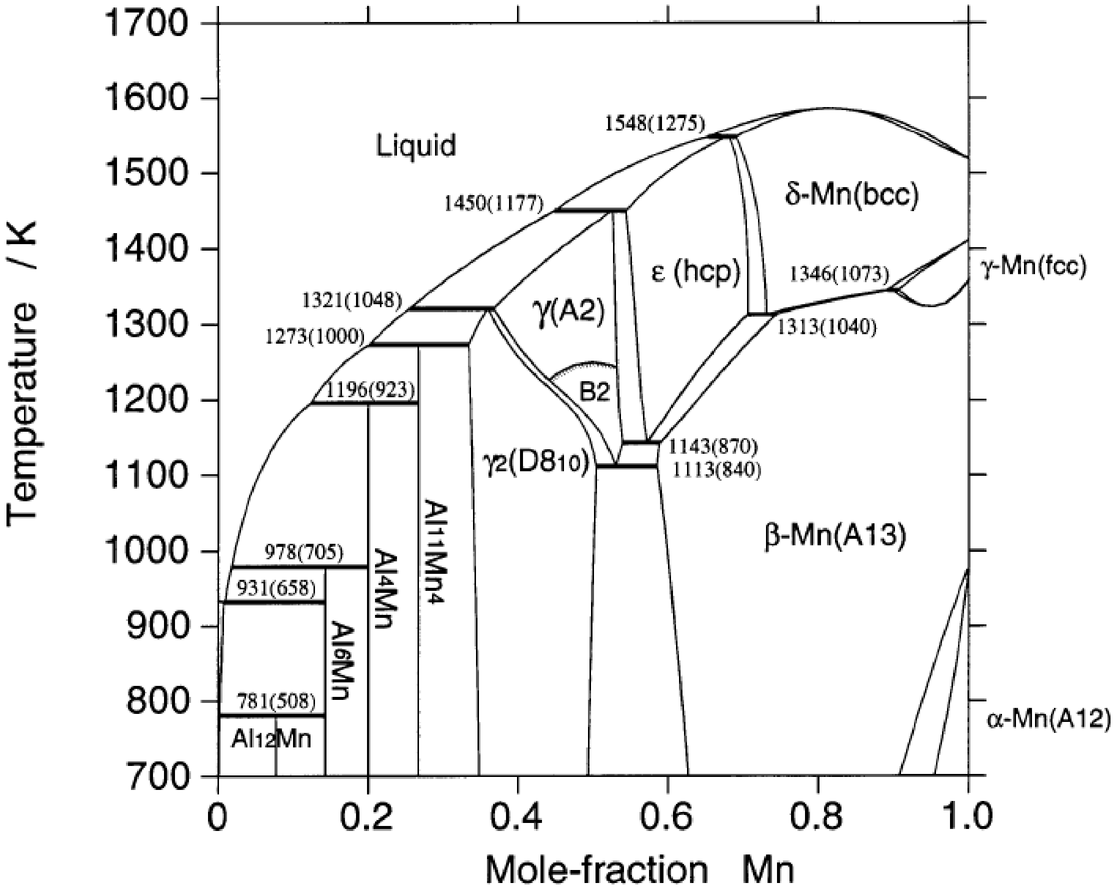

Fig. 7.1 The Mn-Al high temperature phase diagrain, showing that whilst there is a composition dependency on the melting temperature of an MnAl alloy, all temperatures are such that sintering operations of the τ-phase would result in at least partial metastable decay to $\gamma_2 + \beta Mn$ phases. Reproduced from Liu, Ohnuma, Kainuma and Ishida (1999) [100].

7.2.1 Dilatometry of ϵ-MAG-E

To allow thermal expansion during the higher temperature deformations of ϵ-MAG-E to be taken into account, dilatometry measurements were taken. This would allow for corrections to be made in the equipment and data not only on samples undergoing uniaxial compression or PSC testing, defined in Section 4.3.2, but also to provide an insight into potential phase changes in the system (as these will be accompanied by ideally isothermal volume change), accounting for its existence as a quenched high temperature state doped with an additional element, thus potentially deviating from the phase diagram shown in Figure 7.1.

In Figure 7.2, one can see the linear thermal expansion of a cylinder of MAG-E. Within the expansion, one can interpret certain critical temperatures corresponding to a change in phase population. It is interpreted that these changes represent equilibrium transformations rather than metastable transitions, due to the sharp discontinuities clearly visible, indicative of a change in thermal expansion behaviour attributed to a change in phase population. The heating rate of the sample was set to $10°Cmin^{-1}$, leading to the assumption that temperature for the sample (a cylinder of 7mm length and 10mm diameter) was uniform and that the rate of transformation was greater than that of the rate of heating.

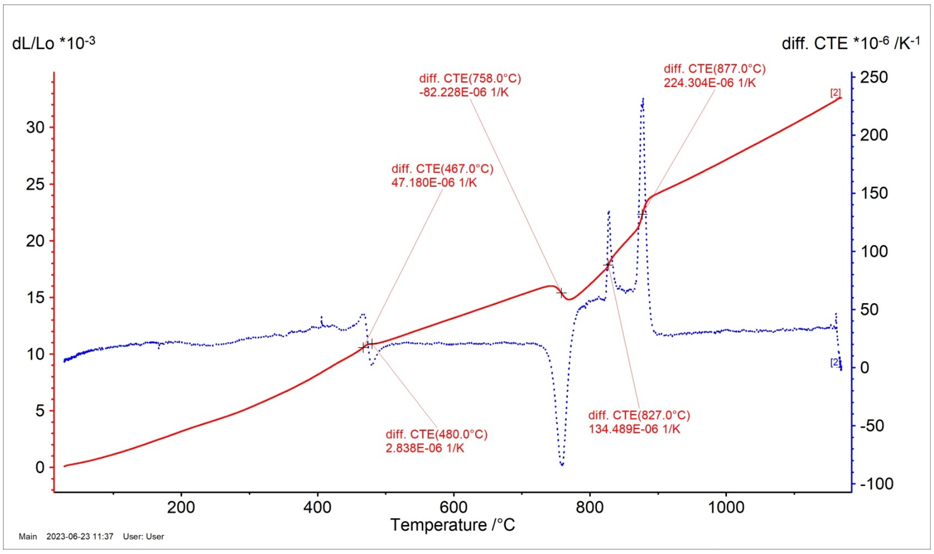

Fig. 7.2 Dilatometry of ϵ-MAG-E with annotated discontinuities, interpreted to be the onset of phase changes within the material as verified by the RHS thermal axis showing the first order differential of the $L/L_0(T)$ behaviour.

By interpreting the discontinuities in the first order derivative as phase changes, it becomes possible to compare Figure 7.2 to the eutectic lines shown in the phase diagram calculated by Liu, Ohnuma, Kainuma and Ishida (1999) in Figure 7.1 [100]. The first discontinuity is observed as a pair of opposite inflection with a midpoint at $467°C$ and can be attributed to the $\epsilon \rightarrow \tau$ transformation as instability in the first order differential can be observed from approximately $400°C$, a temperature previously observed as the initial onset of transformation for the MAG-E composition. With a heating rate of $10°Cmin^{-1}$, it can be assumed that total transformation will have occurred within this window, but that there will not have been time for significant decay. Comparing Figure 7.2 to the transformations shown in Figure 6.12, one can see that the observed magnetisation and thus the $\epsilon \rightarrow \tau$ transformation peaks at $500°C$ at 3.65min, but that this does not undergo significant decay on the timescales of the 10min needed to increase the sample temperature by $100°C$.

This thus implies that the thermal expansion curve between 467°C and the next discontinuity in the dilatometry measurement may be representative of the thermal expansion behaviour of the τ phase.

The following discontinuity at 758°C may represent the thermal decomposition point of MAG-E under these heating conditions. Work by Mix *et. al.* demonstrated that an MnAlGa alloy in the τ phase was thermodynamically stable at temperatures of 700°C, implying that this temperature may be temperature under which the $\tau \rightarrow \gamma_2 + \beta Mn$ decay transformation occurs. Whilst further testing would need to take place to confirm this, either through DSC or HT-XRD, it provides an approximate maximum temperature for the material, though this is approximately $2T_C$ and thus well above any potential motor operating temperature.

The final two discontinuities in first order differential space can be attributed to the eutectic lines in Figure 7.1. With the temperature range being measured as $(827-877)°C$, this implies that the addition of Ga extends the range at which the binary phase system $B2 + \beta Mn$ dominates. The other interpretation of these discontinuities is that 758°C is indicative of the $\gamma_2 + \beta Mn$ eutectic, 827°C the $B2 + \beta Mn$ eutectic and that 877°C indicates the $\gamma + \epsilon \rightarrow \epsilon$ transformation. For the purposes of deformation processing of quenched ϵ-MAG-E, however, the key observation is that deformation must take place under 467°C or above 877°C in order to be deforming and potentially texturing an ϵ-phase system prior to transformation into the ferromagnetic τ-MAG-E state.

7.2.2 Uniaxial Compression of τ-MAG-E

In an initial effort to investigate the possibility of deforming MAG-E to generate texture and anisotropy, the direct approach of deforming the desired τ state was investigated. Cylindrical samples of dimensions 10mm diameter and 15mm length were cut by EDM from an ingot produced by VIM of the MAG-E composition and subjected to uniaxial compression as described in Section 4.3. The temperature range tested was $(100-500)°C$,; no Room Temperature (RT) test was attempted due to the general observation in specimen handling of brittle behaviour in the material under ambient conditions.

No corrections for zero point error were made. This is due to the techniques described in Loveday *et. al.* (2006) [101] requiring final sample geometry. Given all samples underwent brittle fracture before the test was completed, this proved im-

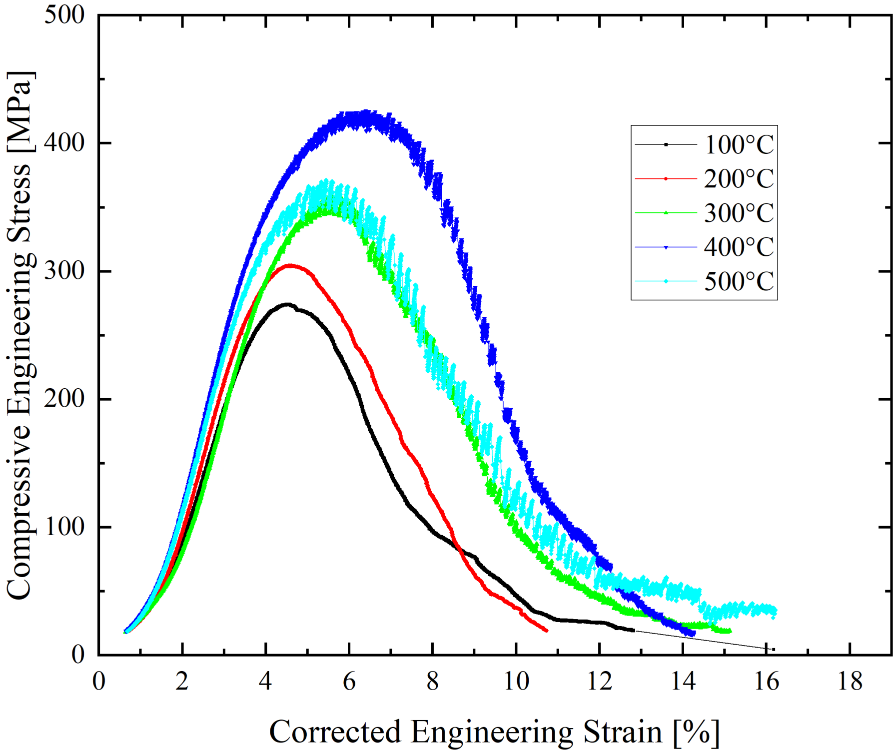

Fig. 7.3 The Stress-Strain behaviour for τ-MAG-E, transformed from the ϵ-state by way of a 3 hour heat treatment at 430°C and water quench. While the σ_{yield} increases as a function of temperature and occurs at higher strain, this data shows that τ-MAG-E behaves as a brittle material at stable temperature ranges.

possible. Instead, the corrections made were performed under the assumption that the initial compressive strain was within an elastic regime obeying Hooke's Law such that,

$$\sigma_{engineering} = E\epsilon_{engineering} \tag{7.1}$$

where E is the elastic modulus. In ideal cases where friction is ignored, deformation would occur instantaneously from $\sigma = 0$ by this equation. As such, the region from initial deformation to $\epsilon_{engineering} = 0.01$ was fit under the assumption that it was a linear relationship and the stress values adjusted such that all curves would pass through the co-ordinates $(\epsilon, \sigma) = (0, 0)$.

Despite all samples being destroyed during testing, two conclusions can still be drawn from the data. The first is that τ-MAG-E is not suitable for deformation processing, with fracture strains being sufficiently low that it was not believed that a sufficient plastic deformation regime was accessible such that texture could be imparted on the material during deformation. The second is that the point of fracture, interpreted to be the maximum stress recorded for each sample, increases as both a function of temperature and strain. Should one find additional alloying elements that increase metastability in the MnAlGa system or the price of Ga falls such that Ga heavier compositions become financially viable, there may exist a higher temperature deformation region such that plastic deformation can occur.

7.2.3 Uniaxial Compression of ϵ-MAG-E

Metastable ϵ-MAG-E Testing Prior to $\epsilon \rightarrow \tau$ Transformations

Looking to the engineering stress-strain curves shown in Figure 7.4, one can see that throughout the stable temperatures that quenched ϵ-MAG-E can exist at, there exist three separate regimes of compression deformation that can be causally linked to the temperature ranges interpreted from the Dilatometry data shown in Figure 7.2 as separate phase regimes. Looking to the first behaviour region, one can see the compression data for samples in the range $(100 \leq T \leq 500)^{\circ}C$ mimics that of the data shown in the previous subsection for τ-MAG-E, fracturing in strain ranges between $(4 \leq \epsilon \leq 8)\%$. The linear nature of the stress-strain relationship for pre-fracture samples within this temperature range suggests that plastic deformation does not occur prior to fracture and that the compression is elastic in nature until sufficient energy has been built to facilitate crack propagation. Fracture is an undesirable outcome for material processing, and for the purposes of deformation for texture, this is also not an effective deformation regime as plastic deformation is required for grain alignment and texture formation.

The sample measured at $500^{\circ}C$ presents an interesting assessment problem. The dilatometry data shown in Figure 7.2 implies that the sample may have undergone the $\epsilon \rightarrow \tau$ phase transformation at $467^{\circ}C$ and the annealing data from Figure 6.12 shows that a maximum magnetisation is reached at this temperature at 3.65min. The sample should have had properties approaching that shown in Figure 7.3 for $500^{\circ}C$. Given that the observed fracture stress is approximately double that of the τ-phase counterpart and fracture occurs at a compression strain approximately 33%

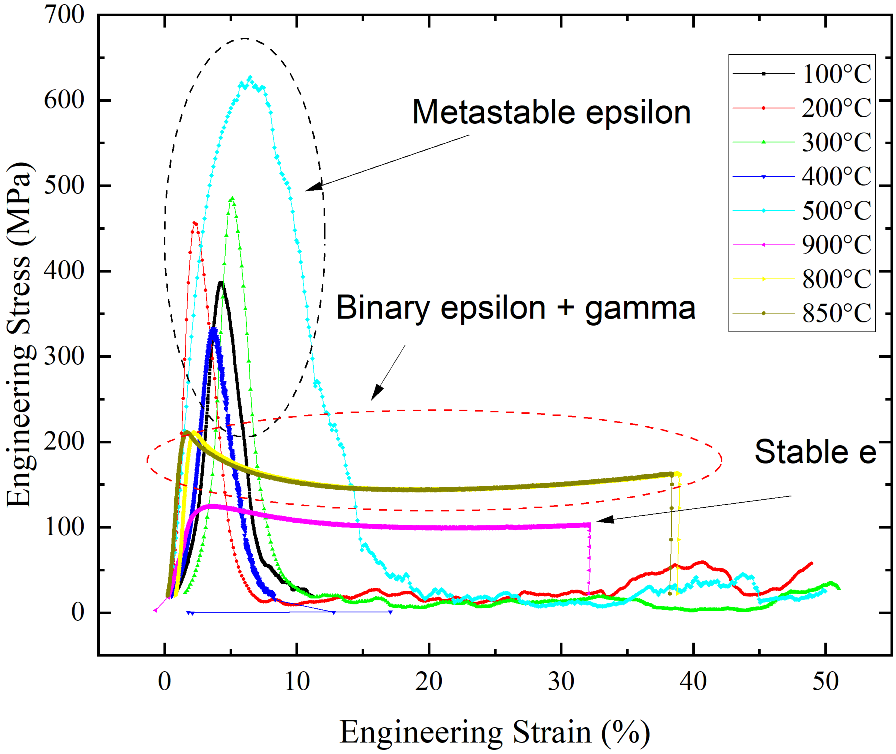

Fig. 7.4 Engineering Stress-Strain data for ϵ-MAG-E. This data is annotated with the three stability regions predicted for ϵ-MAG-E from Figures 7.2 and 7.1, showing that plastic deformation behaviour occurs where the ϵ-phase is thermodynamically stable.

greater than that of said counterpart, a difference in phase population is suggested as the mechanism for change.

Examining the thermal history of the sample recorded from the in-built thermocouple for that test, shown in Figure 7.5, it can be seen the sample was kept at temperature for 60.7sec, meaning that it would be in a mixed $\epsilon + \tau$ state if the trends from Figure 6.12 are to be directly translated over to the MAG-E composition. As such, this may explain the dramatic increase in fracture stress and strain over the τ-MAG-E sample, though the fracture behaviour also does demonstrate that this temperature is also unsuitable for deformation processing. Further, most processing routes would involve holding samples at temperature for a timescale on the scale of minutes rather than seconds, suggesting that compression behaviour would tend to that of τ-MAG-E in practical cases as a result.

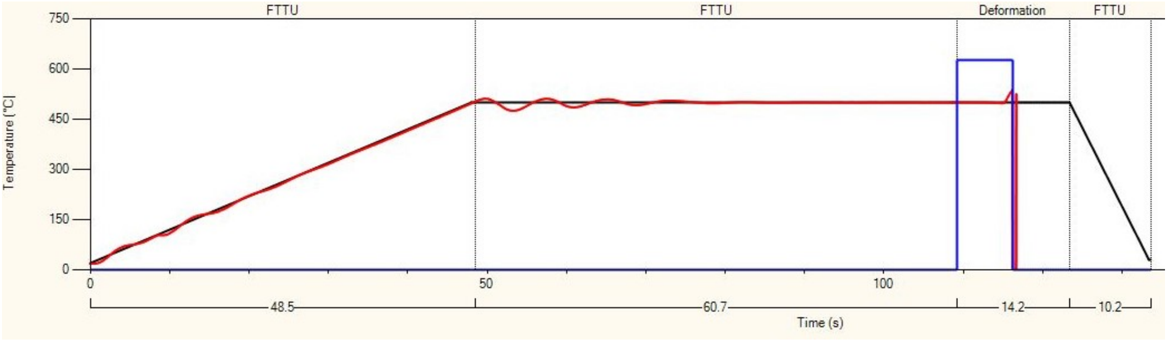

Fig. 7.5 Diagnostic data captured during Uniaxial testing of ϵ-MAG-E, demonstrating that the dwell time at $500°C$ was such that incomplete $\epsilon \rightarrow \tau$ transformation was predicted as determined by Figure 6.12

Ductile Deformation of ϵ-Phase Containing Binary and Ternary Phase Samples

The second observable group is that of materials in the binary $\epsilon + \gamma$ phase region. With sample temperatures beginning at $800°C$, this marks the beginning of ductile behaviour within the material under deformation. With reference to Figure 7.5 being typical for the thermal cycling time and dwell prior to compression testing, it is assumed that samples were unlikely to be in complete equilibrium phase proportions prior to compression. This being said, given that the ϵ-phase was quenched from $1050°C$ and is stable at the temperatures measured within this range, continued presence of ϵ-phase may allow enough plastic deformation for the sample to show macroscopic ductility. Interestingly, the sample measured at $800°C$ underwent plastic deformation within the TMC but, when cut for samples to perform texture analysis, it suffered complete brittle fracture throughout the sample, breaking down into crystallite-like groups. As such, comparing Figures 7.1 and 7.2, it could be concluded that the oxide layer around the sample from heating under normal atmospheres provided sufficient tensile strength during the barrelling process that the ternary phase system of $\epsilon_{quench} + (\gamma_2 + \beta Mn)_{equilibrium}$ fractured but was contained to the sample geometry or that the additional stress of clamping and cutting was sufficient to generate and propagate fractures in the material, leading to brittle failure. It is of note that no other sample measured above this temperature experienced this type of failure during processing, which, given the theoretical eutectic from Figure 7.1 at $840°C$ and the measured first order symmetry break in the dilatometry data in Figure 7.2 at $827°C$, would suggest that this sample belongs in this group by observation and not phase composition. The sample measured at $850°C$ showed additional phases present with the ϵ-MAG-E expected and underwent deformation without internal fracture, showing a smooth, homogeneous surface when bilaterally segmented for XRD texture analysis.

The characteristic behaviour that separates this group of samples from the other deformation regimes is a sharp, initial deformation that is almost linear and elastic in response to applied load before softening into a ductile regime. This softening is characterised by a period of a negative stress-strain relationship before settling into a non-linear, plastic response showing apparent work hardening. To investigate this behaviour, corrections for the barrelling that occurs under high deformation need to first be made.

Corrections for Mid-Sample Radial Growth During Deformation as a Function of Sample Height

When considering the plastic deformation of samples under compression, one must consider that the cross-sectional area of the initially cylindrical sample will not remain constant following plastic compression. However, the volume of the sample should remain constant if one assumes zero porosity within the material. As such, one can solve for the change in sample radius as a function of height reduction.

Ignoring barrelling of the sample, where the midpoint radius of the cylinder expands more than the top and bottom during compression, one can assume from the compression that:

$$V = \pi r_{initial}^2 h_{initial} = \pi r^2(h), \;\; r(h) = r_{initial}\sqrt{\frac{h_{initial}}{h}} \tag{7.2}$$

where V is the total volume of the sample, $r_{initial}$ is the initial starting radius of the cylinder, $h_{initial}$ is the starting height and h is the height as the sample undergoes compression deformation. Whilst additional corrections can be made for barrelling, these were not made during this analysis due to the build up of an oxide layer giving cause to believe that additional material loss may have occurred in midpoint of the samples as the oxide sheared from the body of the cylinder around the taphole for the thermocouple.

As such, one can correct the stress values as a function of strain given the definitions that strain is defined as :

$$\epsilon = \frac{h_{initial} - h}{h_{initial}} \tag{7.3}$$

and stress is defined as :

$$\sigma = FA = F\pi r^2(h) \tag{7.4}$$

Applying these corrections to the stress-strain curves from the mixed state samples, we can see in Figure 7.6, we can see that the corrections significantly change the interpretation of the high strain data with no inflection in the first order derivative present as a result. This means that when accounting for uniform radial expansion of the material, one now observes strain-hardening mechanisms within the material under deformation. Further corrections could be made to account for non-uniform radial expansion, accounting for the barrelling or resulting material loss from oxide layer shearing, but with an observational increase of ≈ 10%, this is beyond the scope of this study as a basic characterisation of the thermomechanical behaviour of quenched ϵ-MAG-E.

Ductile Deformation of Stable ϵ-MAG-E as a Function of Temperature

The final behaviour group is that of the thermodynamically stable ϵ-MAG-E. Distinct from the mixed state group as XRD phase analysis does not show distinguishable secondary phases when examining the bulk of the samples, the compression stress-strain graphs corrected for uniform radial expansion can be seen in Figure 7.7. Much like the mixed phase samples, the degree of barrelling observed in the samples was low enough that the change in stress calculations was modelled without this deviation.

Excluding the data gathered at $900°C$, a clear trend is present within the data with both σ_{yield} and E exhibiting proportionality with sample temperature. Following this yield point, all samples tested exhibit strain softening behaviour, decreasing in effect as higher strains are achieved. Looking to work published by Tang and Schoenung (2008), this may be explained by the small grain size targeted in the production of MAG-E during casting. This work discusses various metals exhibiting work softening behaviour and suggests a mechanical mechanism for such an effect. Given the assumption that a nano-grain material cannot maintain dislocations within a grain due to their attraction to grain boundaries, they postulate that any softening effect cannot be caused by dislocation movement under stress within said grains, instead proposing that deformation within nano-grain alloys is dominated by dislocations created at grain boundaries. As these dislocations sweep through grains to be absorbed at subsequent grain boundaries, a residual stress field is

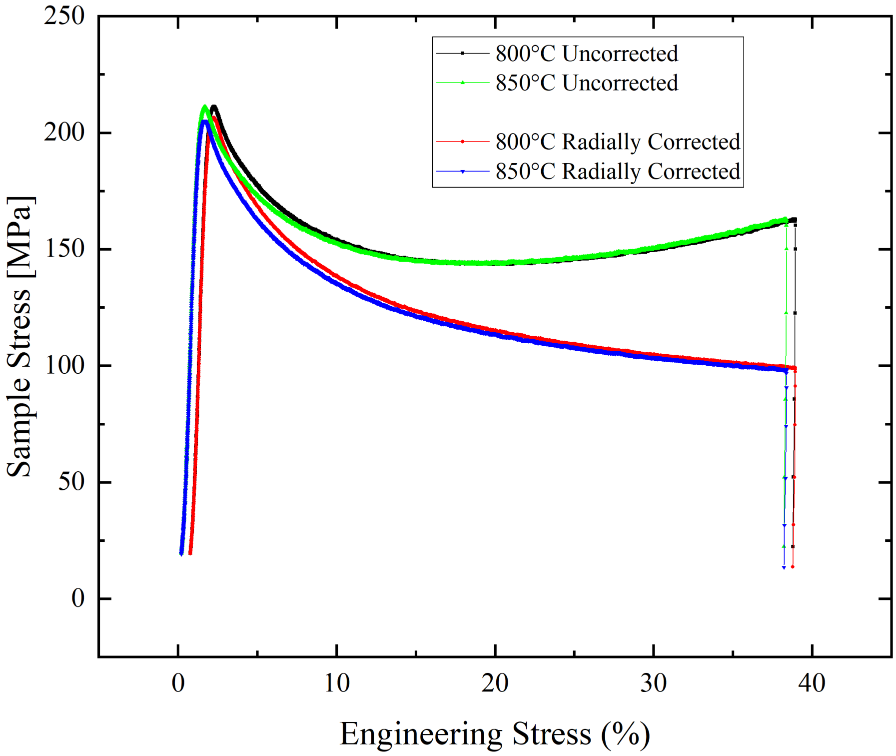

Fig. 7.6 Stress-Strain relationships for uniaxial testing of ϵ-MAG-E measured at $(800,850)°C$ before and after radial stress corrections from expanding contact surface areas as a result of deformation. This implies that work-softening, rather than work-hardening, behaviour occurs in ϵ-MAG-E as fabricated by the methodologies presented in this chapter.

established around the grain, resulting in a lower external stress field required to generate subsequent dislocations [102].

Using the Scherrer equations as an estimate for the minimum grain size within the material, it can be calculated from the XRD data from the deformed sample at $1100°C$ that the average crystallite size is (25 ± 3)nm. Whilst this technique is not without error and has been performed on a sample that has undergone deformation processing and thus will have additional effects contributing to the distortion of specific peak widths due to strain effects on the system, it gives an estimation that the system may indeed be subject to the deformation mechanics previously defined above. Further, when this process is repeated with samples at $900°C$ and $1000°C$ across multiple peaks, an extent of the error and grain size can be made apparent in the box chart shown in Figure 7.8.

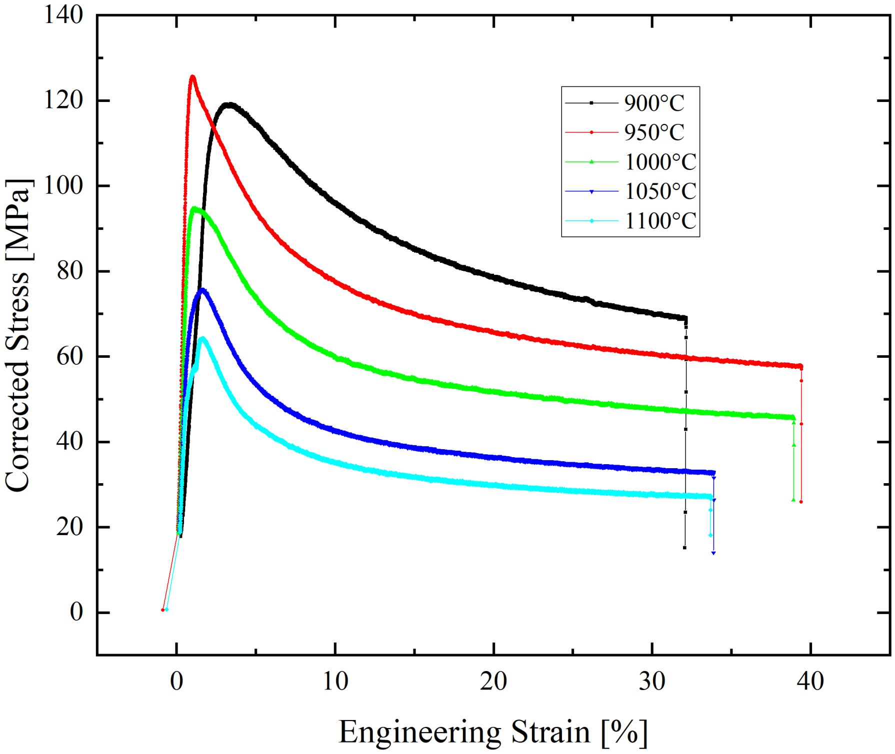

Fig. 7.7 Stress-Strain relationships of thermodynamically stable, single phase ϵ-MAG-E following corrections via Equation 7.4, demonstrating similar work-softening behaviour as the mixed-phase materials.

Whilst this is only an estimation of grain size in the system, with it being a measure of diffraction plane length thus a minimum grain size and subject to error based on a bin size on measurements of 0.01°, it also provides insight as to the anomalous behaviour of the sample measured at $900°C$. The average crystallite size calculated for the sample at $900°C$ is 15 ± 1nm, over 10nm smaller than the calculated crystallite sizes for the samples measured at $1000°C$ and $1100°C$. As such it may be that this decrease in grain size magnifies the previously discussed effect whereby localised stress fields created by dislocation motion through grains makes dislocation motion easier, this effect dominating the decreased dislocation mobility when compared to higher temperature samples, resulting in the lower yield stress observed in the $900°C$ sample compared to the trend.

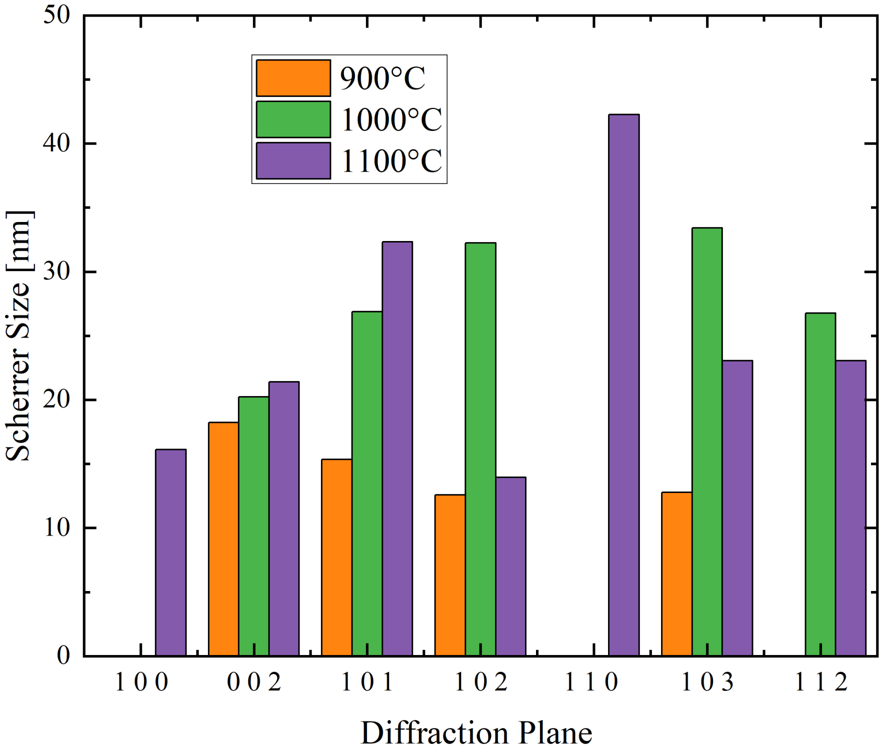

Fig. 7.8 Crystallite Sizes in uniaxially deformed samples of ϵ-MAG-E as determined by Equation 4.3. Whilst these crystallite sizes are interpreted as averages, it is such that they are numerical as opposed to volume averages, suggesting that larger grains may also exist within the system.

It is at this point that it can be considered important to stress that the Scherrer Equation approach is not without issues. Predominantly, it is a measure of diffraction behaviour and coherent scattering. As such, it is a measure of the smallest scale coherent structure, in this case grains, within a material but does not preclude larger scale grains existing. Further, the error associated with each Scherrer size is not a true distribution of the system but a reflection of peak broadening distribution. Whilst thermomechanical behaviour suggests that grain size is indeed small enough to support strain-softening behaviour, the values presented should be interpreted as closer to a minimum average grain size for a material, further corroborated by the study presented in Section 6.2.2. As such, additional testing to accurately determine accurate grain sizes for further understanding is appropriate to best assess the stress-softening/stress-hardening behaviour of cast MAG-E.

Upon sampling of all equilibrium ϵ-MAG-E samples, no fragmentation behaviour like that of the sample cut at $800°C$ was observed. This suggests further that the ternary state was either contained within an oxide shell in a fractured state or deformed to a condition such that the addition stress from segmentation caused near-immediate fracture stresses within the material. It can be deduced that under the measured compression strain limits, nano-grained ϵ-MAG-E is ductile.

7.2.4 Crystallographic Texture of Equilibrium ϵ-MAG-E following Uniaxial Compression

In an effort to mimic an aligned and sintered process and thus the efficiency referenced in Figure 3.5, crystallographic alignment, or texture, is a desired effect in a bulk form MAG-E magnet. As the easy axis of magnetisation for the τ-MnAl system lies in the c-axis of the BCT lattice, it stands to reason that textures aligning these axes together would lead to similar effects. To that end, Pole Figures for the deformed samples were captured using the methodology described in Sections 4.4.2 and 4.4.3. Issues with the output of the required Ag X-ray source led to the poor data quality in some samples but representative scans were able to be taken for samples deformed at $850°C$, $900°C$, $1000°C$ and $1100°C$. Given engineering tolerance variation, thermal expansion and machine limitations, samples underwent compression strain in the range of $\epsilon \approx (30-40)\%$, meaning direct comparison is qualitative rather than quantitative, but given all underwent similar heating and cooling rates within the TMC during testing and sample preparation, no additional error from annealing following deformation is expected. Samples were also cooled by water quench following deformation to trap in any resulting microstructure.

Texture of Hot Deformed MAG-E at $850°C$

Though predicted to be multi-phase, the sample deformed at $850°C$ is predicted to have equilibrium ϵ-phase content and, as such may be suitable as a phase space for deformation for texture. In order to determine whether a preferential texture was formed, in the absence of an isotropic sample of the same heat treatment profile, two surfaces were measured, perpendicular and parallel to the uniaxial compression direction. To also ensure that measurements taken between the two surfaces were as comparable as possible, four diffraction peaks of distinct crystallographic directions were selected to construct an Orientation Distribution Function (ODF) along with backgrounds measured from within 1° of a peak of which pole figures were simulated. The selected peaks were the $(1\,0\,\bar{1}\,0)$, $(0\,0\,0\,2)$, $(1\,1\,\bar{2}\,0)$ and $(1\,1\,\bar{2}\,4)$ to ensure as accurate an ODF as possible whilst also allowing sufficient time to scan in the range of $(0 \leq \chi \leq 360)^{\circ}$ and $(0 \leq \phi \leq 80)^{\circ}$ with a 2s dwell time per pixel. The resulting comparative ODF representations can be seen in Figure 7.9.

Interpreting the difference between the perpendicular and parallel to uniaxial stress ODF-generated pole figures, LHS and RHS respectively in Figure 7.9, one can see that the deviation in the $(0\,0\,0\,1)$ and $(1\,1\,\bar{2}\,1)$ data sets clearly indicates a directional preference and thus crystallographic anisotropy within the material. The near symmetric distribution around the x-axis on the $(0\,0\,0\,1)$ RHS plot also further supports that the uniaxial stresses on the system have had an effect on the texture of the sample, once error in the alignment of the stress vector to the measurement y-axis have been accounted for. This angular dependency is also clearly observable in the raw datasets and cannot be resultant from defects in the sample due to the polished state of the surface which underwent measurement and that the angular difference between the $(1\,0\,\bar{1}\,0)$ and $(0\,0\,0\,2)$ diffraction peaks is $\Delta 2\theta < 1.0^{\circ}$ implying any surface aberration would be insufficiently thick as to attenuate Ag x-rays to cause this effect.

Further analysis of this texture beyond recognising its anisotropy becomes challenging, however, due to the anisotropic nature of the applied stress to the system. As the radius of the contact surfaces expands under applied stress and barreling occurs within the sample through deformation, the applied stress throughout the material will vary as a function of radius and height within the cylinder. As such, the texture measured through the pole maps in Figure 7.9 is representative of the entire surface and is such only an average texture throughout the material.

Further, whilst a dependency between the background of the XRD signal and the angle ϕ is taken into account in the analysis, the effects of defocusing could not be accounted for within these measurements. As the sample is tilted in the angle ϕ with respect to the geometry defined within Figure 4.7, the initially defined irradiation cross-section established by Soller and anti-scatter slits distorts over the surface, accounting for a decrease in intensity as a function of tilt. Measuring this dependency relies on an isotropic sample of the sample crystallographic state to isolate the effect. Given the complex thermal history of the sample measured at $850^{\circ}C$, this was deemed impractical for this sample during this stage and the analysis of the resultant texture left as qualitative between the two perspectives.

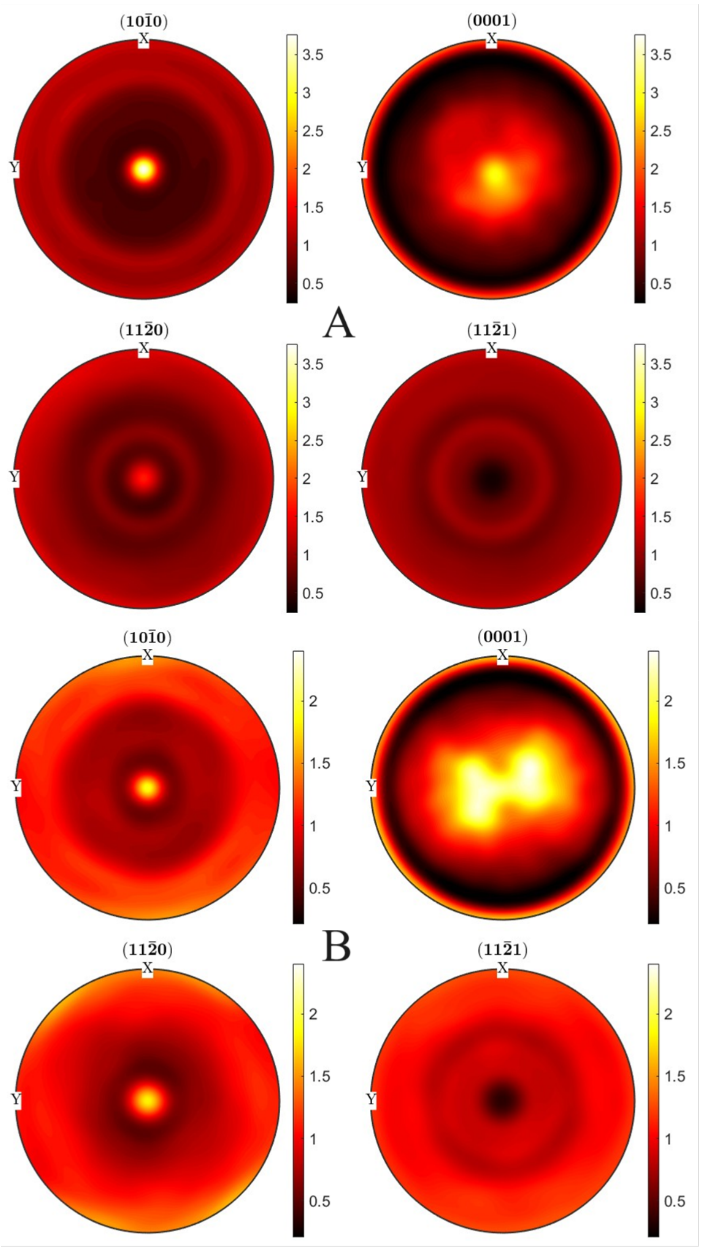

Fig. 7.9 Reconstructed pole figures for a sample of ϵ-MAG-E deformed by uniaxial compression at 850$^{\circ}C$ to an engineering strain of $\approx$ 38%. A) Perpendicular to applied uniaxial stress vector. B) x-axis on radial plot is parallel to applied uniaxial stress vector.

Considering these corrections and the resultant data within Figure 7.9, it can be established that there is some dependency between the applied stress vector on the sample and the resultant alignment of the c-axis of the HCP ϵ-phase of ϵ-MAG-E. Whilst this could be of benefit for further development, estimations of the phase composition of the MAG-E system at equilibrium at this deformation temperature would see a fraction of non-precursor phases to τ-MnAl formation. Whilst previous work has shown that inclusions of these phases can lead to an increase in coercivity through decreased exchange interaction energy, this could come at the expense of M_r and M_S. These inclusions are also generated following to the $\epsilon \rightarrow \tau$ phase transformation rather than prior and may have an effect on said transformation. As such, this temperature and deformation profile was not taken further to PSC testing.

None the less, an effort was made to understand the texture developed within this material to better understand the anisotropy of the system under deformation. Figure 7.10 shows the angular misorientation data for a fibre defined by the $(1\,1\,\bar{2}\,1)$ plane in the $\hat{z}$ or $[0\,0\,1]$ direction against the ODF calculated for parallel texture measurements as defined by Figure 7.9.B. Examining the periodicity of the fit, it shows that the calculated ODF has 2-fold symmetry with the applied fibre, indicating that this fibre captures the symmetry of the system given the inherent symmetry of the direction and fibre. By fitting a Gaussian to the reflection around 180°, one can both assess the axis load vector to measurement vector misalignment and quantify the grain probability of alignment to the modelled texture. The calculated variables for a modelled Gaussian fit defined by

$$I = \frac{1}{\sigma\sqrt{2\pi}} exp(-\frac{1}{2}(\frac{\theta-\mu}{\sigma})^2) \tag{7.5}$$

where σ is the standard deviation of the fit and μ the mean angle of data defined by intensity I and angle θ see $\mu_{850°C} = (181.8 \pm 0.1)°$ and $\sigma_{850°} = (25.9 \pm 0.2)°$. Given the vertical cut used to section the sample for texture measurement, a misalignment of $(1.8 \pm 0.1)°$ is within the engineering tolerance of clamp alignment and blade flex during cutting, leading further confidence that this fibre captures the texture of the system but the standard deviation of the texture corroborates with the intensity displayed on the simulated pole figures from the calculated pole figures from the generated ODF. Noting that the extreme of the circular Pole Figure is 90° from the central point in χ space, features on the pole figures correspond to that of 10s of degrees given a constant proportionality between radius and χ angle. Using the Gaussian model as a grain orientation probability model, it would imply that there was an approximately 95.4% chance of finding a grain with the $(1\,1\,\bar{2}\,1)$ plane within a $(51.9 \pm 0.2)^{\circ}$ deviation from the direction of stress. Given the previously discussed non-uniform stress through a uniaxial sample, this diffuse texture can be justified by a superposition of a distribution of stress-induced textures.

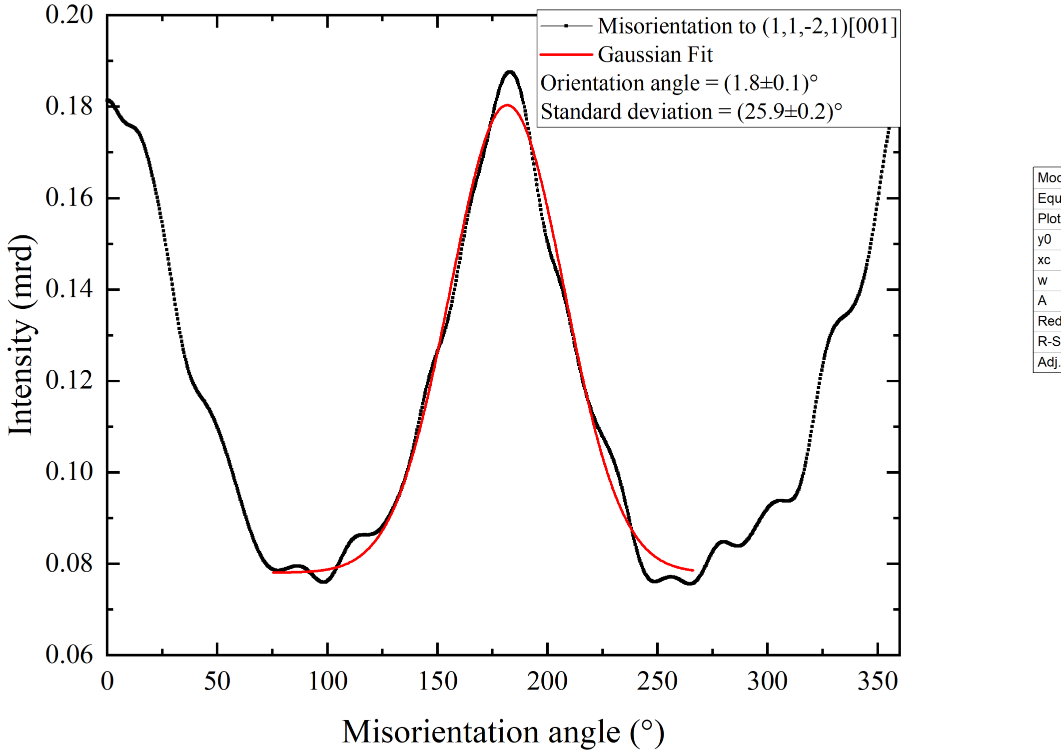

Fig. 7.10 Intensity of the calculated Orientation Distribution Function (ODF) of uniaxially deformed ϵ-MAG-E, deformed at $850^{\circ}C$, with an associated Gaussian fit to determine likely occupation of an idealised grain against the modelled fibre orientation of the $(1\,1\,\bar{2}\,1)$ plain in the $[0\,0\,1]$ direction relative to deformation, i.e. in the radial direction of the uniaxial sample and perpendicular to the applied stress vector.

Following from this approach shown in Figure 7.10, the MTEX *fibreVolume* function was utilised to assess fibre occupation, recognising that calculations from the ODF require symmetry arguments to be made. When using a 20° misorientation angle, the calculated volume occupancy for a $(1\,1\,\bar{2}\,1)[0\,0\,1]$ fibre is 46.29%, implying that a preferential orientation has been achieved as a result of deformation processing when this is compared to the same fibre applied to a sample cut 90° to the initial surface showing a volume occupancy for the same fibre conditions of 43.98%. Whilst this result is small, it does demonstrate that it is possible to generate anisotropy through hot deformation in ϵ-MAG-E.

Texture of Hot Deformed MAG-E at $1000°C$

Using the same approach to assess the resulting metallographic texture of MAG-E deformed to a strain of $\epsilon = (39.9 \pm 0.1)\%$ at $1000°C$ as that of deformation at $850°C$, it can be seen in the calculated and normalised ODF-generated pole figures that a broadly isotropic distribution in the $(1\,0\,\overline{1}\,0)$, $(1\,1\,\overline{2}\,0)$ and $(1\,1\,\overline{2}\,1)$ pole figures in ϕ space, with features emerging in χ space. The external orientation of the measured pole figures is such that the $\hat{z}$-axis is parallel with that of applied stress, assuming for a margin of error associated with misalignment during sample cross-section preparation. Determining resultant texture is similarly difficult due to a non-uniform stress applied to the sample but a fibre texture defined by $(1\,0\,\overline{1}\,0)[0\,0\,1]$ shows a 180° symmetry when examining misorientation angle against the fibre with the associated Gaussian Distribution variables of $\mu_{1000°C} = (138.3 \pm 0.1)°$ and $\sigma_{1000°} = (22.5 \pm 0.7)°$. Given the cross section measured was perpendicular to that of the measured surface for the the sample compressed at $850°C$, the change in fibre angle relative to sample direction can be explained by a 90° rotation in relative reference frame used for measurement relating to the applied stress vector due to processing. Whilst the distribution would imply a more pronounced texture than that of the sample strained at $850°C$, it is of note that the dual phase population of the latter may have influenced the measured texture.

Surface preparation of the cross section involved the grinding of the surface to a P800 ($\approx 20\mu m$) finish in order to provide a flat plane for pole figure mapping and prevent high angle measurements from having χ-dependent path length, and thus attenuation, effects from an uneven surface. It is assumed therefore that this has not had an effect on the measured texture of the surface with any polish-derived texture being undetectable compared to that of deformation-derived texture.

Following the sample methodology as fibre occupation calculation for the sample deformed at $850°C$, it is of note that the volume occupancy for the $(1\,1\,\overline{2}\,1)[0\,0\,1]$ fibre with a 20° misorientation angle is 60.77%, implying that there is an increased intensity of texture anisotropy with increasing temperature, assuming that the deformation strains are broadly comparable with one another. However, due to the $850°C$ sample being deformed at a temperature where additional phases are

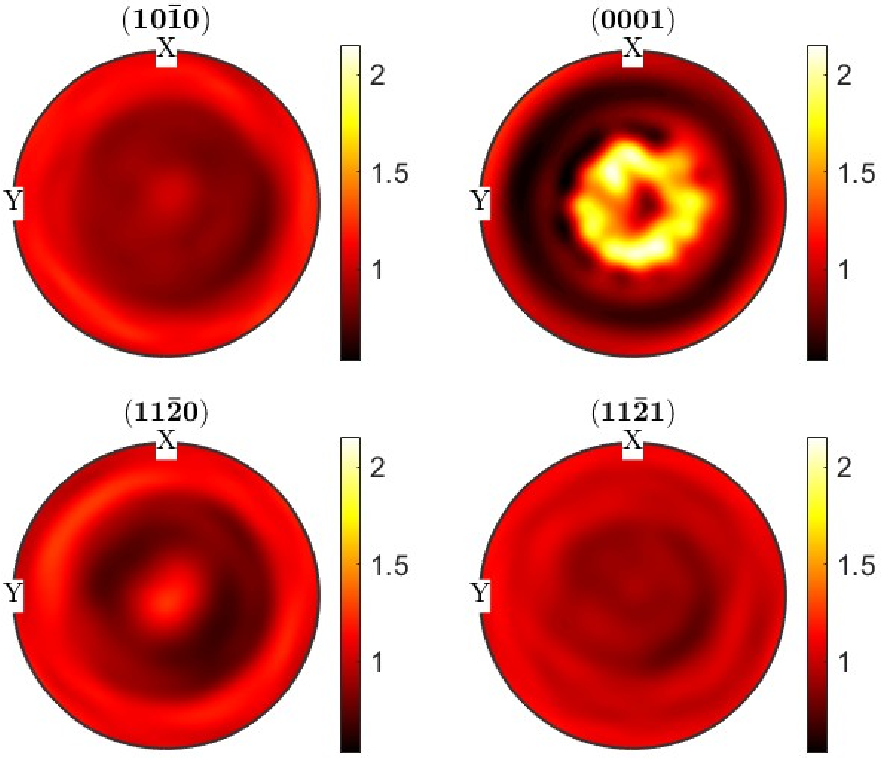

Fig. 7.11 Reconstructed pole figures for ϵ-MAG-E following uniaxial deformation at 1000°C as calculated from an ODF derived from pole figure measurements of a perpendicular-to-stress plain sample

predicted to be present, it may be the case that the resulting texture is influenced by the presence of these additional phases.

Texture of Hot Deformed MAG-E at $1100°C$

Finally, examining the reconstructed pole figures for ϵ-MAG-E deformed at $1100°C$ to a strain of $\epsilon = (33.9 \pm 0.1)\%$, one can see that there is both a radial and angular distribution to the resulting pole figures, implying texture, in Figure 7.12. There is also an off-centre symmetry centre, an artifact from sample mounting/preparation that implies that the textural components are associated with the applied stress vector and not an isotropic feature. Correcting for this off-centre effect and remodelling the same $(1\,1\,\overline{2}\,1)[0\,0\,1]'$ fibre with a 20° misorientation angle, one finds an occupancy of 44.76%, lower than that of the occupancy for the sample deformed at $1000°C$

Conclusions on Texture of Equilibrium ϵ-MAG-E following Uniaxial Compression

Assuming that the two samples selected for ODF analysis are invariant other than the difference in deformation temperature and strain, the difference in occupancy can be defined as either a function of deformation strain, deformation temperature or both. With a variable stress profile throughout the material following uniaxial testing and an off-perpendicular sampling of the material analysed for $1100°C$, it may be the case that the volume fraction of low stressed material to high stressed material is greater than that of the $1000°C$ sample. Uniaxial testing is not best suited for establishing texture-strain relationships due to this variable stress profile, a result of barrelling, contact surface friction and potentially non-parallel surfaces between the two circular faces of the test cylinder but from the resultant asymmetries from the pole figures and variable, direction-dependent fibre occupancy calculations, it can be concluded that hot deformation has an effect on the texture of ϵ-MAG-E. Quantifying this behaviour requires more precise knowledge of the stress profile through deformation, something achievable by, for example, extrusion, rolling or Plane-Strain Compression.

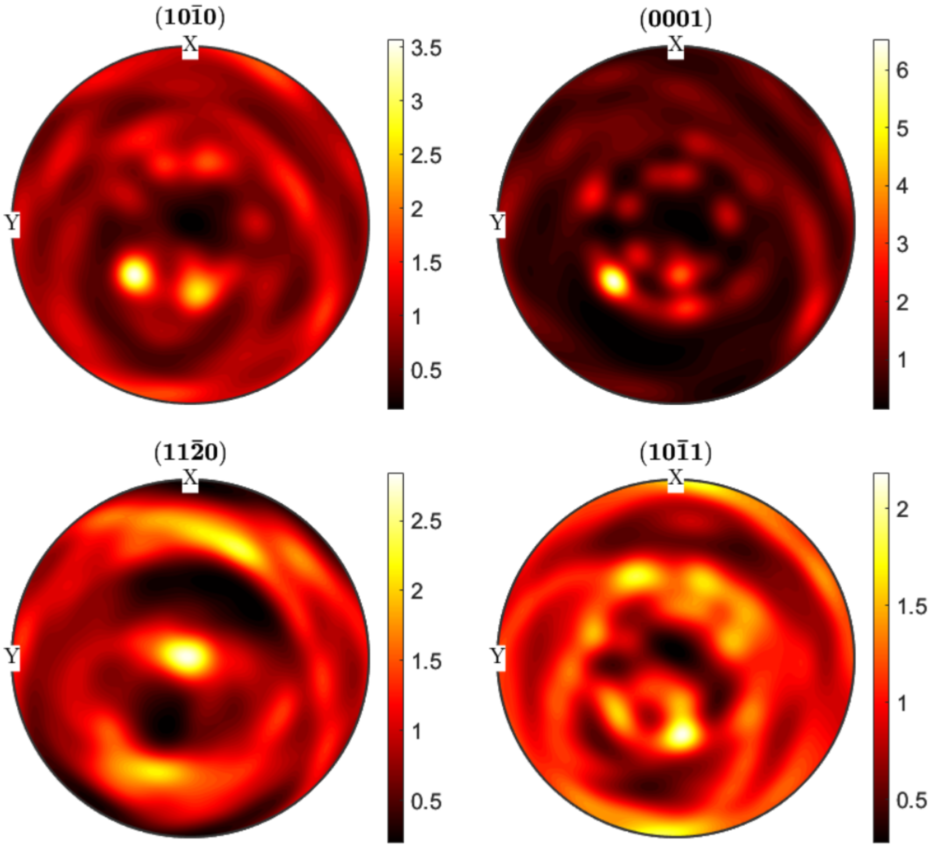

Fig. 7.12 Reconstructed pole figures for ϵ-MAG-E following uniaxial deformation at $1100°C$ as calculated from an ODF derived from pole figure measurements of a perpendicular-to-stress plain sample. The off-centre symmetry is attributed to sample misalignment during extraction and mounting, resulting in a stress-normal transposed by (χ', ϕ') in stereographic space.

7.3 Plane-Strain Compression of ϵ-MAG-E

Following from the uniaxial testing on ϵ-MAG-E showing that high temperature plastic deformation to relatively high strains is possible, and that deformation can show anisotropy in measured XRD-pole figures and reconstructed ODFs, further work to form a consistent texture on a sample through uniform deformation was carried out. In order to investigate whether hot rolling would produce a desirable texture within MAG-E and thus post $\epsilon \rightarrow \tau$ transformation anisotropy in extrinsic magnetic variables, Plane-Strain Compression (PSC) testing was selected to simulate this process, following the methodology explained in Section 4.3.2.

The choice was made to experimentally simulate hot rolling through PSC, rather than to conduct initial rolling trials for a variety of reasons. The first is that, unlike rolling, the deformation can be performed in a continuous fashion at temperature. Given that the ductile, phase stable region of interest exists above $900°C$, it would be challenging to perform rolling operations at this temperature consistently without material cooling and thermal gradients affecting both the mechanical properties of the MAG-E material under deformation and the resultant microstructure forming from hot deformation. There is thus, the caveat for any results discussed in this section that any development from PSC samples to rolled samples would require additional optimisation work to determine rolling-specific parameters such as rolling speed and roll reduction steps not explored by the PSC process.

Following work discussed in Section 6.3.1, the transformation temperature and time used to ensure desired intrinsic magnetic properties in deformed samples was a 3 hour heat treatment at $430°C$. It is acknowledged, however, that the working hypothesis behind this optimisation is that the residual stress dissipation in the system results from the $\epsilon \rightarrow \tau$ transformation by thermally activated dislocation transport mechanisms. As such, the additional residual stress introduced to the parent ϵ-state may result in average lattice parameter shifts such that this may not be optimised for each deformation profile. It is, however, beyond the scope of this initial study to optimise the heat treatment of MAG-E as a function of Plane Strain Compression.

7.3.1 Texture and Magnetic Properties of Undeformed MAG-E

Looking first to the magnetic properties of undeformed, transformed MAG-E, we can reference from the 3 hour annealed sample explored in Section 6.3.1 that there was a remanence to saturation magnetisation ratio of $(\frac{M_R}{M_S})(T = 23°C) = 0.22963 \pm 0.00004$ with the evolution of this ratio as a function of temperature shown in Figure 7.13. If one takes the estimation that in an idealised system, the maximum achievable ratio between M_R and M_S is approximately 0.7, indicating that there is significant room for growth in this property. Given that for an idealised square loop, $BH_{max} = \mu_0 M_R H_C$, if we assume that M_R is a proportion of M_S and that M_S will not change as a result of increasing this ratio, increasing said ratio will increase the maximum energy product of the material and thus its functional use as a permanent magnetic material. In this idealised case, there would be microstructure such that during the magnetic polarity reversal where $H \rightarrow -H_C$ in the second quadrant of the hysteresis loop, assuming an initial positive magnetisation, domain reversal within the material is such that it must happen near-globally throughout the material and must overcome the magnetocrystalline anisotropy field to do so, i.e $H_C \rightarrow H_A$. Whilst perfectly square loops are not feasible for macroscopic, polycrystalline samples, it is possible to tend towards this model with microstructural refinements.

In Figure 7.13, it is assumed that the $\frac{M_R}{M_S}$ ratio is constant as a function of temperature as it is assumed that this property is isotropic. Given that it has been previously stated that the easy axis of magnetisation for τ-MnAl is the c-axis, it would stand to reason that this case would apply if there was no texture present such that there was an anisotropic distribution of c-axis planes in a measured direction. To confirm this, as well as to provide defocusing measurements for texture studies of deformed samples, pole figures of the $(10\bar{1}0)$, (0002), $(10\bar{1}1)$, $(10\bar{1}2)$ and $(11\bar{2}0)$ planes were captured by methodologies defined in Section 4.4.2 in a measurement grid in (ϕ, χ) space of $(2,1)°$ to ranges of $(0-360, 0-80)°$. The MTEX program was then utilised to compile an Orientation Distribution Function (ODF) and corrections made for background effects to produce normalised pole figures reconstructed from the ODF. These reconstructed pole figures can be seen in contour format to best visualise the texture distributions in Figure 7.14 and show that, when considering the $(10\bar{1}0)$, $(11\bar{2}0)$ and $(11\bar{2}1)$ pole figures, the material can be interpreted as broadly isotropic.

Given that there is no defocusing data available for this material, owed to needing a large volume of texture-free powder to produce said result, it is interpreted that the texture resultant from the (0002) pole is resultant from sample symmetry and an artifact from background corrections as it corresponds to a material axis that is not related to a casting symmetry angle or machining angle, thus cannot be linked to sample geometry. In the pole figure data captured for this sample, a shadow is present between $(45 \leq \chi \leq 135)°$, potentially arising from an uncorrected sample tilt,

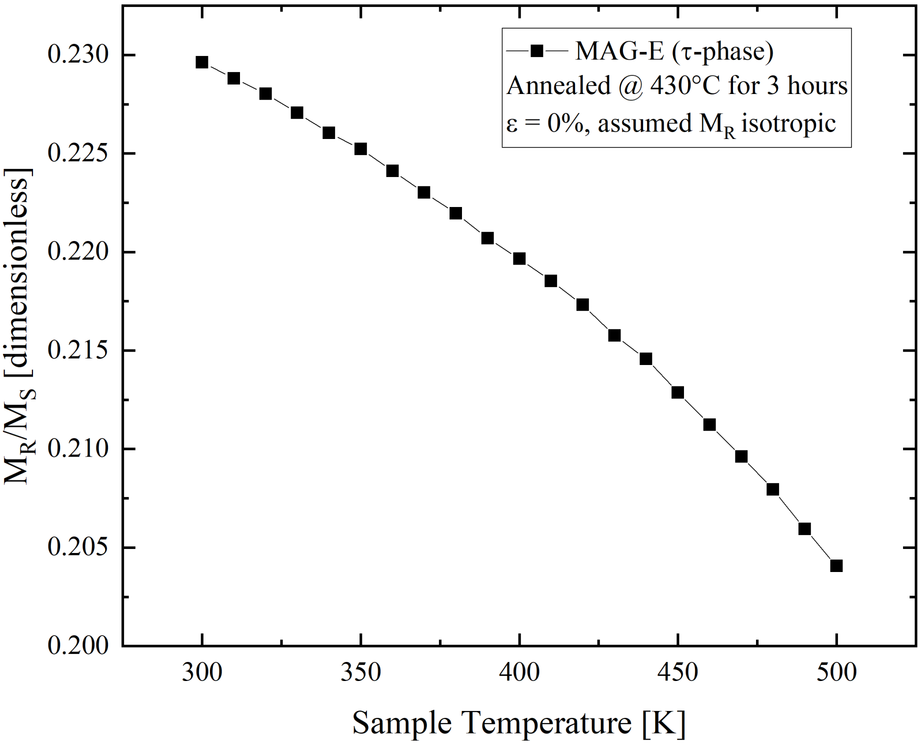

Fig. 7.13 The temperature dependence of M_R/M_S. It is assumed that as the material was extracted from the centre of a casting and undeformed beyond cutting, it can be assumed to be isotropic in comparison to hot deformed material.

as observable in Figure 7.15. This shadow is present in all captured pole figures but all figures still show centrosymmetric symmetry about a point rather than periodic divergence in (χ, ϕ) space typically expected of a textured sample. Thus, it was interpreted that this sample could be considered broadly isotropic and was used to as a defocusing measurement for ODF calculations of deformed samples.

7.3.2 Texture Before and After Transformation of MAG-E ($\epsilon = 30\%$) Compressive Strain

XRD Phase Information Post-Deformation and Post-Transformation

Following the initial uniaxial studies, it was deemed possible to undergo compression deformation processing of ϵ-MAG-E at temperatures above $1000°C$. Given

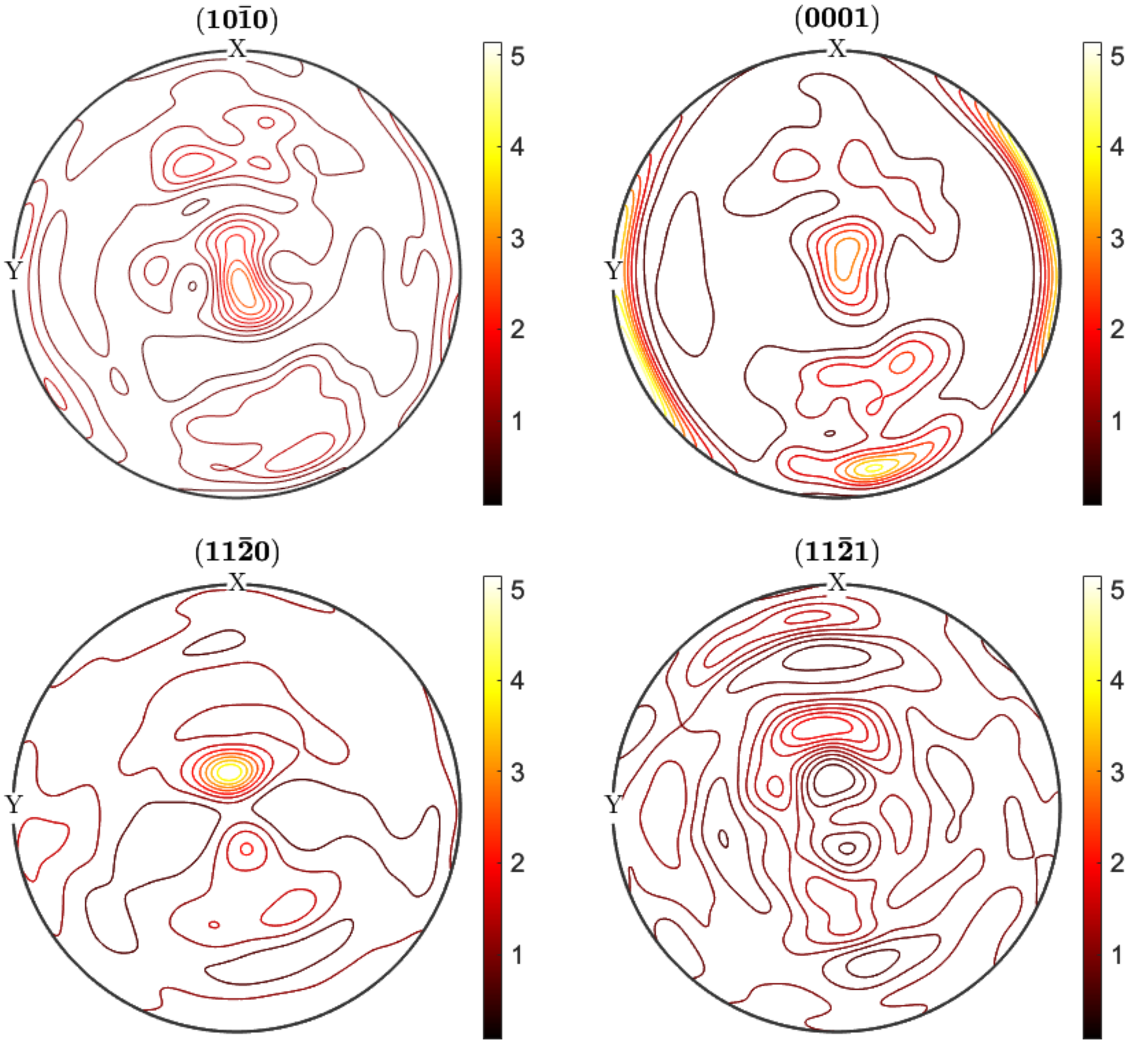

Fig. 7.14 Reconstructed Pole figures for undeformed ϵ-MAG-E calculated from an ODF generated from the experimentally captured (10$\bar{1}$0), (0002), (10$\bar{1}$1), (10$\bar{1}$2) and (11$\bar{2}$0) pole figures. The resulting distribution of the (0002) is explained further in Figure 7.15.

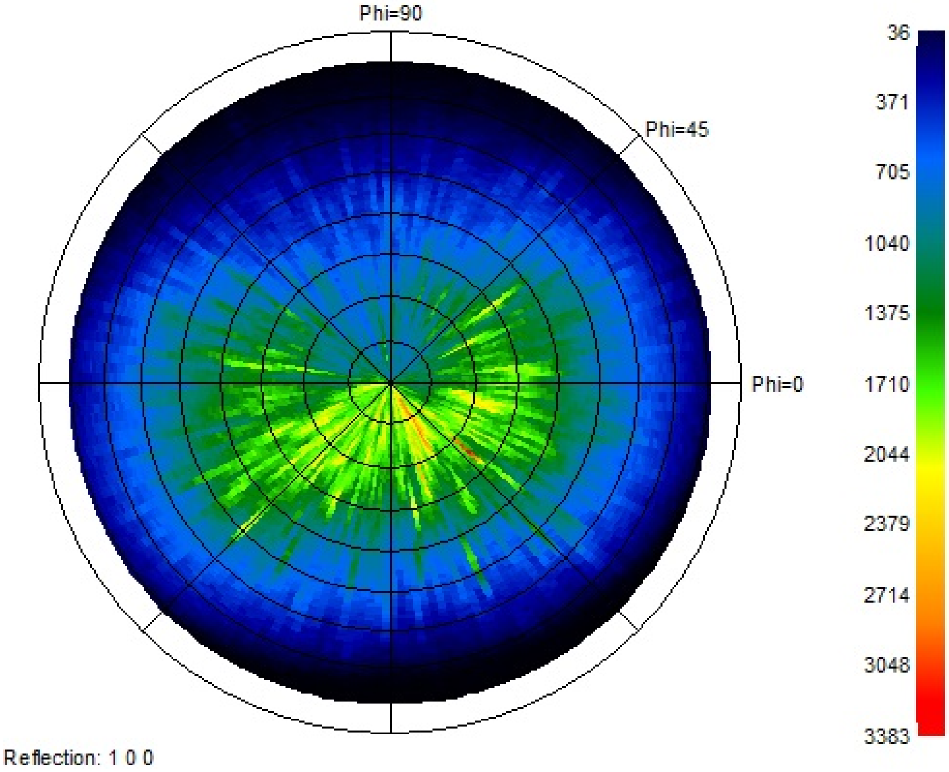

Fig. 7.15 The measured Pole Figure for the undeformed ϵ-MAG-E sample, showing a clear decrease in signal in the range $(45 \leq \chi \leq 135)^{\circ}$ without a ϕ dependency,

that 1050°C has been the heat treatment temperature used to set the ϵ-phase for all MnAlGa compositions examined in this thesis, all deformation processing was undertaken at this temperature to prevent the need for additional heat treatments to compare systems and for a known phase following heat treatment. Figure 7.16 shows the XRD pattern of a PSC deformed sample post deformation to a compressive strain of $\epsilon = 30\%$, showing that the water jet cooling rate observed post deformation was sufficient to prevent equilibrium phase formation, ensuring a single phase ϵ-MAG-E structure was present for transformation.

Following a 3 hour anneal under normal atmosphere at 430°C, the resulting 2θ-XRD scan shows the presence of multiple phases within the material. The presence of a multiple phase state was not expected following these heat treatment conditions, with work explored in Section 6.3 indicating that in an undeformed sample, annealing at 430°C for between 1-6 hours would produce a single phase, τ-MAG-E material. Thus, it can be inferred that the residual stress on the material from plastic deformation changes the $\epsilon \rightarrow \tau$ transformation dynamics such that this optimisation is no longer applicable.

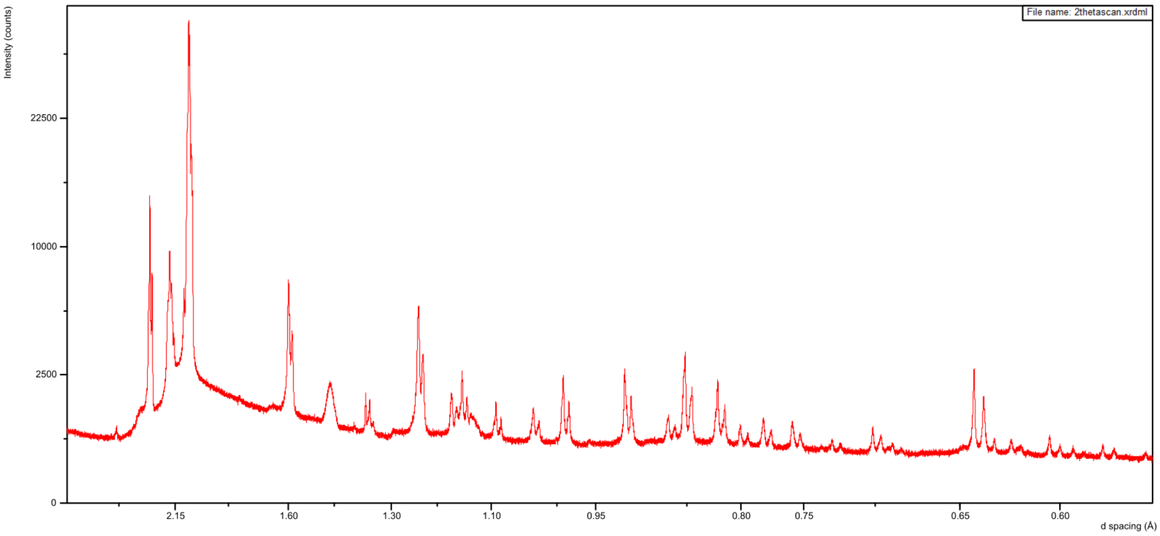

Fig. 7.16 2θ-XRD data captured for a sample of water quenched ϵ-MAG-E deformed by PSC to a compression strain of $\epsilon = 30\%$. All peaks shown correspond to known diffraction peaks for ϵ-phase MnAl, implying that the water jet cooling within the Servotest Thermo-Mechanical Compression (TMC) machine were sufficient to achieve quench status and prevent equilibrium phase formation to detectable limits.

Looking to a 2θ-XRD plot of the transformed material in Figure 7.17, it can be seen that both ϵ and τ peaks are present in the measurement, indicating an incomplete transformation, in disagreement with previously investigated work. Rietfeld refinement of textured material is significantly challenging, with preferred orientation affecting individual peak intensities and thus making phase population calculations challenging without having an exact mathematical model of texture to input into the model to best account for this effect. Further, it can be seen that there exist additional peaks which do not fit either phase, implying the existence of an additional 3rd phase in the system. As such, any phase population calculation is broadly qualitative but the refinement model presented predicts a phase population of approximately 50% τ-phase.

Magnetic Properties and Anisotropy Post-$\epsilon \rightarrow \tau$ Transformation

Looking to Table 7.1, one can see that both the intrinsic and extrinsic properties are dependent on sampling direction from the hot deformed material. In theory, the intrinsic properties should be constant between the two materials, with M_S representing the total magnetisation of all ferromagnetic unit cells within the measured system orientated along the same axis and thus is not a product of texture. However,

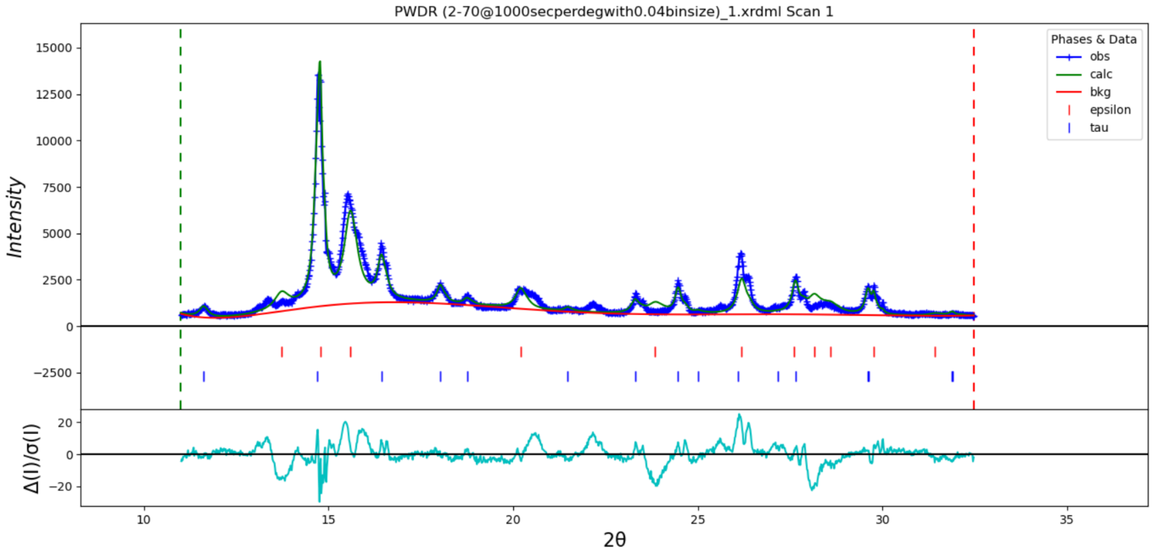

Fig. 7.17 Rietfeld Refinement in GSAS-ii of a sample of water quenched ϵ-MAG-E deformed by PSC to a compression strain of $\epsilon = 30\%$ and transformed to the τ-phase by a 3 hour heat treatment at $430°C$. As phase population calculation by Rietfeld refinement is an intensity-derived calculation and texture within a solid sample introduces direction-dependent intensity variations, exact phase population calculations are extremely challenging but the presence of ϵ-phase peaks implies an incomplete transformation.

looking to Figure 7.17, it can be seen that incomplete transformation has occurred, despite data from Section 6.3 and specifically Figure 6.12 indicating that 3 hours at $430°C$ is sufficient a heat treatment to see optimal $\epsilon \rightarrow \tau$ transformation in an undeformed sample. Thus, it can be inferred that the deformation process has an effect on the transformation between the two states and further optimisation work is required to fully explore this phenomenon. Thus, the differing intrinsic magnetic variables can be explained by the two measurements being taken from two different samples of the material. Geometric differences between the two samples changing the internal demagnetisation field were corrected for by assuming a near-cuboidal geometry and applying a shape factor correction calculated using MAGPAR software [40]. It is also assumed that the residual stress within both samples is equal, given both were taken from positions within the deformed material that were broadly symmetric under the deformation surface. Thus, it is hypothesised that not only does the residual stress from hot deformation change the transformation mechanics of the metastable $\epsilon \rightarrow \tau$ phase transformation but in mixed states between the two systems, phase populations are not constant between samples, instead measurements of the distribution which cannot be assumed to be isotropic.

Orientation	M_S $[kAm^{-1}]$	k $[kJm^3]$	H_A $[kAm^{-1}]$	M_R/M_S	H_C/H_A
$B \cdot ND = 0$	448.1 ± 0.1	1496 ± 5	5310 ± 20	0.20015 ± 0.00007	$(20.3 \pm 0.2) \times 10^{-3}$
$B \cdot RD = 0$	354.5 ± 0.2	1132 ± 9	5080 ± 40	0.2469 ± 0.0001	$(21.7 \pm 0.2) \times 10^{-3}$

Table 7.1 A table of intrinsic and extrinsic magnetic properties of MAG-E following plane-strain compressing to a compression strain of $\epsilon = 30\%$ and target phase transformation via a 3 hour anneal at $430°C$

As such, the comparisons made between both directions are limited. If extrinsic properties are considered as a fraction of intrinsic properties, i.e. M_R is proportional to M_S and H_C is proportional to H_A, then due to measuring two independent samples with two differing sets of intrinsic magnetic variables, simply comparing extrinsic variables like-for-like is inappropriate. In an effort to counter this, the extrinsic data presented in Table 7.1 is normalised by the corresponding intrinsic magnetic variable but it is recognised that a source of the property deviation may be inherent to the choice to use independent samples for each directional measurement. Further, it also questions the assumption that as-cast MnAlGa alloys have a homogenous composition as in mixed states, it is clear that this composition may vary over length scales of milimetres such that intrinsic property variation can be observed.

Understanding that the intrinsic magnetic variables are not constant by sample measurement, M_R is measured and discussed as a function of observed M_S under the assumption that it is a measurement of easy-axis alignment, in this case assumed to be c-axis alignment given previous predictions that average grain diameter should be below that of the critical domain size for a multi-domain state to occur and supported by the broad peaks observed in Figure 7.17 captured on an Ag X-ray source indicating a grain size of the order of 10s of nanometres. As such, comparing normalised variables allows for a method of comparing the two deformation directions and indicates that extrinsic properties are increased in the direction of compression during deformation, i.e during rolling, compression is achieved in a vector parallel to the normal direction, thus when measuring magnetisation with an applied field perpendicular to the rolling direction, it is parallel to the axis of compression. Further, when comparing this change in M_R/M_S to that of a sample with assumed isotropic grain orientation, it can be seen that there is an increase of $(23.36 \pm 0.07)\%$ in the $B \cdot RD = 0$ direction and a decrease of $(12.86 \pm 0.03)\%$ in the $B \cdot ND = 0$ direction. Comparing that to changes in H_C/H_A, it can be seen that, whilst there is a $(7 \pm 1)\%$ increase in the $B \cdot RD = 0$ direction, the decrease of $(18 \pm 1)\%$

in the $B \cdot ND = 0$ directions indicate that hot deformation may have a detrimental effect on coercivity. It is of note as well that this is not a fully transformed state, with mixed states not being comparable to a single state system on a micromagnetic level by way of changing the coupling between the ferromagnetic grains by the inclusion of paramagnetic species. None the less, this result demonstrates that it is possible to observe anisotropy in M_R as a result of hot deformation of the parent ϵ-phase and subsequent transformation to the τ-phase, recognising that additional work will be required to optimise this process and achieve complete τ-phase population.

Texture of Post-Transformation Sample

Following the same procedure as in Section 7.3.1, pole figures were captured for the deformed material post heat treatment and an ODF compiled to describe average plane intensity as a function of observation direction. Using MTEX to simulate inverse pole figures calculated from said ODF calculated relative to sample axis such as to compensate for misalignment during measurement, one can see in Figure 7.18 that preferred orientations are present within the material relative to deformation axis. Normalising the intensity of the two inverse pole figures, it can be noted that the [100] axis has a strong orientation relationship with the Rolling Direction (RD), recognising that [010] and [100] are equivalent directions in a tetragonal system, and the Normal Direction shows a strong response in the [110] direction and [043] direction. This second orientation preference for the ND and general increase compared in the intensity of the [001] plane in the ND direction over that of the RD, with TD direction showing similarly low intensity, would explain the preferential increase in M_R in the ND direction, given that $B \cdot RD = 0$ is a measurement in the ND direction as the RD points out of plane.

The [001] preference in the ND direction is not strong, however. Calculating the volume component of a [001] fibre along the RD, TD and ND respectively with an angular tolerance of 45°, we find that there is a distribution occupation of 30.55%, 26.57% and 32.62% respectively. These three values will not add to 100% as the three solid angles swept out by the fibres do not cover the full surface area of a sphere from which the stereographic projections of pole figures and inverse pole figures are calculated, shown graphically in Figure 7.19. The contributions of these fibres in the case of a rolled example would be in the directions 45° to RD, TD and ND simultaneously. If one assumes all grains are single domain as indicated by the crystallite size, one could assume that M_R as set from a relaxed state taken to

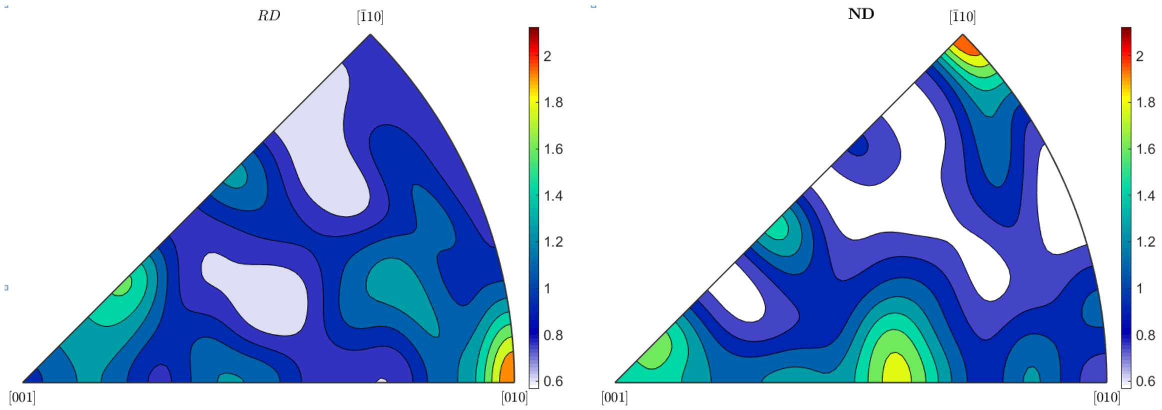

Fig. 7.18 ODF generated Inverse Pole Figures derived from measurements on a sample of water quenched τ-MAG-E deformed by PSC to a compression strain of $\epsilon = 30\%$ in the ϵ-phase. The directions defined are RD, perpendicular to the applied stress vector and ND, parallel to said vector, implying an anisotropic material response to PSC deformation as expected.

saturation can be understood as a preferential orientation of easy axis measured within a system. In a tetragonal system, the easy axis is the c-axis and, as such, this would explain the preferentially higher M_R observed in ND due to it having the highest average c-axis contribution compared to the two in-plane deformation directions.

7.3.3 Texture Before and After Transformation of MAG-E ($\epsilon = 35\%$) Compressive Strain

XRD Phase Information Post-Deformation and Post-Transformation

Moving to the intermediary PSC sample following the same heat treatment profile as optimised for an undeformed sample in Section 6.3, it can be seen in Figure 7.20 that following the same heat treatment as the $\epsilon = 30\%$ sample, the resulting phase population differs significantly. Whilst Rietfeld refinement results from textured bulk materials are closer to qualitative rather than quantitative due to the arguments already presented in the previous section, rough calculations predict a negligible ϵ-phase population, understood by the lack of peaks corresponding to the ϵ-markers displayed on the figure and an approximately $(10 \pm 10)\%$ βMn phase precipitating in the alloy, though this phase population prediction is at the limit of quantification, due to significant peak convolution with the nano-grain τ-phase and texture within the microstructure changing intensity ratios used to determine phase population

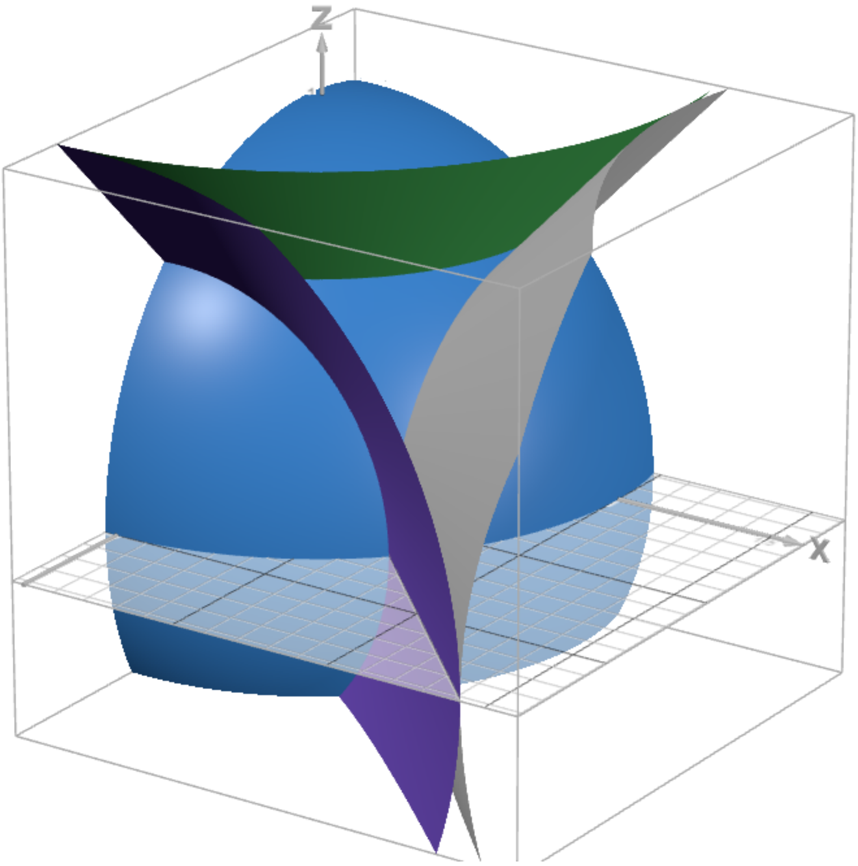

Fig. 7.19 A unit sphere plotted on DESMOS with three superimposed cones of internal angle measured from the axis of the cone of 45° to indicate that there is a segment of the unit sphere not contained within all three measurements. The equation for the sphere is $R = x^2 + y^2 + z^2$ and for each cone is it a permutation of $x_i = \sum_j^{j \neq i} x_j^2$, $i = x, y, z$.

ratios and, as such, should be considered more of a qualitative statement of the phase existing within the microstructure as opposed to an accurate reflection of the phase population.

Magnetic Properties and Anisotropy Post-$\epsilon \rightarrow \tau$ Transformation

Looking to the change in magnetic properties as a result of hot deformation and heat treatment, it can be seen in Table 7.2 that there is anisotropy in the measured values of M_R and M_R/M_S as a function of cardinal deformation directions ND and RD. In parallel to material strained to $\epsilon = 30\%$, measurements perpendicular to the rolling direction, i.e in ND, show a greater ratio of M_R to M_S, suggesting a greater degree of easy axis alignment in that direction. Though there are minor differences

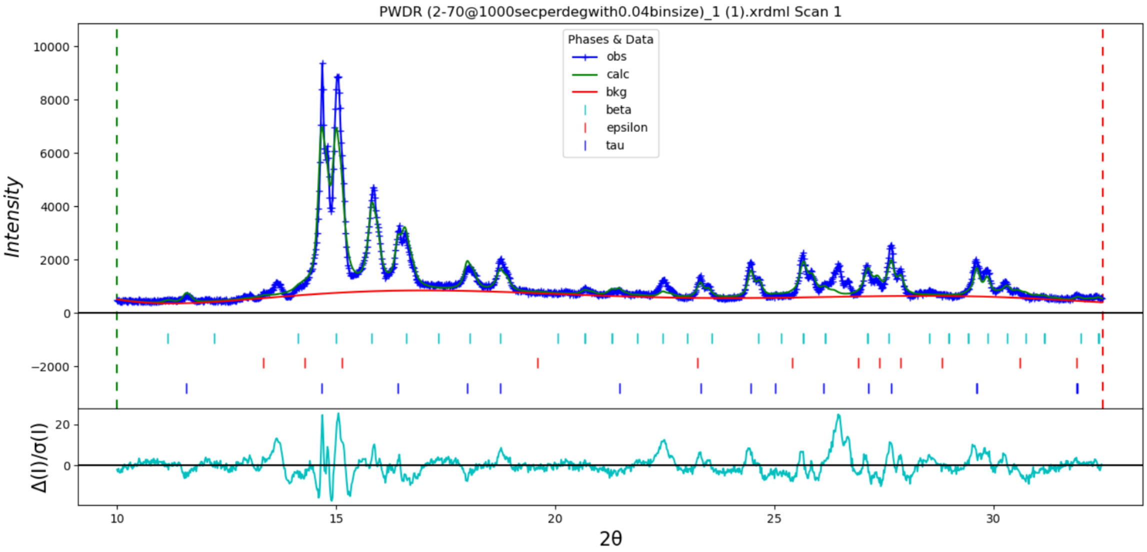

Fig. 7.20 Rietfeld Refinement in GSAS-ii of a sample of water quenched ϵ-MAG-E deformed by PSC to a compression strain of $\epsilon = 35\%$ and transformed to the τ-phase by a 3 hour heat treatment at $430°C$. Unlike that of $\epsilon = 30\%$, the estimated ϵ-phase population is assumed to be near zero, indicating complete transformation to a $\tau + \beta Mn$ state

Orientation	M_S $[kAm^{-1}]$	k $[kJm^3]$	H_A $[kAm^{-1}]$	M_R/M_S	H_C/H_A
$B \cdot ND = 0$	396.84 ± 0.07	1379 ± 3	5530 ± 10	0.20911 ± 0.00004	$(20.3 \pm 0.1) \times 10^{-3}$
$B \cdot RD = 0$	372.6 ± 0.3	1270 ± 20	5420 ± 70	0.2586 ± 0.0002	$(20.7 \pm 0.3) \times 10^{-3}$

Table 7.2 A table of intrinsic and extrinsic magnetic properties of MAG-E following plane-strain compressing to a compression strain of $\epsilon = 35\%$ and transformation to the target τ-phase via a 3 hour anneal at $430°C$

in intrinsic magnetic variables, attributed to the system being multi-phase in the same fashion as material strained to $\epsilon = 30\%$, the difference is of a lesser degree and may be inherent to assumptions made when accounting for demagnetisation fields across sample geometry, specifically modelling said sample as cuboidal in geometry. Further, difference in coercive field to anisotropy field found across the two samples is a product of differing calculated anisotropy fields, with observed coercivities being in good agreement between the two samples, indicating similar microstructures between the two samples and thus both samples being broadly representative of the bulk material, with composition and microstructure likely to be consistent for samples on the order of millimetres cut from PSC material deformed under the conditions discussed in this section.

When comparing the degree of anisotropy measured for M_R/M_S ratios for this sample, the sample that was deformed to a compression strain of $\epsilon = 30\%$ and an assumed isotropic sample, it is of note that the increase in $M_R/M_S(RD)$ is greater for $\epsilon = 35\%$ than that of lesser strains and that of the isotropic sample but the same can be said of $M_R/M_S(ND)$ in the case of the higher strain. An argument can be put forward, however, that unlike the higher strain case, the data presented in Table 7.1 is not as directly comparable in this case when comparing the differing ND results due to the difference in intrinsic magnetic variables and coercivities suggesting differing microstructures between the two samples, further corroborated by the phase population calculations suggesting a near even balance between ϵ- and τ-phases in the case of $\epsilon = 30\%$ but no detectable ϵ-phase presence in the sample deformed to $\epsilon = 35\%$.

In a similar argument to sample variation and inhomogeneity presented for the $\epsilon = 30\%$ sample, independent samples were used for each measurement direction. However, when comparing the intrinsic magnetic property divergence between the two samples, the difference for the $\epsilon = 35\%$ is $\approx 26\%$ that of the difference observed for the $\epsilon = 30\%$ samples. Thus, although both systems are not single phase, it can be inferred that the $\epsilon = 35\%, (\epsilon + \beta Mn)$ phase material is more homogenous in its phase distribution than that of the $\epsilon = 30\%, (\epsilon + \tau)$ phase material, though SEM testing would be needed to confirm this hypothesis.

Texture of Post-Transformation Sample

Generating deformation-direction dependent inverse pole figures, it can be seen in Figure 7.21 that a strong textural preference in ND can be observed for the [032] direction, such that other pole intensities are difficult to observe in comparison. The results for RD and TD are near-identical and thus only RD is displayed, showing textural preference in the [100] and [111] directions, more apparent when not using a consistent contouring scheme between the two directions. This texture is consistent with that observed for the sample that underwent compression strain of $\epsilon = 30\%$ but shows a greater directional preference in the normal direction to deformation, suggesting that there may be a causal link between 'strength' of texture and strain given similar strain rates and thermal history between the two samples. It may also be that the inclusion of the parent phase in the $\epsilon = 30\%$ sample is the cause of the more diffuse texture observed, as the measurement is that of a superposition of the two phases, reducing the intensity of the τ-phase diffraction peaks as scan parameters and surface preparation conditions were not varied between the two samples.

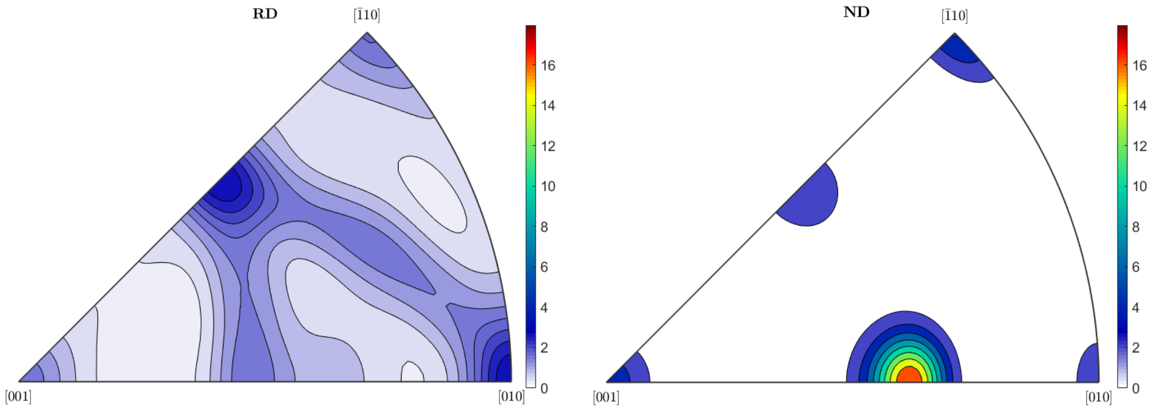

Fig. 7.21 ODF generated Normalised Inverse Pole Figures derived from measurements on a sample of τ-MAG-E deformed by PSC to a compression strain of $\epsilon = 35\%$ in the ϵ-phase. The directions defined are RD, perpendicular to the applied stress vector and ND, parallel to said vector, implying an anisotropic material response to PSC deformation as expected. Near-zero signal intensity regions within the ND plot are a product of a strong [032] signal as opposed to a lack of data, with colour scales insufficient to accurately display all data within available scale quantisation.

Considering directional planar occupancy, it can be seen that for the same 45° tolerance of a [001] in each cardinal deformation direction, the volume fractions are 25.56%, 26.64%, 21.37% for RD, TD and ND specifically. This would initially suggest M_R/M_S should have a greater ratio in the RD-TD plane. Examining instead cones in stereographic space orientated at the midpoints between the three directions, $(RD+TD)$, $(RD+ND)$ and $(TD+ND)$, the volume fractions calculated from the ODF are respectively 26.46%, 30.86% and 32.95%. Thus, it can be explained that whilst the individual predicted volume of c-axis orientation with ND is not greater than that of RD or TD, it is more likely still to find grains with c-axis aligned on a vector orientated out of the plane of deformation, explaining the anisotropy observed in M_R/M_S measurements. This logic can be further explained looking to the inverse pole figure for ND in Figure 7.21 and the strong signal for the [032] direction, thus implying that the texture resultant from deformation and heat treatment results in a microstructure where it is likely to align grains such that there is a greater proportion of c-axis alignment normal to the plane RD-TD than within it. This can be visualised in Figure 7.22, with non-normalised intensities showing that the RD+TD direction has a similar pole intensity distribution as RD shown in Figure 7.21 which has already been stated to be similar again to the TD inverse pole figure but that the directions RD+ND and TD+ND show strong [001] alignment, corroborating the theory explained above.

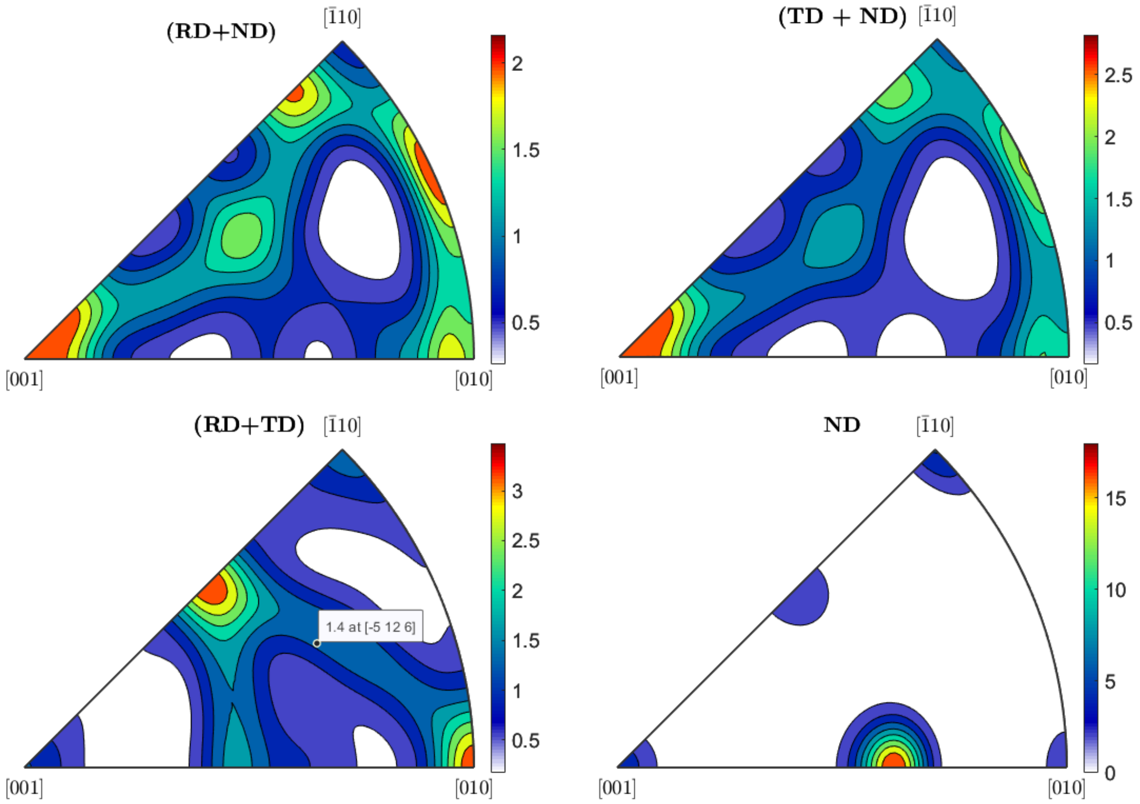

Fig. 7.22 ODF generated Inverse Pole Figures derived from measurements on a sample of τ-MAG-E deformed by PSC to a compression strain of $\epsilon = 35\%$ in the ϵ-phase. The directions defined are combinations of the cardinal deformation vectors such that total out-of-deformation-plane orientations can be visualised. The [001] signal in the $(RD + ND)$ and $(TD + ND)$ supports observations of a greater M_R/M_S ratio in measurement directions such that $B \cdot RD = 0$.

7.3.4 Texture Before and After Transformation of MAG-E ($\epsilon = 40\%$) Compressive Strain

XRD Phase Information Post-Deformation and Post-Transformation

The 2θ-fit for the as-transformed sample can be seen in Figure 7.23 and shows that, in a similar case to that of $\epsilon = 35\%$, there is evidence of βMn formation, indicating that increased strain can induce equilibrium phases during transformation when compared to undeformed samples. The caveat of Rietfeld refinement being challenging when conducted on textured samples and thus leading to an increased error on phase population identification still being present, much like the other two deformed samples, initial phase population predictions show undetectable ϵ-phase formation, implying complete $\epsilon \rightarrow \tau$ transformation occurred. Overall, predicted τ-phase population is approximately $(95 \pm 5)\%$ with detectable βMn traces with a phase population of approximately $(2 \pm 2)\%$.

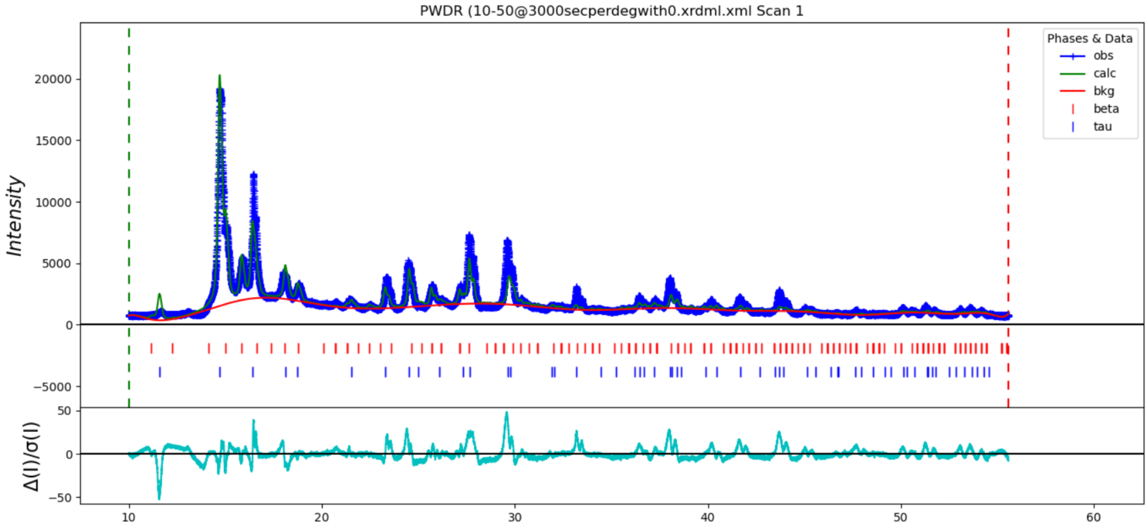

Fig. 7.23 Rietfeld Refinement in GSAS-ii of a sample of water quenched ϵ-MAG-E deformed by PSC to a compression strain of $\epsilon = 40\%$ and transformed to the τ-phase by a 3 hour heat treatment at $430°C$. Unlike that of $\epsilon = 30\%$, the estimated ϵ-phase population is assumed to be near zero, indicating complete transformation to a $\tau + \beta Mn$ state

Magnetic Properties and Anisotropy Post-$\epsilon \rightarrow \tau$ Transformation

Looking to the magnetic properties of transformed MAG-E ($\epsilon = 40\%$) in Table 7.3 , clear directional anisotropy in the values of M_R/M_S can be observed depending on whether the material was magnetised relative to RD or ND whilst also showing M_S that can be considered identical once additional error factored in from the cuboidal demagnetisation factors have been accounted for. This would imply that the deformation processing was successful in producing a greater degree of anisotropy than previous tests, but this is also amplified by the increased observed values of M_S, being comparable to that of optimised MAG-E discussed in Section 6.3.

In the same fashion as samples taken for $\epsilon = 30\%$ and $\epsilon = 35\%$, independent samples were used measure the directional response to magnetisation. The deviation in M_S between the two samples taken from the material deformed to $\epsilon = 40\%$ is 2 orders of magnitude lower than that of samples taken from material deformed to either $\epsilon = 30\%$ or $\epsilon = 35\%$. Comparing this to the phase population distribution calculated

Orientation	M_S $[kAm^{-1}]$	k $[kJm^3]$	H_A $[kAm^{-1}]$	M_R/M_S	H_C/H_A
$B \cdot ND = 0$	655.8 ± 0.1	1945 ± 7	4720 ± 20	0.07319 ± 0.000002	$(4.08 \pm 0.02) \times 10^{-3}$
$B \cdot RD = 0$	655.1 ± 0.4	1780 ± 20	4330 ± 60	0.2149 ± 0.0002	$(4.53 \pm 0.06) \times 10^{-3}$

Table 7.3 A table of intrinsic and extrinsic magnetic properties of MAG-E following plane-strain compressing to a compression strain of $\epsilon = 40\%$ and a 3 hour anneal at $430°C$ to precipitate the $\epsilon \rightarrow \tau$ transformation.

for each material set, it can be inferred that the cause behind the intrinsic magnetic property variability in each sample is the presence of a secondary phase and that the variability, and thus inhomogeneity, of each deformed material increases as non-τ-phase population increases.

Of particular interest to the design of deformation processing, however, is the significant decrease in H_C/H_A following transformation. Whilst broadly comparable with one another, the measured coercivities are an order of magnitude lower than previously observed deformed samples have exhibited. Given the increase in directional M_R observed is lower than that of the isotropic M_R for undeformed τ-MAG-E, the decrease in H_C would mean an overall decrease in BH_{Max} for the system, thus drawing the process further away from Gap Magnet Criteria as laid out in Table 1.1. To further explore the reasoning behind this, additional 2θ-XRD measurements were taken with a Cu-source in order to perform Scherrer analysis and determine the sample grain size when compared to that of an undeformed sample. The calculated average grain size for the sample following compression strain $\epsilon = 40\%$ is $D_{grain,40\%} = (24 \pm 2)nm$ compared to the average grain size of the $\epsilon = 35\%$ sample being $D_{grain,35\%} = (38 \pm 2)nm$.

Given that the critical diameter for MAG-E as a function of heat treatment in Figure 6.28, the difference between the average grain size of both samples and the change in coercivitiy may be inherently linked. Depending on whether strict adherence to Bloch's $T^{\frac{3}{2}}$ law is observed or whether there is a free-fitting temperature dependence allowance to fit more strictly to the observed $T^{\frac{7}{4}}$ dependency, the critical domain diameter for undeformed MAG-E annealed for 3 hours at $430°C$ is either $(400 \pm 10)nm$ or $(660 \pm 20)nm$ respectively. Regardless, this would imply that both systems have grains that are, on average, single domain but increasing deformation decreases grain size, theoretically through re-crystallisation following plastic free-flow. This decrease in the average grain size means both that the population of multi-domain grains will decrease but that grains will grow closer to the superparamagnetic limit, lowering the overall coercivity of the material.

Calculating the superparamagnetic size limit, the characteristic equation relating measurement time to particle relaxation, i.e change in magnetisation vector, time is that of the Neel-Arrhenius equation

$$\tau = \tau_0 exp(\frac{kV}{k_B T}) \tag{7.6}$$

where τ is the measurement time whereby a particle may relax, τ_0 is the characteristic attempt time where the magnetisation vector may change and all other variables use previously defined magnetic and thermodynamic definitions [103]. Assuming spherical particle geometry of radius R, measurement time to be that of $\tau \rightarrow 10^9 s$ (of the order of 10 years) to represent potential service life of a permanent magnet material and that $\tau_0 \approx 10^{-9} s$, one can rearrange this equation to be

$$R^3 = \frac{3ln(10^{18})k_B T}{4k\pi}. \tag{7.7}$$

At $T = 23°C$ and using k values fitted from both deformed samples, the critical radius for the $\epsilon = 40\%$ sample is of the order of $3nm$, which is an order of magnitude smaller than the observed average grain size for the alloy, meaning that within the distribution of grains there is an insignificant proportion of superparamagnetic grains that could be expected to be present with reasonable normal distribution models of grain size variation. Further discussion as to the decrease in H_C observed in this sample when compared to the undeformed control are discussed in Section 7.3.5

Texture of Post-Transformation Sample

Examining the inverse pole figures generated respectively to mapped rolling specific directions RD, TD and ND as seen in Figure 7.24, it can be seen that no specific deformation cardinal direction exhibits a preferential [001] texture. In a similar fashion to that of material deformed to a compression strain of $\epsilon = 35\%$, the ND inverse poll figure shows a strong [032] signal, implying that for deformed and transformed MAG-E, this is the resulting alignment for the system. However, when comparing the two systems, both the relative intensity of the [032] measurement in ND and the comparison between RD and TD vary, with a greater deviation between RD and TD and a decrease in [032] intensity being observed for $\epsilon = 40\%$. Given the observed anisotropy in M_R/M_S measurements with respect to deformation directions and no strong direction-dependent [001] signal, composite direction

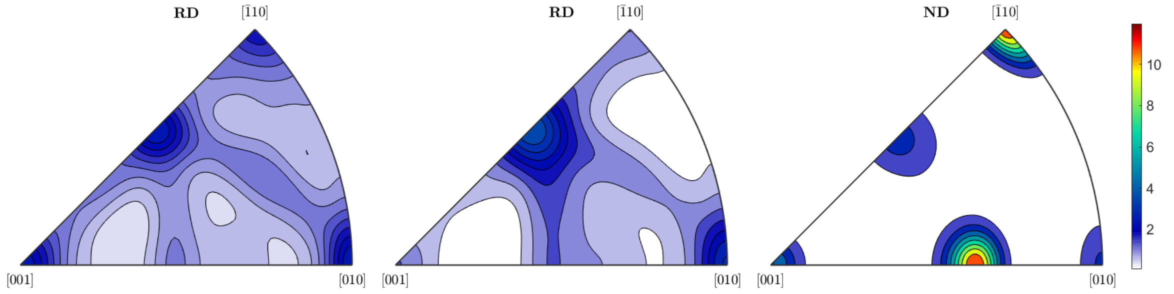

Fig. 7.24 ODF generated Normalised Inverse Pole Figures derived from measurements on a sample of τ-MAG-E deformed by PSC to a compression strain of $\epsilon = 35\%$ in the ϵ-phase. The directions defined are RD and TD, perpendicular to one another and the applied stress vector, and ND, parallel to said vector, implying an anisotropic material response to PSC deformation as expected. As with $\epsilon = 35\%$, the near-zero signal intensity regions within the ND plot are a product of a strong [032] signal as opposed to a lack of data, with colour scales insufficient to accurately display all data within available scale quantisation once normalisation has occurred.

inverse pole figures were also generated in the same manner as those generated for material compressed to a strain of $\epsilon = 35\%$. This composite direction inverse pole figures can be seen in Figure 7.25 and the maxima intensity observed relative to one composite direction is in the $TD + ND$ direction. The deviation between the three composite directions further compounds the difference between RD and TD directions with the compound direction showing a similar planar distribution but with intensity variations and the compound directions with ND showing maxima in the [365] and [001] directions.

Using a fibre occupancy model and assuming a 45° angular tolerance in a given direction would imply that easy axis alignment would contribute to M_R we find that for RD, TD and ND, the volume occupancy or probability that a given grain would have the [001] direction aligned with said deformation direction to be 28.43%, 27.87% and 23.26% respectively and with the compound directions $RD + TD$, $RD + ND$ and $TD + ND$ showing volume occupancy of 27.77%, 28.73% and 30.87%. Thus, this would explain the resulting measurement anisotropy, given that the anisotropy is greater when measuring with the applied field perpendicular to RD, thus assuming that there is a greater M_R contribution from easy axis-alignment with the direction of applied field, the associated direction would be a sum of the distribution of the alignment in directions including those off from the cardinal deformation direction, explaining the greater M_R. However, the maxima predicted by this logic would be for a magnet cut from the deformed material such that it was magnetized along the

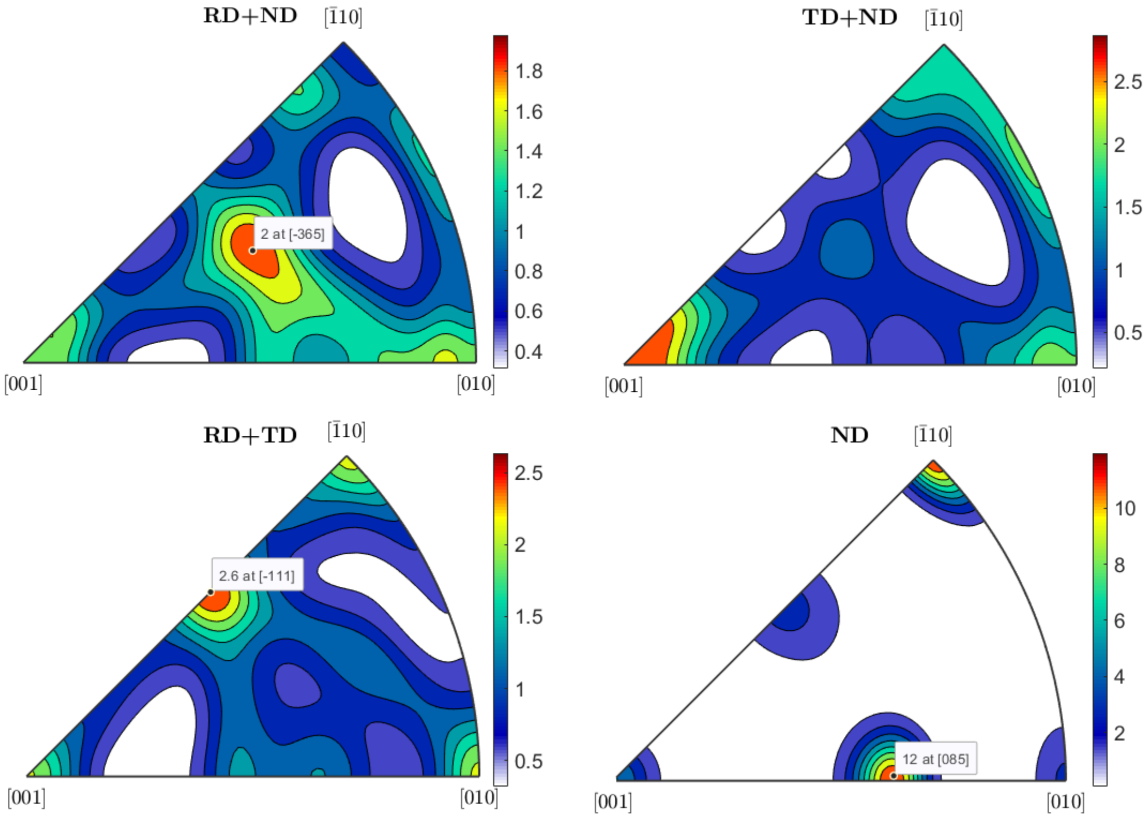

Fig. 7.25 ODF generated Inverse Pole Figures derived from measurements on a sample of τ-MAG-E deformed by PSC to a compression strain of $\epsilon = 40\%$ in the ϵ-phase. The directions defined are combinations of the cardinal deformation vectors such that total out-of-deformation-plane orientations can be visualised. The [001] signal in the $(TD + ND)$ and $(TD + ND)$ supports observations of a greater M_R/M_S ratio in measurement directions such that $B \cdot RD = 0$

TD+ND direction, a further deviation from the material deformed to $\epsilon = 35\%$ which showed lower dependency on whether the magnetisation was relative to RD or TD as long as it was approximately 45° to the plane of deformation.

7.3.5 Comparisons Between the Three Deformation Samples

Phase Population Variation

The initial observation between the three samples is that the phase population measured is not consistent between the three samples, nor with the undeformed control sample. Compared to the phase population for the sample strained to $\epsilon = 35\%$, the sample compressed by a strain of $\epsilon = 40\%$ would initially indicate that the increased strain would see a decrease in equilibrium phase formation. However, given that the cooling achieved on the tooling was from water jets onto the tooling and sample, it is not possible to ensure exactly the same cooling profile for both samples. Given this observation, Rietfeld fitting of the precursor state was undertaken for the $\epsilon = 40\%$ sample to investigate the emergence of the βMn phase. From this fitting and with the same caveat that phase population from textured samples as calculated by Rietfeld refinement is non-trivial and thus data presented has significant associated errors, the βMn phase population was calculated to be non-zero, with clearly emergent peaks in the data that could not be attributed to either τ- or ϵ- phases. This indicates that either the cooling rate achieved within the tooling was insufficient to ensure a single phase state but that the difference between the $\epsilon = 35\%$ and $\epsilon = 40\%$ samples showing a decreasing βMn population with increasing strain would not indicate a strain-induced phase difference. Given that the undeformed sample shows no βMn transformation, the inclusion of this phase can be attributed to a less-than-ideal cooling rate achieved within the tooling. The measured cooling rate for the $\epsilon = 40\%$ is $(680 \pm 7)°Cs^{-1}$ and for the $\epsilon = 35\%$ sample, cooling appears to have occurred in three distinct phases, namely an initial cooling from deformation temperature, $1050°C$ to $800°C$ at a cooling rate of $(740 \pm 20)°C$, a more gradual cooling rate of (103.6 ± 0.2) in the range of $(800 - 560)°C$ followed by another rapid cooling period in the range of $(560 - 60)°C$ at a measured cooling rate of $(3300 \pm 200)°C$. The three cooling regimes can be seen in Figure 7.26 and show that the cooling rate for the sample deformed to a strain of $\epsilon = 35\%$ is the outlier, potentially explaining the increase in βMn and disproving the hypothesis that the βMn phase population is strain-induced. It is reasonable to assume that this change in cooling rate was due to issues in water supply resulting in a period of air cooling, but that the βMn phase formed during this break in water cooling.

βMn is not present in undeformed samples, however. This could be explained as the cooling rate achievable by a full water quench would be assumed to be higher than cooling by a stream of water, as it would allow isotropic heat flow from the sample into the cooling medium rather than a mixture of sample-to-coolant heat flow occurring where the stream makes contact and radiant/sample-to-air cooling at the rest of the surface. Further, the thermocouple measurements for the as-deformed sample may not be truly representative of the bulk temperature of the system. Given that the thermocouple is recessed into the bulk of the sample and held in place by friction, it could be hypothesised that coolant water trapped itself within this recess, locally cooling the thermocouple at a faster rate than the bulk of the sample. This hypothesis can be further justified by the steady state of some samples remaining at approximately $100°C$ following the initial cooling rate, implying that there is a localised boiling event occurring within the thermocouple and that the thermocouple and boiling coolant have reached thermal equilibrium. It is recognised that this is a hypothesis though, with significant simulation work required to prove it. At present, however, the main conclusion is that βMn precipitates form due to insufficient and inconsistent cooling that can be perfected in further trials to ensure repeatability.

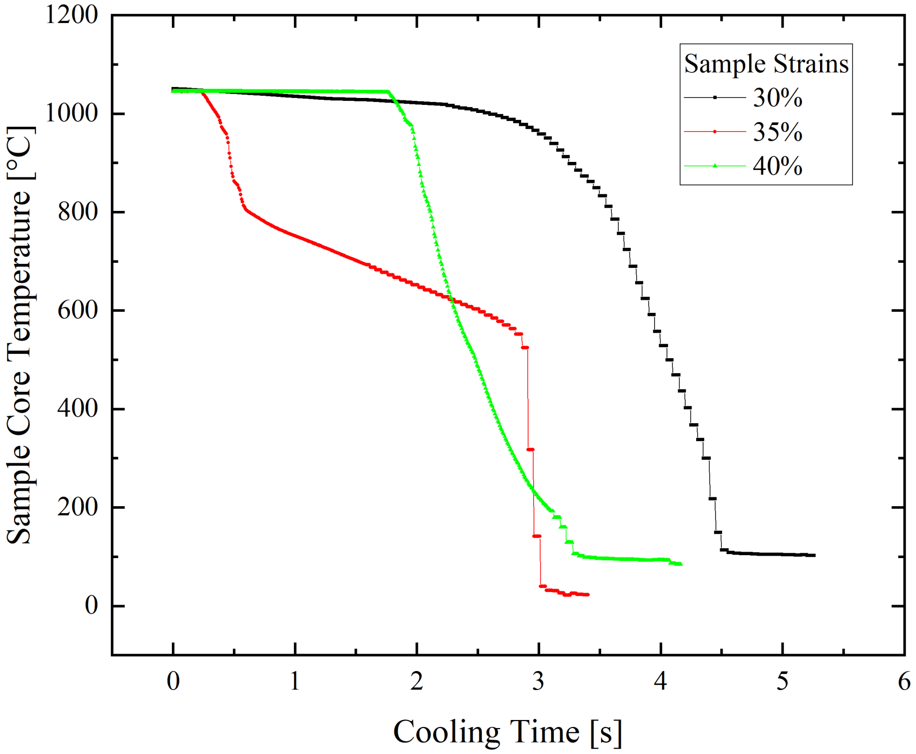

Fig. 7.26 The thermocouple measurements for all three PSC samples following deformation, showing three differing cooling rates and a dwell time at an intermediate temperature for the sample deformed to a compression strain of $\epsilon = 35\%$, potentially explaining the additional βMn precipitation not predicted from undeformed samples.

The anomalous phase population of the $\epsilon = 30\%$ sample, however, cannot be explained by this. Initial scans of the deformed sample did not show βMn precipitation to a detectable phase population and given the uncertainty surrounding the effectiveness of water jet cooling following deformation processing and thus comparability with the water quench of the undeformed sample, it may be that cooling rates were sufficient in the case of the $\epsilon = 30\%$ strain sample such that there was insufficient time for βMn formation but that the additional residual stress of the system changes the dynamics of the $\epsilon \rightarrow \tau$ phase transformation. The transformation has already been shown to be sensitive to composition in Figure 3.2 and temperature in Figure 6.12 and so it may be the case that it is sensitive also to residual stress within the system. Further, given that in cases where βMn is present, complete transformation occurs and consistent intrinsic magnetic properties are observed between samples taken from each deformed material, it may also be the case that the presence of βMn also changes the transformation dynamics by providing nucleation sites or breaking up long range ordering effects. Further investigating these hypotheses is beyond the scope of this thesis, but this issue compounds the notion that the annealing process must be optimised for a given material not only for composition but also for deformation to ensure maximum τ-phase population and to determine whether lattice parameter tuning as observed in undeformed MAG-E is possible in cases where deformation has occurred.

Magnetic Property Variation

Considering the variation in cooling rates between the three samples as a result of processing, it becomes challenging to compare directly the intrinsic and extrinsic magnetic properties of the three deformed samples and that of the undeformed sample. It is clear that all three samples showed M_R anisotropy with measurements taken with the applied magnetic field parallel to the direction normal to deformation (i.e $\hat{B} \cdot \hat{ND} = B$) showing a consistently higher M_R/M_S ratio than that of the assumed isotropic undeformed sample, indicating that deformation processing and the resulting texture can increase this ratio, presenting a mechanism to improve extrinsic properties and thus increase BH_{Max}. A plot of all three samples magnetised along both $\hat{ND}$ and $\hat{RD}$ can be seen in Figure 7.27. It is of note that the changes in shape and the point at which the hysteresis loops meet for each plot can be used as a means of interpreting the degree of easy axis alignment with a given magnetisation direction. Given that for each sample there is no alignment between $\hat{ND}$ and $\hat{RD}$, this implies that there is a preferential direction for the easy axis to align itself with respect to mechanical deformation and thus a texture is present.

Looking to the intrinsic magnetic variables, in no case was 100% τ-phase observed, unlike in the undeformed case, following a 3 hour anneal at $430°C$. Thus, intrinsic magnetic properties were not at the material maximum due to a decrease in ferro-

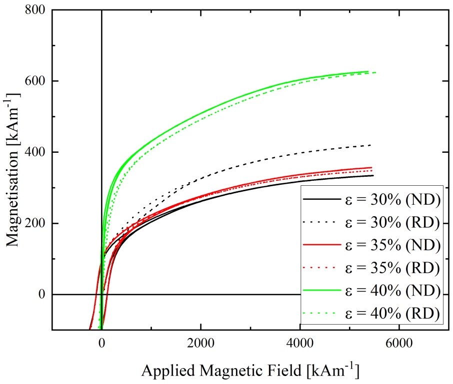

Fig. 7.27 Magnetic hysteresis loops for post $\epsilon \rightarrow \tau$ transformation heat treatment MAG-E samples deformed to compression strains of $\epsilon = 30\%$, $\epsilon = 35\%$ and $\epsilon = 40\%$ at $1050°C$ magnetised in the rolling direction $\hat{RD}$ and normal direction $\hat{ND}$.

magnetic phase density with the inclusion of the precursor ϵ-phase or equilibrium βMn phase in the population. Thus, to further optimise this technique, greater control over cooling would be necessary to ensure sufficient thermal control to prevent βMn formation post-deformation and additional heat treatment trials to investigate the relationship between residual strain and $\epsilon \rightarrow \tau$ transformation timelines as a function of temperature to ensure optimum properties can be achieved.

Finally, considering changes in H_C, all deformed samples show a decrease in H_C when compared to that of the undeformed sample. Whilst the inclusion of additional phases within the material may contribute negatively to H_C, grain size variation is also a factor to consider. For a heat treatment of 3 hours at $430°C$, an undeformed sample of MAG-E has been shown to have an average grain size of $D_{grain,0\%} = (26 \pm 2)nm$, referencing Table 6.5. Comparing that to the calculated grain sizes of samples deformed to compression strains of $\epsilon = 35\%/40\%$, we measure that the average grain size is $D_{grain,35\%} = (38 \pm 2)nm$ and $D_{grain,40\%} = (24 \pm 2)nm$ implying for comparable grains, there is a significant drop in coercivity between the undeformed state and $\epsilon = 40\%$ state, with $H_C(0\%) = (118.4 \pm 0.8)kAm^{-1}$, $H_C(35\%) = (112.0 \pm 0.6)kAm^{-1}$ and $H_C(40\%) = (48.00 \pm 0.01)kAm^{-1}$. Referencing Equation 6.2, there initially can be two conclusions drawn from this change for comparable grains.

The first is that the intergranular coupling constant α has decreased as a result of deformation, implying that the contribution to H_C from the magnetocrystalline anisotropy is decreasing as a result of deformation. Referencing Skomski and Coey, this coupling constant is understood as a representation of the microstructure from a micromagnetic perspective, including such effects as pinning and nucleation [16]. Given that it has been measured that the average grain within each measured system is below the critical diameter to exist in a single domain state, these factors may differ but this should be consistent between the undeformed and deformed state. Given the purpose of hot deformation was to create a preferential grain orientation within the material, it is entirely plausible to infer that this would lead to a significant change in microstructure such that the α constant would change relative to each material.

In reference to Xue *et. al.*, it is also important to calculate exchange lengths to determine which regime within Grain Size Dependence of Coercivity and Permeability (GSDCP) theory the MAG-E samples fall within [43]. The three regimes are defined as dependent on the average grain size, D_{eff}, such that

- $D_{eff} < l_{ex}$: $H_C \propto D^6$
- $l_{ex} < D_{eff} < \delta_0$: $H_C \approx const.$
- $D_{eff} > \delta_0$: $H_C \propto D^{-1}$

where $l_{ex} = \sqrt{\frac{A}{K_1}}$ is defined as the exchange length and $\delta_0 = \pi\sqrt{\frac{A}{K_1}}$ is defined as the domain wall thickness [37]. Assuming that the Exchange constant is near constant for all measured samples, this would imply that the undeformed sample existed in the D_{eff}^{-1} regime, with the calculated values for l_{ex} and δ_0 equalling $(1.60 \pm 0.02)nm$ and $(5.02 \pm 0.06)nm$ for the undeformed sample with deformed samples showing insufficient intrinsic magnetic variable variation to see an order of magnitude increase in these variables. Thus for the same α and N_{eff} coefficients, one would predict that the sample deformed to $\epsilon = 35\%$ would see a decrease in H_C of $(32 \pm 3)\%$ when compared to the undeformed state and that the sample deformed to $\epsilon = 40\%$ should see an increase of H_C of $8 \pm 1\%$ when compared to the sample deformed to $\epsilon = 35\%$. However, given that this is not the case, one can assume that the Kronmüller coefficients α and N_{eff} have changed as a result of hot deformation. Testing these new coefficients would require further testing, however, with single phase materials in order to isolate the effect of the grain morphological changes resulting in relative coercivitiy changes.

Texture Variation - Alignment and Strength

When considering the resultant of the τ-phase texture following deformation processing of the ϵ-phase, it is of note that in all three deformed samples, the direction

	Deformation Strain [%]			
phase	0	30	35	40
$t(\epsilon)$	1.8160	2.1495	1.9024	2.2530
$t(\tau)$	N/A	1.9371	5.6325	4.1546

Table 7.4 A table of Texture Index Coefficients calculated from constructed Orientation Distribution Functions from samples of MAG-E following plane-strain compression (ϵ) and a 3 hour anneal at 430°C (τ)

normal to deformation, ND, shows a strong intensity for the [032] plane, with a diffuse distribution including planes of similar orientations. In an effort to quantify the texture resulting from deformation, a Texture Index coefficient, t, must be introduced to quantify the systems for comparison, as defined in Section 4.4.2. This coefficient can be defined as the mean square of the calculated Orientation Distribution Function, often cited as multiples of the Misorientation Distribution Function, with results of the order of unity being interpreted as isotropic and increasing as 'texture intensity' increases [75].

Calculating this Texture Index for all 8 measured states, these can be found in Table 7.4. Pole figures were not captured for transformed, undeformed MAG-E due to time constraints and equipment malfunction but examining the initial state, it can be seen that a weak texture is already present in the material. Whilst this can be partially explained by the reasoning presented in Section 7.3.1, there may also be a texture within the material resulting from nucleation from solidification on casting and resulting cooling zones. However, when compared to any of the deformed samples, it can be seen that t increases as a result of deformation and it is possible to hypothesise that there is a positive correlation between deformation strain and increase in t, though further data would be needed to confirm and characterise this relationship. The decrease observed in the ϵ-phase of the sample deformed to $\epsilon = 35\%$ is attributed to the precipitation of βMn during the non-idealised cooling contributing to intensity fluctuations due to convoluted peaks, decreasing observed texture-induced intensity anisotropy during pole figure measurements.

Of particular interest, is t as a function of strain. Noting that all three have varying phase balances as well as varying deformation profiles, comparisons can be made both as a function of transformation and as a function of deformation. The initial sample deformed to a strain of $\epsilon = 30\%$ shows a decrease in Texture Index from the initial state to post heat treatment state not seen in the other deformed samples. Given this index can be interpreted as a ratio of orientation to misorientation, this would imply that the heat treatment increases the misorientation of the resulting deformation texture from deformation. However, as discussed in Section 7.3.2, we know this sample to be in a mixed $\epsilon + \tau$ state. As such, during transformation, a greater degree of misalignment would be expected as τ-phase crystallites form within the alloy, which whilst preferentially orientated as a result of forming from orientated ϵ-phase material, are not the majority phase, resulting in a lesser relative intensity peak in ND for the [032] peak when compared to the other deformed samples. Thus, it can be considered that resulting texture increases from metastable transformation from a textured parent phase will only result in an increase in Texture Index following complete transformation.

As for the two fully transformed samples, $\epsilon = 35\%$ and $\epsilon = 40\%$, it can be clearly observed that the Texture Index increases as a result of transformation. Looking to the maxima on the inverse pole figures for ND in the ϵ-phase state, a maxima is observed in the [001] direction, though the relative occupancy is of a lesser extent when compared to the [032] plane for the transformed state, as seen in Table 7.5. Comparing preferential orientations, the [100] direction preferentially orientates itself with the direction of simulated rolling and this preferential orientation increases as a result of increasing plastic deformation. However, this does not necessarily result in an increase in maxima signal measured for the resulting τ-phase structure. Whilst this could be resultant from differing cooling rates, grain sizes or phase balances, it does suggest that whilst preferential volume occupancy can be achieved in the parental ϵ-phase, this increase in anisotropy does not directly correlate to an increase in the anisotropy post transformation and further investigation is required.

It is of note that when considering misorientation angles for a given fibre, i.e a plane associated with a given material direction, one is in effect measuring a cone of misorientation angle θ on a solid surface area of possible orientations. Thus, one can compute the ratio of the spherically capped cone to spherical surface area and find the ratio is equal to $2sin^2(\frac{\theta}{2})$, which for a cone on a hemispherical system, having been reduced by symmetry, of angle 45° would sweep out a solid angle ratio of approximately 22.29% of the surface area. Thus, any volume fraction can be considered preferential or non-preferential by its deviation from this percentage when measured using this misorientation cone and the same cone measured on three orthonormal directions will not be equal to the entire surface area of the cone, implying that the sum of the volume fractions of a sample measured for a specific plane measured on three orthonormal vectors can be less than 1.

	Volume Occupation in ND			
phase	0	30	35	40
ϵ [001]	0.3195	0.3193	0.2443	0.1538
ϵ [100]	0.6800	0.6809	0.7559	0.8567
τ [032]	N/A	0.8910	0.9017	0.8418

Table 7.5 A table of calculated percentages of grain alignment with a certain plane orientated along a given deformation direction, with a misorientation allowance of 45° following plane-strain compressing to a compression strain of $\epsilon = 30\%$ a 3 hour anneal at $430°C$

Limitations of conclusions

Given the time and resources required to manufacture PSC samples as well as service issues with the equipment at the University of Sheffield during the timeframe that these experiments were conducted, no additional measurements, including repeat measurements, were able to be conducted. As such, the comparisons stated are not ideal in this section, with cooling rates differing between samples and thus changing phase populations and final conditions. Whilst it is possible to demonstrate that preferential texture can be generated in MAG-E samples through hot deformation of the ϵ-phase and retained following heat treatment to the τ-phase, there is insufficient data to provide commentary as to volume occupations for precursor and transformed states as a function of compression strain. Further testing with greater control of cooling rates would be required for greater comparison as well as repeat testing of $\epsilon = 30\%$ in order to explore if similar composition variations are observed.

7.4 Conclusions

Considering the three objectives set out at the start of this chapter, it can be said that all three have been achieved. A ductile phase and temperature set was identified, where thermodynamically stable ϵ-MAG-E was shown to deform plastically under compression. Further, texture measurements of uniaxial samples show that preferential alignment can be achieved as a result of deformation. Finally, PSC measurements show that an directional dependence in this alignment can be achieved through deformation processing though it is recognised that due to experimental limitations, the third objective remains open to significant further work to develop understanding and increase the measurement count to more than three samples.

Throughout this chapter, the thermomechanical properties of MAG-E in both the ϵ-phase and τ-phase have been discussed in the compressive regime. Initial tests of both phases were conducted in the Uniaxial compression mode, where a central force is applied to a cylinder allowed to deform radially in the cross section as the height is compressed. Whilst additional correction factors may be applied for 'barrelling' where the cross sectional radii are not constant throughout the material and for the the deformation around the thermocouple hole, initial tests show that the τ-phase is unsuitable for deformation at stable temperatures under this regime, showing fracture events at strains in the region of $\epsilon = (6 \pm 1)\%$, thus demonstrating a brittle behaviour. The purpose of deformation processing was not for near net shape design but to instill a metallographic texture in the material to try to improve extrinsic magnetic properties. As such, it was deemed that the deformation of the τ-state was not an effective methodology to instill texture in bulk MAG-E without returning to the sintering problems discussed in the Literature Review Chapter.

Looking to the parental ϵ-phase, three distinct phase regions were investigated for potentially ductile behaviour as shown in Figure 7.4:

(a) The metastable low temperature region $(100 \leq T \leq 500)^{\circ}C$,

(b) A multi-phase region where $\epsilon + \gamma$ phases are stable $T = (800,\ 850)^{\circ}C$,

(c) A single phase region where the ϵ-phase is thermodynamically stable but the material is still solid $(900 \leq T \leq 1100)^{\circ}C$.

The low temperature region showed similar, brittle behaviour to that of the τ-phase, albeit with a higher fracture stress. As such, it was eliminated from candidate temperatures for deformation processing due to a lack of a significant ductile region for texture development. The second regime showed ductile behaviour when measured to strains in the region of $\epsilon > 35\%$ which, upon correction for radial changes as a result of deformation, shows a strain-softening behaviour upon deformation, attributed to grain sizes insufficient to contain dislocations. This behaviour is also observed for the third regime, with the critical applied stress to transition to the strain-softening regime decreasing with temperature. Pole figure analysis showed anisotropy in measured material suggesting the formation of metallographic texture but as the uniaxial testing produces a non-uniform stress field across a test sample during compression, this texture cannot be attributed to a specific strain and strain rate, meaning that it is a qualitative assessment. However, it thus demonstrated that deformation processing of the parental ϵ-phase was possible and that a texture may be possible to generate as a result of plastic compression deformation.

Following this, a rolling-simulation technique, Plane Strain Compression, was utilised to investigate the effects of uniform deformation in a single plane on the material to best characterise the strain-texture relationship. Three deformation strains were measured $\epsilon = 30$, 35, 40% at strain rates of $d\epsilon/dt = 10\%s^{-1}$ and compared to an undeformed sample. Recognising that the magnetic properties of MAG-E are present in the τ-phase and not the ϵ-phase, the optimised transformation heat treatment expressed in Section 6.3 was utilised to test the resultant texture and extrinsic magnetic variable anisotropy post heat treatment. All three deformation profiles resulted in ductile deformation, with no observable fracturing in the deformation plane. Pole Figures were generated for both the deformed ϵ-phase and the transformed state, showing three distinctly separate systems.

The sample deformed to $\epsilon = 30\%$ showed an incomplete $\epsilon \rightarrow \tau$ transformation following a heat treatment at $430°C$ for 3 hours, in stark difference to that of the undeformed samples discussed in Section 6.3, with Rietfeld Refinement estimating a broadly equal phase balance between the precursor and metastable state. Given the identical heat treatment between the undeformed and deformed material, both being excised from the same casting, one must assume that it is not a composition effect, nor can it be an artifact of the initial phase population post-deformation, with the deformed sample being calculated to be a single phase system. As such, it must be concluded that the residual stress within the system as a result of deformation processing has an effect on the $\epsilon \rightarrow \tau$ transformation rate.

This lack of complete metastable transformation resulted in intrinsic magnetic property variation but examining extrinsic magnetic variables normalised against the varying intrinsic variables, there is anisotropy in M_R/M_S observable with an applied magnetic field magnetising the sample normal to the direction of rolling, $\hat{RD}$. Due to the constraints of measurements, field to deformation directions were most easily defined as perpendicular, thus the magnetised direction is considered a in the planar group normal to rolling, namely some combination of the Transverse Direction, $\hat{TD}$, and Normal Direction, $\hat{ND}$. This phenomena is explored in Figure 7.18 and Table 7.5 but shows that there is a strong probability that the transformed grains will be oriented such that the $< 032 >$ plane is in the plane $RDTD$, i.e the direction [032] is parallel to ND. Thus, there is a strong probability that a grain is orientated with an out of deformation plane easy-axis orientation, understanding that in a uniaxial system the easy-axis of magnetisation is the [001] direction, thus explaining the anisotropy as grains are free to rotate about this axis, meaning a greater degree of disorder in the RD or TD vector components of the easy-axis, but a consistent ND components as a result.

Examining $\epsilon = 35\%$ and $\epsilon = 40\%$, the experiment was affected by less than ideal cooling rates, resulting in the precipitation of the equilibrium phase βMn to significant quantities, especially in the former, again seeing deviations from idealised intrinsic magnetic properties. Both samples showed M_R anisotropy and the same preferential [032] orientation in ND as the sample deformed to $\epsilon = 30\%$ but to a more significant intensity.

Of particular interest, however, was the effect of deformation processing on H_C. For varying grain sizes, the microstructure of material deformed to $\epsilon = 35\%$ resulted in a similar coercivity as the undeformed material despite having a larger average grain diameter and the material deformed to $\epsilon = 40\%$ showed a significantly reduced coercivity when compared to the undeformed material, despite similar grain sizes. Using GSDCP theory, it can be estimated that, due to the average grain size being bigger than that of domain wall thickness, H_C should be inversely proportional to average grain diameter for the same microstructure. Thus, it can be inferred that PSC processing changes the microstructure in the transformed deformed state such that there is either a decrease in relative α coefficient or increase in N_{eff} as defined by Equation 6.2, i.e either the grain morphology changes such that the demagnetising effect of the grain geometry becomes more significant or the intergranular coupling sees a diminished state, resulting in a decrease in H_C.

Thus, in conclusion for this chapter, it can be said that hot deformation processing of MAG-E in a bulk format is only possible in conditions where the ϵ-phase is thermodynamically stable without fracturing the material and returning to problems discussed in Chapter 3.2 where sintering of the resulting material is required to manufacture bulk magnets, leading to issues surrounding metastable decay and the precipitation of undesirable equilibrium phases. It has been shown that material cast by VIM exhibits average grain sizes small enough to exhibit strain-softening behaviour following plastic deformation and that metallographic textures may form under deformation. Under plane strain conditions, this texture and residual strain has been shown to change metastable phase transformation rates and induce M_R anisotropy. It has also been shown to negatively impact microstructure regarding H_C optimisation.

The consequence of this trade-off between M_R and H_C implies that additional techniques are required to increase H_C on a textured material to fulfil the Gap

Magnet Criteria as defined in Table 1.1. Fundamentally, MAG-E has been shown to have the potential to fulfil Type B, with the intrinsic properties measured at $23°C$ for a sample heat treated for 3 hours at $430°C$ showing k values well above Type B and M_S within 95% of the target specification. However, permanent magnetic materials are utilised in applications where they are working against applied fields, i.e. in the 2nd quadrant of a $B(H)$ curve for a magnet, meaning that the extrinsic magnetic properties define applicability for electric motor applications. Whilst these properties have their maxima determined by intrinsic magnetic properties, it is the optimisation of said properties that is the subject of significant engineering research.

Given that H_C was calculated to be similar between the undeformed sample and that of the $\epsilon = 35\%$ material, a comparison of BH_{Max} or maximum energy product, an expression of maximum possible magnetic energy density that can be contained within a material, is useful to assess the benefit of inducing M_R anisotropy. The two energy densities can be calculated as $BH_{Max}(\epsilon = 0\%) = (4190 \pm 10) Jm^{-3}$ and $BH_{Max}(\epsilon = 35\%) = (1854 \pm 2) Jm^{-3}$ which implies that not only are both systems 2 orders of magnitude lower than the specification requirement, initial examination would imply that hot deformation results in a decreased BH_{Max} for the system. It is of note, however, that the intrinsic magnetic properties define the extrinsic and that the ratio $M_S(\epsilon = 35\%)/M_S(\epsilon = 0\%) = (54.52 \pm 0.04)\%$. If one assumes that this deviation in M_S is purely a product of equilibrium phase formation from insufficient cooling rates post deformation, that undeformed value can be achieved with optimised cooling rates and transformation heat treatments and that M_R scales directly with the increase in M_S, one could theorise that the maximum energy product would increase to $BH_{Max,opt}(\epsilon = 35\%, M_{R,opt}) = (3400 \pm 5) Jm^{-3}$ which is still lesser than that of undeformed material.

However, one must also factor in that k varies between the two samples and referencing Equation 6.2, one can consider H_C a function of both k and M_S. Under the assumption that the Kronmüller coefficients α and N_{eff} do not change as a function of optimisation, one can compute both a set of realistic coefficients that the material state could occupy, modelling $(0 \leq N_{eff} \leq 1)$ by making no assumption of granular geometry with respect to easy axis orientation, it can be calculated that inputting undeformed intrinsic magnetic properties may actually predict negative values of H_C. Whilst one might expect these coefficients to change in a single phase material, $H_A(\epsilon = 35\%)/H_A(\epsilon = 0\%) = (114 \pm 1)\%$, implying that transitioning to optimised variables without a change in Kronmüller coefficient would see a decrease in H_C as a result.

Understanding that it is possible to increase M_R/M_S as a result of hot deformation resulting in preferential texture, it is important to understand that this also results in the decrease of H_C and thus BH_{Max}, even in systems of optimised intrinsic magnetic properties. Thus, whilst further investigations into hot deformation under these conditions to maximise M_R/M_S with optimal intrinsic magnetic variables is a critical step to the bulk processing of MAG-E for application in permanent magnetic material applications, there must also then be further work invested in post-processing of textured material such that H_C may increase, such as the investigation of inter-granular precipitate diffusion, which has shown success in NdFeB systems to raise H_C [104].

Chapter 8

Conclusions

Throughout this body of work, efforts have been made to address a key problem in the magnetic materials sector: there exists a capability gap in permanent magnetic material capabilities between hard ferrites and NdFeB. Filing this gap could offer new materials for particular roles within electricity generation and use, and reduce the demands on the expensive rare earth containing compositions. It is understood by industry and academia that a new material to fulfil this gap should not contain heavy rare earth elements to prevent growing concerns about industrial access to these resources, having learned from prior dependency on Dy for high temperature NdFeB magnets at the beginning of the 21st century.

Initial scoping discussions presented in Section 1 down select from existing rare-earth free permanent magnetic systems (understanding that the experimental discovery of novel and unique systems is less effective than from a theoretical methodology and that viable candidate materials already exist), to settle on the τ-MnAl system. This system is a metastable phase formed from an off-stochiometric alloy of Mn and Al via the high-temperature stable ϵ-phase, either by rapid quenching and annealing or by a controlled cooling methodology. Whilst this material fulfills intrinsic candidate criteria, specified by Coey as Gap Magnet Criteria and expressed in Table 1.1, its metastable nature implies that the optimisation of the final property required, the maximum energy product or BH_{Max}, is a nuanced and complicated operation to undertake, with several research streams having already attempted to find a solution to this problem

8.1 State of Field Prior to Investigation

Broadly, the state of τ-MnAl research prior to the commencement of this body of work was such that there were three parallel streams of research: Sintering/Milling research to attempt to produce τ-MnAl through traditional aligned powder manufacturing techniques used with thermodynamically stable magnetic materials, alloying studies investigating whether additional elements could improve intrinsic magnetic properties or metastability and deformation processing trials to attempt to create a textured product such that the sintering production route was unnecessary. Whilst success had been shown in the MnAlGa ternary system to increase metastability and potentially provide a route to sinter, no lower limit on required Ga content had been stated, driving an economic argument to investigate this. Further, thermomechanical data for ϵ-phase or τ-phase MnAl was not available, nor was the final state of deformed material discussed such that there was confidence in near net-shape manufacture, thus showing a gap in research for these topics to be discussed.

8.2 Investigations Conducted within This Thesis

The scientific investigations covered in this thesis were threefold: to investigate whether the MnAlBi ternary system exhibits similar magnetic property improvement or stabilisation as the MnAl(C/Ga) system, to investigate the MnAlGa ternary system in the range $Ga \leq 6\ at.\%$ and to begin preliminary trials of bulk hot deformation of an optimised MnAlGa system, characterising the thermomechanical properties of said alloy.

8.2.1 MnAlBi Ternary System Investigations

Two alloys of MnAlBi were cast of compositions $Mn_{60.3}Al_{36.7}Bi_3$ and $Mn_{59.7}Al_{36.4}Bi_{3.9}$ and compared to control compositions of MnAlC and MnAlGa with regards to intrinsic and extrinsic magnetic properties. Significant decreases in intrinsic magnetic properties were observed for equivalent heat treatment times between MnAlBi and MnAlC alloys, with $k(Bi_1)/k(MnAlC) = (49 \pm 1)\%$ and $k(Bi_2)/k(MnAlC) = (19.3 \pm 0.7)\%$, with M_S ratios being comparable. Thus, it can be concluded from an M_R perspective, the inclusion of Bi as an alloying element is significantly detrimental to material performance with the loss of property caused by the unalloyed Bi and precipitation of the intermetallic LTP-MnBi phase.

Whilst M_R scales with Bi additions in a similar fashion to M_S, it is of note that Bi additions lead to an increase in H_C that is broadly invariant between the two MnAlBi alloys. It may be that the new phases act as pinning sites to prevent switching events occurring, magnetically hardening the material. In the direct comparison examples, where MnAlBi compositions underwent identical heat treatments to that of MnAlC and MnAlGa compositions, $H_C(MnAlBi)$ was observed to be approximately $(70 \pm 10)\%$ greater than that of MnAlC, with no significant composition variation in this observation between the two MnAlBi alloys, only sample variation, attributed to phase population variation in the samples. Even when extending this further to heat treatment variations to optimise the system, an increase H_C over that observed for MnAlC and MnAlGa alloys was observed upon the precipitation of a ferromagnetic phase above $350°C$. Further investigations as to the composition limit of this increase in H_C, the maximum H_C increase as a result of Bi alloying and an optimum point between $M_{S/R}$ sacrifice and H_C increase determined to best utilise this effect.

Overall, the three research objectives set out at the start of the chapter were achieved, with manufacture of $\tau - MnAl$ demonstrated, Bi alloying shown to be detrimental to magnetic material performance at measured alloying concentrations, thus discounting it from ternary alloying studies at concentrations above Bi $2at\%$ and MnAlGa $\epsilon \rightarrow \tau$ transformations being feasible at cooler and shorter heat treatments than in previously published literature. The follow on work for the third objective, namely the optimisation of both Ga content and transformation heat treatment parameters, became objectives for the Ga-lean MnAlGa investigations.

8.2.2 Ga-lean MnAlGa Investigations

With regards to Ga-lean compositions when compared to the work of Mix *et. al.*, initial findings showed that the heat treatments prescribed within the literature were longer and hotter than required to see near-100% τ-MnAl compositions and maximised intrinsic magnetic properties [61]. For a 2 hour anneal at $430°C$, a composition of $Mn_{57.1}Al_{39.5}Ga_{3.4}$ was down-selected as an optimum composition regarding intrinsic magnetic variables M_S, k and H_A as well as examining the change in magnetisation during transformation and observing $\frac{dM}{dt}(t = 2h,\ T = 430°C) > 0$, implying that further transformation is occurring, leading to a net increase in susceptibility, interpreted to be an increase in M_S below T_C. It also surpassed all intrinsic and cost criteria for a Type A Gap Magnet as defined by Table 1.1.

Further studies were undertaken to investigate optimum transformation heat treatment parameters, t and T to maximise M_S, k and H_A for $Mn_{57.1}Al_{39.5}Ga_{3.4}$, denoted here as MAG-E (Manganese Aluminium Gallium - Electrical), as well as ensure the $\epsilon \rightarrow \tau$ transformation reaches a maxima for the system. Initial temperature studies of the transformation showed that a critical transformation temperature existed in the region $(400 < T_{trans} < 450)°C$ for 2 hour heat treatments, where annealing under $400°C$ saw no appreciable hysteresis develop, implying that the first peak in the $M(T)$ plot shown for ϵ-MnAlGa in Figure **??** may not be the onset of $\epsilon \rightarrow \tau$ transformation. Looking to observed maxima and rate of change amongst the 4 measured temperatures resulting in hysteresis, $430°C$ was down-selected, showing the lowest $\frac{dM}{dt}$ value of the set whilst still maintaining the criteria $\frac{dM}{dt} > 0$.

Work optimising transformation times at $430°C$ showed that lattice parameter variation was observed as a function of annealing time, implying that a strained crystallographic lattice is induced as a result of the metastable transformation, presenting the opportunity to tune intrinsic magnetic properties for a fixed phase population as a function of heat treatment conditions. As a result of this, whilst near 100% τ-phase population was observed from 1 hour of annealing, intrinsic magnetic property instability was observed as a function of measurement temperature for this first sample, implying that the reduction in residual stress as a result of metastable transformation is still taking place at room temperature following 1 hour of annealing; thus the material cannot be considered stable. Examining the evolution of grain size, lattice parameters, Kronmüller micromagnetic coefficients and Spin Wave Stiffness constants as a function of annealing time, optimum heat treatment parameters were defined for MAG-E as 3 hours at $430°C$, though it is recognised that further study to expand the experimental matrix to include additional annealing time studies at differing temperatures may also be beneficial to best utilise the residual strain effect on lattice parameters.

A final aside of testing was investigating the thermal stability of Ga-lean MnAlGa alloys, given claims made by Mix *et. al.* about the improved thermal stability to the τ-MnAl phase induced by Ga addition. MAG-E when annealed for 24 hours at $430°C$ saw intrinsic and extrinsic magnetic property degradation as a result of βMn precipitation. Samples from Ga_1, Ga_3 and Ga_4 (alloy compositions defined in Table 6.1) underwent a 24 hour heat treatment at $420°C$ following the initial 2 hour transformation heat treatment at $430°C$. The results from this study can be seen in Table 6.7 but show that M_S is stable to within approximately ±3.5% of initial transformation values but that k, M_R and H_C change as a result. Considering extrinsic magnetic variable change implies microstructural changes as a result of heat treatment but the lack of change in M_S implies phase stability is comparable to that shown for MnAlC compositions at heat treatment temperatures of $500°C$ and $550°C$ as shown by Zhao *et. al* [50].

Comparing the 4 studies and making the assumption that a $10°C$ difference between the two heat treatments is both approximate assuming temperature fluctuations within box furnaces of $\pm 2°C$ and thus assuming that the results are broadly comparable, long term heat treatments on low Ga-compositions do not show significant M_S decreases indicative of βMn precipitation but do show decreases in k, resulting in magnetic softening, implying that the microstrained-post transformation state may beneficial for magnetic hardening and alternative techniques of introducing residual stress may harden the system. However, no consistent trend was observed in terms of coercivity improvement across the 4 systems, implying that $H_C(t_{anneal})$ has composition dependency.

Considering the three research objectives established for this chapter, namely the measurement of the $Mn_{5060}Al_{balance}Ga_{010}$ composition range for a set heat treatment to determine an optimum composition for intrinsic magnetic properties, the determination of intrinsic and extrinsic magnetic properties as a function of heat treatment parameters and the optimisation of said parameters for a targeted composition, the first objective can be considered achieved with an optimised composition of $Mn_{57}Al_{39.5}Ga_{3.5}$ targeted for further study, fulfilling the economic motivation of developing a lower cost MnAlGa alloy than previously published in literature to fulfil industrial applications. The second objective cannot be considered fully achieved as it was discovered during measurements that both intrinsic and extrinsic magnetic properties were subject to change as a result of heat treatment variation, thus further work should be directed into exploring heat treatments to isolate these two variable spaces. Finally the third objective can again be only considered partially completed, with a targeted heat treatment time and temperature set at 3 hours at $430°C$ to optimise the $\epsilon \rightarrow \tau$ transformation but with further, more sensitive measurements required to fully understand the transformation mechanics present. As such, the overall conclusion of this chapter is that Ga-lean MnAlGa can be an industrially-viable, low-cost permanent magnetic material and optimisation has taken place towards observed maxima but that further testing should be explored in order to explore if any further optimisations can be achieved.

8.2.3 Thermomechanical Characterisation and Hot Deformation Processing of MAG-E

Broadly the results from this section can be broken down into two sections, determining plastic deformation ranges for MAG-E compression deformations in ϵ- and τ-phases as well as assessing magnetic property changes as a result of deformation processes. It was assessed that compression deformation of the τ-phase of MAG-E was unfeasible in the as-cast state due to a fracture strain in the range of $\epsilon_{frac} \approx (6-8\%)$ within known stable temperature ranges. It was assumed that within this deformation range, texture was unlikely to develop and that additional heating would lead to equilibrium phase formation during processing.

The ϵ-phase material showed significantly better mechanical properties in three distinct regimes:

(a) The metastable low temperature region $(100 \leq T \leq 500)°C$, where mechanical properties were arguably similar to that of the τ-phase, in part due to partial $\epsilon \rightarrow \tau$ transformation as a function of deformation process time at higher temperatures leading to the variation in stress-strain curves, but showed an increased ϵ_{frac} at higher temperatures. This regime, however, was similarly assessed as unsuitable for deformation processing.

(b) A multi-phase region where $\epsilon + \gamma$ phases are stable $T = (800, 850)°C$, exhibiting a plastic deformation region following an initial activation stress of $\sigma_{yield} \approx 200MPa$. Whilst showing appropriate mechanical properties, this temperature region was similarly judged as inappropriate due to a multi-phase state leading to either a need to reheat the material to ensure homogeneous single phase material or accept a reduced τ-phase yield upon transformation.

(c) A single phase region where the ϵ-phase is thermodynamically stable but the material is still solid $(900 \leq T \leq 1100)°C$. This regime showed a temperature dependence such that $d\sigma_{yield}/dT_{deform} < 0$, $(950 \leq T \leq 1100)°C$, implying a decreased energy barrier for plastic deformation with increasing temperature.

Due to the constraints of Uniaxial testing, the resulting texture from compression can only be considered qualitatively due to complex deformation throughout the sample. Both plastic deformation regimes showed strain-softening behaviour, attributed to a grain size insufficient to contain a stable dislocation and the dislocation transport-induced stress field lowering the energy barrier for further dislocation production. The strain-rate sensitivity of this property remains unexplored and thus a potential area of investigation as to texture and mechanical property effects.

Plane-Strain Compression (PSC) deformation on MAG-E samples to strains of $\epsilon_{deform} = (30, 35, 40)\%$ showed that, following a heat treatment optimised for undeformed MAG-E, M_R anisotropy can be induced in a deformed material such that there is an increase in M_R/M_S with respect to the direction normal to the plane of deformation, the Normal Direction (ND), when compared to an undeformed sample, assumed to be isotropic in this property. XRD analysis shows that following deformation processing and heat treatment transformation, a strong [032] alignment with ND was observed, which was attributed to the anisotropy. However, both final phase populations, intrinsic magnetic properties and H_C varied across the samples. Whilst this could be somewhat attributed to non-ideal cooling of the deformed ϵ-phase material, the change in H_C is attributed to a change in grain morphology and thus moving from assumed near-spherical grain morphology to grains tending to prolate ellipsoids, thus transitioning the system from single domain grains to multi grain domains as a function of deformation, reducing H_C as a function of grain size due to deformation.

Assessing the research objectives expressed at the start of the associated results chapter, the first objective was achieved - a ductile region was measured for thermodynamically stable ϵ-MAG-E but no such region was measured for τ-MnAl, meaning any hot deformation processing would need to be conducted on the precursor phase to improve the magnetic performance of the transformed magnetic material. The second objective can also be considered achieved, with preferential alignment detected in the transformed state as a result of deformation of precursor state, providing a potential methodology to improve magnetic material performance of the τ-phase despite its brittle nature. Expanding this to PSC testing, it can be seen that in the case of uniform deformation of the precursor phase, anisotropy can be developed in terms of magnetic properties and texture, but that significant further work is required to develop an understanding of the limitations of this and develop deformation processing as an industrially viable manufacturing technique to develop MAG-E as a product for low requirement permanent magnetic material applications.

8.3 Overall Thesis Conclusions and Further Work

Overall, it can be concluded that MAG-E has potential as a Type A Gap Magnet Candidate, demonstrating that the composition is metastable such that it may be transformed in the undeformed state on reasonable timescales that equilibrium phases do not form, fulfils all intrinsic magnetic and price properties but still has significant engineering work to increase BH_{Max} such that it is a viable product. Whilst heat treatment studies demonstrate that intrinsic and extrinsic properties may be affected by heat treatment due to microstructural and microstrain changes, alone it is insufficient to increase this metric. Hot Deformation processing demonstrated that it is possible to increase M_R/M_S for a given direction, but at the expense of lowered H_C and intrinsic properties, implying that a deformed state will require alternative heat treatment optimisation and that additional research is required to increase H_C.

Whilst the work shown in Section 7.2 shows that ϵ-MAG-E can undergo plastic deformation at temperatures where the ϵ-phase is stable, resulting in texture before and after metastable transformation, it is only a preliminary study, with a wide variable space to optimise within. One key area that remained unexplored was that of strain-rate dependency. The strain rate of $d\epsilon/dt = 0.1s^{-1}$ was selected as it was the lowest achievable strain rate the Servotest TMC was rated to conduct and still maintain accurate measurements. To expand on the results of this chapter, both lower and higher strain rates should be investigated in order to determine if there is any dependency on both extrinsic magnetic properties and volume occupancies on strain rates.

As a concept, however, texturing through mechanical deformation at thermodynamically stable precursor temperatures may prove useful to investigate for alternative metastable functional materials such as $\alpha'' - FeN$. As discussed in the introduction, the decomposition temperature for this material is such that it was discounted from this study but should it prove ductile at RT or a potential precursor ductile, it may provide a pathway to increase M_R/M_S without the need to align and sinter.

Further work on MAG-E would be to establish a technique to reliably increase H_C without significant decreases in M_R. Whilst this is no trivial task, one potential avenue for investigation is that of grain boundary diffusion of Bi into a textured sample of MAG-E post-transformation. Given the melting point of Bi is lower than temperatures where MAG-E has been demonstrated to be broadly stable, liquid Bi could be introduced to deformed sheets MAG-E as has been shown with Grain

Boundary effects in NdFeB magnets as discussed by Liu *et. al.* to increase non-magnetic grain boundary phase population, isolating grains from one another and smoothing grain boundaries by the formation of continuous grain boundary phases, thereby reducing the effective demagnetising field of each grain as defined by Equation 6.2 coefficient N_{eff}[105]. The process for achieving appropriate diffusion and concentration into the alloy would be a significant body of work but combined with M_R anisotropy improvements derived from hot deformation, may represent a potential research stream to develop the τ-MnAl system into an industrially viable material meeting the Gap Magnet Type A specifications laid out by Coey in Table 1.1. Work in MnAlCBi has already been published at the time of writing, demonstrating that there is interest in the inclusion of this element though combining it with a textured, bulk sample may provide a two-step process towards the manufacture of an industrially-viable, Type A Gap Magnet [106].

It is intended to publish this work as a series of academic papers, with a particular drive to publish the Ga-lean data and thermomechnical properties observed for both the ϵ-phase and τ-phase in order to facilitate further experimentation in this system. Arguably, the most important results for dissemination is that the ϵ-phase MAG-E is mechanical deformable and its resulting texture in the τ-phase shows magnetic anisotropy, though there is much work left in this area to truly understand and optimise this production method in order to produce a low cost, rare-earth free permanent magnetic material for low requirement applications such as small motors or sensors where NdFeB is used due to the capability gap.

References

[1] I. Meyer, M. Leimbach, and C.C. Jaeger. International passenger transport and climate change: A sector analysis in car demand and associated co2 emissions from 2000 to 2050. *Energy Policy*, 35(12):6332–6345, 2007.

[2] Lee Chapman. “Transport and Climate Change: A Review”. *Journal of Transport Geography*, 15(5):354–367, 2007.

[3] Oliver Gutfleisch, Matthew A. Willard, Ekkes Brück, Christina H. Chen, S. G. Sankar, and J. Ping Liu. “Magnetic Materials and Devices for the 21st Century: Stronger, Lighter, and More Energy Efficient”. *Advanced Materials*, 23(7):821–842, 2011.

[4] A. S. Kim and F. E. Camp. “High performance NdFeB magnets”. *Journal for Applied Physics*, 79:5035, 1996.

[5] Oliver Gutfleisch, Matthew A. Willard, Ekkes Brück, Christina H. Chen, S. G. Sankar, and J. Ping Liu. Magnetic materials and devices for the 21st century: Stronger, lighter, and more energy efficient. *Advanced Materials*, 23(7):821–842, 2011.

[6] Y.Matsuura, M. Sagawa, and *et. al.*. “Process for Producing Permanent Magnet Materials”. *US Patent 4,597,938*, 1986.

[7] Ekkes Brück. *“Handbook of Magnetic Materials Vol 27”*, page 2. Elsevier, 2018.

[8] M. Calin and E. Helerea. “Temperature influence on magnetic characteristics of NdFeB permanent magnets”. In *“2011 7th International Symposium on Advanced Topics in Electrical Engineering (AIEE)”*, pages 1–6, 2011.

[9] Paul Tenaud, Henri Lemaire, and Freddie Vial. “Recent improvements in NdFeB sintered magnets”. *Journal of Magnetism and Magnetic Materials*, 101(1):328 – 332, 1991.

[10] L.Q. Yu, Y.H. Wen, and M. Yan. “Effects of Dy and Nb on the magnetic properties and corrosion resistance of sintered NdFeB”. *Journal of Magnetism and Magnetic Materials*, 283(2):353 – 356, 2004.

[11] K Binnemans, P T Jones, and T Müller *et al.*. “Rare Earths and the Balance Problem: How to Deal with Changing Markets?” *J. Sustain. Metall.*, 4:126 – 146, 2018.

[12] James D. Widmer, Richard Martin, and Mohammed Kimiabeigi. “Electric vehicle traction motors without rare earth magnets”. *Sustainable Materials and Technologies*, 3:7 – 13, 2015.

[13] Nawshad Haque, Anthony Hughes, Seng Lim, and Chris Vernon. “Rare Earth Elements: Overview of Mining, Mineralogy, Uses, Sustainability and Environmental Impact”. *Resources*, 3(4):614–635, 2014.

[14] B.M Ma, J.W Herchenroeder, B Smith, M Suda, D.N Brown, and Z Chen. “Recent development in bonded NdFeB magnets”. *Journal of Magnetism and Magnetic Materials*, 239(1):418–423, 2002. International Symposium on Physics of Magnetic Materials/Internat ional Symposium on Advanced Magnetic Technologies.

[15] J.M.D. Coey. “Permanent magnets: Plugging the gap”. *Scripta Materialia*, 67(6):524–529, 2012. Viewpoint Set No. 51: Magnetic Materials for Energy.

[16] R. Skomski and J.M.D. Coey. Magnetic anisotropy — how much is enough for a permanent magnet? *Scripta Materialia*, 112:3–8, 2016.

[17] J.M.D. Coey. “Perspective and Prospects for Rare Earth Permanent Magnets”. *Engineering*, 6(2):119–131, 2020.

[18] J Cui, J P Choi, G Li, E Polikarpov, J Darsell, N Overman, M Olszta, D Schreiber, M Bowden, T Droubay, M J Kramer, N A Zarkevich, L L Wang, D D Johnson, M Marinescu, I Takeuchi, Q Z Huang, H Wu, H Reeve, N V Vuong, and J P Liu. “Thermal stability of MnBi magnetic materials”. *Journal of Physics: Condensed Matter*, 26(6):064212, jan 2014.

[19] Y.B. Yang, X.G. Chen, S. Guo, A.R. Yan, Q.Z. Huang, M.M. Wu, D.F. Chen, Y.C. Yang, and J.B. Yang. “Temperature dependences of structure and coercivity for melt-spun MnBi compound”. *Journal of Magnetism and Magnetic Materials*, 330:106–110, 2013.

[20] United States Geological Survey. “Bismuth Data Sheet - Mineral Commodity Summaries 2020”. *Mineral Commodity Summaries*, 2020.

[21] Jian-Ping Wang. “Environment-friendly bulk Fe16N2 permanent magnet: Review and prospective”. *Journal of Magnetism and Magnetic Materials*, 497:165962, 2020.

[22] Sara Hamidizadeh, Natheer Alatawneh, Richard R. Chromik, and David A. Lowther. Comparison of different demagnetization models of permanent magnet in machines for electric vehicle application. *IEEE Transactions on Magnetics*, 52(5):1–4, 2016.

[23] Peter Stoeckl, Przemyslaw Wojciech Swatek, and Jian-Ping Wang. Theoretical study of thermal stability of –Fe16N2 against other iron nitrides. *AIP Advances*, 14(1):015047, 01 2024.

[24] P. Campbell. *“Permanent Magnet Materials and their Application”*, pages 55–57. Cambridge University Press, 1996.

[25] M.F. de Campos. “Chemical Composition and Coercivity of $SmCo_5$ magnets”. *Journal of Applied Physics*, 84:368, 1998.

[26] S Pandian, V Chandrasekaran, G Markandeyulu, K.J.L Iyer, and K.V.S Rama Rao. “Effect of Co, Dy and Ga on the magnetic properties and the microstructure of powder metallurgically processed Nd–Fe–B magnets”. *Journal of Alloys and Compounds*, 364(1):295 – 303, 2004.

[27] Joël P. T. Kapusta. “Cobalt Production and Markets: A Brief Overview”. *JOM*, 58(10):33–36, 10 2006. Copyright - Copyright Minerals, Metals & Materials Society Oct 2006; Document feature - Graphs; Tables; ; Last updated - 2014-08-16; CODEN - JOMMER.

[28] Nicolas Tsurukawa, Siddharth Prakash, and Andreas Manhart. “Social impacts of artisanal cobalt mining in Katanga, Democratic Republic of Congo”. *Öko-Institut eV, Freiburg*, 2011.

[29] Célestin Lubaba, Nkulu Banza, Tim S. Nawrot, and *et. al.* “High human exposure to cobalt and other metals in Katanga, a mining area of the Democratic Republic of Congo”. *Environmental Research*, 109(6):745 – 752, 2009.

[30] Karlien Cheyns, Célestin Banza Lubaba Nkulu, and *et. al.*. “Pathways of human exposure to cobalt in Katanga, a mining area of the D.R. Congo”. *Science of The Total Environment*, 490:313 – 321, 2014.

[31] Célestin Banza Lubaba Nkulu, Lidia Casas, Vincent Haufroid, Thierry De Putter, Nelly D. Saenen, Tony Kayembe-Kitenge, Paul Musa Obadia, Daniel Kyanika Wa Mukoma, Jean-Marie Lunda Ilunga, Tim S. Nawrot, Oscar Luboya Numbi, Erik Smolders, and Benoit Nemery. “Sustainability of artisanal mining of cobalt in D.R Congo”. *Nature Sustainability*, 1(9):495–504, Sep 2018.

[32] Ahmed A. El-Gendy and George C. Hadjipanayis. Nanostructured d022-mn2ga alloys with high magnetization and coercivity. *The Journal of Physical Chemistry C*, 119(16):8898–8903, 2015.

[33] Jinbo Yang, Wenyun Yang, Zhuyin Shao, Dong Liang, Hui Zhao, Yuanhua Xia, and Yunbo Yang. Mn-based permanent magnets. *Chin. Physics B*, 27(11):117503, November 2018.

[34] David C Jiles. *Introduction to magnetism and magnetic materials, third edition.* Apple Academic Press, Oakville, MO, 3 edition, October 2015.

[35] Nicola A Spaldin. *Magnetic materials.* Cambridge University Press, Cambridge, England, March 2003.

[36] J.M.D Coey. *“Magnetism and Magnetic Materials”.* Cambridge University Press, Cambridge, 2010.

[37] H. Kronmüller and M.F. Fähnle. *Micromagnetism and the Microstructure of Ferromagnetic Solids.* Cambridge studies in magnetism. Cambridge University Press, 2003.

[38] John Crangle. *The magnetic properties of solids.* Hodder Arnold, London, England, August 1977.

[39] Alex Hubert and Roy Schäfer. *Magnetic domains.* Springer, Berlin, Germany, 1 edition, August 1998.

[40] Amikam Aharoni. Demagnetizing factors for rectangular ferromagnetic prisms. *Journal of Applied Physics*, 83(6):3432–3434, 03 1998.

[41] R. Cabassi. Singular point detection for characterization of polycrystalline permanent magnets. *Measurement*, 160:107830, 2020.

[42] Akimasa Sakuma. Electronic structure and magnetocrystalline anisotropy energy of mnal. *Journal of the Physical Society of Japan*, 63(4):1422–1428, 1994.

[43] Desheng Xue, Guozhi Chai, Xiling Li, and Xiaolong Fan. Effects of grain size distribution on coercivity and permeability of ferromagnets. *Journal of Magnetism and Magnetic Materials*, 320(8):1541–1543, 2008.

[44] Hiroshi Kōno. "On the Ferromagnetic Phase in Manganese-Aluminum System". *Journal of the Physical Society of Japan*, 13(12):1444–1451, 1958.

[45] J.J. Van Den Broek, H. Donkersloot, G. Van Tendeloo, and J. Van Landuyt. "Phase transformations in pure and carbon-doped $Al_{45}Mn_{55}$ alloys". *Acta Metallurgica*, 27(9):1497–1504, 1979.

[46] Van Tang Nguyen, Florent Calvayrac, Anna Bajorek, and Nirina Randrianantoandro. "Mechanical alloying and theoretical studies of MnAl(C) magnets". *Journal of Magnetism and Magnetic Materials*, 462:96 – 104, 2018.

[47] L Pareti, F Bolzoni F, Leccabue, and A.E Ermakov. "Magnetic anisotropy of MnAl and MnAlC permanent magnet materials". *Journal of Applied Physics*, 59(11):3824–3828, 1986.

[48] Alina Daniela Crisan, Aurel Leca, Cristina Bartha, Ioan Dan, and Ovidiu Crisan. "Magnetism and $\epsilon - \tau$ Phase Transformation in MnAl-Based Nanocomposite Magnets". *Nanomaterials*, 11(4), 2021.

[49] P.C. Kuo, Y.D. Yao, J.H. Huang, and C.H. Chen. "Fabrication and magnetic properties of manganese-aluminium permanent magnets". *Journal of Magnetism and Magnetic Materials*, 115(2):183–186, 1992.

[50] Shuang Zhao, Yuye Wu, Chi Zhang, Jingmin Wang, Zhongheng Fu, Ruifeng Zhang, and Chengbao Jiang. "Stabilization of τ-phase in carbon-doped MnAl magnetic alloys". *Journal of Alloys and Compounds*, 755:257–264, 2018.

[51] Nicola A. Spaldin. *"Magnetic Materials: Fundamentals and Applications"*. Cambridge University Press, 2 edition, 2010.

[52] Jun Cui, Matthew Kramer, Lin Zhou, Fei Liu, Alexander Gabay, George Hadjipanayis, Balamurugan Balasubramanian, and David Sellmyer. “Current progress and future challenges in rare-earth-free permanent magnets”. *Acta Materialia*, 158:118–137, 2018.

[53] Jung-Goo Lee, Xiao-Lei Wang, Zhi-Dong Zhang, and ChuI-Jin Choi. “Effect of mechanical milling and heat treatment on the structure and magnetic properties of gas atomized Mn–Al alloy powders”. *Thin Solid Films*, 519(23):8312–8316, 2011. First International Conference of the Asian Union of Magnetics Societies (ICAUMS 2010).

[54] C. Muñoz-Rodríguez, L. Feng, E.M. Palmero, T. Mix, J. Rial, F. Olsson, B. Skårman, H. Vidarsson, P.-O. Larsson, T.G. Woodcock, and A. Bollero. “Fabrication of bulk τ MnAl–C magnets by hot-pressing from ϵ-phase gas-atomized and milled powder”. *Journal of Alloys and Compounds*, 847:156361, 2020.

[55] F Jiménez-Villacorta, J.L Marion, T Sepehrifar, M Daniil, M.A Willard, and L.H Lewis. “Exchange anisotropy in the nanostructured MnAl system”. *Applied Physics Letters*, 100(11):112408, 2012.

[56] Hailiang Fang, Johan Cedervall, Daniel Hedlund, Samrand Shafeie, Stefano Deledda, Fredrik Olsson, Linus von Fieandt, J. Bednarcik, Peter Svedlindh, Klas Gunnarsson, and Martin Sahlberg. “Structural, microstructural and magnetic evolution in cryo milled carbon doped MnAl”. *Scientific Reports*, 8:2525, 02 2018.

[57] A Pasko, M LoBue, E Fazakas, L K Varga, and F Mazaleyrat. “Spark plasma sintering of Mn–Al–C hard magnets”. *Journal of Physics: Condensed Matter*, 26(6):064203, jan 2014.

[58] Muriel Tyrman, Smail Ahmim, Alexandre Pasko, Victor Etgens, Frédéric Mazaleyrat, Simon Quetel-Weben, Loïc Perrière, and Ivan Guillot. “Anisotropy of the ferromagnetic L10 phase in the Mn-Al-C alloys induced by high-pressure spark plasma sintering”. *AIP Advances*, 8(5):056217, 2018.

[59] Z.W. Liu, C Chen, Z.G. Zheng, B.H. Tan, and R.V. Ramanujan. “Phase transitions and hard magnetic properties for rapidly solidified MnAl alloys doped with C, B, and rare earth elements”. *Journal of Materials Science*, 47(5):2333–2338, 2012.

[60] Hui-Dong Qian, Ping-Zhan Si, Chul-Jin Choi, Jihoon Park, and Kyung Mox Cho. “Phase transformation and magnetic properties of MnAl powders prepared by elemental-doping and salt-assisted ball milling”. *AIP Advances*, 8(5):056216, 2018.

[61] T. Mix, F. Bittner, K.-H. Müller, L. Schultz, and T.G. Woodcock. “Alloying with a few atomic percent of Ga makes MnAl thermodynamically stable”. *Acta Materialia*, 128:160–165, 2017.

[62] Zhengying Jiao, Yuxiao Jia, Bochen Li, Jingmin Wang, and Chengbao Jiang. Microstructure and magnetic properties of (mn54al46)98c2 magnets fabricated by liquid-phase sintering with the mn65ga35 as an additive. *Journal of Magnetism and Magnetic Materials*, 534:168037, 2021.

[63] Angshuman Sarkar and Amitava Basu Mallick. Synthesizing the hard magnetic low-temperature phase of mnbi alloy: Challenges and prospects. *JOM*, 72, 04 2020.

[64] Nguyen Truong and Vuong Nguyen. Fabrication of mnbi alloys with high ferromagnetic phase content: effects of heat treatment regimes and dopants. *Journal of Materials Science: Materials in Electronics*, 30, 04 2019.

[65] J.X. Shen, Roger D. Kirby, and D.J. Sellmyer. “Magneto-optic properties of evaporated Mn-Bi-Al films”. *Journal of Magnetism and Magnetic Materials*, 81(1):107–111, 1989.

[66] F. Bittner, J. Freudenberger, L. Schultz, and T.G. Woodcock. The impact of dislocations on coercivity in l10-mnal. *Journal of Alloys and Compounds*, 704:528–536, 2017.

[67] P. Nieves, S. Arapan, T. Schrefl, and S. Cuesta-Lopez. Atomistic spin dynamics simulations of the mnal τ-phase and its antiphase boundary. *Phys. Rev. B*, 96:224411, Dec 2017.

[68] Ping-Zhan Si, Hui-Dong Qian, Chul-Jin Choi, Jihoon Park, and Hong-Liang Ge. A novel method for measuring the phase transformation temperature and enhanced coercivity in cold-rolled mnalcx (x=0–5) alloys. *Journal of Magnetism and Magnetic Materials*, 451:540–545, 2018.

[69] X. Wang, H. Li, K. Chandrashekhara, S.A. Rummel, S. Lekakh, D.C. Van Aken, and R.J. O’Malley. Inverse finite element modeling of the barreling effect on experimental stress-strain curve for high temperature steel compression test. *Journal of Materials Processing Technology*, 243:465–473, 2017.

[70] M. A. R. Miranda and J. M. Sasaki. The limit of application of the Scherrer equation. *Acta Crystallographica Section A*, 74(1):54–65, Jan 2018.

[71] Francisco Tiago Leitão Muniz, Marcus Aurélio Ribeiro Miranda, Cássio Morilla dos Santos, and José Marcos Sasaki. The Scherrer equation and the dynamical theory of X-ray diffraction. *Acta Crystallographica Section A*, 72(3):385–390, May 2016.

[72] B.D. Cullity and S.R. Stock. *Elements of X-ray Diffraction, Third Edition.* 2001.

[73] Kai He, Nuofu Chen, Congjie Wang, Lishuai Wei, and Jikun Chen. Method for determining crystal grain size by x-ray diffraction. *Crystal Research and Technology*, 53(2):1700157, 2018.

[74] Brian H. Toby and Robert B. Von Dreele. *GSAS-II*: the genesis of a modern open-source all purpose crystallography software package. *Journal of Applied Crystallography*, 46(2):544–549, Apr 2013.

[75] U.F. Kocks, C.N. Tomé, and H.R. Wenk. *Texture and Anisotropy: Preferred Orientations in Polycrystals and Their Effect on Materials Properties.* Cambridge University Press, 2000.

[76] F. Bachmann, Ralf Hielscher, and Helmut Schaeben. Texture analysis with mtex – free and open source software toolbox. In *Texture and Anisotropy of Polycrystals III*, volume 160 of *Solid State Phenomena*, pages 63–68. Trans Tech Publications Ltd, 3 2010.

[77] Yoosuf N. Picard. Scanning Electron Microscopy. In *Materials Characterization.* ASM International, 12 2019.

[78] Ifan Hughes and Thomas P. A. Hase. *Measurements and their uncertainties : a practical guide to modern error analysis.* Oxford University Press, Oxford : New York, NY, 2010.

[79] Thomas Keller and Ian Baker. Manganese-based permanent magnet materials. *Progress in Materials Science*, 124:100872, 2022.

[80] Tiannan Man, Lin Zhang, Naikang Xu, Wenbin Wang, Zhaolong Xiang, and ENGANG WANG. Effect of rare-earth ce on macrosegregation in al-bi immiscible alloys. *Metals*, 6:177, 07 2016.

[81] John R. Rumble. Crc handbook of chemistry and physics., 2020.

[82] M. Liu, G.B. Han, W. Yang, and R.W. Gao. Dependence of coercivity on the intergranular phase for nanocrystalline nd–fe–b magnet. *Journal of Alloys and Compounds*, 486(1):257–260, 2009.

[83] T. Schrefl, J. Fidler, and H. Kronmüller. Remanence and coercivity in isotropic nanocrystalline permanent magnets. *Physical Review B*, 49(9):6100 – 6110, 1994. Cited by: 585.

[84] Jun Cui, Jung-Pyung Choi, Guosheng Li, Evgueni Polikarpov, J Darsell, N Overman, M Olszta, D Schreiber, M Bowden, T Droubay, et al. Thermal stability of mnbi magnetic materials. *Journal of Physics: Condensed Matter*, 26(6):064212, 2014.

[85] Yu He, Shunkang Pan, JingJing Yu, and YongHe Liu. Magnetic, microwave absorbing performance of al8mn5 alloy with la dopant. *Journal of Superconductivity and Novel Magnetism*, 32, 02 2019.

[86] M. Ellner. Crystal chemical parameters of the liquid-quenched mnal0.8. *Journal of Alloys and Compounds*, 422(1):192–193, 2006.

[87] Wei Lu, Junchao Niu, Taolei Wang, Kada Xia, Zhen Xiang, Yiming Song, Zhongliang Mi, Weifang Zhang, Wei Tian, and Yan Yan. Phase transformation kinetics and microstructural evolution of mnal permanent magnet alloys. *Journal of Alloys and Compounds*, 685:992–996, 2016.

[88] Taisuke Sasaki Tadakatsu Ohkubo Jiangnan Li, Hossein Sepehri-Amin and Kazuhiro Hono. Most frequently asked questions about the coercivity of nd-fe-b permanent magnets. *Science and Technology of Advanced Materials*, 22(1):386–403, 2021. PMID: 34121927.

[89] T. Schrefl, J. Fidler, and H. Kronmüller. Remanence and coercivity in isotropic nanocrystalline permanent magnets. *Phys. Rev. B*, 49:6100–6110, Mar 1994.

[90] Henry E. Sostman. Melting point of gallium as a temperature calibration standard. *Review of Scientific Instruments*, 48(2):127–130, 02 1977.

[91] C Mitsumata and M Kotsugi. Interpretation of kronmüller formula using ginzburg-landau theory. *Journal of the Magnetics Society of Japan*, 46(5):90–96, 2022.

[92] Balamurugan Balasubramanian, Pinaki Mukherjee, Ralph Skomski, Priyanka Manchanda, Bhaskar Das, and David J Sellmyer. Magnetic nanostructuring and overcoming brown's paradox to realize extraordinary high-temperature energy products. *Scientific reports*, 4(1):6265, 2014.

[93] Charles Kittel. *Introduction to Solid State Physics.* Wiley, 8 edition, 2004.

[94] Simon Bance, Florian Bittner, Thomas G. Woodcock, Ludwig Schultz, and Thomas Schrefl. Role of twin and anti-phase defects in mnal permanent magnets. *Acta Materialia*, 131:48–56, 2017.

[95] Richard M. Bozorth. *Ferromagnetism.* 1993.

[96] S. Bance, B. Seebacher, T. Schrefl, L. Exl, M. Winklhofer, G. Hrkac, G. Zimanyi, T. Shoji, M. Yano, N. Sakuma, M. Ito, A. Kato, and A. Manabe. Grain-size dependent demagnetizing factors in permanent magnets. *Journal of Applied Physics*, 116(23):233903, 12 2014.

[97] Kanika Anand, J.J. Pulikkotil, and S. Auluck. Study of ferromagnetic instability in -mnal, using first-principles. *Journal of Alloys and Compounds*, 601:234–237, 2014.

[98] P.S. Liu and G.F. Chen. Chapter two - making porous metals. In P.S. Liu and G.F. Chen, editors, *Porous Materials*, pages 21–112. Butterworth-Heinemann, Boston, 2014.

[99] Vipul Jain, Pranabananda Modak, Sudipta Patra, and Abhijit Ghosh. Origin of goss texture in grain oriented electrical steel: Role of shear bands. *Materialia*, 22:101398, 2022.

[100] X. J. Liu, I. Ohnuma, R. Kainuma, and K. Ishida. Thermodynamic assessment of the aluminum-manganese (al-mn) binary phase diagram. *Journal of Phase Equilibria*, 20(1):45–56, 1999.

[101] Malcolm Loveday, G.J. Mahon, B. Roebuck, A.J. Lacey, Eric Palmiere, C.M. Sellars, and M.R. Winden. Measurement of flow stress in hot plane strain compression tests. *Materials at High Temperatures*, 23:85–118, 05 2006.

[102] Feng Tang and Julie M. Schoenung. Strain softening in nanocrystalline or ultrafine-grained metals: A mechanistic explanation. *Materials Science and Engineering: A*, 493(1):101–103, 2008. Mechanical Behavior of Nanostructured Materials, a Symposium Held in Honor of Carl Koch at the TMS Annual Meeting 2007, Orlando, Florida.

[103] Artek R. Chalifour, Jonathon C. Davidson, Nicholas R. Anderson, Thomas M. Crawford, and Karen L. Livesey. Magnetic relaxation time for an ensemble of nanoparticles with randomly aligned easy axes: A simple expression. *Phys. Rev. B*, 104:094433, Sep 2021.

[104] D. Salazar, A. Martín-Cid, R. Madugundo, J. M. Barandiaran, and G. C. Hadjipanayis. Coercivity enhancement in heavy rare earth-free NdFeB magnets by grain boundary diffusion process. *Applied Physics Letters*, 113(15):152402, 10 2018.

[105] Zhongwu Liu, Jiayi He, and Raju V. Ramanujan. Significant progress of grain boundary diffusion process for cost-effective rare earth permanent magnets: A review. *Materials Design*, 209:110004, 2021.

[106] H.L. Fang, J. Liu, P.W. Huang, and D.W. Shi. Tripling in coercivity (hc) for the thermal and structural highly stabilized mnalbi-c rare earth free permanent magnet via bi doping. *Materials Design*, 230:111887, 2023.

Appendix A

Additional Data

A.1 MnAlBi Alloy EDX Spectra

Below contains the EDX spectral data from the SEM image captured of as-cast $Mn_{58.9}Al_{37.9}Bi_{3.2}$ as discussed in Section 5.3.2, displayed in Figure 5.8. During data capture, potential elements were preselected to prevent erronous contaminant identification and as such, only Mn, Al, Bi, Fe, Cu O and C were permitted for identification. This was in recongition of the high purity of casting reagents, potential contamination from residual C and Fe from arc melting crucible cleaning products and steel wool, contamination from the Cu crucible and oxidation of phases from atmospheric contamination. It is of note that C contamination is rarely confirmed by EDX due to peak corroboration and EDX signal being dependent on atomic number, implying that any detection of C is, at best, qualitative without significant additional refinement and most likely a result of diamond solution polishing agents embedding into the surface of scanned material.

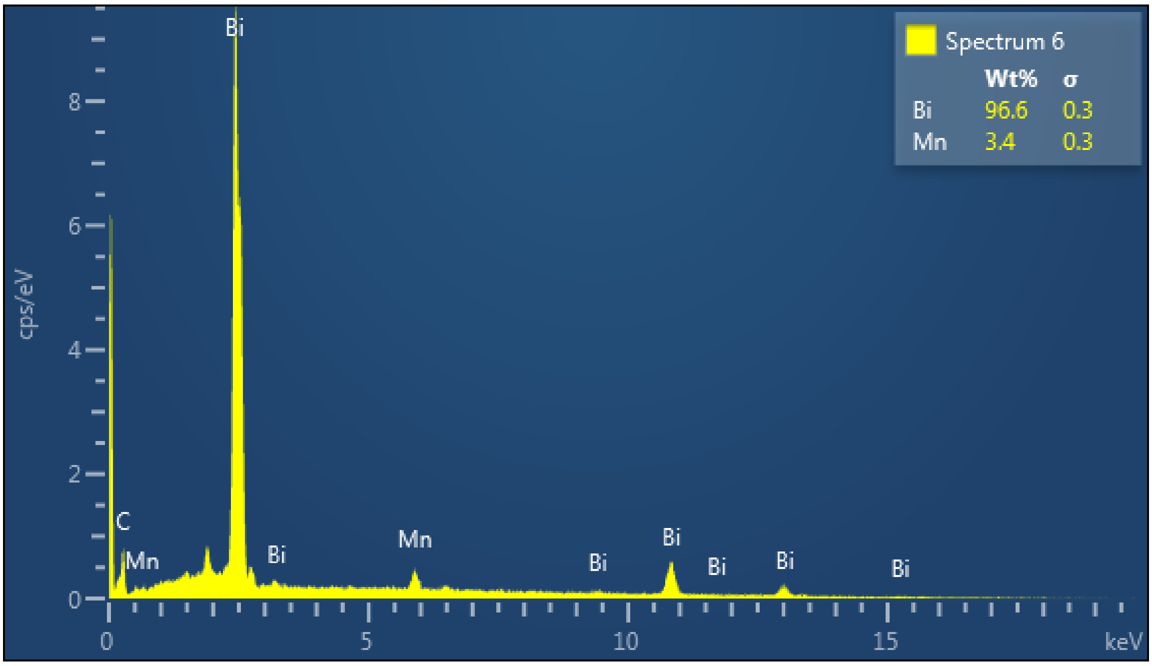

Fig. A.1 The Energy Dispersive X-Ray spectrum of point Spectrum 6 of Figure 5.8 of as-cast $Mn_{58.9}Al_{37.9}Bi_{3.2}$

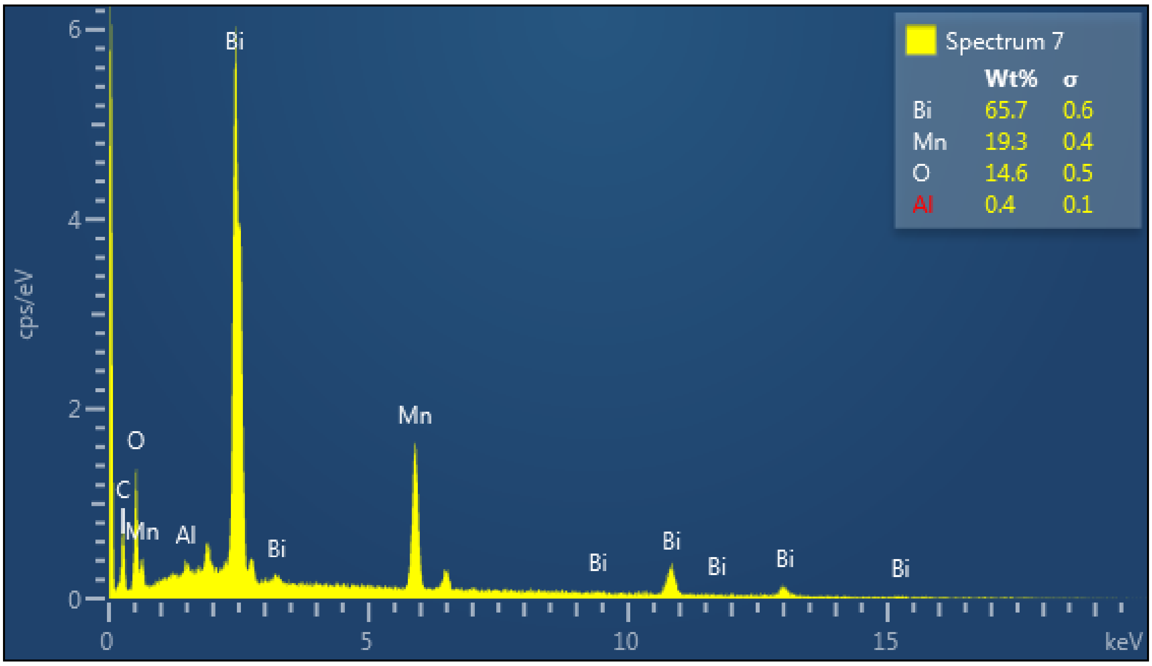

Fig. A.2 The Energy Dispersive X-Ray spectrum of point Spectrum 7 of of Figure 5.8 as-cast $Mn_{58.9}Al_{37.9}Bi_{3.2}$

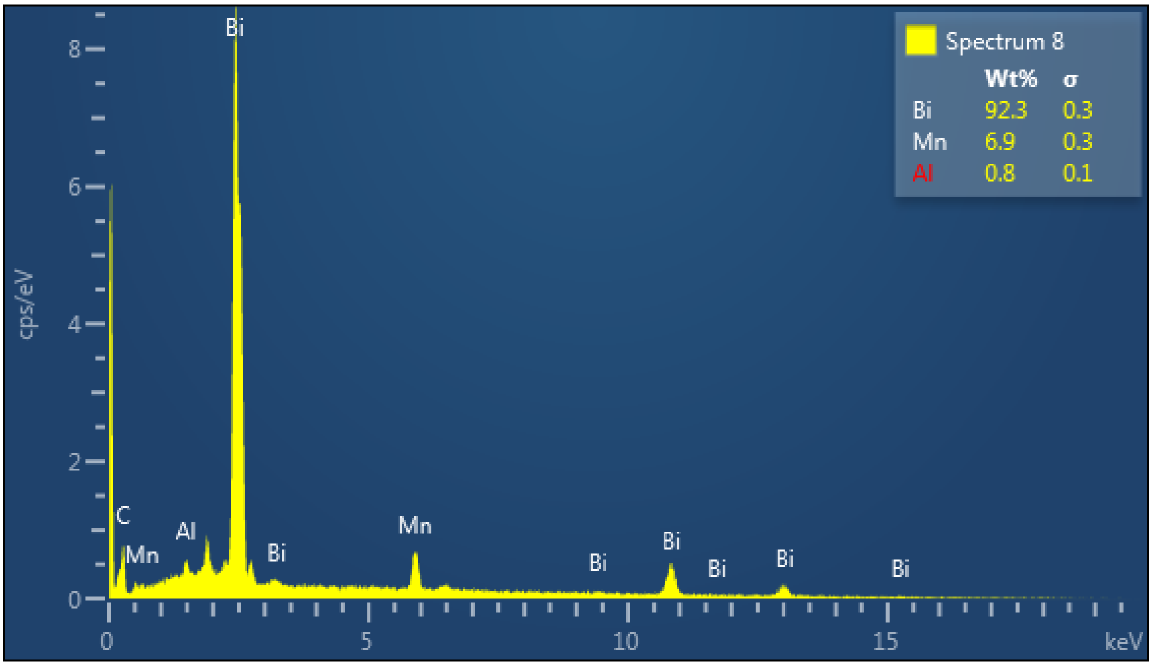

Fig. A.3 The Energy Dispersive X-Ray spectrum of point Spectrum 8 of Figure 5.8 as-cast $Mn_{58.9}Al_{37.9}Bi_{3.2}$

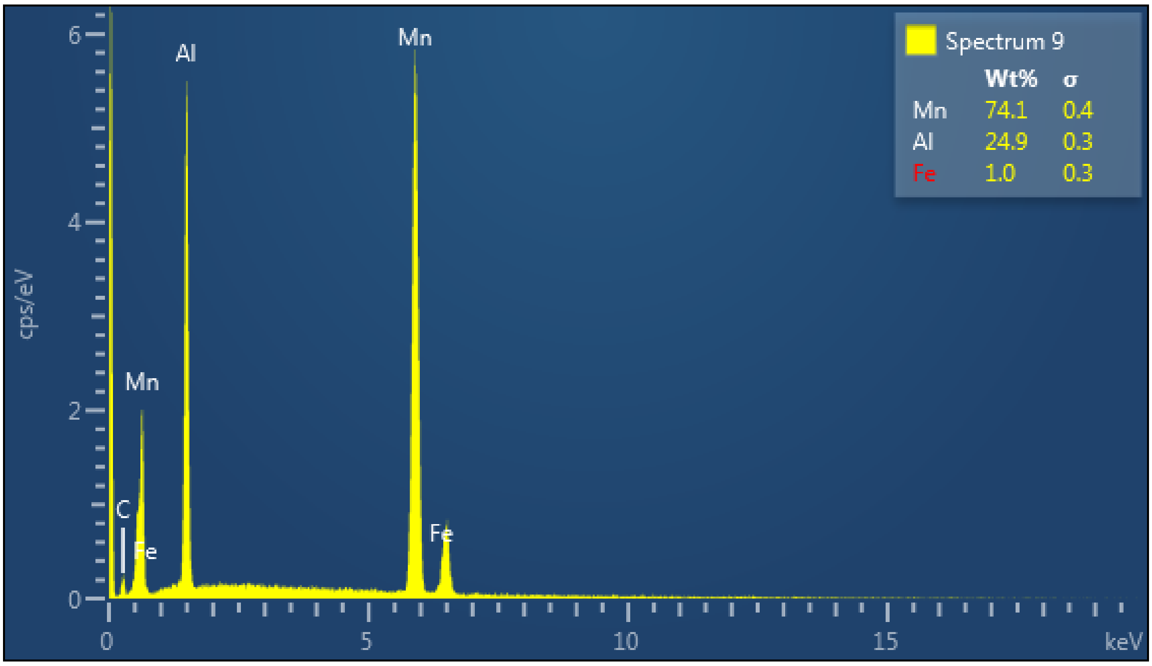

Fig. A.4 The Energy Dispersive X-Ray spectrum of point Spectrum 9 of Figure 5.8 as-cast $Mn_{58.9}Al_{37.9}Bi_{3.2}$

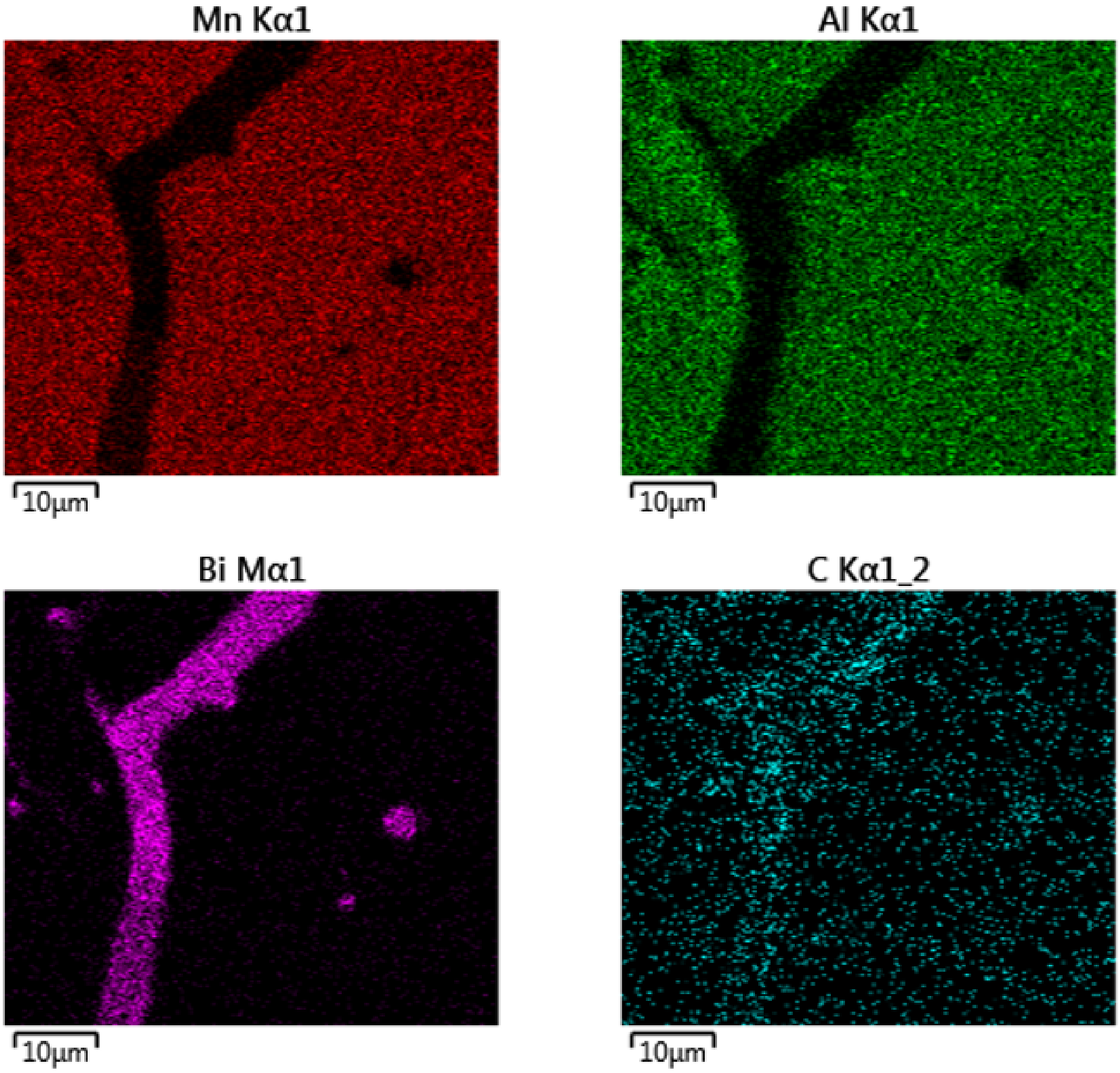

Fig. A.5 A colour spectrum of a 2D area EDX scan of the SEM image shown in Figure 5.8, showing the distribution of different respective elements throughout the alloy.

A.2 Proof of Bloch Fit

Initially, if one supposes the following relationship from Kronmuller and Fahnle [37]

$$J_S(T,0) = J_{S,0}(1-(\frac{T}{T_0})^{\frac{3}{2}}) \tag{A.1}$$

thus

$$\Delta(\frac{J_S}{T^{\frac{3}{2}}}) \rightarrow J_{S,0}\cdot(\frac{D_{sp}}{k_B}\cdot(\frac{J_{S,0}}{0.117\mu_0\mu_B})^{\frac{2}{3}})^{\frac{-3}{2}} = \Phi \tag{A.2}$$

therefore

$$\Phi = 0.117\mu_0\mu_B\cdot(\frac{D_{sp}}{k_B})^{\frac{-3}{2}}, [\Phi] = [T][K]^{\frac{-3}{2}} \tag{A.3}$$

Rearranging,

$$D_{sp} = k_B\cdot(\frac{\Phi}{0.117\mu_0\mu_B})^{\frac{-2}{3}}, [D_{sp}] = [J][m]^2 \tag{A.4}$$

Percentage of solid angle measured by dual-cone

Surface area of unit sphere

$$A_{sphere} = 4\pi \tag{A.5}$$

Surface area of spherically capped cone of angle

$$A_{cone} = 4\pi sin^2(\frac{\theta}{2}) \tag{A.6}$$

Ratio of cone to hemisphere

$$\frac{A_{cone}}{A_{hemisphere}} = \frac{2A_{cone}}{A_{sphere}} = \frac{8\pi sin^2(\frac{\theta}{2})}{4\pi} = 2sin^2(\frac{\theta}{2}) \tag{A.7}$$